

High Pressure Investigations of Some  
Topologically Non-trivial Compounds by  
Transport Techniques and Spectroscopic Methods

*By*

Utpal Dutta

PHYS01201504025

Bhabha Atomic Research Centre, Mumbai

A thesis submitted to the  
Board of Studies in Physical Sciences

*In partial fulfillment of requirements  
for the Degree of*

**DOCTOR OF PHILOSOPHY**

*of*

**HOMI BHABHA NATIONAL INSTITUTE**



January, 2020

## STATEMENT BY THE CANDIDATE

This dissertation has been submitted in partial fulfillment of requirements for an advanced degree at Homi Bhabha National Institute (HBNI) and is deposited in the Library to be made available to borrowers under rules of the HBNI.

Brief quotations from this dissertation are allowable without special permission, provided that accurate acknowledgement of source is made. Requests for permission for extended quotation from or reproduction of this manuscript in whole or in part may be granted by the Competent Authority of HBNI when in his or her judgment the proposed use of the material is in the interests of scholarship. In all other instances, however, permission must be obtained from the author

**Name & Signature of the Candidate**

# DECLARATION

I, hereby declare that the investigation presented in the thesis has been carried out by me. The work is original and has not been submitted earlier as a whole or in part for a degree / diploma at this or any other Institution / University.

**Name & Signature of the Candidate**

## List of Publications arising from the thesis

### Journals

1. Pressure-induced superconductivity in semimetallic  $1T$ -TiTe<sub>2</sub> and its persistence upon decompression: **U. Dutta**, P.S. Malavi, S. Sahoo, B. Joseph, S. Karmakar, Physical Review B 97, 060503 (2018) (Rapid Communication).
2. Infrared spectroscopic measurements of structural transition and charge dynamics  $1T$ -TiTe<sub>2</sub> under pressure: **U. Dutta**, S. Sahoo, P. S. Malavi, F. Piccirilli, P. Di Pietro, A. Perucchi, S. Lupi, and S. Karmakar, Physical Review B 99, 125105 (2019).

### Conferences

1. High pressure structural and electrical investigations of Sb<sub>2</sub>S<sub>3</sub>: (Presented in DAE SSPS 2017).
2. High pressure magneto-resistance measurements on Weyl semimetals NbP and NbAs: Oral presentation in EHPRG-2019 (Prague).

### Other Publications

1. High Pressure structural and superconducting properties of Ca<sub>1-x</sub>Eu<sub>x</sub>FeAs<sub>2</sub>: **Utpal Dutta**, Subodha Sahoo, Pallavi S Malavi, Boby Joseph and S. Karmakar (Conference: DAE-SSPS-2016) (DOI: 10.1063/1.4980726).
2. High Pressure Structural and Vibrational Properties of Cu<sub>3</sub>VS<sub>4</sub>: Subodha Sahoo, **Utpal Dutta**, Pallavi S. Malavi, and S. Karmakar (Conference: DAE SSPS-2016) (DOI: 10.1063/1.4980182).
3. Pressure induced structural, electronic topological, and semiconductor to metal transition in AgBiSe<sub>2</sub>; V. Rajaji, Pallavi S. Malavi, Sharma S. R. K. C. Yamijala, Y. A. Sorb, **Utpal Dutta**, Satya N. Guin, B. Joseph, Swapan K. Pati, S. Karmakar, Kanishka Biswas, and Chandrabhas Narayana, APPLIED PHYSICS LETTERS 109, 171903 (2016).

4. Structural, vibrational, and electrical properties of  $1T$ -TiTe<sub>2</sub> under hydrostatic pressure: Experiments and theory: V Rajaji, **Utpal Dutta**, PC Sreeparvathy, Saurav Ch Sarma, YA Sorb, B Joseph, Subodha Sahoo, Sebastian C Peter, V Kanchana, Chandrabhas Narayana, Physical Review B 97, 085107 (2018).
5. Pressure-induced suppression of charge density wave and emergence of Superconductivity in  $1T$ -VSe<sub>2</sub>, S. Sahoo, **U. Dutta**, L. Harnagea, A.K. Sood, S. Karmakar, arXiv:1908.11678 (2019).

**Name & Signature of the Candidate**

---

*Dedicated to*  
*My*  
*Mother*

---

## ACKNOWLEDGEMENTS

First and foremost, I would like to express my deep respect and gratitude to my supervisor, Dr. Sukanta Karmakar, for his guidance, continuous support and kindness. It would not be possible for me to complete the thesis work without his valuable suggestions, encouragement and constant guidance throughout my PhD.

I am thankful to all the members of my Doctoral committee, Dr. T. V. Chandrasekhar Rao, Dr. Chitra Murli, Dr. Alka Garg and Dr. Awadhesh Mani, for their useful discussions and meaningful advice. I am grateful to Dr. Pallavi Malavi for teaching me the basic high pressure and low temperature techniques during the initial days of my PhD. My special thanks to Subodha Sahoo, for spending a good time during all my years. I would like to thank all the members and office staffs of HP & SRPD for their various academic supports. I am grateful to Dr. Chandrabhas Narayana and his groups for fruitful collaboration. Furthermore, I also want to thank all the staff from Helium Plant facility of TPD, BARC for providing liquid Helium time to time for making the cryostat based low temperature experiments possible. I thank Dr. N. Naveen Kumar and Dr. R. Tewari of MSD, BARC for helping in LEED measurements on some of my samples.

I am deeply grateful for the financial support from Department of Atomic Energy (DAE), Department of Science and Technology (DST), India and Elletra Synchrotron facility, Italy. Furthermore, I am thankful to all the beamline staffs of XRD1 & SISSI beamline of Elettra synchrotron facility.

I would also like to express my heartiest gratitude towards all my friends, in particular; Rim, Soumik, Debasis, Sayid, Anupam, Debasmit, Soumen, Raman, Avinash, Pujan, Tapas, Srinivas, Shitaljit, Santosh, Mrinal, Nirmalendu, Ananya, Chinu, and Arpita.

Finally but most importantly, I am extremely grateful to my family for their constant love and mental supports all through my life. More than anyone, I am grateful to my mother, without her I would have no existence and the thesis is dedicated to her.

# Table of Contents

List of Publications	iii
ACKNOWLEDGEMENTS	vi
Table of Contents	vii
List of Figures	x
List of Tables	xxv
List of Abbreviations	xxvi
Synopsis	1
Bibliography	8
<b>1 Introduction</b>	<b>11</b>
1.1 Overview . . . . .	11
1.2 Topological Insulator and superconductors: . . . . .	17
1.2.1 Two Dimensional topological insulators: . . . . .	17
1.2.2 Three Dimensional topological insulators: . . . . .	19
1.2.3 Transport signature of topological insulator: . . . . .	22
1.2.4 Effect of pressure on topological insulator: . . . . .	23
1.2.5 TQPT and pressure induced topological Superconductor: . . . . .	26
1.3 Topological semimetal . . . . .	29
1.3.1 Topological consequences of Weyl semimetal: . . . . .	30
1.3.2 Optical properties of WSMS: . . . . .	31
1.3.3 Transport properties of Weyl semimetals: . . . . .	33
1.3.4 Classifications of Weyl semimetals: . . . . .	36
1.3.5 High Pressure studies on type-I WSMS: . . . . .	38
1.3.6 High Pressure studies on type-II WSMS: . . . . .	40
1.4 Materials investigated in this thesis: . . . . .	42
1.4.1 $\text{TiTe}_2$ . . . . .	43
1.4.2 $\text{Sb}_2\text{S}_3$ . . . . .	43
1.4.3 $\text{AgBiSe}_2$ . . . . .	44
1.4.4 NbP . . . . .	45
1.4.5 NbAs . . . . .	46
1.4.6 $\text{TaIrTe}_4$ . . . . .	46
1.5 Outline of the thesis: . . . . .	47
<b>2 Experimental techniques</b>	<b>48</b>
2.1 Synthesis and ambient pressure characterization: . . . . .	48
2.1.1 Synthesis: . . . . .	49
2.1.2 Ambient pressure Characterization: . . . . .	50

2.2	Basics principle of high pressure physics: . . . . .	52
2.2.1	Diamond Anvil Cell (DAC): . . . . .	53
2.2.2	Gasket: . . . . .	57
2.2.3	Pressure transmitting medium: . . . . .	57
2.2.4	Pressure calibration: . . . . .	59
2.3	Low temperature techniques at high pressure: . . . . .	65
2.3.1	Helium bath type cryostat: . . . . .	65
2.3.2	Cryogenic S700X SQUID: . . . . .	68
2.3.3	Liquid Nitrogen based microscope cryostat: . . . . .	69
2.4	High pressure transport and magneto-transport techniques: . . . . .	70
2.4.1	Electrical resistance measurements under high-P and low-T: . . . . .	71
2.4.2	Magnetoresistance and Hall Effect under pressure: . . . . .	76
2.4.3	High pressure magnetic measurements: . . . . .	78
2.5	High pressure spectroscopic methods: . . . . .	80
2.5.1	X-ray diffraction under pressure: . . . . .	80
2.5.2	IR reflectance measurements under pressure: . . . . .	81
<b>3</b>	<b>Transport and spectroscopic investigations of <math>\text{TiTe}_2</math> under pressure</b>	<b>87</b>
3.1	Introduction . . . . .	87
3.2	Experimental Details . . . . .	91
3.2.1	Synthesis and characterization . . . . .	91
3.2.2	Resistance measurement techniques under pressure: . . . . .	94
3.2.3	Non hydrostatic XRD measurements: . . . . .	95
3.2.4	IR reflectance measurements under pressure: . . . . .	96
3.3	Results and Discussions: . . . . .	97
3.3.1	Room temperature resistance measurements on polycrystalline $\text{TiTe}_2$ under pressure . . . . .	97
3.3.2	Low temperature resistance measurements on single crystalline $\text{TiTe}_2$ under pressure . . . . .	101
3.3.3	High Pressure X-ray Diffraction under non-hydrostatic compression: . . . . .	111
3.3.4	Infrared spectroscopic measurements in single crystalline $1T$ - $\text{TiTe}_2$ under pressure . . . . .	117
3.4	Conclusions: . . . . .	130
<b>4</b>	<b>High pressure structural and electrical investigations of <math>\text{Sb}_2\text{S}_3</math></b>	<b>133</b>
4.1	Introduction . . . . .	133
4.2	Experimental details: . . . . .	135
4.3	Results and Discussions: . . . . .	136
4.3.1	High pressure XRD measurements: . . . . .	136
4.3.2	High pressure transport measurements: . . . . .	138
4.3.3	Discussions: . . . . .	142
4.4	Conclusions: . . . . .	144

<b>5</b>	<b>High pressure electrical transport and optical reflection study of AgBiSe<sub>2</sub></b>	<b>146</b>
5.1	Introduction . . . . .	146
5.2	Experimental Details: . . . . .	148
5.3	Results: . . . . .	149
5.3.1	Mid-IR reflectance measurements: . . . . .	149
5.3.2	Resistance measurements: . . . . .	152
5.4	Discussions: . . . . .	154
5.5	Conclusions: . . . . .	156
<b>6</b>	<b>High pressure magneto-resistance measurements on Weyl semimetals NbP and NbAs</b>	<b>157</b>
6.1	Introduction . . . . .	157
6.2	Experimental techniques: . . . . .	158
6.3	Results on NbP: . . . . .	159
6.3.1	XRD measurements: . . . . .	159
6.3.2	Resistance measurements: . . . . .	159
6.3.3	Hall Measurements: . . . . .	161
6.3.4	MR measurements: . . . . .	163
6.4	Results on NbAs . . . . .	165
6.4.1	XRD under pressure: . . . . .	165
6.4.2	High Pressure Magnetotransport measurements on NbAs: . . .	167
6.5	Discussions: . . . . .	169
6.6	Conclusions: . . . . .	170
<b>7</b>	<b>High pressure transport and magneto-transport measurements in the type-II Weyl semimetal TaIrTe<sub>4</sub></b>	<b>172</b>
7.1	Introduction . . . . .	172
7.2	Experimental Details: . . . . .	174
7.3	Results: . . . . .	175
7.3.1	Resistance and magnetoresistance measurements under pressure	175
7.3.2	XRD measurements under pressure: . . . . .	178
7.4	Discussions: . . . . .	179
7.5	Conclusions: . . . . .	180
<b>8</b>	<b>Conclusions and Outlook</b>	<b>181</b>
	<b>Bibliography</b>	<b>186</b>

## List of Figures

- 1.1 (a) Edge states as skipping cyclotron orbits in a Quantum Hall state.  
(b) A sketch of the band structure of a Chern insulator, where the linear chiral edge band present at the interface with a trivial insulator is represented by a red line. The figure is taken from reference [8]. . . . . 12
- 1.2 A quantum spin Hall insulator can be constructed by two Chern insulators that are related by the time-reversal symmetry. (a) A Chern insulator with a Chern number of  $n = +1$  has a chiral edge mode as a result of an out-of-plane magnetization. (b) The bottom edge projection of the electronic structure of the  $n = +1$  Chern insulator. (c,d,) Same as Panels (a,b) but with a time-reversal operation onto the system. (e,f,) A quantum spin Hall state can be obtained by combining the above-two Chern insulator states. The resulting electronic structure on the edges is described by two counterpropagating edge modes that cross each other at  $k = 0$  (or  $k = \pi$ ). The crossing is protected by the time-reversal symmetry as a result of the Kramers theorem. The figure is taken from reference [8]. . . . . 14
- 1.3 2D TI phase in CdTe/HgTe QWs (A) The band ordering in the constituent materials HgTe and CdTe. (B) schematic picture of quantum well geometry and lowest sub-bands for two different thicknesses. Band inversion occurs when the well thickness is larger than the critical thickness. This figure is taken from reference [36]. . . . . 18
- 1.4 The surface-band-dispersion second-derivative image of  $\text{Bi}_{0.9}\text{Sb}_{0.1}$  along  $\Gamma$  and M. Figure is taken from reference [43]. . . . . 21

- 1.5 (a) Temperature dependent electrical resistance of  $\text{SmB}_6$  sample. The inset shows the crystal structure of it. (b) Temperature dependence resistivity of various samples of  $\text{Bi}_2\text{Te}_2\text{Se}$  and the inset shows the temperature dependent Hall coefficient,  $R_H$ , for the respective samples. (c) Temperature dependent normalized resistance of  $\text{LaSb}$  at  $H = 0$  (green) and  $H = 9$  T (red). (d) Temperature dependent normalized resistance of  $\text{SbB}_6$  at 7 GPa (green) and ambient pressure (red). Figures are taken from references [48, 54, 56] . . . . . 23
- 1.6 Temperature dependent electrical resistance of  $\text{Bi}_2\text{Te}_3$  in the vicinity of the superconducting transition.(b) P-T phase diagram with various structural phases as taken from [57]. (c) P-T phase diagram and pressure dependence of superconducting volume fraction of  $\text{Bi}_2\text{Te}_3$  as taken from [58]. (d) Pressure dependence electrical resistivity of  $\text{Bi}_2\text{Te}_3$  at room temperature. The arrows indicate the anomaly in the resistivity related to the structural transition. The inset presents the enlarge view in the low pressure region. Figures are taken from [57–59]. 24
- 1.7 Phase diagrams of  $\text{Bi}_2\text{Se}_3$  (a) P-T phase diagram of  $\text{Bi}_2\text{Se}_3$  as taken from reference [26]. (b) Structural phase diagram of  $\text{Bi}_2\text{Se}_3$  as taken from reference [27]. . . . . 25
- 1.8 (a) Schematic illustration of Topological quantum phase transition (TQPT). NI, TSM and TI stand for normal insulator, topological semimetal and topological insulator respectively. (figure is taken from reference [65]). (b) Pressure dependence  $c/a$  ratio which shows a minimum at TQPT. This figure is taken from reference [65]. (c) Reflectance at low pressure and low photon energy after fringe removal. Detailed description is given in reference [65]. (d) P-T phase diagram of  $\text{BiTeI}$  including TQPT, SC and structural transitions. Detailed description is given in reference [67]. . . . . 28

1.9	Electronic P-T phase diagram for $\beta$ -Bi <sub>4</sub> I <sub>4</sub> . (a) Superconducting T <sub>c</sub> shows dome-like behavior. The resistivity values at 300 K are also shown. The resistivity of $\beta$ -Bi <sub>4</sub> I <sub>4</sub> exhibits a more complicated feature, which demonstrates that high pressure dramatically alters the electronic properties in $\beta$ -Bi <sub>4</sub> I <sub>4</sub> . (b) Schematic illustrations of the band structure evolution under various pressures. Detailed description is given in reference [69]. . . . .	29
1.10	Optical conductivity of TaAs at 5 K. The blue and black solid lines through the data are linear guides to the eye. The inset shows the spectral weight as a function of frequency at 5 K (red solid curve), which follows an $\omega^2$ behavior (blue dashed line). This figure is taken from reference [80]. . . . .	32
1.11	Landau level indices $n$ as functions of $1/B$ for NbAs. The solid and open symbols represent the data points at $p = 0$ and 2.31 GPa, respectively. The two dot lines are guidelines for 0.125 and 0.375, respectively. Figure is taken from the reference [86]. . . . .	35
1.12	Universal triangular T-H phase diagram of various semimetals. Figure is taken from reference [55] . . . . .	36
1.13	Possible types of Weyl semimetals. a, Type-I WP with a pointlike Fermi surface. b, A type-II WP appears as the contact point between electron and hole pockets. The grey plane corresponds to the position of the Fermi level, and the blue (red) lines mark the boundaries of the hole (electron) pockets. Figure is taken from reference [104] . . .	37

1.14	Temperature-dependent resistance with increasing and decreasing pressures. a Temperature-dependent resistance from 92 to 100 GPa with increasing pressure. The $R(T)$ curves under different pressures with decreasing pressure are shown in b. The upper-left inset in a shows the resistance vs. temperature under different fields at 92 GPa, and the lower-right inset shows the enlarged view of the data measured near 71 GPa in low-temperature region. The superconductivity is further evident by a sharp 75% drop of the normal state resistance under 30 GPa, as shown in the left inset in b. The inset on the right-hand side in b shows the pressure dependence of $T_c$ in decreasing pressure. This figure is taken from reference [29] . . . . .	39
1.15	Pressure-temperature phase diagram of $WTe_2$ and pressure dependent Hall coefficient. Figure is taken from [99] . . . . .	41
1.16	Summary of the experimental results on $TaIrTe_4$ . (a) P-T phase diagram with structural information for $TaIrTe_4$ .(b) Pressure dependence of Hall coefficient measured at 10 K and (c) ) Pressure dependence MR measured at 10 K. Figure is taken from [114] . . . . .	42
2.1	Schematic view of the arrangement of the diamond anvils and the gasket in a DAC (left), and enlarged view of the sample chamber and its surrounding (right). Figure is taken from reference [148]. . . . .	54
2.2	(a) Layout of the Stuttgart type DAC. For pressure generation the piston holding the upper diamond is pressed towards the main body of the DAC holding the lower diamond by the levers. Fine tuning of the threaded rods control the mechanical movement of the levers. (b)The pictures of the main body, piston and the gear set are shown. (c) A complete picture of the DAC when it is closed and its dimension in shown. Figures are taken from reference [149]. . . . .	55
2.3	(a)Dimensions of the easyLab make Mcell ultra DAC for magnetic and magnetoresistance measurement. (b) Individual parts of the cell. (c) Schematic of the Cell and its components. . . . .	56
2.4	A schematic diagram of a typical ruby fluorescence set-up for pressure measurement. . . . .	59

2.5	The The 3d levels of $\text{Cr}^{3+}$ in the free ion and in the cubic and trigonal crystal field of the ruby crystal $\alpha\text{-Al}_2\text{O}_3$ . The 3d levels of the free $\text{Cr}^{3+}$ ions are split under the cubic and trigonal crystal field. The absorption and emission processes related to the ruby photoluminescence are also indicated. Figure is taken from reference [152]. . . . .	60
2.6	Temperature dependence of the luminescence spectra. (a) Spectra of a single crystal of sapphire (not intentionally doped with Cr) at different temperatures. Below $T=50$ K, the line width is mainly limited by the spectrometer resolution and residual internal strain. (b) Energies of the R1 and R2 emission lines as a function of temperature. The inset shows the temperature dependence of the corresponding line widths. Figure is taken from [152]. . . . .	62
2.7	Normalized R-lines spectra taken at two different pressures (1 GPa and 4.6 GPa) at room temperature. Data is taken during one of the measurements in this thesis. . . . .	63
2.8	Ruby measurements taken at various pressures. Data is taken during one of the measurements in this thesis. . . . .	64
2.9	Layout of the DAC in the helium-bath cryostat. Pressure can be tuned by the pressure tuning rode without removing the DAC from the cryostat. Figure is taken from reference [148] . . . . .	66
2.10	(Color online) Schematics of the cryogenic arrangement for DAC-based high pressure low temperature resistance measuring setup along with the in situ ruby pressure measurement facility and the sample viewing arrangement. Hs and V1 denote the valves, Ms, pressure gauge; $P_s$ , various types of vacuum pumps; F, helium gas flowmeter; DM, the dichroic mirror; M, silver-coated mirror, $10\times$ objective; L, achromatic lens; F, edge filter; ILL, back illumination lamp and D, DAC. Figure is taken from reference [157] . . . . .	67
2.11	Diagram of the Cryogenic S700X SQUID magnetometer. (b) Schematic illustration of the temperature control in S700X SQUID. Figure is taken from reference [137]. . . . .	69

2.12	(a) Schematics of the cryostat and its components. (b) Figure of the cryostat used for high pressure low temperature IR reflectance measurements. (c) Picture of the DAC mounted inside the cryostat. . . . .	70
2.13	Schematic of van der Pauw configuration . . . . .	72
2.14	(a) Illustration of the typical van der Pauw configuration in a DAC. (b) Four platinum electrodes are arranged on top of one of the diamond culets. (c) Picture of the mounted sample attach with the electrodes. (d) Optical image of the sample space. . . . .	75
2.15	Schematics of the resistance measurements under non-hydrostatic condition. . . . .	76
2.16	(a) Schematic for magnetoresistance measurements. (b) Picture of the sample attached with the electrodes. (c), (d) respective figures for Hall measurements. . . . .	78
2.17	Schematic illustration of the x-ray powder diffraction setup at a typical synchrotron beamline. Figure is taken from reference [148]. . . . .	81
2.18	Schematic of a FTIR spectrometer. Figure is taken from reference [172].	83
2.19	Experimental configuration of high pressure reflectivity measurements. Figure is taken from [149] . . . . .	83
2.20	Schematic layout of the SISSI Beamline. Figure is taken from [149]. . . . .	85
3.1	X-ray powder diffraction pattern of as grown $1T$ - $\text{TiTe}_2$ at room temperature ( $\lambda=1.5406\text{\AA}$ ). Le-Bail fitted pattern using the known trigonal structure, as show in inset. Photograph of as grown single crystal flakes are also shown. . . . .	92
3.2	Reciprocal lattice patterns of $1T$ - $\text{TiTe}_2$ single crystal from [100] and [001] axis directions obtained from Low Energy Electron Diffraction measurements at room temperature with the help of TEM JEOL 2000FX instrument. . . . .	92
3.3	In-plane measured resistance data and obtained resistivity curves of $\text{TiTe}_2$ single crystal in the temperature range 1.4 -300K. . . . .	93
3.4	Zero field cooled (ZFC) magnetic susceptibility of as grown single crystals of $\text{TiTe}_2$ over the temperature range 2-250K. Inverse susceptibility plot is also shown. . . . .	94

- 3.5 Pressure-dependent electrical resistance of  $\text{TiTe}_2$  (black square and a line corresponding to the left y axis) and its first derivative (blue line corresponding to the right y axis). The red arrow at  $\sim 8.8$  GPa indicates the structural transition. The solid green arrows at 2.1 GPa and 3.4 GPa indicate the isostructural electronic transitions in the trigonal ( $\bar{P}3m1$ ) phase. The inset highlights the resistance minimum in the vicinity of the structural transition [187]. . . . . 98
- 3.6 Pressure dependent electrical resistance plot for the  $\text{TiTe}_2$  compound up to  $\sim 16$  GPa. The significant hysteresis has been found between the pressure increasing and decreasing cycle [187]. . . . . 99
- 3.7 (a)  $c/a$  ratio as a function of pressure for polycrystalline  $1T\text{-TiTe}_2$ . (b) FWHM of  $A_{1g}$  and  $E_g$  mode as a function of pressure. The solid and vertical dotted lines signify a guide to the eye and structural phase transition, respectively. . . . . 102
- 3.8 (a) In-plane resistance of  $1T\text{-TiTe}_2$  as a function of temperature at various quasihydrostatic pressures. Inset shows a significant resistance drop below SC onset  $T_c$  2.5 K at 5 GPa. (b) The magnified R-T data near SC transition at various pressures. (c) Variation of the R-T curve near  $T_c$  under magnetic fields at 8.9 GPa. . . . . 103
- 3.9 (a) Low-T longitudinal resistance, measured at zero field and at 7 T, at various quasihydrostatic pressure. (b)  $R(T)$  plots across  $T_c$  at 9.5 GPa under different fields up to 7 T. Lower inset: plots of  $T_c$  vs H at 7.5 and 9.5 GPa; solid lines are best fits using the empirical formula  $H_{c2}(T) = H_{c2}(1 - T/T_c)^{1+\alpha}$ . Upper inset: dc susceptibility of the SC state at 8.5 GPa. Plots of (c) magnetoresistance  $\text{MR} (\%) = [(R_{7T} - R_{0T}) \times 100 / R_{0T}]$  at 10 K and onset  $T_c$  and (d) Hall coefficient  $R_H$  at 10 K and  $\text{RRR} (=R_{280K}/R_{10K})$  as a function of pressure. Insets are schematic illustrations. . . . . 104
- 3.10 Plots of magneto-resistance ( $\text{MR} \%$ ) data at 10 K as a function of squared magnetic field at various quasi-hydrostatic pressures . . . . . 105

3.11	(a) DC magnetic susceptibility measured near superconducting $T_c$ at 8.5 GPa under ZFC and FC scheme. (b) Resistance measurements across the SC $T_c$ at 8.5 GPa at two different excitation currents (10 mA and 1 mA). Inset shows the first derivative of resistance data of 1 mA current excitation, to determine the onset and zero resistance SC $T_c$ . . . . .	107
3.12	Excitation (current) dependence of SC $T_c$ of the pressurized sample (7.8 GPa). . . . .	108
3.13	Temperature-dependent in-plane resistance of 1T-TiTe <sub>2</sub> single crystal under (a)-(c) various nonhydrostatic compression up to 29 GPa and (d) decompression pressures. Insets in respective panels show magnified R-T data near superconducting transitions at various pressures.	109
3.14	Field dependence of the resistance drop near SC transition of the pressure released sample (0.5 GPa) from uniaxially compressed to 29 GPa. . . . .	110
3.15	(a) Angle dispersive x-ray powder diffraction of 1T-TiTe <sub>2</sub> at some selected pressures at $T = 300$ K. A clear structural phase transition takes place above 10.2 GPa where additional peaks appear in the diffraction data. (c) Rietveld profile fitted XRD pattern of TiTe <sub>2</sub> in its trigonal phase (space group $P\bar{3}m1$ ) at 1.6 GPa and (b) Le-Bail profile fitted pattern in the NbTe <sub>2</sub> structured monoclinic phase (space group $C2/m$ , $z=6$ ) at 10.2 GPa. The black crosses are background subtracted data points, the red line represents the fitted pattern, green tick marks are the calculated Bragg reflections and the residuals are shown by the blue line. Inset, the (001) peak intensity of the trigonal phase gets suppressed irreversibly above 4.5 GPa, which can be visibly observable in image pattern too, shown in (d) . . . . .	111

- 3.16 TiTe<sub>2</sub> in its (a) trigonal (CdI<sub>2</sub>-type)  $P\bar{3}m1$  space group at 1 bar and (b) monoclinic (NbTe<sub>2</sub>-type)  $C2/m$  space group at 10.2 GPa. The Ti atoms are represented by silver spheres, Te atoms are represented by green spheres. (c) Volume per formula unit as plotted as a function of pressure, open circles are during decompression; dashed line is the EOS found in hydrostatic case (obtained from ref. [187]). . . . . 113
- 3.17 (a)  $c/a$  ratio as a function of pressure; dashed line is from hydrostatic pressure study (ref. [187]) (b) Te-Ti-Te layer and interlayer thickness variation as a function of pressure. . . . . 114
- 3.18 The phase diagram for  $1T$ -TiTe<sub>2</sub> under nonhydrostatic compression (bottom pressures) and decompression (top pressures). Resistances at 10 and 280 K have been plotted on logarithmic scale (labels on the right axis, arrows in legends indicate corresponding scale). Top decompression pressure scale has been adjusted in order to match the  $T_c$ 's and resistance values roughly with that of compression.  $P_c$  denotes onset pressure and zero resistance SC has been observed at  $P/c$  upon decompression. . . . . 116
- 3.19 [001] zone axis LEED pattern of (a) the starting sample and (b) pressure released sample . . . . . 117
- 3.20 (a) Superconducting transition temperature ( $T_c$ ) variation of TiTe<sub>2</sub> under various compression and decompression pressures. (b) Te-Ti-Te layer and interlayer thickness variation as a function of pressure, as determined from Rietveld refinement of x-ray diffraction patterns. Hatched regions denote the respective average layer thickness in the high-pressure monoclinic structure. The anomalous change in interlayer spacing at  $\sim 2.5$  GPa and the structural transition at 11 GPa are marked by vertical dashed lines. . . . . 118

- 3.21 (a) Room-temperature IR reflectance spectra at the diamond-sample interface  $R_{s-d}(\omega)$  for  $1T$ - $\text{TiTe}_2$  at 1 GPa. Open circles are the experimental data, and the orange solid line is the calculated reflectance spectra using Drude-Lorentz oscillators (shown up to  $16\,000\text{ cm}^{-1}$ ). (b) Room-temperature far-IR  $R_{s-d}(\omega)$  spectra at various high pressures. Spectra at higher pressures are arbitrarily shifted. R represents the released pressure. . . . . 120
- 3.22 Imaginary part of dielectric response (as derived from reflectance spectra using KK transformation; see the text) for  $1T$ - $\text{TiTe}_2$ , at various high pressures and at low temperatures. Room-temperature spectra at 0.5, 2.3, and 5.2 GPa have been fitted with Lorentzian peaks. The decomposed phonon peaks are shown in blue for spectra at 5.2 GPa (fit shown in orange).  $E_u$  corresponds to the IR phonon mode from centrosymmetric ambient structure ( $P\bar{3}m1$ ), whereas  $E_1$  and  $A_1$  modes represent phonon modes of the high-pressure noncentrosymmetric structure ( $P3m1$ ). Doublets represent two inequivalent Te sites of the high-pressure phase. R represents the released pressure. . 121
- 3.23 Reflectance  $R_{s-d}$  at the sample-diamond interface at various increasing pressures up to 22 GPa.  $\omega_{sp}$  indicates the screen plasma frequency. (b) Calculated real part of optical conductivity  $\sigma_1(\omega)$  at various pressures. The same color code has been used in both panels for each pressure. . . . . 125
- 3.24 (Color online) (a) Re Optical conductivity  $\sigma_1(\omega)$  at various low pressures up to 3.8 GPa. (b) A schematic illustration of the electronic states near Fermi level in  $1T$ - $\text{TiTe}_2$  structure. The Drude part as well as the band originate from the intraband transition and correlation effects, whereas the MIR bands ( $\alpha$  and  $\beta$ ) and an high energy band HEI arise due to various interband transitions. (c) Sketch of band structure along L-A-L symmetry line of the Brillouin zone with the Fermi level in dashed line . . . . . 126

- 3.25 (a) Drude-Lorentz fit (thick dark yellow) of the optical conductivity (solid circle) at 6 GPa. The fit is composed of two Drude responses and several Lorentzian features. dc conductivity ( $\sigma_{dc} = 1/\rho_{dc}$ ) is also shown at  $\omega = 0$  at this pressure (red diamond). (b) Drude spectral weight of the D1 peak (hole) and the D2 peak (electron) as a function of pressure (increasing and decreasing). Room-temperature dc conductivity  $\sigma_{dc}$  has been plotted from high-pressure resistance measurement. (c) Integrated spectral weight  $SW = \int_{\Omega_0}^{\Omega} \sigma(\omega)d(\omega)$  for increasing pressures with  $\Omega_0 = 1000 \text{ cm}^{-1}$ . (d) Pressure-dependent spectral weight variation, normalized to the lowest pressure value at  $3000 \text{ cm}^{-1}$  upon compression and decompression pressures. . . . . 128
- 3.26 (a) Reflectance  $R_{s-d}$  at the sample-diamond interface at various decreasing pressures from 22 GPa. (b) Calculated optical conductivity  $\sigma_1(\omega)$  at various pressures. . . . . 129
- 4.1 (a),(b) Selected X-ray diffraction patterns at various pressures at two different measurements. The new peaks are indicated by black arrows. The inset of (b) shows the low angle new peak which is not clearly seen in the main figure . . . . . 136
- 4.2 (a),(b) Refined XRD patterns of  $\text{Sb}_2\text{S}_3$  at 6.5 GPa (Pnma) and at 12.8 GPa (Pnma+  $P2_1/m$ ). Dots indicate the measured spectra and the red solid red lines represent the best refinements. Blue lines represent the difference spectra between the measured and the refined patterns. Bragg peak positions are marked by vertical lines. Insets show the corresponding crystal structures. . . . . 137
- 4.3 (a) Reduced lattice parameters as a function of pressure. (b) a/b ratio as a function of pressure (c) a/c ratio as a function of pressure (d) Plot of the unit cell volume as a function of pressure. The inset shows the pressure dependence of the Bragg peak width of  $\text{Sb}_2\text{S}_3$  (202) peak and Au (111) peak. . . . . 138

4.4	Temperature dependence electrical resistance of $\text{Sb}_2\text{S}_3$ under various pressures up to 45 GPa. The upper inset shows the enlarged $R(T)$ plot at lower pressure up to 22 GPa and the lower inset shows the hysteresis in $R(T)$ curve during cooling and heating at 32 GPa. . . . .	139
4.5	(a) Resistance ratio ( $R(T=280\text{ K})/R(T=220\text{ K})$ ) as a function of pressure. The inset shows the pressure dependences of the resistance at 280 K upon both compression and decompression.(b)Log (R) as a function of $1000./T$ at several pressures. The upper inset shows the variation of the band gap with pressure and the lower inset shows the linear fitting of the above mentioned plot at 1.5 GPa in the temperature range 215K to 290K. . . . .	141
4.6	(a) Temperature dependence of resistance at various pressures upon decompression. (b) Comparison of the $R(T)$ behavior between 1.5 GPa during compression and 0.5 GPa during decompression. (c) Variation of the band gap during compression and decompression. . . . .	142
5.1	Crystal Structure of $\text{AgBiSe}_2$ . . . . .	147
5.2	(a) Reflectance Spectra of $\text{AgBiSe}_2$ at 0.5 GPa. The Blue line is the fit of the reflectance spectrum with Lorentz oscillators. (b) Optical Conductivity obtained from the fitted reflectance data with Lorentz oscillators. The Five main interband transition in the experimental range are labelled as A, B, C, D and E. . . . .	149
5.3	(a), (b) Real part of the optical conductivity ( $\sigma_1(\omega)$ ) spectra at various pressures. (c) Pressure dependence of the spectral weight for the A, B and C interband transitions. . . . .	150
5.4	(a) Real part of the measured reflectance at 5.6 GPa and 10.0 GPa. (b) Pressure dependences of $\sigma_1(\omega)$ at two different energies. (c) ,(d) Variation of the spectral weight as a function of pressure at two different energy region. . . . .	151
5.5	(a) and (b) Room temperature resistance as a function of pressure in two independent measurements. Inset of figure (a) shows the enlarge view in the vicinity of insulator to metal transition [3]. . . . .	152

5.6	Temperature dependence resistance in the vicinity of the transition pressure. The inset shows the $dR/dT$ as a function of temperature at the respective pressures. . . . .	153
5.7	Electrical resistances of $\text{AgBiSe}_2$ as a function of temperature at different pressures up to 11.5 GPa. The inset shows the $dR/dT$ as a function of temperature at 7.6 GPa and 8.3 GPa. . . . .	154
5.8	(a) Pressure dependent of the band-gap measured from the resistance measurement. (b) $\log(R)$ Vs. $1/T$ plot at the insulating region. . . . .	155
6.1	(a) Selected XRD patterns of NbP under various pressures up to 5.2 GPa at room temperature with $\lambda = 0.7001 \text{ \AA}$ . (b) Unit cell volume as a function of pressure for NbP. The solid line represents the fitted results using the third order Birch-Murnaghan equation of state. . . . .	159
6.2	(a) Normalized Electrical resistance plotted as a function of temperature at various pressures up to 6.1 GPa at zero field as well as at 7 T. (b), (c) Comparison of the effect of magnetic field and pressure on NbP. (b) At 0.7 GPa, the normalized resistance of NbP is plotted as a function of temperature at zero field (red line) and at a field of 7 T (Green). (c) Temperature dependence normalized resistance at 0.7 (Red) GPa and at 6.1 (Blue) GPa with no applied magnetic field . . . . .	160
6.3	(a) Temperature dependence resistance under various pressures in a semi log scale (b) $dR/dT$ as function of temperature defining the transition temperatures $T_m$ and $T_i$ (c) Pressure dependence of $T_m$ and $T_i$ (d) Normalized $\ln(R)$ as a function of $1000/T$ . The yellow lines represent the fitting results $R(T) = R(0) + e^{E_a/2KT}$ . Inset shows the pressure dependence of the activation gap. . . . .	162
6.5	Field dependence magnetoresistance of NbP single measured at 2 K under several pressures up to 6.1 GPa. The inset shows the pressure dependent average mobility and MR ( at 7 T). Average mobility $\mu$ at each pressure is obtained by fitting the field dependence MR to the formula $\text{MR} = (\mu_a B)^m$ with $m=1.2$ . Both $\mu_{avg}$ and MR show similar pressure dependence. . . . .	164

6.6	(a) Powder XRD patterns of NbAs at selected pressures. The wavelength of the used monochromatic X-ray was 0.70001 Å. (b) Evolution of the (112) peak as a function of pressure. . . . .	165
6.7	Pressure dependence of the unit cell volume of NbAs. Solid line represents the fitted $3_{rd}$ order Birch-Murnaghan equation of state. . . . .	166
6.8	(a) Electrical resistance (R(T)) as a function of temperature under various pressures up to 5.8 GPa. (b) Pressure dependent resistance at two different temperatures of 300 K and 2K. (c) Resistance ration (R300/R2K) as a function of pressure. . . . .	167
6.9	Temperature dependence normalized electrical resistance at various pressures and magnetic fields. . . . .	168
6.10	(a) Field dependence magnetoresistance (MR) at 2K under various pressures up to 5.8 GPa. (b) Field dependence Hall resistivity under similar environments. The inset shows the enlarge view of the Hall resistivity at low field. . . . .	169
6.11	(a) Temperature dependence of MR at 7 T under various pressures. (b) Temperature dependence of hall resistivity at 7 T under various pressures. The inset shows pressure dependence of MR and Hall resistivity at 2K and 7 T. . . . .	170
7.1	Crystal structure of TaIrTe <sub>4</sub> ; space group 31 (Pmn2 <sub>1</sub> ). . . . .	172
7.2	(a) Temperature dependence of electrical resistance of polycrystalline TaIrTe <sub>4</sub> sample under various pressures up to 13 GPa. (b) Temperature dependence of normalized resistance displaying the superconducting transition temperature. (c) Pressure dependence of T <sub>c</sub> and RRR. . . . .	175
7.3	(a) Temperature dependence of resistance at various pressures and magnetic fields. (b) MR as a function of pressure . . . . .	176
7.4	(a), (b) Temperature dependence of resistance at various magnetic fields measured as 8.4 GPa and 13 GPa respectively. (c) Corresponding H <sub>c2</sub> Vs. T <sub>c</sub> plots . . . . .	177
7.5	Synchrotron based XRD patterns of TaIrTe <sub>4</sub> at various pressures up to 11.4 GPa ( $\lambda = 0.4957\text{Å}$ ). . . . .	178

7.6	Unit cell volume as a function of pressure in polycrystalline TaIrTe <sub>4</sub> . Black solid line represents the fitting line based on third order Birch- Murnaghan equation of state. . . . .	179
-----	---	-----

## List of Tables

3.1	Lattice parameters and internal coordinates of $\text{TiTe}_2$ phases obtained from non-hydrostatic pressure studies . . . . .	112
4.1	Comparison of the different transition reported to date in $\text{Sb}_2\text{S}_3$ and the isostructural $\text{Sb}_2\text{Se}_3$ and $\text{Bi}_2\text{S}_3$ . ST, ETT, IMT and SC represent the structural transition, electronic topological transition, insulator to metal transition and superconductivity respectively. . . . .	144
5.1	Comparison of the different transition reported to date in $\text{AgBiSe}_2$ and other isostructural compounds. ST, ETT, IMT and SC represent the structural transition, electronic topological transition, insulator to metal transition and superconductivity respectively. . . . .	156

## List of Abbreviations

<b>2D</b>	Two Dimensional
<b>3D</b>	Three Dimensional
<b>BCS</b>	Bardeen Cooper Schrieffer
<b>CDW</b>	Charge Density Wave
<b>DAC</b>	Diamond Anvil cell
<b>DSM</b>	Dirac SemiMetal
<b>ETT</b>	Electronic Topological Transition
<b>EOS</b>	Equation of State
<b>FS</b>	Fermi Surface
<b>FC</b>	Field Cooling
<b>FWHM</b>	Full Width at Half Maximum
<b>GSAS</b>	General structure Analysis Software
<b>KK</b>	Kramers-Kronig
<b>LEED</b>	Low Energy Electronic Diffraction
<b>MR</b>	MagnetoResistance
<b>NLSM</b>	Nodal Line SemiMetal
<b>OC</b>	Optical Conductivity
<b>PTM</b>	Pressure Transmitting Medium
<b>QCP</b>	Quantum Critical Point
<b>QHE</b>	Quantum Hall Effect
<b>QSH</b>	Quantum Spin Hall
<b>SC</b>	Superconductivity
<b>SQUID</b>	Superconducting QUantum Interference Device

<b>SdH</b>	Shubnikov-de Haas
<b>TR</b>	Time Reversal
<b>TDSM</b>	Triply Degenerate SemiMetal
<b>TI</b>	Topological Insulator
<b>TSM</b>	Topological SemiMetal
<b>TSC</b>	Topological SuperConductor
<b>TQPT</b>	Topological Quantum Phase Transition
<b>VTI</b>	Variable Temperature Insert
<b>WSM</b>	Weyl SemiMetal
<b>XRD</b>	X-Ray Diffraction
<b>ZFC</b>	Zero Field Cooling

## Synopsis

This thesis reports the transport and spectroscopic investigations of some topologically non-trivial compounds under extreme conditions of high pressure (up to  $\sim 45$  GPa), low temperature (down to 1.5 K) and high magnetic field (up to 7 T). Various high pressure techniques viz., four probe electrical resistance and magnetoresistance, SQUID based magnetization, X-ray diffraction and IR reflectance measurement techniques have been carried out to study the electronic, magnetic and structural evolution of the topological compounds under pressure. Various kinds of diamond anvil cells have been used to generate high pressures. Temperature and magnetic field have been incorporated as additional thermodynamic parameters.

The thesis contains a total of eight chapters. The first chapter introduces various topological systems followed by the literature survey on high pressure effects on the respective systems. The second chapter describes the various experimental techniques and apparatus employed throughout this work. The next five chapters are devoted to the discussion of the high pressure investigations on the materials used in this thesis. Each material specific chapter begins with proper background, and motivations followed by suitable experimental techniques, various experimental results and the relevant discussions concerning each material. The end chapter summarizes the main experimental results in the thesis and suggest some future works. A brief summary of all the chapters is presented below.

**Chapter 1: Introduction:** This chapter provides an overview and background of the topological systems and a brief review of how pressure induces various novel phenomena in these compounds. First, I present a brief introduction on various topological phases in condensed matter physics including topological insulator, topological semimetals and topological superconductors. Topological insulators are characterized by a full energy gap in their bulk and gapless edge or surface states which are topologically protected by time-reversal symmetry [1]. Whereas, the topological superconductors are characterized by full pairing gap in the bulk and topologically protected gapless surface state consisting of Majorana fermions [2]. HgTe/CdTe quantum well (QW) system is potential candidate which was first predicted as a two dimensional topological insulators or QSH insulators [3]. Topological semimetals are the newly discovered class of topologically non-trivial materials beyond the gapped topological materials such as topological insulators and topological superconductors [4]. Unlike topological insulators, topological semimetals do not have a band gap in their electronic band structure but most of the topological semimetals have in common that their unusual band topology arises from a band inversion.

There are several classes of TSMs namely Dirac semimetals (DSMs), Weyl semimetals (WSMs), and nodal line semimetals (NLSMs) [4].

The discovery of such topological systems stimulates the high pressure community for studying the pressure induced changes in the crystal structural, electronic structure and topological states of these materials. As pressure is a clean and effective tool, the high pressure exploration of the various novel phenomena such as pressure induced electronic topological transition (ETT), topological phase transition and topological superconductivity have recently attracted significant attention in the topological material research field [5, 6]. Thus the similar high pressure investigations on the topological systems are very important and many other interesting and new physical phenomena are naturally expected when studying these materials under pressure. At the end of this chapter, we thus, also, introduce the materials investigated in this thesis. I had the opportunity to study materials from distinctive families of topological compounds which include three proposed pressure induced topological insulators ( $\text{Sb}_2\text{S}_3$ ,  $\text{AgBiSe}_2$ ,  $\text{TiTe}_2$ ), two type-I Weyl semimetals ( $\text{NbP}$ ,  $\text{NbAs}$ ) and one type-II Weyl semimetal ( $\text{TaIrTe}_4$ ).

**Chapter 2: Experimental techniques:** In this chapter, I discuss an overview of the experimental techniques which are used to investigate the various topological systems at high pressure. We first provide a brief description of the sample synthesis process and the ambient pressure characterization techniques. Then we give an extensive and through description of the basics of high pressure equipments which include the description of different kind of high pressure cells, gasket materials, pressure transmitting medium and pressure measurement techniques.

Later, we introduce the different low temperature instrumentations under pressure which include helium bath type cryostat, SQUID magnetometer and liquid nitrogen based flow type microscope cryostat. The helium bath type cryostat can be operated between room temperature and a temperature as low as 1.5 K which permits in-situ pressure measurement at room temperature as well as at low temperature [7]. Cryogenic Ltd. S700X SQUID is used for magnetic and magnetoresistance measurements at ambient pressure as well as at high pressure up to a magnetic field up to 7 T. A liquid nitrogen based flow type microscope cryostat is used for low temperature reflectance measurements which is capable to cool the sample environment down to  $\sim 100$  K. Then the importance of the association of the extreme conditions of high pressure, low temperature and magnetic field is discussed. Then I discuss various transport measurement procedures under pressure which contain (i) high pressure resistance measurements procedure under quasi-hydrostatic pressure conditions as well as non hydrostatic pressure conditions, (ii) high pressure magnetoresistance and

Hall Effect measurement procedure and (iii) DC magnetization measurement procedure. Powder x-ray diffraction is used as the primary technique for determining the structure of materials at high pressure. All X-Ray diffraction experiments included in the current thesis were performed at the XRD1 beamline of Elettra synchrotron, Trieste, Italy. A brief overview of the synchrotron based high pressure XRD techniques and the relevant data analysis methods are presented. Finally, synchrotron based high pressure and low temperature IR reflectivity measurement technique, performed at SISSI beamline of Elettra synchrotron, is discussed.

**Chapter 3: Transport and spectroscopic investigations of  $\text{TiTe}_2$  under pressure:**

$1T$ - $\text{TiTe}_2$  belongs to quasi-2D layered transition metal dichalcogenides family of compounds and crystallizes in trigonal structure with a space group of  $P\bar{3}m1$  (No. 164) [8]. These compounds provide an important playground to reveal exotic ground-state electronic order exhibiting the verities of CDW transitions and superconductivity. In contrast to the other compounds in this family,  $1T$ - $\text{TiTe}_2$  does not show any charge density wave (CDW) behaviour at ambient condition and its band structure shows enhanced indirect band overlap, characterized by semimetallic resistivity [8,9]. Recently, it is proposed theoretically that  $\text{TiTe}_2$  shows series of topological transition under pressure and a suitable strain can induce phonon induced superconductivity in this compound [10,11]. The emergence of SC in the topological surface states is of fundamental interest from the point of view of the realization of topological superconductors, hosting massless Majorana fermions. Here, we have studied high pressure transport and spectroscopic investigations of both polycrystalline and single crystalline  $\text{TiTe}_2$  and the results are discussed as follows.

First, we have performed high pressure electrical measurements of polycrystalline  $\text{TiTe}_2$  at room temperature to conclude about the theoretical prediction of the pressure induced series of topological transitions [12]. The anomalous increase in resistance near  $\sim 8.8$  GPa is associated with structural phase transition from trigonal to monoclinic structure confirmed by XRD and Raman measurements. The anomalies at  $\sim 2$  GPa and  $\sim 4$  GPa are indicated as isostructural electronic transitions which are closely related to the theoretical predictions and hence may be due to nontrivial TQPT and trivial metallic transition, respectively.

Then we study high pressure resistance and magnetoresistance behaviour of pristine  $1T$ - $\text{TiTe}_2$  single crystal under various quasihydrostatic and nonhydrostatic compressions and reported in [13]. In nearly hydrostatic condition, superconductivity emerges at  $\sim 5$  GPa and the system remains semimetallic up to the highest pressure of the measurement. In contrast, application of nonhydrostatic pressure ( $\sim 1.8$  GPa)

leads to dramatic changes in its resistance behavior to a characteristic of quasicommensurate CDW ordered state, as seen in isomorphous  $1T$ -TaS<sub>2</sub> [14]. With increasing pressure, this resistance anomaly gets suppressed by a systematic decrease of overall resistance and superconductivity emerges at 6.2 GPa.  $T_c$  increases rapidly to 5.3 K up to 12 GPa, followed by a rather slow but monotonic increase up to 29 GPa, the highest pressure of this measurement of nonhydrostatic compressions. For quasihydrostatic measurements,  $T_c$  also increases in similar fashion. Thus, pressure studies indicate that  $1T$ -TiTe<sub>2</sub> exhibits superconductivity irrespective of the formation of the CDW-like state, implying the existence of phase-separated domains. Most surprisingly, the SC state persists upon decompression at least down to 0.5 GPa, also coexisting with the re-entrant CDW-like phase. The persistent nature of SC at almost ambient pressure upon decompression is extremely rare, but highly desirable for practical applications. The irreversible nature of structural evolution under nonhydrostatic compression further supports the resistance results and establishes the unique  $P$ -rescaled phase diagram.

we also perform infrared reflectance measurements of pristine single crystal TiTe<sub>2</sub> under various quasihydrostatic pressures up to 22 GPa and is reported in [15]. First, the emergence of new modes including Raman-active modes in the far infrared phonon spectra indicates irreversible structural modification (with broken inversion symmetry) at a moderate pressure ( $\sim 2.5$  GPa). High pressure structural modification is believed to be responsible for the emergence of superconductivity with  $T_c \sim 6$  K under quasihydrostatic compression, contrasting an earlier theoretical prediction where CdI<sub>2</sub>-type structure is assumed to be stable at high pressure [11]. An irreversible increase of low-energy optical conductivity spectral weight under quasihydrostatic pressures suggests irreversible modification of its electronic band structure, which is argued to be the reason for the pressure-quenched superconducting state. The structural transition at  $\sim 2.5$  GPa makes it necessary to revisit theoretically the high-pressure topological phases, keeping in mind that the simple parity analysis may not be reliable for exploring possible band inversion in a non-centrosymmetric structure.

**Chapter 4: High pressure structural and electrical investigations of Sb<sub>2</sub>S<sub>3</sub>:** Antimony trisulfide (Sb<sub>2</sub>S<sub>3</sub>) is a well known binary semiconductor which belongs to A<sub>2</sub>B<sub>3</sub> (A=Bi, Sb, As; B = S, Se, Te) family layered chalcogenide with an optical bandgap energy ( $E_g$ ) of  $\sim 1.7$  eV [16]. Application of pressure on the other compounds in this A<sub>2</sub>B<sub>3</sub> series show various novel phenomena including structural transition, electronic topological transition (ETT), metallization and superconductivity [6, 17–19]. Much research has also been reported on Sb<sub>2</sub>S<sub>3</sub> under pressure

including its structural, vibrational and electrical properties. But there has been an inconsistency between the different experimental results regarding the pressure induced ETT and structural transition. Recently pressure induced irreversible metallization is reported in this compound on the basis of temperature dependent (80-240 K) electrical conductivity measurement [20]. But the detailed study of the pressure dependent activation gap was absent there and no low temperature measurement below 80 K was performed to search for pressure induced superconductivity in this compound.

So aiming at clarifying the observed pressure induced irreversible metallization and to search pressure induced superconductivity we have conducted low temperature resistance measurement down to 1.4 K under various pressures up to 45 GPa. The activation energy decreases with applied pressure but the gap does not close up to the highest pressure of our measurement i.e. the system remains insulating up to 45 GPa and the experimental band gap is reversible under decompression which contradicts with the recent results where the authors show pressure induced irreversible metallization at  $\sim 32$  GPa. In addition, to conclude about the controversial results on pressure induced ETT at  $\sim 6$  GPa and structural transition, we have carried out high pressure XRD (up to 25 GPa), and optical absorption measurements (up to  $\sim 10$  GPa). Our XRD measurements up to 25 GPa reveal anomalous change of compressibility at  $\sim 6$  GPa and clear structural phase transition near  $\sim 10$  GPa. An isostructural transition at  $\sim 6$  GPa is further supported by direct to indirect bandgap type transition of its electronic structure. So our results solve the controversy about the high pressure structural transitions in  $\text{Sb}_2\text{S}_3$  and reveal persistence insulating nature up to  $\sim 45$  GPa in this compound.

**Chapter 5: High pressure electrical transport and optical reflection study of  $\text{AgBiSe}_2$ :**  $\text{AgBiSe}_2$  crystallizes in ordered hexagonal structure (S.G : P-3m1, Z=3) at ambient conditions [21]. Its narrow optical bandgap of 0.6 eV implies that  $\text{AgBiSe}_2$  is on the edge of pressure induced insulator to metal transition which is an important subject of condensed matter physics. Presence of bond anharmonicity in  $\text{AgBiSe}_2$  causes intrinsic low lattice thermal conductivity which originates high thermoelectric figure of merit (Z) of  $\sim 1$ .  $\text{AgBiSe}_2$  also exhibits strong spin orbit coupling (SOC) and it has a symmetrical equivalence with  $\text{Bi}_2\text{Se}_3$ . High pressure investigations will thus help to understand whether  $\text{AgBiSe}_2$  exhibits similar pressure response to that of  $\text{Bi}_2\text{Se}_3$  and it will also be useful for the fabrications of semiconductor device operating in the mechanically strained environment. No low temperature measurements was also reported to search pressure induced superconductivity similar to the topological insulators.

Here, we report the signature of the pressure induced electronic topological transition (ETT) and semiconductor-to-metal transition in  $\text{AgBiSe}_2$  using synchrotron based mid-IR reflectivity and electrical transport measurements. IR-reflectivity data reveals an abrupt change in the interband transition above  $\sim 2$  GPa. Optical conductivity spectral weight in the low energy region also shows anomalous change above 2 GPa. Pressure dependent room temperature resistance shows a sudden drop at 2.8 GPa which is similar to that of the 3D topological insulators  $\text{Bi}_2\text{Se}_3$  and  $\text{Bi}_2\text{Te}_3$ . Low temperature resistance measurements show a change in behavior of the temperature dependence resistances above 2 GPa. All the observations confirm the pressure induced ETT in  $\text{AgBiSe}_2$  above  $\sim 2$  GPa. Higher pressure IR-reflectivity measurements also reveal overall increase in optical conductivity in the whole energy range above  $\sim 8$  GPa and over the same pressure range the high pressure resistance measurements show a sign change in the temperature dependent of the  $dR/dT$  which confirm the pressure induced semiconductor to metal transition in  $\text{AgBiSe}_2$  near  $\sim 8$  GPa. We have not observed any evidence of pressure induced superconductivity in our transport measurements up to 11.5 GPa.

**Chapter 6: High pressure magneto-resistance measurements on Weyl semimetals NbP and NbAs:** Binary Weyl semimetal compounds NbP and NbAs (having inversion symmetry broken lattice) are of tremendous current research interest due to their potential application exploiting extremely large magneto-resistance and ultrahigh carrier mobility stemming from the chiral anomaly [22, 23]. In another class of Weyl semimetal (WTe<sub>2</sub>), upon increasing pressure superconductivity emerges as a result of suppression of such large magneto-resistance [24]. Although NbAs displays robustness of its Fermi-surface upon moderate pressure application [23], a dramatic change of temperature dependence of resistivity of NbP and TaP has been noticed under pressure, which has been correlated to the pressure induced shift of Weyl points compared to the Fermi energy [110].

Here we present our detailed high pressure-low temperature resistivity and magneto-resistance results on oriented single crystal NbP and NbAs up to  $\sim 10$  GPa. Pressure induced conspicuous change in resistivity behavior is observed above  $\sim 5$  and 7 GPa respectively. At higher pressures observation of resistance plateau features in both cases indicate transition to topological insulating state. The nature of this transition and the carrier details of the high pressure phase have been investigated by longitudinal magneto-resistance and Hall measurements under pressure. The results are discussed in view of the pressure-induced iso-structural transitions observed in these compounds [26, 27] and similar field-induced transition in a centro-symmetric compound LaSb [54].

**Chapter 7: High pressure transport and magneto-transport measurements in the type-II Weyl semimetal TaIrTe<sub>4</sub>:** Recently, orthorhombic ternary compound, TaIrTe<sub>4</sub> has been predicted and experimentally identified as type-II Weyl semimetals (WSMs) [28]. WTe<sub>2</sub> and MoTe<sub>2</sub> are the two other examples of type-II Weyl semimetallic compounds [29, 30]. High pressure research on WTe<sub>2</sub> and MoTe<sub>2</sub> suggest that superconducting transition temperature ( $T_c$ ) shows dome-shaped pressure dependence and the emergence of superconductivity occurs after significant suppression of magnetoresistance [29, 30]. So the similar high pressure investigations on the iso-structural TaIrTe<sub>4</sub> will help to understand the general dome shaped superconducting phase diagram which may provide insights into the interplay between superconductivity and topological physics.

Here, we have synthesized polycrystalline TaIrTe<sub>4</sub>, a recently discovered type-II Weyl semimetal and have performed high pressure resistance and magnetoresistance measurements by four point contact method up to 13 GPa. At the initial pressure of 1.0 GPa, the resistance shows metallic behaviour similar to the ambient pressure behaviour. In addition to that a low temperature resistance drop at  $\sim 7$  K is observed at this pressure which is suggested as the pressure induced superconductivity and as the pressure is increased further the drop become more pronounced. High pressure XRD measurement has also been carried out in this compound and the ambient structure is robust up to the highest pressure of the measurement (11 GPa).

**Chapter 8: Conclusions and Outlook:** This chapter summarizes and concludes the main experimental results of the thesis. Some of the future experiments have also been suggested for each of the compounds separately. At the end of this chapter, I also include a more general remark regarding the purpose and important of the thesis.

## Bibliography

- [1] M. Z. Hasan and C. L. Kane, Colloquium: Topological insulators, *Rev. Mod. Phys.* 82, 3045-67 (2010).
- [2] X. L. Qi, S. C. Zhang, Topological insulators and superconductors, *Rev. Mod. Phys.* 83, 1057-1110 (2011).
- [3] B. A. Bernevig, T. L. Hughes, and S. C. Zhang, Quantum spin Hall effect and topological phase transition in HgTe quantum wells, *Science*, 314, 1757 (2006).
- [4] F. F. Tafti, Q. D. Gibson et al., Resistivity plateau and extreme magnetoresistance in LaSb, *Nature Physics* 12(3), 272-277 (2016).
- [5] K. Kirshenbaum, P. S. Syers et al., Pressure-Induced Unconventional Superconducting Phase in the Topological Insulator Bi<sub>2</sub>Se<sub>3</sub>, *Phys. Rev. Lett.* 111, 087001 (2013).
- [6] P. P. Kong, J. L. Zhang et al., Superconductivity of the topological insulator Bi<sub>2</sub>Se<sub>3</sub> at high pressure. *J Phys-Condensed Matter*, 25, 362204 (2013).
- [7] S. Karmakar, Measurement of improved pressure dependence of superconducting transition temperature, *High Pressure Research: An International Journal*, 33:2, 381-391 (2013).
- [8] R. Claessen, R. O. Anderson, G.-H. Gweon et al., Complete band-structure determination of the quasi-two-dimensional Fermi-liquid reference compound TiTe<sub>2</sub>, *Phys. Rev. B* 54(4), 2453 (1996).
- [9] D. K. G. de Boer, C. F. van Bruggen et al., Titanium ditelluride: Band structure, photoemission, and electrical and magnetic properties, *Phys. Rev. B* 29, 6797 (1984).
- [10] Q. Zhang, Y. Cheng, and U. Schwingenschlogl, Series of topological phase transitions in TiTe<sub>2</sub> under strain, *Phys. Rev. B* 88, 155317 (2013).
- [11] R. C. Xiao, W. J. Lu et al., Manipulating superconductivity of 1T-TiTe<sub>2</sub> by high pressure, *J. Mater. Chem. C* 5, 4167 (2017).
- [12] V. Rajaji, U. Dutta et al., Structural, vibrational, and electrical properties of 1T-TiTe<sub>2</sub> under hydrostatic pressure: Experiments and theory, *Phys. Rev. B* 97, 085107 (2018).

- [13] U. Dutta, P. S. Malavi et al., Pressure-induced superconductivity in semimetallic  $1T$ - $\text{TiTe}_2$  and its persistence upon decompression, *Phys. Rev. B* **97**, 060503(R) (2018).
- [14] B. Sipos, A. F. Kusmartseva et al., From Mott state to superconductivity in  $1T$ - $\text{TaSe}_2$ , *Nature Materials* **7**, 960 (2008).
- [15] U. Dutta, S. Sahoo et al., Infrared spectroscopic measurements of structural transition and charge dynamics  $1T$ - $\text{TiTe}_2$  under pressure, *Phys. Rev. B* **99**, 125105 (2019).
- [16] A. Efsthathiou and E. R. Levin, Optical Properties of  $\text{As}_2\text{Se}_3$ ,  $(\text{As}_x\text{Sb}_{1-x})_2\text{Se}_3$ , and  $\text{Sb}_x\text{S}_3$ , *J. Opt. Soc. Am.* **58**, 373 (1968).
- [17] J. Zhang, C. Liu et al., Electronic topological transition and semiconductor-to-metal conversion of  $\text{Bi}_2\text{Te}_3$  under high pressure, *Appl. Phys. Lett.* **103**, 052102 (2013).
- [18] F. J. Manjon, R. Vilaplana et al., High-pressure studies of topological insulators  $\text{Bi}_2\text{Se}_3$ ,  $\text{Bi}_2\text{Te}_3$ , and  $\text{Sb}_2\text{Te}_3$ , *Phys. Status Solidi B* **250**, No. 4, 669-676 (2013).
- [19] R. Vilaplana, D. Santamaria-Perez et al., Structural and vibrational study of  $\text{Bi}_2\text{Se}_3$  under high pressure, *Phys. Rev. B* **84**, 184110 (2011).
- [20] L. Dai, K. Liu et al., Pressure-induced irreversible metallization accompanying the phase transitions in  $\text{Sb}_2\text{S}_3$ , *Phys. Rev. B.*, 97.024103 (2018).
- [21] S. N. Guin, V. Srihari et al., Promising thermoelectric performance in n-type  $\text{AgBiSe}_2$ : effect of aliovalent anion doping, *J. Mater. Chem. A*, **3**, 648-655 (2015).
- [22] C. Shekhar, A. K. Nayak et al., Extremely large magnetoresistance and ultra-high mobility in the topological Weyl semimetal candidate  $\text{NbP}$ , *Nature Physics* **11**(8):645-649 (2015).
- [23] Y. Luo, N. J. Ghimire et al., 'Hard' crystalline lattice in the Weyl semimetal  $\text{NbAs}$ , *J. Phys.: Condens. Matter* **28** 055502 (2016).
- [24] D. Kang, Y. Zhou et al., Superconductivity emerging from a suppressed large magnetoresistant state in tungsten ditelluride, *Nature Communication* **6**, 7804 (2015).
- [25] M. Einaga, K. Shimizu et al., Resistivity of Weyl semimetals  $\text{NbP}$  and  $\text{TaP}$  under pressure, *Phys. Status Solidi RRL*, 1700182 (2017).

- [26] S. N. Gupta, A. Singh et al., Pressure-induced Lifshitz and structural transitions in NbAs and TaAs: experiments and theory, *J. Phys.: Condens. Matter* 30 185401 (2018).
- [27] S. N. Gupta, A. Singh et al., Pressure-induced Lifshitz transition in NbP: Raman, x-ray diffraction, electrical transport, and density functional theory, *Phys-RevB*.97.064102 (2018)
- [28] E. Haubold, K. Koepnik et al., Experimental realization of type-II Weyl state in noncentrosymmetric TaIrTe<sub>4</sub>, *Phys. Rev. B* 95, 241108 (2017).
- [29] X. C. Pan, X. Chen et al., Pressure-driven dome-shaped superconductivity and electronic structural evolution in tungsten ditelluride, *Nature Communication* 6, 7805 (2015).
- [30] Y. Qi, P. G. Naumov et al., Superconductivity in Weyl semimetal candidate MoTe<sub>2</sub>, *Nature Communication* 7, 11038 (2016).

# Chapter 1

## Introduction

### 1.1 Overview

One of the most important concepts in condensed matter physics is the classification of states of matter by the principle of spontaneous symmetry breaking [1]. For example, translation symmetry is broken in a crystalline solid, where, the interaction among its atomic building blocks remains translationally invariant, rotational symmetry is broken in a magnet, where, the fundamental interactions are isotropic and gauge symmetry is broken in a superconductor, which leads to novel phenomena such as flux quantization and Josephson effects [2]. For a long time it was believed that this theory of spontaneous symmetry breaking provides a universal description of all quantum states of matter. However, in 1980, von Klitzing discovered experimentally a new quantum state of matter, the so-called integer quantum Hall Effect (QHE) [3] which cannot be fitted into this simple paradigm. The Quantum Hall State occurs in two dimensional (2D) materials, where the bulk of the sample is insulating and the electric currents are carried only along the edge of the sample (Fig. 1.1(a)). The unidirectional edge currents are immune to dissipation and gives rise to the QHE and the quantum Hall State is the first state discovered to be topologically distinct from all previous states of matter. The precise quantization of the Hall conductance is explained by the fact that it is a topological invariant, which can only take integer values in units of  $e^2/h$ , independent of material details [2, 4]. The quantized magneto-conductivity  $\sigma_{xy} = ne^2/h$ , can be probed by transport experiments, which also provides a measure of the topological invariant (the Chern

number)  $n$  that characterize these quantum Hall states. Now in the presented theory of the QHE, because of the presence of the cyclotron orbits, the generators of translations  $(k_{x,y})$  do not commute with one other, so that electronic states cannot be properly labeled with momentum  $k$ . For this reason, after the discovery of the QHE, many theoretical works proposed systems with the same conducting properties, but without an external magnetic field, so that they could be described inside the Bloch band theory framework. The first proposed theory is the Haldane model [5], starting from the graphene Hamiltonian with a magnetic field that is zero on the average, but has all of the spatial symmetries of the honeycomb lattice. And Haldane showed that although the average magnetic field is zero, it opens up a gap at the Dirac nodes of graphene, and furthermore this gapped state is not an ordinary insulator, but rather has a quantized Hall conductivity (a nonzero Chern number). This system is called Chern insulator (Fig. 1.1(b)) and is also referred as a quantum anomalous Hall insulator, which was recently predicted and experimentally realized in Cr-doped  $(\text{Bi}_{1-x}\text{Sb}_x)_2\text{Te}_3$  thin films [6] and in ultracold Fermion systems [7] where no external magnetic field is required and the time-reversal symmetry breaking is provided by the magnetization of the sample itself.

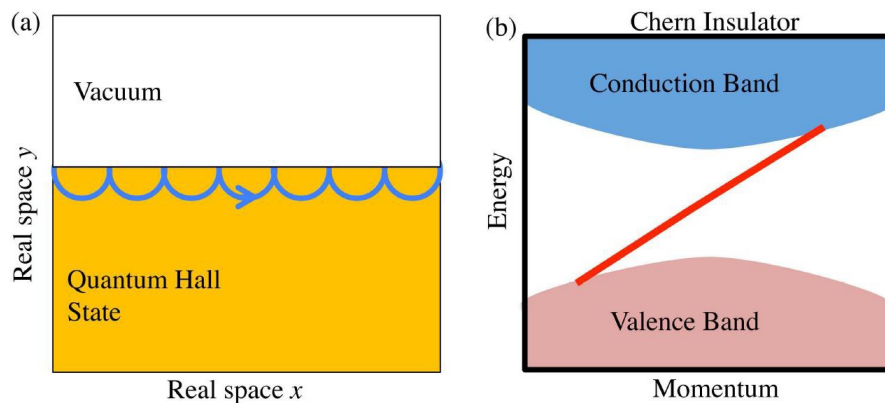


Figure 1.1: (a) Edge states as skipping cyclotron orbits in a Quantum Hall state. (b) A sketch of the band structure of a Chern insulator, where the linear chiral edge band present at the interface with a trivial insulator is represented by a red line. The figure is taken from reference [8].

Although the Haldane model introduces non trivial topology without the need

of an external magnetic field, the local periodic magnetization introduced in his model still causes the breaking of time reversal symmetry. The possibility to have a topological phase preserving time reversal symmetry was the objective of a strong theoretical effort, motivated by the fact that most of materials in nature are time reversal invariant. This possibility is naturally offered by the spin orbit interaction and the first proposed solution was a model for graphene with spin orbit coupling (SOC) and led to the prediction of a new kind of topological state of matter, i.e. the quantum spin Hall (QSH) insulator [9, 10]. In a QSH insulator, the bulk is insulating and features a pair of counter-propagating edgestates, which are related by time-reversal symmetry and the whole system, unlike a Chern insulator, respects time-reversal symmetry. We provide a physical picture to build a quantum spin Hall insulator from two Chern insulators in Fig 1.2. The topological number that describes the QSH phase is a  $Z_2$  invariant ( $\nu$ ). The  $Z_2$  invariant can only take two values, 0 or 1, where  $\nu = 0(1)$  is topologically trivial (nontrivial) [11].

Besides Chern insulators and quantum spin Hall insulators in 2D, there exist further free-fermions systems in various dimensions which have insulating bulk yet differ from trivial insulators by a topological invariant defined from their bulk electronic structure. These types of systems are called topological insulators (TIs) in general. In 2007, it was theoretically realized that the  $Z_2$  topological number in a QSH insulator can be generalized into three dimensions [12–14]. In three dimensions, there exist four  $Z_2$  topological invariants that define the topological property of a 3D bulk material, namely  $(\nu_0; \nu_1, \nu_2, \nu_3)$ , where  $\nu_0$  is the strong topological invariant and  $\nu_1$ - $\nu_3$  are the weak topological invariants, respectively. If the strong topological invariant is nonzero ( $\nu_0 = 1$ ), the system is a 3D strong  $Z_2$  TI [12–14].

Similar to TIs, there are gapped superconducting systems which are different from the conventional BCS superconductors in terms of topological invariants.

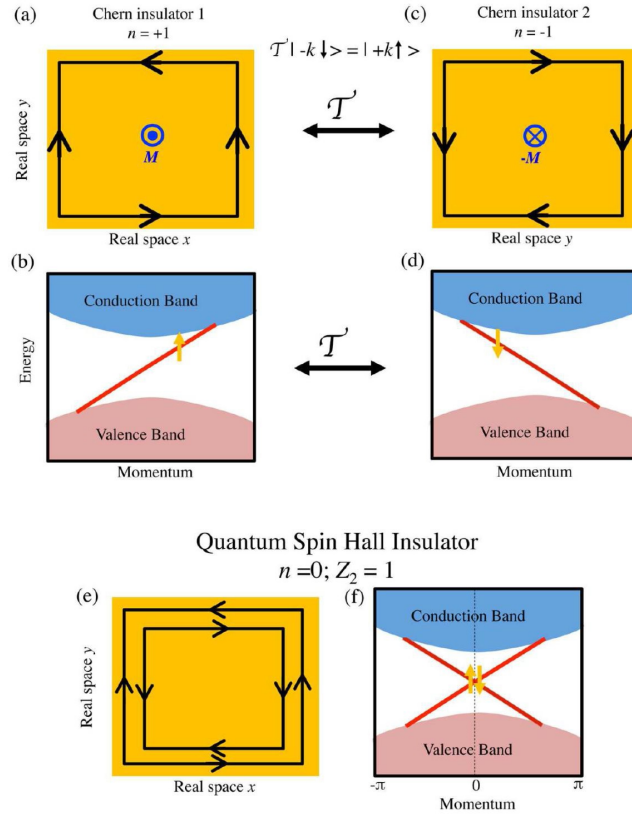


Figure 1.2: A quantum spin Hall insulator can be constructed by two Chern insulators that are related by the time-reversal symmetry. (a) A Chern insulator with a Chern number of  $n = +1$  has a chiral edge mode as a result of an out-of-plane magnetization. (b) The bottom edge projection of the electronic structure of the  $n = +1$  Chern insulator. (c,d,) Same as Panels (a,b) but with a time-reversal operation onto the system. (e,f,) A quantum spin Hall state can be obtained by combining the above-two Chern insulator states. The resulting electronic structure on the edges is described by two counterpropagating edge modes that cross each other at  $k = 0$  (or  $k = \pi$ ). The crossing is protected by the time-reversal symmetry as a result of the Kramers theorem. The figure is taken from reference [8].

These are known as topological superconductors (TSCs) [15–17]. Topological superconductivity connects the two exciting fields in condensed matter physics; unconventional superconductivity and topological materials. At the crossroads of these two fascinating fields, topological superconductivity has been theoretically established but has yet to be experimentally realized. A topological superconductor is an unconventional superconductor with a gap classified by a non-trivial topological invariant. Similar to the topological insulator, the superconducting topological invariant can cause the superconducting gap to close due to a symmetry protected

surface state. On the other hand, unlike the topological insulator, the surface state on the topological superconductor may support Majorana fermions - a particle that is its own antiparticle.  $\text{Bi}_2\text{Se}_3$  is a topological insulator that has attracted special interest since Cu, Sr, or Nb intercalation between quintuple layers of  $\text{Bi}_2\text{Se}_3$  can induce superconductivity [18–20]. It is proposed that doped  $\text{Bi}_2\text{Se}_3$  is a topological superconductor, which has a full pairing gap in the bulk and a topologically protected gapless surface state consisting of Majorana fermions [18].

So far we have been focusing on topological states of matter which have a finite gap, i.e., insulators and fully gapped superconductors. However, there exists another large class of gapless topological states of matter, where the gapless excitations in the systems are topologically protected. These systems are called topological semimetals [21–25] and among the topological semimetals, Dirac semimetals [22, 23] and Weyl semimetals [24, 25] attract great attention. While the surface states on topological insulator provide an analog to the 2D Dirac electrons in graphene, interesting concepts of Weyl semimetals and 3D Dirac semimetals were also developed as examples of 3D Dirac electrons. With a linear energy-momentum dispersion, both Weyl semimetals and Dirac semimetals can be viewed as 3D analogs of the 2D graphene. Besides, Weyl semimetals provide a solid-state realization of the Weyl fermions that have been studied theoretically for a long time in high energy physics. Weyl fermions are a type of massless fermions with handedness, i.e. chirality. The chirality describes whether a particle spins clockwise or anti-clockwise when viewed in front of the traveling direction. In a crystal with both time reversal symmetry and inversion symmetry, such separated Weyl pairs do not exist because the bands involved are always degenerate. When two Weyl nodes with opposite chiralities meet in a crystal, they generally annihilate and open a band gap. However, Wang et. al. found that with certain crystal symmetries, paired Weyl nodes can overlap in the

momentum space and it results in a new crystal with a linear energy-momentum dispersion, namely a 3D Dirac semimetal. Unlike a WSM, a 3D Dirac crystal respects time reversal and inversion symmetries at the same time.

The discovery of such topological systems stimulates the high pressure community for studying the pressure induced changes in the crystal structural, electronic structure and topological states of these materials. As pressure is a clean and effective tool, the high pressure exploration of the various novel phenomena such as pressure induced electronic topological transition (ETT), topological phase transition and topological superconductivity have attracted significant attention in the topological material research field in the last couple of years. One particularly relevant example is  $\text{Bi}_2\text{Se}_3$ , one of the simplest three-dimensional topological insulators.  $\text{Bi}_2\text{Se}_3$  shows a progressive structural evolution from an ambient rhombohedra phase (Space group (SG): R-3m) to monoclinic phase (SG: C2/m) at  $\sim 11$  GPa and a further structural transition occurs at  $\sim 30$  GPa to a body-centered tetragonal phase (SG: I4/mmm) [26]. In addition to that pressure induced ETT, semiconductor to metal transition and superconductivity was also observed in this material [26–28]. Application of pressure also induces exotic phenomena in topological semimetals such as a new pressure-induced Weyl semimetallic phase was observed in TaAs with less number of Weyl fermions compared to the ambient structure. Pressure induced superconductivity was also observed in type I Weyl semimetal, TaP [29] and in type II Weyl semimetals,  $\text{WTe}_2$  [30] and  $\text{MoTe}_2$  [31]. The superconducting transition temperature ( $T_c$ ) of the doped- topological superconductors ( $\text{Cu}_x\text{Bi}_2\text{Se}_3$ ,  $\text{Nb}_x\text{Bi}_2\text{Se}_3$  and  $\text{Sr}_x\text{Bi}_2\text{Se}_3$ ) has different pressure dependent:  $T_c$  decreases upon application of pressure for  $\text{Cu}_x\text{Bi}_2\text{Se}_3$  and  $\text{Sr}_x\text{Bi}_2\text{Se}_3$  whereas for  $\text{Nb}_x\text{Bi}_2\text{Se}_3$  it increases [18–20, 32, 33].

Thus, similar high pressure investigations on the topological systems are very important and many interesting and new physical phenomena are naturally expected when studying these materials under pressure. The current thesis study high

pressure investigation on several topological systems which include three proposed pressure induced topological insulators ( $\text{TiTe}_2$ ,  $\text{Sb}_2\text{S}_3$ ,  $\text{AgBiSe}_2$ ), two type-I Weyl semimetals ( $\text{NbP}$ ,  $\text{NbAs}$ ) and one type-II Weyl semimetal ( $\text{TaIrTe}_4$ ). The following sections briefly review the various topological systems and related high pressure studies with special attention of topological insulator and Weyl semimetals.

## 1.2 Topological Insulator and superconductors:

The topic of topological insulators and superconductors is now one of the most exciting fields of research in condensed matter physics [2]. Topological insulators are characterized by a full energy gap in their bulk and gapless edge or surface states which are topologically protected by time-reversal symmetry [34]. Whereas, the topological superconductors are characterized by full pairing gap in the bulk and topologically protected gapless surface state consisting of Majorana fermions [2]. Topological superconductivity is sometimes achieved by applying pressure on the topological insulators. The following subsections discuss various topological insulators and how pressure leads to various quantum topological transitions which may finally leads to topological superconducting states.

### 1.2.1 Two Dimensional topological insulators:

Quantum spin Hall (QSH) state is realized as the 2D topological insulator where the TR symmetry is preserved unlike the Quantum Hall State where TR symmetry is broken. It has a bulk energy gap and conducting edge states that are protected by TR symmetry. Such edge states are termed as helical edge states because two electrons with opposite spin move in opposite directions at a given edge i.e., the spin and the direction of motion of the electrons are correlated [2, 35]. According to the Kramer's theorem, the edge states always comes in pair and TR symmetry

secures that their energy levels will cross at certain high-symmetry points in the Brillouin zone (BZ) known as Kramer's degeneracy. The presence of such level crossings does not allow adiabatic deformation from QSH insulators into trivial insulators. Earlier, I have introduced  $Z_2$  topological invariants which characterize the topological properties of the QSH state mathematically. Depending upon the number of Kramers pairs (even or odd) of edge states at a given edge, the  $Z_2$  topological invariant changes (0 or 1) and the systems are called topologically trivial or nontrivial respectively [2, 35].

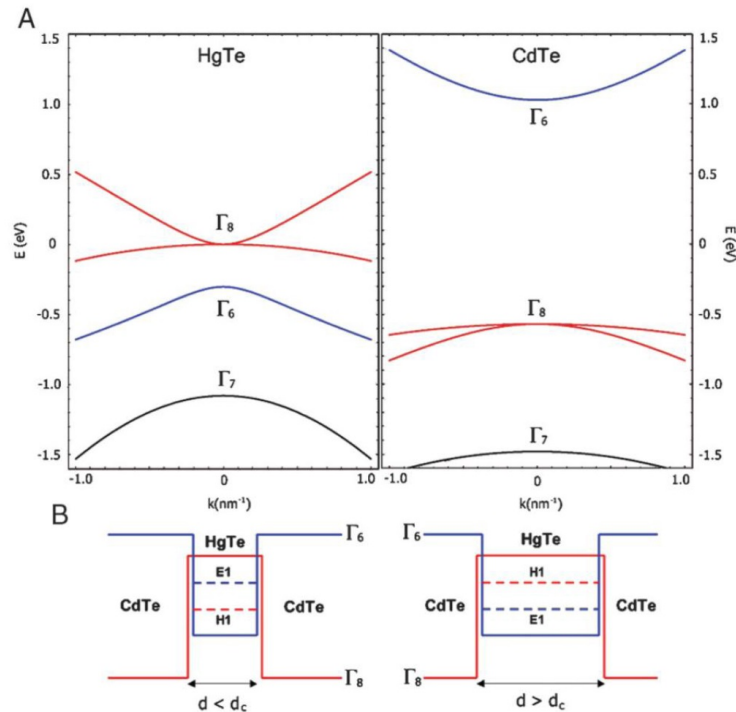


Figure 1.3: 2D TI phase in CdTe/HgTe QWs (A) The band ordering in the constituent materials HgTe and CdTe. (B) schematic picture of quantum well geometry and lowest sub-bands for two different thicknesses Band inversion occurs when the well thickness is larger than the critical thickness. This figure is taken from reference [36].

HgTe/CdTe quantum wells (QWs) are a potential candidate which was first predicted as a QSH state theoretically [36]. The prediction of the HgTe/CdTe QWs to be a topological insulator in 2D was made on the basis of the band ordering of the constitute materials CdTe and HgTe. CdTe has a normal band ordering while the band structure of HgTe shows a band inversion at the point due to the strong

SOC in HgTe [36,37]. This was a revolutionary insight which paved the way for the experimental realization of TIs [37]. Fig. 1.3(A) and (B) show the band diagram for the CdTe/HgTe quantum well structure. In HgTe/CdTe QWs, when the well thickness is less than the critical thickness the band structure will be the same as CdTe and the band structure indicates a trivial insulator. On the other hand, if the HgTe quantum well thickness is greater than a critical thickness, the band structure within the well will remain inverted similar to HgTe. Somewhere between these two extrema, the lowest conduction bands will meet the highest valence bands. Electronic transport measurements [36] on HgTe/CdTe QWs at different thickness confirmed the transition from the normal to the inverted band structure. This work reported the observation of a nominally insulating state which conducts only through 1D edge channels. Later on, the nonlocal measurements and the measurements of the spin polarization also confirmed the helical edge transport and the polarization of the edge states [38,39].

In addition to HgTe/CdTe QWs, bilayer bismuth [40], the broken-gap type-II AlSb/InAs/GaSb QWs [41] and the transition metal oxide  $\text{Na}_2\text{IrO}_3$  [42] are also proposed as QSH insulators.

### 1.2.2 Three Dimensional topological insulators:

In this section we discuss the topological insulating phases in three dimensions (3D) in materials point of view. 3D topological insulators are the first example in nature of topologically ordered electronic phases which exist in bulk solids [35]. They are characterized by a gapped spectrum in their bulk coexisting with gapless metallic surface protected by TR symmetry. The 3D topological insulators differ from the QSHs by various important aspects: (a) 3D TIs have 2D metallic surfaces rather than the 1D edges in QSHs, (b) They can be realized at room temperature rather than the cryogenic temperatures required to realize the QSH insulators and

(c) 3D TI phases exist in standard bulk semiconductors rather than the complex semiconductor heterostructures as in the case of QSH phases [35]. The experimental demonstration of the 3D TI required angle resolved photoemission spectroscopy (ARPES) which is an ideal tool to probe the topological nature of the surface states.

Although there are many 3D TIs discovered up to date, the first 3D TI state is experimentally realized in bismuth-antimony alloy system ( $\text{Bi}_{1-x}\text{Sb}_x$ ) by Hassan's group using ARPES [43]. ARPES is a technique which uses a photon to inject electrons from the lattice to determine the bulk and the surface electronic structure by analyzing the momentum of the ejected electrons [11]. Incident-photon-energy-dependent ARPES studies allow us to distinguish between the 2D surface bands from the 3D bulk bands because the surface bands do not disperse along a direction perpendicular to the surface, in contrast to the bulk bands [35]. Topologically  $Z_2$ -nontrivial state can be realized only when the singly degenerate metallic surface states intersect the Fermi level at an odd number of points. If there are even numbers of surface state crossings, the surface states are topologically  $Z_2$ -trivial because disorder or correlations can remove pair of such crossings by pushing the surface bands entirely above or below the Fermi energy ( $E_F$ ). Fig. 1.4 shows the ARPES spectrum of the  $\text{Bi}_{1-x}\text{Sb}_x$  where five (an odd number) crossings of the surface bands are reported [43].

However, the bulk bandgap in  $\text{Bi}_{1-x}\text{Sb}_x$  is rather small and its topological surface states are quite complex to analyze. Therefore, we need to find out TIs with a simpler surface band structure and a wider bandgap for the purpose of both studying their physical properties in fundamental physics and utilizing them in devices. In 2009 it was predicted and experimentally verified that the binary compounds in tetradymite family such as  $\text{Bi}_2\text{Se}_3$ ,  $\text{Bi}_2\text{Te}_3$  and  $\text{Sb}_2\text{Te}_3$  can be realized as a 3D TI insulator with larger bandgap and simpler surface band structure [44–46]. Among them, it was expected that  $\text{Bi}_2\text{Se}_3$  would be the most promising one for experimental

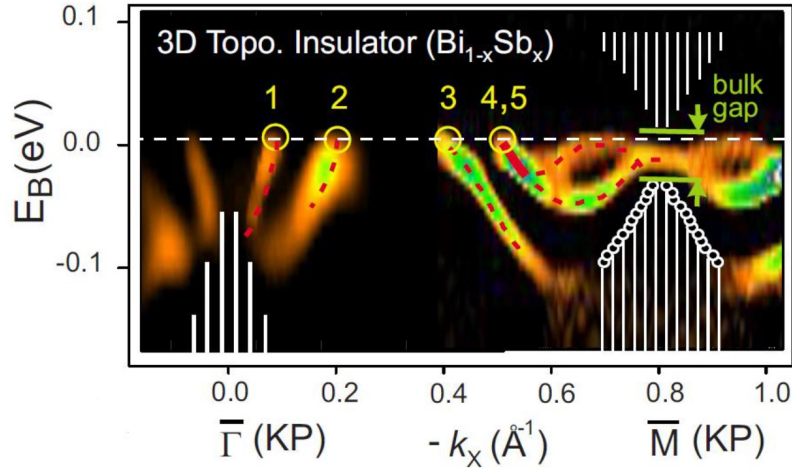


Figure 1.4: The surface-band-dispersion second-derivative image of  $\text{Bi}_{0.9}\text{Sb}_{0.1}$  along  $\Gamma$  and  $M$ . Figure is taken from reference [43].

investigation and potentially also in industrial application [46, 47].

In spite of the simple structure of the surface states in these  $\text{Bi}_2\text{Se}_3$  family of compounds, they possess various difficulties concerning material purity and stoichiometry which lead to a deteriorated insulating character of the bulk [48, 49]. Large amount of Se vacancies or antisite defects are always present in these compounds. As for example, in  $\text{Bi}_2\text{Se}_3$ , the strength of the selenium vacancies exceeds the strength of the antisite defects which implies that near-stoichiometric  $\text{Bi}_2\text{Se}_3$  ( $\text{Bi}_{2+x}\text{Se}_3$ ) always exhibit n-type conductivity [50, 51]. Similarly the isostructural  $\text{Bi}_2\text{Te}_3$  is grown as p-type but the present antisite defects due to the similar electronegativity of Bi and Te make it highly metallic [48, 52]. Therefore the searching of the TI material with better bulk insulating state is highly desirable and various research focused on how to optimize these systems and so decrease the bulk conductivity [49]. To overcome these difficulties researchers found that Se vacancies and antisite defects can be decreased in an ordered stoichiometric structure and stoichiometric  $\text{Bi}_2\text{Te}_2\text{Se}$  with an ordered tetradymite structure can exhibit topological insulating phase [48]. Topological insulator,  $\text{Bi}_2\text{Te}_2\text{Se}$  shows a high resistivity exceeding  $1 \Omega\cdot\text{cm}$  together with a variable-range hopping (VRH) behavior (hallmark of an insulator) yet presents Shubnikov-de Haas (sdH) oscillations signifying the 2D

metallic surface [48]. Angle-resolved photoemission spectroscopy (ARPES) experiments confirmed the topological surface states are consistent with this transport result [53].

### 1.2.3 Transport signature of topological insulator:

As an ideal topological insulator has metallic surface states with no bulk conductance, the transport signature of such a combination is an initial increase of the electrical resistance with decreasing temperature followed by a resistance saturation where the metallic surface conductance saturates the insulating bulk resistance [54, 55]. This is the universal transport behavior of a topological insulator where TR symmetry is always preserved. Although  $\text{Bi}_2\text{Se}_3$  family of topological insulators do not show such behavior because of the aforementioned difficulties, this universal resistance behavior is followed by various TI materials ranging from  $\text{Bi}_2\text{Te}_2\text{Se}$  to  $\text{SmB}_6$  [48, 56] (as shown in Fig. 1.5(a) and 1.5(b)). The other transport signature of a 3D topological insulator with high temperature bulk insulating and only low temperature surface conducting behavior is that the sample thickness should not affect the measured low temperature limiting resistance but be independent of it [56].  $\text{SmB}_6$  has clear thickness independent resistance at low temperature which implies complete insulating bulk and metallic surface separation at low temperature [56].

The aforementioned universal TI resistivity behavior is also observed in several semimetals only when TR symmetry is broken in presence of magnetic field (Fig. 1.5(c)). But, in those materials this magnetic field induced metal to insulator transition is originated from a particular orbital texture on the electron pocket giving rise to their small residual resistivity at zero field and subject to strong scattering induced by a magnetic field [55]. In Fig. 1.5(c) and (d) the normalized resistance of  $\text{LaSb}$  is compared with the normalized resistance of the topological material  $\text{SmB}_6$

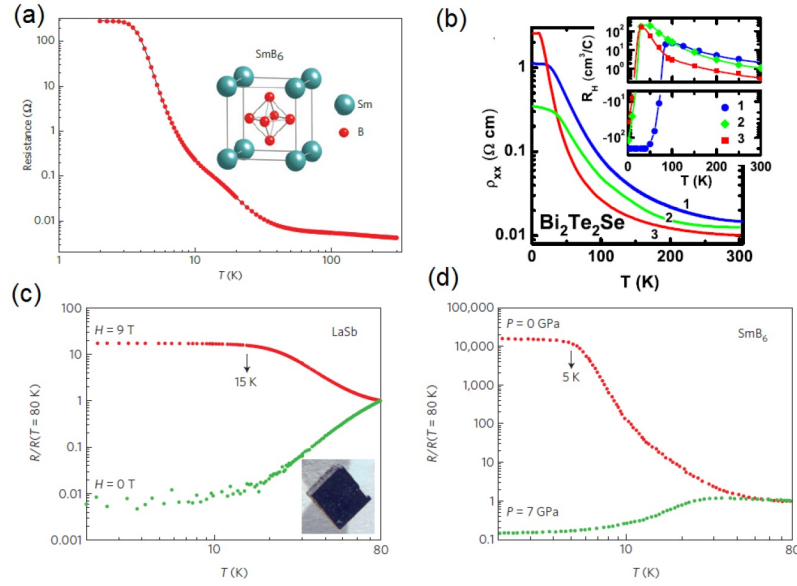


Figure 1.5: (a) Temperature dependent electrical resistance of SmB<sub>6</sub> sample. The inset shows the crystal structure of it. (b) Temperature dependence resistivity of various samples of Bi<sub>2</sub>Te<sub>2</sub>Se and the inset shows the temperature dependent Hall coefficient,  $R_H$ , for the respective samples. (c) Temperature dependent normalized resistance of LaSb at  $H = 0$  (green) and  $H = 9$  T (red). (d) Temperature dependent normalized resistance of SbB<sub>6</sub> at 7 GPa (green) and ambient pressure (red). Figures are taken from references [48, 54, 56]

and it is illustrated that increasing the field in LaSb is analogous to the decreasing the pressure in SmB<sub>6</sub> [54].

### 1.2.4 Effect of pressure on topological insulator:

Here, I discuss the existing high pressure studies on the simplest 3D topological insulators, the A<sub>2</sub>B<sub>3</sub>-type Bi<sub>2</sub>Se<sub>3</sub>, Bi<sub>2</sub>Te<sub>3</sub> and Sb<sub>2</sub>Te<sub>3</sub> compounds. After the discovery of topological insulator the first great achievement of the high pressure research was the discovery of the topological superconductivity in Bi<sub>2</sub>Te<sub>3</sub> [57]. Combined high pressure structural and transport measurements indicated that the superconductivity occurred in Bi<sub>2</sub>Te<sub>3</sub> at the ambient phase without crystal structure phase transition as shown in Fig. 1.6 (a) and (b) [57]. But later it was observed Bi<sub>2</sub>Te<sub>3</sub> exhibited superconducting transition followed by a structural transition (Fig. 1.6(c)) [58]. Thus, determining the exact pressure for the superconducting transition is the key

to settling whether  $\text{Bi}_2\text{Te}_3$  can be a topological superconductor. The later report is more reliable because helium was used as a pressure transmitting medium [58]. Apart from the pressure induced superconductivity,  $\text{Bi}_2\text{Te}_3$  undergoes a series of pressure induced structural phase transition and the three high pressure structural phase transitions of  $\text{Bi}_2\text{Te}_3$  have been found to induce the discontinuous changes in electrical transport parameters at  $\sim 8$ ,  $\sim 12$  and  $\sim 17.8$  GPa (Fig. 1.6(b)) [59]. In addition electronic topological transition and the semiconductor-to-metal transition have confirmed at  $\sim 4$  GPa and  $\sim 9.2$  GPa respectively (Fig. 1.6(d)) [59].

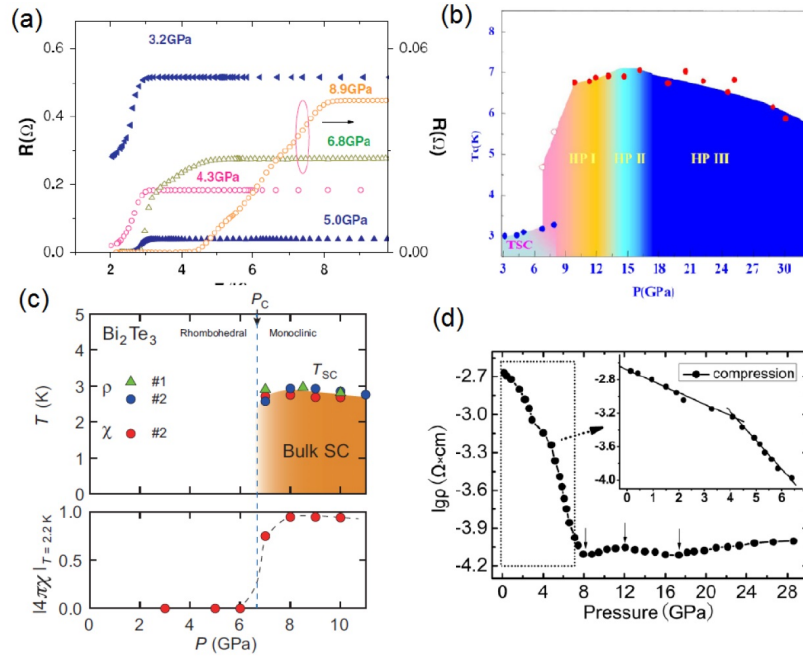


Figure 1.6: Temperature dependent electrical resistance of  $\text{Bi}_2\text{Te}_3$  in the vicinity of the superconducting transition. (b) P-T phase diagram with various structural phases as taken from [57]. (c) P-T phase diagram and pressure dependence of superconducting volume fraction of  $\text{Bi}_2\text{Te}_3$  as taken from [58]. (d) Pressure dependence electrical resistivity of  $\text{Bi}_2\text{Te}_3$  at room temperature. The arrows indicate the anomaly in the resistivity related to the structural transition. The inset presents the enlarge view in the low pressure region. Figures are taken from [57–59].

Pressure induced superconductivity of  $\text{Sb}_2\text{Te}_3$  was investigated by high pressure resistance measurement using fine hBN powder as a pressure transmitting medium [60]. A prominent low temperature resistance drop was observed at  $\sim 4$  GPa although the superconducting zero resistance was first observed at 6.8 GPa

with the first structural phase transition at 12.9 GPa. Although this results indicate  $\text{Sb}_2\text{Te}_3$  as a prominent topological superconductor, the use of non-hydrostatic hBN medium demand other experimental verifications with better pressure transmitting medium to verify whether the superconductivity occurs after structural transition as in the case of  $\text{Bi}_2\text{Te}_3$  [48,57].  $\text{Sb}_2\text{Te}_3$  also shows three structural phase transitions at 12.9 GPa (R-3m-C2/m), 16 GPa ( $\beta$ -C2/m -  $\gamma$ -C2/m), and 20 GPa ( $\gamma$ -C2/m - Im-3m) and pressure induced ETT was also observed at  $\sim 3$  GPa [61].

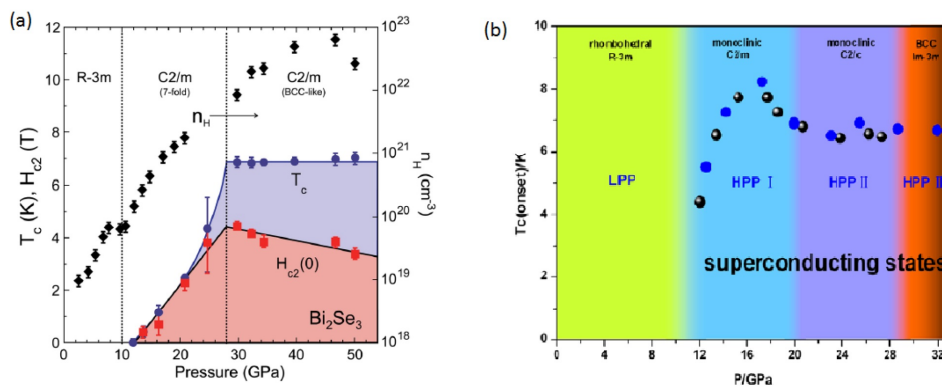


Figure 1.7: Phase diagrams of  $\text{Bi}_2\text{Se}_3$  (a) P-T phase diagram of  $\text{Bi}_2\text{Se}_3$  as taken from reference [26]. (b) Structural phase diagram of  $\text{Bi}_2\text{Se}_3$  as taken from reference [27].

Simultaneous low-temperature electrical resistivity and Hall Effect measurements under pressure on the topological insulator  $\text{Bi}_2\text{Se}_3$  revealed that the system went into superconducting state above 11 GPa and both the transition temperature  $T_c$  and the upper critical field  $H_{c2}$  increased with pressure up to 30 GPa, where they reached maximum values of 7 K and 4 T, respectively [26]. Upon further increase of pressure,  $T_c$  remained anomalously constant up to the highest achieved pressure but in contrary the carrier concentration increased continuously including a tenfold increase over the pressure range where  $T_c$  remained constant as shown in Fig. 1.7(a) [26]. This result, together with the quasilinear temperature dependence of  $H_{c2}$  points to an unconventional pressure induced pairing state in  $\text{Bi}_2\text{Se}_3$  which is unique among the other superconducting topological insulators. High pressure

structural investigations on  $\text{Bi}_2\text{Se}_3$  [27, 28] revealed that it transformed from ambient pressure rhombohedral (R-3m) to monoclinic (C2/m) phase near 10-12 GPa that followed the superconducting transition. In this case, new theories and further experiments are required to clarify whether  $\text{Bi}_2\text{Se}_3$  with such a monoclinic structure would still keep its topological characteristics. Two more structural transitions were also observed at 20 and 29 GPa [27, 28]. A phase diagram of superconductivity versus pressure related to the structural transition was illustrated by P.P. Kong et al. (Fig. 1.7(b)) [27]. In addition to the structural and superconducting transition  $\text{Bi}_2\text{Se}_3$  shows pressure induced ETT at 5.8 GPa and insulator to metal transition at 9.7 GPa [62].

### 1.2.5 TQPT and pressure induced topological Superconductor:

Previous section discussed that the realizations of pressure induced topological superconductivity in the  $\text{Bi}_2\text{Se}_3$  family of compounds are controversial. However, application of reasonable hydrostatic pressure may turn a trivial insulator into a topological insulator (as shown in Fig. 1.8(a)) with many interesting features including topological superconductivity. Such transition from a trivial insulator into a nontrivial topological insulator is called topological quantum phase transition (TQPT) which is always accompanied by a band inversion in some K points of the Brillouin Zone. Among the Bismuth-tellurohaldes  $\text{BiTeX}$  ( $X = \text{Cl}, \text{Br}, \text{and I}$ ), the so-called Rashba semiconductors,  $\text{BiTeI}$  is theoretically proposed to be a new inversion-asymmetric topological insulator under pressure at 1.7-4.1 GPa [63]. But the experimental verification of topological quantum phase transition (TQPT) remained highly controversial. The measurements of Shubnikov-de Haas oscillation [64] and combined x-ray powder diffraction (by observing a minimum in  $c/a$

ratio between 2.0 - 2.9 GPa as shown in 1.8(b)) and infrared spectroscopy measurements (by observing a maximum in free carrier spectral weight as shown in figure 1.8(c)) [65] confirmed the topological quantum phase transition (TQPT) under pressure but the other optical investigation concluded the absence of TQPT at high pressure [66]. TQPT was also confirmed by high pressure transport measurements where a resistance minimum was observed at the same pressure range (as shown in Fig. 1.8(d) [67]. Pressure induced superconductivity was also observed in this compound with a maximum of  $T_c$  of 5.2 K at 23.5 GPa [67]. A comparative high pressure optical study on BiTeCl and BiTeBr reported that BiTeCl showed a clear structural transition at 6 GPa but the pressure evolution of BiTeBr was more subtle [68]. Their data was consistent with a potential Weyl phase in BiTeBr at 5-6 GPa, followed by the onset of a structural phase transition above 7 GPa [71]. In another study by combined theoretical and experimental it is also reported that there is a possibility of ETT and topological quantum phase transition in BiTeBr [67]. Pressure induced superconductivity was also observed in BiTeBr similar to BiTeI [67]. High pressure resistivity, Hall coefficient and Raman measurements on single crystal BiTeCl revealed pressure induced superconducting phase with an insulating normal state [68]. Upon heavy compression, another different superconducting phase is entered into with a metallic normal state. A domelike evolution of the superconducting transition temperature with pressure is obtained with a crossover from the electron to hole carriers across the boundary of the two superconducting phases suggesting the realization of a possible topological superconductor in the coexisted insulating and superconducting phases of this material [68]. Thus, the BiTeX series of compounds are naturally expected to be possible candidates of topological superconductors under compression.

Recently, pressure induced multiple topological quantum phase transitions and superconductivity was achieved in quasi 1D topological insulator bismuth iodide

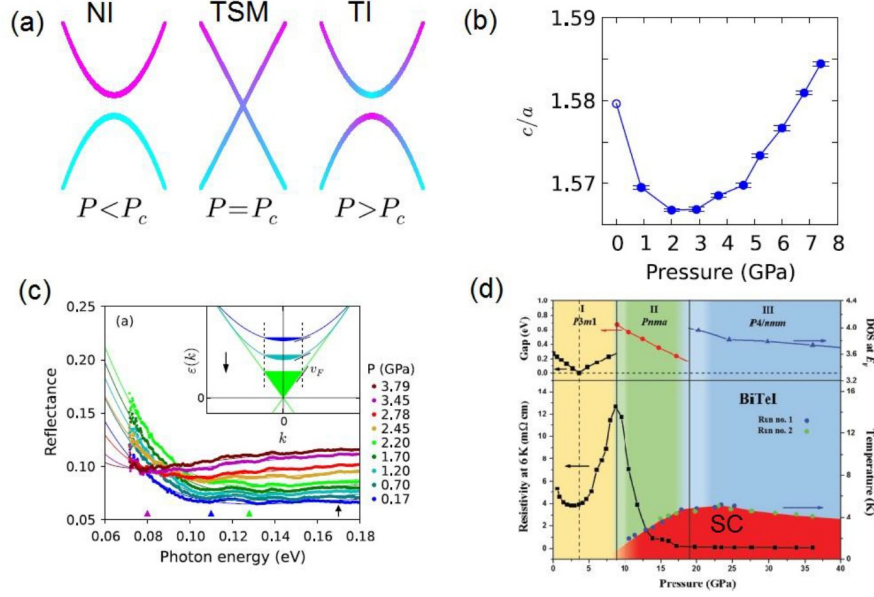


Figure 1.8: (a) Schematic illustration of Topological quantum phase transition (TQPT). NI, TSM and TI stand for normal insulator, topological semimetal and topological insulator respectively. (figure is taken from reference [65]). (b) Pressure dependence  $c/a$  ratio which shows a minimum at TQPT. This figure is taken from reference [65]. (c) Reflectance at low pressure and low photon energy after fringe removal. Detailed description is given in reference [65]. (d) P-T phase diagram of BiTeI including TQPT, SC and structural transitions. Detailed description is given in reference [67].

$\beta$ -Bi<sub>4</sub>I<sub>4</sub> [69]. Fig. 1.9(a) summarizes the pressure dependence resistivity at room temperature and the critical temperature whereas, Fig. 1.9 (b) illustrates the multiple TQPT under pressures. The system transformed from a ambient pressure strong TI (STI) to weak TI (WTI) and back to STI which induced corresponding anomalies in the resistivity. The observed superconductivity was related to a nonmetal-to-metal transition in  $\beta$ -Bi<sub>4</sub>I<sub>4</sub>. The transition temperature  $T_c$  increased with applied pressure, and a typical dome-like evolution was observed as shown in the figure Fig. 1.9 (a) [69]. Another report showed pressure induced amorphization in this compound [70].

Pressure induced series of topological phase transition was theoretically predicted in TiTe<sub>2</sub> [72]. The other A<sub>2</sub>B<sub>3</sub> type of compound such as As<sub>2</sub>Te<sub>3</sub> [73], Sb<sub>2</sub>Se<sub>3</sub> [74] and Bi<sub>2</sub>S<sub>3</sub> [75] also shows various interesting phenomena including ETT, TQPT,

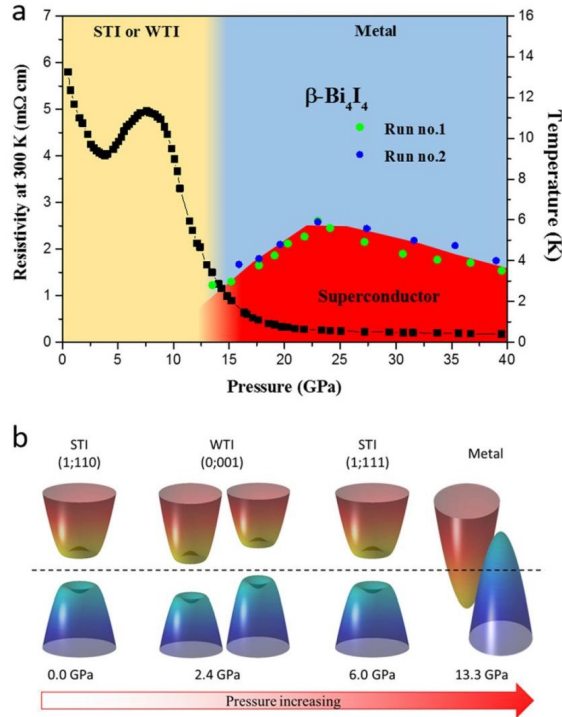


Figure 1.9: Electronic P-T phase diagram for  $\beta$ -Bi<sub>4</sub>I<sub>4</sub>. (a) Superconducting T<sub>c</sub> shows dome-like behavior. The resistivity values at 300 K are also shown. The resistivity of  $\beta$ -Bi<sub>4</sub>I<sub>4</sub> exhibits a more complicated feature, which demonstrates that high pressure dramatically alters the electronic properties in  $\beta$ -Bi<sub>4</sub>I<sub>4</sub>. (b) Schematic illustrations of the band structure evolution under various pressures. Detailed description is given in reference [69].

insulator to metal transition and superconductivity under pressure. Topological phase transition was also predicted in TlBiS<sub>2</sub> and TlSbS<sub>2</sub> under hydrostatic pressure as well as uniaxial and biaxial strain [76]. These observations motivates for searching new materials for studying pressure induced ETT, TQPT and superconductivity and in the current thesis I investigate the high pressure effects on similar compounds such as Sb<sub>2</sub>S<sub>3</sub> (similar to Sb<sub>2</sub>Se<sub>3</sub>, Bi<sub>2</sub>Se<sub>3</sub>, As<sub>2</sub>Te<sub>3</sub>), AgBiSe<sub>2</sub> (similar to TlBiS<sub>2</sub> and TlSbS<sub>2</sub>) and TiTe<sub>2</sub> by spectroscopic and transport techniques.

### 1.3 Topological semimetal

The term "topological semimetal" is widely used and basically includes all semimetals that exhibit some non-trivial band topology [77]. They are a newly discovered

class of topologically non-trivial materials beyond the gapped topological materials such as topological insulators and topological superconductors. Unlike topological insulators, topological semimetals (TSMs) do not have a band gap in their electronic band structure but most of the topological semimetals have in common that their unusual band topology arises from a band inversion. There are several classes of TSMs: Dirac semimetals (DSMs), Weyl semimetals (WSMs), and nodal line semimetals (NLSMs) [77, 78]. Among these TSMs, I investigate the WSMs in this thesis.

In the following sections, I will discuss the Characteristics of topological Weyl semimetals including its remarkable Fermi arcs and chiral anomaly induced negative magnetoresistance properties. Then the optical and transport properties of Weyl semimetals are discussed followed by the importance on high pressure research. This sections ends with the discussions on the classifications of Weyl semimetals and there pressure studies.

### 1.3.1 Topological consequences of Weyl semimetal:

Topologically non-trivial systems exhibit two different manifestations of topology. The first is to look for nontrivial surface states, and the second is to study the response to an applied electric and/or magnetic field [77]. In contrast to topological insulators where only the surface states are interesting, a Weyl semimetal features unusual band structure on the surface and also in the bulk [78]. The Weyl nodes of opposite chirality are separated in momentum space and are connected only through the crystal boundary by an exotic non-closed surface state. These surface states take the form of Fermi arcs connecting the projection of bulk Weyl nodes in the surface Brillouin zone (BZ). The other consequence is the chiral anomaly which is important in understanding some structures of the standard model of particle physics based on quantum field theory [78]. Weyl semimetals provide an electronic route to realizing

the chiral anomaly in condensed matter physics. Since the Weyl nodes are separated in momentum space, parallel magnetic and electric fields can pump electrons between Weyl nodes of opposite chirality that are separated in momentum space. This process violates the conservation of chiral charge and leads to an axial charge current, making a Weyl semimetal more conductive in an increasing magnetic field that is parallel to the electric field [77, 78].

### 1.3.2 Optical properties of WSMs:

The unconventional electronic band structure of Weyl semimetals causes remarkable optical properties which may lead one of the most important demonstrations of how these materials differ from trivial metals and insulators [79]. Theoretically it is proposed that, in a noninteracting electron system with two symmetric energy bands touching each other at the Fermi energy, the real part of the optical conductivity arising from the interband transitions follows a power-law of frequency ( $\omega$ ) dependence which is mathematically written as,

$$\sigma_1(\omega) = \left( \frac{\hbar\omega}{2} \right)^{\frac{d-2}{z}} \quad (1.1)$$

where,  $d$  represents the dimensions of the system and  $z$  represents the power law of the band dispersion [80, 81]. This universal behavior was verified in graphene ( $d=2$ ,  $z=1$ ) by the experimental observation of frequency independent optical conductivity [82]. Therefore for 3D WSMs ( $d=3$ ) with linear band dispersion ( $z = 1$ ) the optical conductivity should follow a linear behavior with frequency. Further theoretical calculations suggests that the  $\omega$  dependent optical conductivity associated with the interband transition near the Weyl points can mathematically be written as,

$$\sigma_1(\omega) = \frac{NG_0\omega}{24v_F} \Theta(\omega - 2|\mu|) \quad (1.2)$$

where  $N$  is the number of Weyl points,  $G_0 = 2e^2/h = 7.748 \times 10^{-5}$  represents the quantum conductance,  $v_F$  denote the Fermi velocity and  $\mu$  is the chemical potential

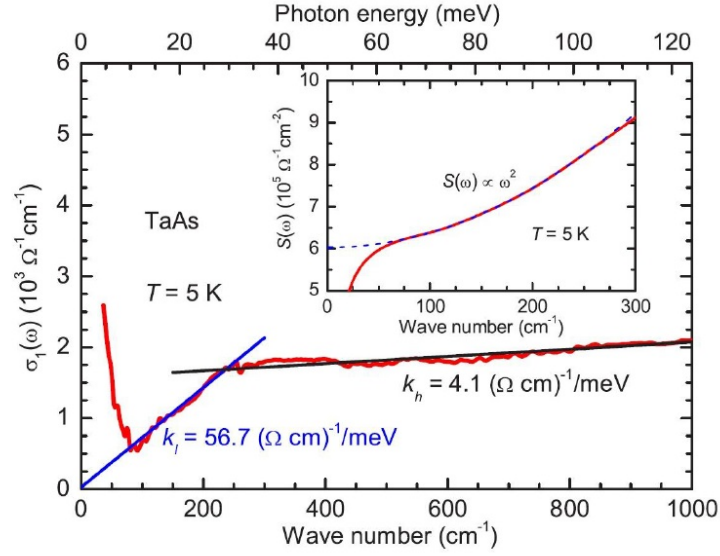


Figure 1.10: Optical conductivity of TaAs at 5 K. The blue and black solid lines through the data are linear guides to the eye. The inset shows the spectral weight as a function of frequency at 5 K (red solid curve), which follows an  $\omega^2$  behavior (blue dashed line). This figure is taken from reference [80].

with respects to the Weyl points [80]. This equation clearly represents that, regardless of whether or not the Weyl points are on the Fermi surface, the obtained  $\omega$ -linear conductivity arising from the Weyl points extrapolates to the origin. Such  $\omega$ -linear conductivity extrapolated to the origin was experimentally observed in type-I WSM TaAs [80]. Fig. 1.10 shows the optical conductivity spectra of TaAs at 5K which is characterized by two  $\omega$ -linear components with distinct slopes. The low energy  $\omega$ -linear component of the optical conductivity, which extrapolates to the origin, arises purely from the interband transitions near the Weyl points. The deviation from the origin of the higher energy  $\omega$ -linear conductivity suggests the high-energy  $\omega$ -linear component is a combination of contributions from Weyl points and the trivial bands [80]]. Such  $\omega$ -linear conductivity has also been observed in other 3D Dirac and Weyl-semimetals including ZrTe<sub>5</sub> [82] and NbP [83] and nowadays, it is widely considered as a hallmark for 3D Dirac physics.

During pressure induced TQPT between trivial insulator to topological insulator, as the pressure reaches the critical value ( $P_c$ ) the gap closes initiating a Weyl

semimetal phase and further reopens the gap resulting in a topological insulator phase characterized by a band-inversion phenomena [65]. Therefore, the linear frequency dependence of the optical conductivity spectra is naturally expected at the critical pressure.

### 1.3.3 Transport properties of Weyl semimetals:

Apart from the chiral anomaly induced negative magnetoresistance and nonlocal transport phenomena, Shubnikov-de Haas (SdH) oscillation and extreme magnetoresistance (XMR) are the other two important transport properties of Weyl semimetals. ShH oscillation measurement is one of the standard transport experiments to confirm the unusual phase in Weyl semimetals by measuring the nontrivial Berry phase [84]. SdH oscillation originates from the Landau quantization of electronic states in presence of high magnetic field. The magnetoresistance oscillates periodically with the inverse of magnetic field ( $1/B$ ) as the Fermi level crosses one and another Landau level [84]. The frequency of the oscillation is directly related to the cross section of the Fermi surface ( $A_F$ ) by Onsager relation,  $F=(\Phi_0/\pi^2)^2 A_F$ , where  $\Phi_0$  is the magnetic flux quantum [85]. The cyclotron effective mass ( $m^*$ ) and the quantum lifetime ( $\tau$ ) of the carriers is obtained by fitting the temperature dependences of the amplitude of the oscillations to the Lifshitz-Kosevich formula,

$$\frac{\Delta\rho_{xx}(T, B)}{\rho_{xx}(0)} = e^{(-2\pi^2 K_B T_D/\beta)} \frac{2\pi^2 K_B T_D/\beta}{\sinh(2\pi^2 K_B T_D/\beta)} \quad (1.3)$$

where,  $K_B$  is the Boltzmann's constant,  $\beta = ehB/2m^*$  and  $T_D = h/4\pi^2\tau K_B$  are the fitting parameters, which are directly related with the effective mass ( $m^*$ ) and quantum lifetime ( $\tau$ ) of the charge carriers [85].

Nevertheless, to analyze the effect of pressure on the SdH oscillations of  $\rho_{xx}$  in a Weyl semimetal, one needs to utilize the following expression,

$$\frac{\Delta\rho_{xx}}{\langle\rho_{xx}\rangle} = A(T, B) \cos \left[ 2\pi \left( \frac{F}{B} - \gamma + \delta \right) \right] \quad (1.4)$$

where,  $A(T, B)$  is the amplitude of the oscillations given by the Lifshitz-Kosevich formula,  $\langle \rho_{xx} \rangle$  is non-oscillatory part of  $\rho_{xx}$ ,  $F$  is the frequency of the oscillation,  $\gamma$  is the Onsenger phase related to the nontrivial topology, and  $\delta$  is a phase shift determined by the dimensionality (it is 0 for 2D and is  $1/8$  for 3D) [86]. By studying the pressure dependence frequency of the oscillation one can obtain that how pressure affects the cross section of the Fermi surface. To investigate pressure induced topological phase transition Landau level index is plotted as a function of  $1/B$ . The intercept of the plot to the infinite field limit give the information of the Onsenger phase,  $\gamma = 1/2 - \Phi_B/2\pi$ , with  $\Phi_B$  is the Berry phase. For a trivial material  $\Phi_B$  is 0 and  $\gamma = 1/2$  whereas, for a topological material  $\Phi_B$  is  $\pi$  and thus  $\gamma = 0$  [86]. So from the value intercept one can decide the trivial or nontrivial nature of a particular band and the topological transition is determined by observing the change in the value of Berry phase According to this the pocket of NbAs is referred as topologically trivial and pocket is referred as topologically nontrivial and no pressure induced topological transition is observed in this compound as no change in the phase factor  $(-\gamma + \delta)$  of the oscillations is occurred in the experimental pressure range 1.11 [86]. On the contrary a sudden change in the phase factor is observed in Cd<sub>3</sub>As<sub>2</sub> at 1.3 GPa which is well below the structural transition (2.5 GPa) [87]. This result implies a possible topological phase transition in pressurized Cd<sub>3</sub>As<sub>2</sub> without structural transition [87].

The other important property of the WSMs is that they show extreme nonsaturating magnetoresistance under transverse magnetic field. Including type-I WSMs (TaAs family) [85, 86, 88, 89] and type-II WSMs (WTe<sub>2</sub>, MoTe<sub>2</sub>, TaIrTe<sub>4</sub>) [31, 90, 91], extreme magnetoresistance (XMR) is also observed in other semimetals including Na<sub>3</sub>Bi [92], Cd<sub>3</sub>As<sub>2</sub> [93], PtSn<sub>4</sub> [94], LaBi [55], LaSb [54], NbSb<sub>2</sub> [95], TaSb<sub>2</sub> [96], (Hf/Zr)Te<sub>5</sub> [98, 235] etc. Various mechanisms are proposed to explain the XMR

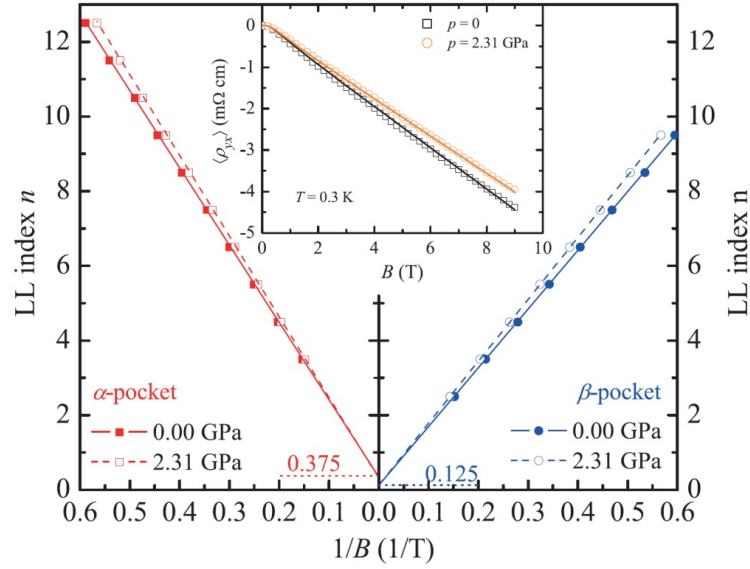


Figure 1.11: Landau level indices  $n$  as functions of  $1/B$  for NbAs. The solid and open symbols represent the data points at  $p = 0$  and 2.31 GPa, respectively. The two dot lines are guidelines for 0.125 and 0.375, respectively. Figure is taken from the reference [86].

phenomena in these materials. In NbP [85], the XMR is attributed to the electron-hole compensation, which means a perfect balance between the electron and hole populations similar to various reports on LaBi, LaSb, and WTe<sub>2</sub> [54, 55, 90]. The large MR in PtSn<sub>4</sub> was usually associated with its ultrahigh mobility [94]. For Cd<sub>3</sub>As<sub>2</sub> and other compounds in TaAs family, the XMR is can be ascribed to a remarkable protection mechanism that strongly suppresses backscattering in zero magnetic field [93]. Recent theoretical calculations combined with experimental results unify the phenomenology of XMR in various semimetals and it is suggested that XMR originates from a combination of compensated electron-hole pockets and a particular orbital texture on the electron pocket [55]. Similar orbital structure resulting universal triangular T-H phase diagram (Fig. 1.12), in seemingly unrelated materials implies that XMR is a ubiquitous phenomenon and expected to be found in many more compounds [55].

There are various high pressure reports which investigate the relation between XMR and pressure induced superconductivity. Pressure generally suppresses the

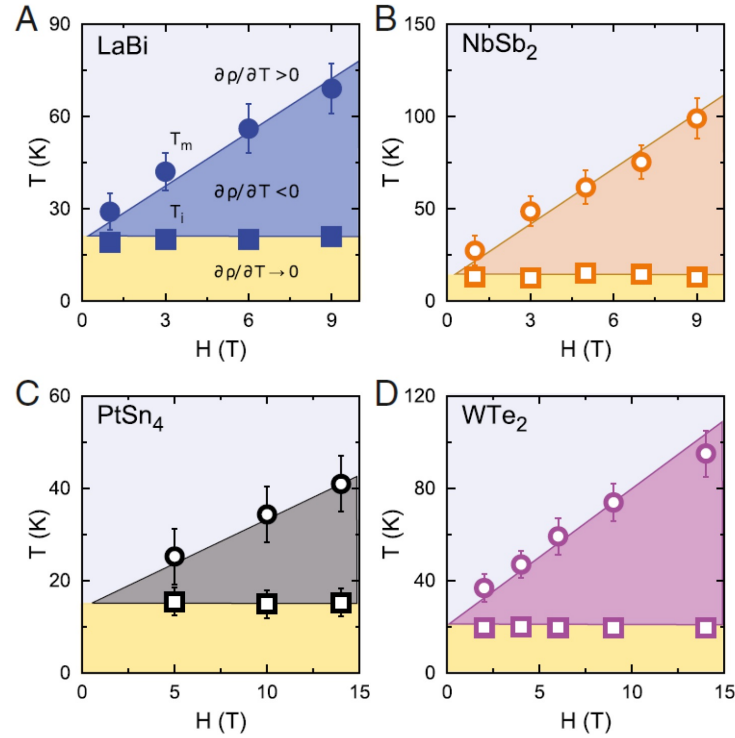


Figure 1.12: Universal triangular T-H phase diagram of various semimetals. Figure is taken from reference [55]

XMR and gives rise to superconductivity in several materials including  $\text{WTe}_2$  [30, 99],  $\text{MoTe}_2$  [31],  $\text{NbAs}_2$  [100],  $\text{ZrTe}_5$  [101],  $\text{HfTe}_5$  [102],  $\text{LaBi}$  [55, 103] etc. The most common feature is that rapid onset of superconductivity arises where XMR is suppressed followed by a slow suppression of transition temperature with pressure [103]. A common region of coexistence between superconductivity and XMR is found in  $\text{LaBi}$  [103] in contrast to other superconducting XMR materials such as  $\text{WTe}_2$  [30, 99] where superconductivity appears when MR is fully suppressed (discussed later). Therefore, these kinds of investigations are very important for understanding the interplay between XMR, topological states, and superconductivity.

### 1.3.4 Classifications of Weyl semimetals:

Depending on the tilting of the Weyl cones and whether the Lorentz symmetry is respected, Weyl semimetals (WSMs) can be divided into two topologically distinct types as type-I and type-II WSMs [104]. In type-I WSMs the Lorentz symmetry is

respected and the Weyl cone is only weakly tilted so that the electron-like states and hole-like states occupy separate energy ranges, above or below the Weyl point i.e. they have a point-like Fermi surface and consequently zero density of states at the energy of Weyl points. On the other hand in type-II WSMs the Lorentz symmetry is violated and the Weyl cones are significantly tilted i. e. they have non-vanishing thermodynamic density of states at the energy of Weyl points [104].

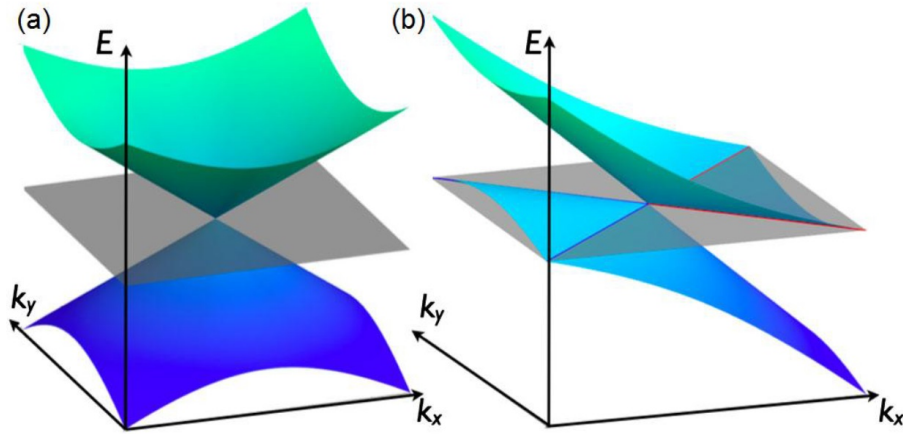


Figure 1.13: Possible types of Weyl semimetals. a, Type-I WP with a pointlike Fermi surface. b, A type-II WP appears as the contact point between electron and hole pockets. The grey plane corresponds to the position of the Fermi level, and the blue (red) lines mark the boundaries of the hole (electron) pockets. Figure is taken from reference [104]

Type-I Weyl semimetals have complex 3D crystal structure and the large number (12 pairs) of Weyl points and they are identified in TaAs class of compounds. The Weyl semimetal of type-II always have less number of Weyl pairs and they are found in  $MTe_2$  ( $M = Mo, W$ ) with eight Weyl points and  $TaIrTe_4$  with only four Weyl points. Experimentally, the Fermi arc has been detected by angle resolved photoemission spectroscopy measurements for both types of materials, while the negative longitudinal magnetoresistance (MR) i. e. the chiral anomaly has been observed only for the type-I WSM [78].

### 1.3.5 High Pressure studies on type-I WSMs:

First high pressure investigation of transition-metal monpnictides was performed in NbAs [105] after their immediate discoveries [24, 25, 106–108]. High pressure synchrotron-XRD and low temperature resistance measurements on the Weyl semimetal NbAs revealed that the crystal structure was stable up to 26 GPa and no superconducting transition was observed down to 0.3K under pressure up to 20GPa [105]. Therefore, no dramatic pressure effects were observed on both crystal structure and electronic state of WSM NbAs and they had related the robustness of the WSM state in NbAs to its stable crystal structure. Later, Yongkang Luo et al. investigated the effect of hydrostatic pressure on the magnetotransport properties on NbAs up to 2.31 GPa [86]. Although the Fermi surfaces (both  $\alpha$ - and  $\beta$ -pockets) undergo an anisotropic evolution with pressure the topological features of the two pockets observed at atmospheric pressure remained unchanged up to 2.31 GPa. From the large Debye temperature for this compound,  $\theta_D = 450(9)$  K, it was indicated that a NbAs had a 'hard' crystalline lattice structure that supported the relatively weak pressure effect [86].

Experimental SdH oscillations measurements and band-structure calculations of NbP revealed that the electronic structure was very robust and the characteristics topological features of the Fermi surface with two electron and two hole pockets remained unchanged in their experimental pressure range up to 2.8 GPa [109] similar to that of NbAs [86]. Pressure dependent resistance measurements showed a minimum in resistivity near 6 GPa [110]. It was also reported that at 4.4 GPa the temperature dependent resistivity showed a minimum around 100 K. For pressures higher than 6.5 GPa, the resistivity monotonously decreased with increasing temperature. Recent, high pressure Raman, synchrotron x-ray diffraction, and electrical transport studies along with first-principles density functional theoretical (DFT)

analysis on NbP revealed a pressure induced Lifshitz transition near  $\sim 9$  GPa [111].

By combining theoretical calculations and experimental transport and synchrotron based structural investigations on TaAs Yonghui Zhou et al. confirmed a pressure induced new Weyl semimetal phase at 14 GPa [112]. It was reported that TaAs transformed from ambient I41md phase (t-TaAs) with 24-Weyl nodes distributed at two different energy levels to a high-pressure hexagonal P-6m2 (h-TaAs) phase with 12Weyl nodes at the same energy level. Decompression XRD experiments confirmed that the hexagonal phase is metastable at ambient pressure once it is formed beyond 14 GPa, which provides an excellent platform to study the interplay between surface states and other exotic properties without the limitation of access due to high pressure environments [112].

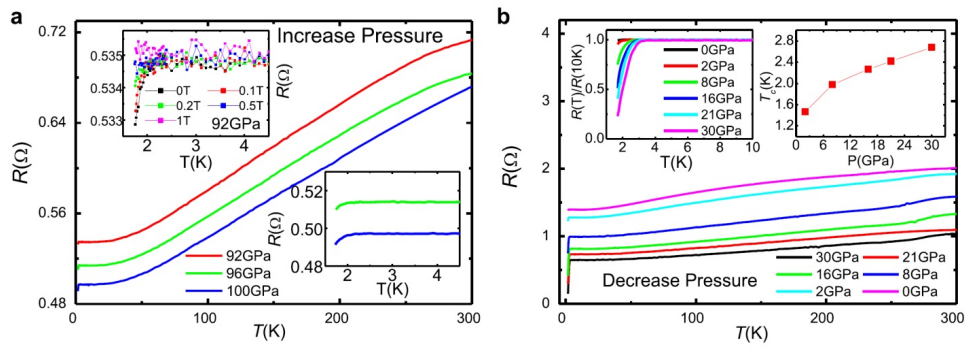


Figure 1.14: Temperature-dependent resistance with increasing and decreasing pressures. a Temperature-dependent resistance from 92 to 100 GPa with increasing pressure. The  $R(T)$  curves under different pressures with decreasing pressure are shown in b. The upper-left inset in a shows the resistance vs. temperature under different fields at 92 GPa, and the lower-right inset shows the enlarged view of the data measured near 71 GPa in low-temperature region. The superconductivity is further evident by a sharp 75% drop of the normal state resistance under 30 GPa, as shown in the left inset in b. The inset on the right-hand side in b shows the pressure dependence of  $T_c$  in decreasing pressure. This figure is taken from reference [29]

Among the transition metal monopnictides, TaP is the first compound which shows pressure induced superconductivity. High pressure resistance measurements and synchrotron based structural measurements on TaP confirmed the concurrence of superconductivity along with a structural transition at about 70 GPa (Fig. 1.14)

[29]. The high pressure P-6m2 was confirmed as a new topological Weyl semimetal, similar to TaAs high-pressure phase [112]. It was found that this high-pressure phase and superconductivity retained when the pressure was released (Fig. 1.14). The discovery of pressure induced superconductivity in TaP will stimulate further efforts in investigating superconductivity in topological materials and paving a possible path to the ultimate discovery of topological superconductors [29].

### 1.3.6 High Pressure studies on type-II WSMs:

Ambient and high pressure (up to  $\sim 2.3$  GPa) quantum oscillation study on the recently discovered type II Weyl semimetal  $\text{WTe}_2$  [113] reported that the perfect balance between the electron and hole populations was the origin of the extremely large magnetoresistance in  $\text{WTe}_2$ . Later, higher pressure measurements [99] revealed the suppression of the large magnetoresistance and emergence of superconductivity (Fig. 1.15) in pressurized  $\text{WTe}_2$  via high-pressure synchrotron X-ray diffraction, electrical resistance, magnetoresistance and alternating current magnetic susceptibility measurements. Structural investigations did not report any structural phase transition up to 20 GPa which meant that the observed superconductivity was not from structural origin. In situ high-pressure Hall coefficient measurements at low temperatures demonstrated that elevating pressure decreased the population of hole carriers but increased that of the electron ones [30]. Significantly, at the critical pressure, a sign change of the Hall coefficient was observed (Fig 1.15). Another similar study [30] also reported the pressure induced superconductivity in  $\text{WTe}_2$  but at a lower pressure compared to the above mentioned report. Thus the phenomena of complete suppression of magnetoresistance and the appearance the superconductivity may provide a new platform for our understanding of superconductivity phenomena in similar compounds.

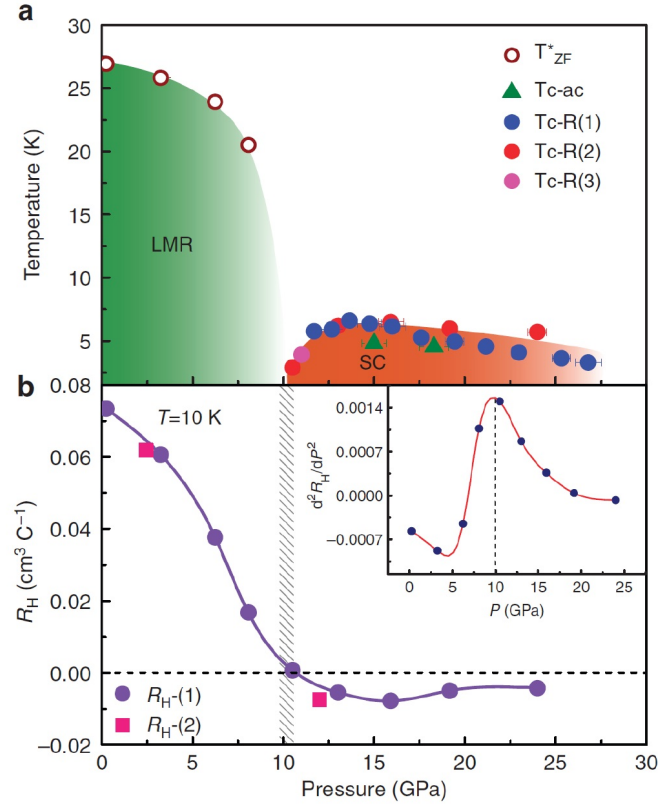


Figure 1.15: Pressure-temperature phase diagram of  $\text{WTe}_2$  and pressure dependent Hall coefficient. Figure is taken from [99]

The sister compound of  $\text{WTe}_2$ ,  $\text{MoTe}_2$ , exhibits superconductivity with a transition temperature of 0.10 K. Application of external pressure dramatically enhances the transition temperature up to maximum value of 8.2 K at 11.7 GPa [31].

While performing the high pressure experiments on  $\text{TaIrTe}_4$  for this thesis, another group has carried out high pressure transport and structural measurements on this compound and they found pressure induced superconductivity with transition temperature ( $T_C$ ) of 0.57 K at the pressure of  $\sim 23.8$  GPa. Structural investigations suggested that the superconductivity emerged in a pressure-induced distorted phase. Similar to the other compounds, positive MR was suppressed as the pressure was increased and above the critical temperature is disappeared simultaneously [114]. However, the nature of the superconductivity in  $\text{TaIrTe}_4$  remained controversial as other recent report observed unconventional surface superconductivity at ambient pressure [115].

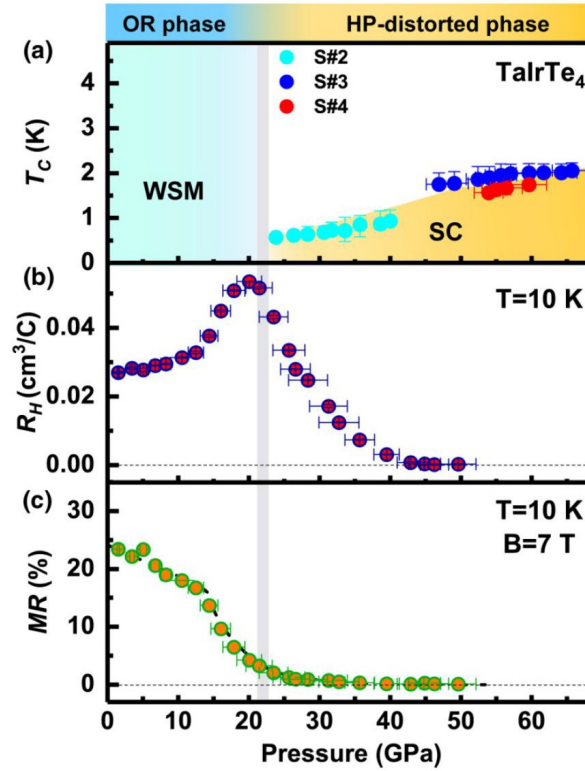


Figure 1.16: Summary of the experimental results on TaIrTe<sub>4</sub>. (a) P-T phase diagram with structural information for TaIrTe<sub>4</sub>.(b) Pressure dependence of Hall coefficient measured at 10 K and (c) ) Pressure dependence MR measured at 10 K. Figure is taken from [114]

## 1.4 Materials investigated in this thesis:

The above discussions suggest that the topological materials are very sensitive to pressure and similar investigations are very desirable. Motivated by those studies, in the current thesis, I have studied various topological systems which include three proposed pressure induced topological insulators (Sb<sub>2</sub>S<sub>3</sub>, AgBiSe<sub>2</sub>, TiTe<sub>2</sub>), two type-I Weyl semimetals (NbP, NbAs) and one type-II Weyl semimetal (TaIrTe<sub>4</sub>) by high pressure transport and spectroscopic techniques. Here, in the following sections, I will present a short induction on these systems with a particular importance on the significance of the high pressure studies.

### 1.4.1 $\text{TiTe}_2$

At ambient conditions,  $1T$ - $\text{TiTe}_2$  crystallizes in a layered hexagonal structure (SG  $P\bar{3}m1$ , No. 164) [125]. Unlike the other transition metal dichalcogenide (TMD) compounds,  $\text{TiTe}_2$  does not show any charge density wave (CDW) behavior at ambient pressure because of its semimetallic character with an indirect overlap of valence and conduction bands of 0.6 eV [125]. Recent theoretical research proposed that  $\text{TiTe}_2$  showed series of topological transition under pressure [72]. To verify this theoretical prediction we perform high pressure electrical resistance measurements on polycrystalline  $\text{TiTe}_2$  corroborated with high pressure Raman and XRD measurements. Theoretically it is also reported that suitable strain can induce superconductivity in  $\text{TiTe}_2$  and it was also reported that different pressure conditions have different effects on superconductivity [126]. So if it is possible to observe pressure induced superconductivity and/or CDW in this compound it will help to understand the interplay between CDW and superconductivity. Motivated by this we have performed high pressure resistance measurements on single crystalline  $\text{TiTe}_2$  under both quasi-hydrostatic and non-hydrostatic compression. Pressure induced topological phase transition is alternatively probed by high pressure infrared reflectance measurements [65, 127]. For this we have also performed high pressure IR reflectance measurements up to 24 GPa on single crystalline  $\text{TiTe}_2$  to identify the topological phases.

### 1.4.2 $\text{Sb}_2\text{S}_3$

Antimony trisulfide ( $\text{Sb}_2\text{S}_3$ ) is a well known binary semiconductor which belongs to  $A_2B_3$  ( $A=\text{Bi, Sb, As}$ ;  $B = \text{S, Se, Te}$ ) family layered chalcogenide with an optical bandgap energy ( $E_g$ ) of 1.7 eV [116]. This material can be utilized as a

promising candidate for various applications such as solar energy conversion, optoelectronic devices, fuel cells and gas sensors [117, 118]. Application of pressure on the other compounds in this  $A_2B_3$  series show various novel phenomena including structural transition, electronic topological transition (ETT), metallization and superconductivity [27, 28, 57, 59–61]. Much research has also been reported on  $Sb_2S_3$  under pressure including its structural, vibrational and electrical properties. But there has been an inconsistency between the different experimental results regarding the pressure induced ETT and structural transition [119–122]. Recently pressure induced irreversible metallization is reported in this compound on the basis of temperature dependent (80-240 K) electrical conductivity measurement [122]. But the detailed study of the pressure dependent activation gap was absent there and no low temperature measurement below 80 K was performed to search pressure induced superconductivity in this compound. So aiming at clarifying the observed pressure induced irreversible metallization and to search pressure induced superconductivity we have conducted low temperature resistance measurement down to 1.4 K under various pressures up to 45 GPa. In addition, to conclude about the controversial results on pressure induced ETT and structural transition, we have carried out high pressure XRD (up to 25 GPa), IR reflectance measurements (up to 8.5 GPa) and optical absorption measurements (up to 8 GPa).

### 1.4.3 $AgBiSe_2$

$AgBiSe_2$  crystallizes in ordered hexagonal structure (S.G : P-3m, Z=3) at ambient conditions [123]. Its narrow optical bandgap of 0.6 eV implies that  $AgBiSe_2$  is on the edge of pressure induced insulator to metal transition which is an important subject of condensed matter physics. Earlier high pressure research on this compound shows that at 0.7 GPa,  $AgBiSe_2$  undergoes a pressure induced structural phase transition from hexagonal to rhombohedral (R-3m) [124]. In addition to

that pressure induced electronic topological transition (at 2.8 GPa) and insulator to metal transition (above 7 GPa) is also reported in that work. No low temperature measurements below 170 K was reported to search for pressure induced superconductivity similar to the topological insulators. Therefore we perform temperature dependent electrical resistance measurements at various pressures up to 30 GPa to search for pressure induced superconductivity in this compound. High pressure infrared (IR) spectroscopy is an important tool to study the electronic structure of the materials. Therefore, to verify the observed ETT and insulator to metal transition we also perform high pressure IR reflectance measurement (up to 22 GPa) as an auxiliary probe.

#### 1.4.4 NbP

A WSM is a 3D analogue of graphene where two bands cross linearly near the Fermi level. Recently, NbP is experimentally verified as a topological Weyl semimetal after its theoretical prediction [85]. NbP crystallizes in a body-centred-tetragonal lattice. It is a type-I Weyl semimetal with one hole pocket from the normal quadratic band and one electron pocket from the linear Weyl semimetal band [85]. From the band structure calculation it is seen that there are 12 pairs of Weyl points that can be classified into two groups: four pairs lie in the  $k_z = 0$  plane (labeled as W1) and eight pairs stay in planes of  $k_z \sim \pi/c$  (labeled as W2) [54]. All of them lie slightly away from the Fermi energy. Now as the application of pressure can modify the topology of the Fermi surface, it is interesting to study how the pressure changes the electronic structure of the material [109]. Apart from that magnetic field induced metal to non-metal transition was reported at ambient pressure [85]. A high pressure resistivity study on NbP also reveals pressure induced metal to non-metal transition [110]. So the investigations of combined effect of high pressure and magnetic field on NbP will be very interesting. We have

performed high pressure resistance, magnetoresistance and XRD measurements on single crystalline NbP.

### 1.4.5 NbAs

NbAs is also a recently discovered Weyl semimetal which crystallizes in the same structure to that of NbP [128]. High pressure XRD and resistance measurements up to 20 GPa show that the Weyl semimetallic phase is robust in NbAs: No structural changes and superconductivity was observed up to 20 GPa [105]. Theoretical research predicts that when NbAs crystal is compressed it shows a structural phase transition at 31 GPa similar to TaAs where this transition is observed at 14 GPa [112, 129]. The high pressure phase of TaAs is predicted to be new Weyl semimetallic phase with 12 Weyl nodes at isoenergy level whereas the ambient pressure Weyl semimetallic phase is consisted of 24 Weyl nodes [112]. The reduced no of Weyl nodes in high pressure Weyl semimetallic phase in TaAs minimizes the interference between the surface and bulk states. So it is naturally expected to have a new Weyl semimetallic state in NbAs above 31 GPa and it is also interesting the effect of the structural transition on the transport properties of NbAs. Here, we have performed high pressure resistance measurements on NbAs well above the transition pressure to observe the effect of the structural phase transition on the transport properties.

### 1.4.6 TaIrTe<sub>4</sub>

Recently, orthorhombic ternary compound, TaIrTe<sub>4</sub> has been predicted and experimentally identified as type-II Weyl semimetals (WSMs) [130]. WTe<sub>2</sub> and MoTe<sub>2</sub> are the two other examples of type-II Weyl semimetallic compounds [104, 131]. High pressure research on WTe<sub>2</sub> suggests that superconducting transition temperature

(Tc) shows dome-shaped pressure dependence and the emergence of superconductivity occurs after significant suppression of magnetoresistance [99]. Although, MoTe<sub>2</sub> exhibits superconductivity at ambient pressure, application of pressure establishes the similar dome-shaped superconducting phase diagram [31]. So the similar high pressure investigations on the iso-structural TaIrTe<sub>4</sub> will help to understand the general dome shaped superconducting phase diagram which may provides insights into the interplay between superconductivity and topological physics. Here we investigate high pressure transport and magnetotransport measurements on both single crystal and polycrystalline TaIrTe<sub>4</sub>.

## 1.5 Outline of the thesis:

The thesis contains a total of eight chapters. First chapter provides an overview and background of the topological systems. Then I present a brief discussion on various topological phases in condensed matter physics including topological insulator, topological semimetals and topological superconductors followed by the literature survey on high pressure effects of the respective systems. The materials investigated in this thesis are also introduced at the end of this chapter. The remaining chapters of the thesis are organized as follows. **Chapter 2** describes the various experimental techniques and apparatus employed throughout this work. The next five chapters are devoted to the discussion of the high pressure investigations on the aforementioned materials. Each material specific chapter begins with proper background followed by suitable experimental techniques, various experimental results and the relevant discussions. The end chapter summarizes the main experimental results in the thesis and suggest some future works.

# Chapter 2

## Experimental techniques

In this chapter, I discuss an overview of the experimental techniques which are used to investigate the various topological systems at high pressure. We first provide a brief description of the sample synthesis process and the ambient pressure characterization techniques. Then we give a detailed description of the basics of high pressure equipments which include the description of different kind of pressure cells, Gasket materials, pressure transmitting medium and pressure measurement techniques. The next section introduces the different low temperature instrumentation under pressure. Then I describe the various experimental techniques which contain different transport techniques and spectroscopic methods under suitable extreme conditions of high pressure, low temperature and high magnetic field.

### 2.1 Synthesis and ambient pressure characterization:

The first and foremost important step in the experimental research in condensed matter physics and material science is the synthesis and characterization of the materials. The quality of the prepared samples depends to a great extent on the synthesis method used. There are various methods available for the synthesis of polycrystalline and single crystalline bulk materials. All the polycrystalline materials investigated in the current thesis have been synthesized using solid state reaction method. Single crystalline layered transition metal dichalcogenide compounds have been synthesized using chemical vapor transport technique. In order to characterize

the grown samples we perform X-ray diffraction, four probe DC resistance measurements, magnetic susceptibility, and low energy electron diffraction at ambient conditions. The following section gives a brief explanation about various synthesis methods and characterization techniques.

### 2.1.1 Synthesis:

#### Solid State Reaction:

Solid state reaction is the most widely used method for synthesizing the polycrystalline materials and some of the single crystalline materials. As solids do not usually react together at room temperature over normal time scale, it is necessary to have high temperature and controlled atmospheres for reaction to occur at an appreciable rate. In solid state reaction there are two important factors namely thermodynamic and kinetic. The former determines the possibility of any chemical reaction to occur by the involved free energy consideration and the later determines the rate at which the reaction occurs [133]. The general steps for synthesizing the materials in solid state reaction method are listed below

1. All the starting materials are weighted for desired composition using high precision electronic weighing machine.
2. To obtain the homogeneous distribution of the starting materials in required proportions of the desired stoichiometric compound it is very important to mix and grind the powders thoroughly for long duration.
3. Once the mixing is done properly, the powder mixture is then palletized by using a hydraulic press and the pallet is the vacuum sealed in a quartz tube.
4. The composite system is the heated to a suitable high temperature inside a suitable furnace where the diffusion of the atoms occurred to form a stable compound of minimum free energy.
5. The process of grinding and palletization is repeated until a single phase

material is prepared.

### **Chemical vapour transport (CVT):**

Chemical vapour transport (CVT) is a technique where a chemical reaction between the source materials and the transport agent occurs and crystalline solids are deposited elsewhere [134, 135]. Typical transport agents are halogens and halogen compounds. Transport occurs between two zones having different temperatures (a two-zone tube furnace is used with source at T2 and sink at T1). The reactant and the transport agent are vacuum sealed in a quartz ampoule. The ampoule is then heated to desired temperature and kept for suitable time duration inside a two zone tube furnace. The respective single crystals are obtained at the other end of the ampoule.

### **2.1.2 Ambient pressure Characterization:**

#### **X-ray diffraction:**

For the structural characterization, X-ray powder diffraction is used to identify the phase purity, type of the phases and the crystallographic structure of the sample. The interaction of the incident x-rays (generally Cu-K $_{\alpha}$  is used as x-ray source: = 1.54 Å) with the sample produces constructive interference (and a diffracted ray) when conditions of Bragg's Law ( $n\lambda = 2d \sin\theta$ ) is satisfied. This law correlates the wavelength of electromagnetic radiation to the diffraction angle and the lattice spacing in a crystalline materials. Diffraction profiles are analyzed by indexing method and full profile structural refinement.

**Four probe resistivity measurements:**

Measurements of electrical resistivity provide much useful information about the electrical properties of the sample [136]. Temperature dependent resistivity measurement gives the information about the quality of the sample by measuring the RRR ratio ( $RRR = R(300K)/R(2K)$ ). Standard four point contact method is performed to determine the electrical resistance ( $R$ ) of the materials in the temperature range of 1.4 K to 300 K. To measure the resistivity ( $\rho$ ) in this technique the samples are cut into a rectangular bar shape with length  $l$  and cross section area  $A$  and the resistivity is obtained as ( $\rho = R.A/l$ ). 10 micron gold wires are used as the electrodes. For the electrical contacts of the electrodes with the sample, silver paste is used. Fine slurry of the silver paint is made by dissolving it with an appropriate solvent (n-butyl acetate). This silver paste is applied at the four sample-electrode junctions. The whole assembly was mounted on the helium cryostat sample holder and the temperature (2 K to 300 K) dependent resistance is measured with the help of an AC resistant bridge (lakeshore 370).

**Magnetic measurements:**

For magnetic characterization of the samples, a cryogenic S700X SQUID magnetometer is used. To perform the measurement, a sample is mounted onto a suitable sample holder (generally a drinking straw is used in our measurements) which in turn is screwed to the sample probe for putting into the VTI insert of the SQUID [137]. The probe is then moved vertically so that the sample moves through the pick up coils. To achieve the best results the sample should be well centered in the pick up coils. Once the sample is mounted, loaded and centered, vertical  $z$  scan is performed to measure the magnetic moments of the sample at each physical position  $z$  of the sample in the pick up coils. The voltage across the SQUID sensor is measured to obtain a voltage curve  $V(z)$ . This curve is then fit to that expected for an ideal

magnetic dipole, to obtain a quantitative value of the magnetization [137].

### Low energy electron diffraction:

Low energy electron diffraction (LEED) is one of the most powerful techniques available for the determination of surface structures of single crystalline materials [138, 139]. A focused beam of electrons, of momentum  $p$ , may be equally interpreted as a succession of waves ( $\lambda = h/p$ ) incident normally on the sample surface. The surface atoms which can be considered to act as point scatterers, will scatter these electron waves. In this thesis the Low energy electron diffraction experiment is carried out (For Single crystalline  $\text{TiTe}_2$  compound only) in a qualitative way. Diffraction pattern is recorded and the analysis of the spot positions gives the information on the crystal symmetry which helps to identify any Charge Density Wave (CDW) order present in the compound.

## 2.2 Basics principle of high pressure physics:

As one of the independent thermodynamic parameters apart from those usually studied temperature and composition, pressure has been playing an increasingly important role in condensed matter physics. Modern high-pressure research was pioneered by P.W. Bridgman, who received the Nobel Prize in Physics in 1946 for "the invention of an apparatus to produce extremely high pressures, and for the discoveries he made therewith in the field of high-pressure physics [140]. Of all the physical variables, pressure spans the largest range of over 60 orders of magnitude in the universe, from the non-equilibrium "pressure" of hydrogen gas in intergalactic space ( $10^{-31}$  atm) to the pressure at the centre of neutron star ( $10^{28}$  atm) [141, 142]. Application of pressure is a very powerful tool that can be used to smoothly manipulate the electronic properties of materials without introducing disorder, provided

that the applied pressure is isotropic and hydrostatic. Given the complexity in research of many novel phenomena in the condensed matter physics, high pressure is often an indispensable tool for unraveling the essential information of various competing mechanisms involved in the description of unusual physical properties of novel materials. In the following sections, I discuss the basic requirements to perform a high pressure experiment.

### **2.2.1 Diamond Anvil Cell (DAC):**

Diamond is the hardest material and hence it is ideal for pressure generation [143]. Since the beginnings of high pressure techniques, many different pressure devices have been developed but due to its various advantages, DAC is the most extensively used one and static pressures above several tens of GPa are uniquely achieved with DACs only. The highest thermoconductivity and being transparent over a wide range of electro-magnetic spectrum from far infrared to high energy x-rays also make it ideal for high pressure spectroscopic and cryogenic related research [143–145]. Today, DACs can be used to reach static pressures exceeding 500 GPa [146, 147]. Due to its small size it can be fit into experimental equipment with limited working space such as small cryostat magnet bores with very high magnetic field. Different types of DAC are designed depending upon the type of the measurements that are being performed.

#### **Working principle of DAC:**

There are several good review articles on the design and operation of anvils cells [141–145]. Fig. (2.1) explains the basic working principle of a DAC [148]. Two similar sized diamonds with brilliant-cut shape are placed with their culets facing each other. Both the table and tip of the diamonds are kept parallel to the (100) crystallographic plane. The diamonds are aligned first to check the parallelism of

the cell by observing the interference fringes produced when the two diamonds are in contact with each other. Once the alignment is complete a metallic gasket (we use hardened steel or non magnetic Cu-Be gasket) with an initial thickness of  $250\ \mu\text{m}$  is placed between the culets of the two diamonds and the center of the gasket is thinned down to less than  $100\ \mu\text{m}$ . This process is called indentation of gasket i.e. the gasket is indented to a thickness less than  $100\ \mu\text{m}$ . Later, a hole with a diameter of about  $100 - 200\ \mu\text{m}$  is drilled at the center of the indented portion. The space created inside the hole of the metallic gasket between the two diamonds acts as the sample chamber. The sample chamber is loaded with a small piece of sample together with a small ruby ball serving for the pressure calibration, as discussed in one of the following section. The typical volume of a sample inside a DAC is about  $80\ \mu\text{m} \times 80\ \mu\text{m} \times 30\ \mu\text{m}$ . Finally the pressure transmitting medium is loaded to maintain a quasi-hydrostatic pressure environment. By pressing the two diamonds against each other, the pressure medium is sealed inside the sample space. Pressure is generated by further pushing the two diamonds which basically decreases the volume of the sample chamber through the plastic deformation of the gasket.

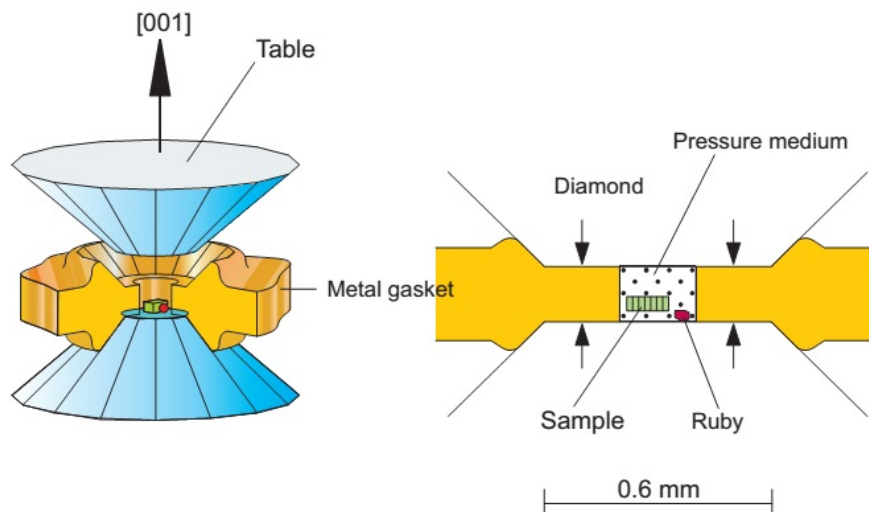


Figure 2.1: Schematic view of the arrangement of the diamond anvils and the gasket in a DAC (left), and enlarged view of the sample chamber and its surrounding (right). Figure is taken from reference [148].

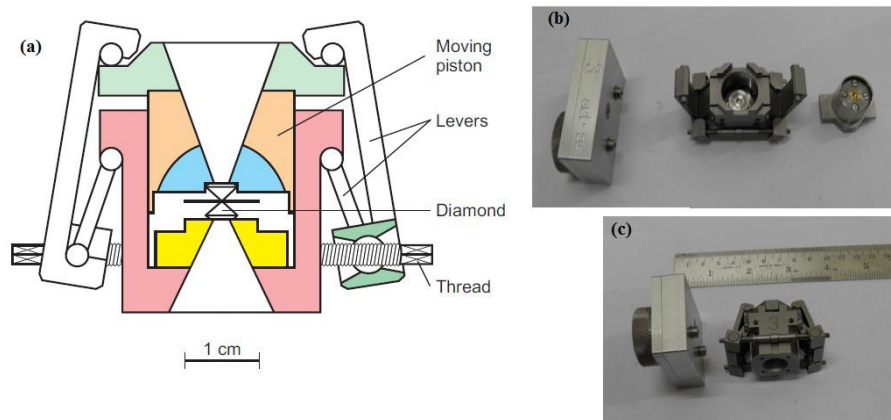
**Stuttgart type DAC:**

Figure 2.2: (a) Layout of the Stuttgart type DAC. For pressure generation the piston holding the upper diamond is pressed towards the main body of the DAC holding the lower diamond by the levers. Fine tuning of the threaded rods control the mechanical movement of the levers. (b) The pictures of the main body, piston and the gear set are shown. (c) A complete picture of the DAC when it is closed and its dimension is shown. Figures are taken from reference [149].

For most of the high pressure measurements (cryostat based resistance measurements, XRD and IR reflectivity measurements), a miniature version of the Syassen-Holzapfel type DAC (called Stuttgart DAC) is used [149]. It is basically a clamped piston-cylinder cell. One of the two diamonds (bottom diamond) is mounted on a XY translational stage incorporated in a fixed backing plate. The other diamond (upper diamond) is mounted on a tilting stage in a movable piston. By fine tilting and translational movement, a precise adjustment of the two diamond anvils with respect to each other is achieved. Fig. 2.2.(a) illustrates the force transmission principle of this type of DAC. By turning the threaded rods with a gear box, the upper diamond is pressed towards the bottom diamond through the mechanical transmission of the levers. The special geometry of this construction provides a large force multiplication. The guidance of the long moving piston assures parallelism of the diamond face at high load. This provides excellent alignment stability even at very high pressure. The height and length of the used Stuttgart DAC in this thesis is

$\sim 38.7$  mm and  $\sim 60$  mm respectively (as shown in the Fig. 2.2.(c)) Both the diamond anvils are made of type-IIa diamonds with a culet diameter of  $\sim 450$   $\mu\text{m}$ . The maximum achievable pressure in this Stuttgart DAC with  $\sim 450$   $\mu\text{m}$  diameter culet is around  $\sim 50$  GPa. The opening angle of the apertures at the piston and the cylinder assemblies are around  $40^\circ$  and  $50^\circ$  respectively.

**Mcell ultra (easyLab):**

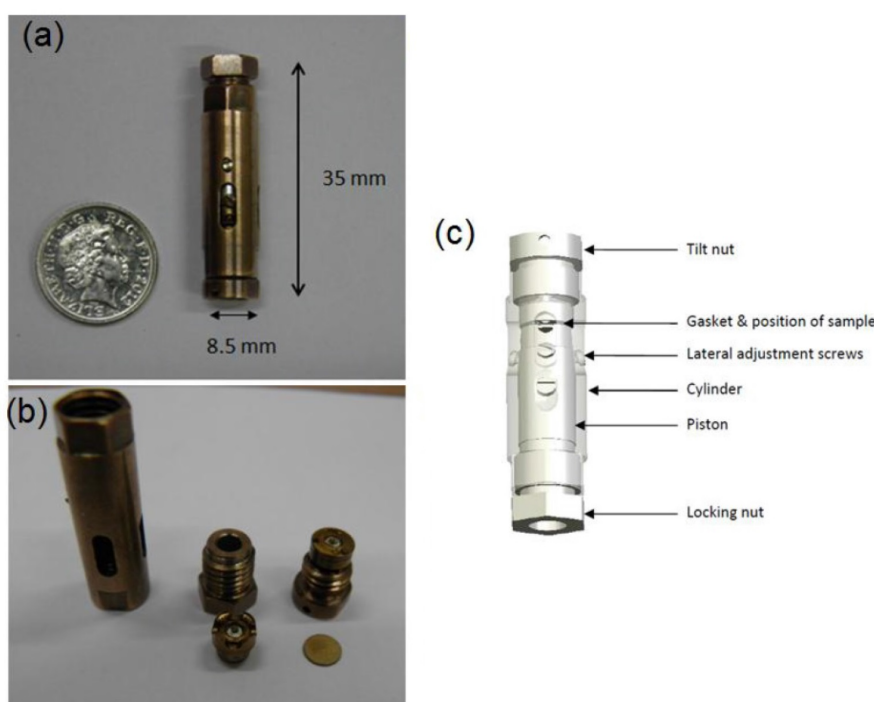


Figure 2.3: (a) Dimensions of the easyLab make Mcell ultra DAC for magnetic and magnetoresistance measurement. (b) Individual parts of the cell. (c) Schematic of the Cell and its components.

For high pressure (up to  $\sim 12$  GPa) magnetoresistance and magnetic measurements we use a non-magnetic Cu-Be DAC (Mcell ultra; easyLab, UK). Its design is based on the principle of DACs where pressure is generated by applying force on two opposite diamond anvils. The total weight of the cell is about  $\sim 12$  g and its length and diameter is 35 mm and 8.5 mm respectively (as shown in Fig. 2.3 (a)). Figure 2.3 (b) shows the individual parts of the cell. In figure 2.3 (c) the schematic

diagram of this cell and its main components is shown. Both the tilt and translation adjustments provide proper alignment of the diamond anvils which reduces the risk of failure during measurements. The force is applied using a novel easyLab Mpress MK2. This Mpress is equipped with an electrical force gauge enabling the monitoring of the applied force so that one can gradually increase the force on the anvils in a controlled fashion.

### **2.2.2 Gasket:**

In performing high pressure experiments in DAC, gasket plays an important role and the choice of the suitable gasket material is very crucial. The gasket is the metal disc which sits between the top and the bottom anvils and undergoes the pressurization process. At the center of the gasket, a concentric hole is drilled which contains the sample, pressure gauge (Ruby ball), and pressure transmitting medium as described in the section of working principle of DAC. The gasket should be both hard and ductile. Although the ductility and hardness are generally inversely related, the hard gasket will be able to hold out against the high pressure generated during the experiments whereas if the gasket's ductility is too low, it can suffer brittle failure under pressure, resulting in destruction of the diamonds. Although several materials have been used for gasket hardened stainless steel is used in this thesis for XRD, IR reflectivity and electrical resistance measurements. For magnetic measurements non magnetic CuBe alloy is used as the gasket materials

### **2.2.3 Pressure transmitting medium:**

The main aim of the use of a pressure transmitting medium (PTM) is to maintain hydrostatic pressure environments in high pressure experiments. The results obtained from such hydrostatic conditions are intrinsic of the studied sample and can be compared with the theoretical and other various experimental results, avoiding

the complications and uncertainties introduced by the differences in the pressure conditions. Therefore, depending upon the experimental need the use of a suitable pressure transmitting medium (PTM) is of great importance. To create hydrostatic pressure environments the sample is immersed in a PTM. The main hallmark of the medium is that it should have lower shear strength so that the shear stress acting on the sample remains very small. When to choose a suitable PTM, depending upon the samples and specific experiments, there are various limitations. For example, the investigated sample should not dissolve into or react with the pressure medium and in case of IR reflectance measurements the pressure medium should be transparent to the IR radiation. In addition to that, in case of high resistance measurements liquid medium cannot be used when the sample and the electrodes are not connected by silver paste or by spot welding. Usually for high pressure measurements at room temperature, a mixture of methanol-ethanol 4:1 is a common choice which can maintain hydrostatic conditions up to  $\sim 10$  GPa. Adding water, a mixture of Methanol-Ethanol-Water (16:3:1) can extend the hydrostatic limit up to  $\sim 15$  GPa. Especially for samples reacting with alcohols, some inert fluid media like paraffin, or silicone oil are used as the pressure medium. For magnetic measurements non-magnetic Daphne oil is used as the pressure medium. As the application of pressure increases the melting point of the fluids, it is always a challenging task to maintain hydrostaticity in high pressure and low temperature measurements. The best choice is then the use of condensed gases, such as nitrogen, argon, and helium as pressure media. I mainly used Methanol-Ethanol-Water (16:3:1) and silicone oil as the PTM in the room temperature XRD measurements. Methanol-Ethanol-Water (16:3:1) can maintain the hydrostatic environments up to 15 GPa whereas, silicone oil brings non-hydrostaticity above 2 GPa. For high pressure resistance and magnetoresistance measurements solid PTM NaCl is used in this thesis. In IR reflectance measurements also solid PTM, KBr or KCl is used. For magnetic measurements,

Daphne Oil is used as the pressure medium to maintain the hydrostaticity.

### 2.2.4 Pressure calibration:

Measurement of the pressure at the sample place had been a major challenge in high pressure experiments and a survey of high pressure research history reveals that much early effort was devoted to the development of practical and accurate methods for measuring the applied pressure [150,151]. There are various calibration techniques which have been developed to measure the pressure inside the sample chamber. Ruby luminescence technic is the most commonly used technique to measure the pressure inside the sample hole. During XRD measurements, x-ray pressure markers like Cu, W, Pt are used to measure the pressure. As ruby luminescence technique is routinely used in this thesis, this technique is briefly discussed bellow.

#### Ruby luminescence technique:

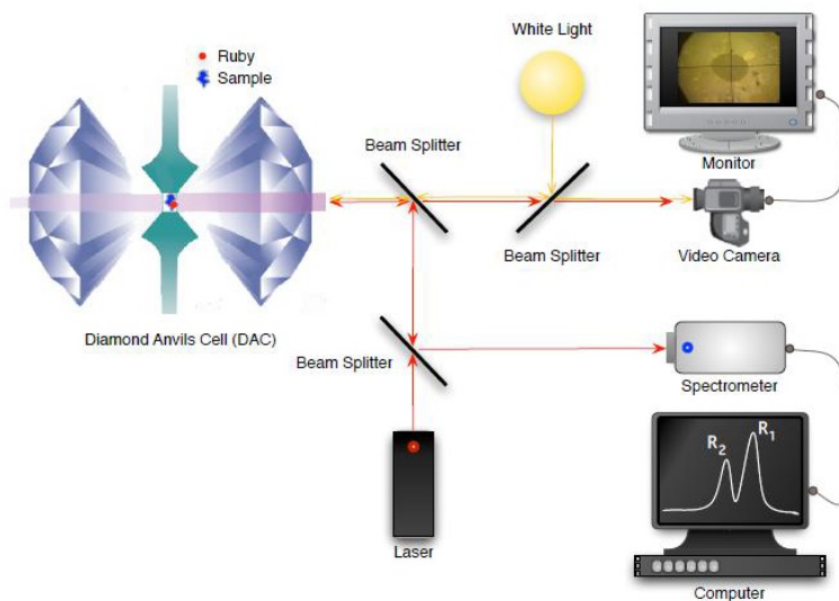


Figure 2.4: A schematic diagram of a typical ruby fluorescence set-up for pressure measurement.

The most convenient method to measure the pressure in high pressure experiment is the ruby luminescence method where the pressure is measured by measuring the pressure-induced frequency shift of the ruby luminescence R1 line [152]. A schematic diagram of a typical ruby fluorescence set-up for pressure measurement is shown in figure (2.4). Ruby is  $\alpha\text{-Al}_2\text{O}_3$  (corundum with trigonal crystal structure) doped with 0.05 wt.  $\text{Cr}^{3+}$  impurity substituted for  $\text{Al}^{3+}$  ions [152]. Because of the high intensity of the ruby fluorescence, small ruby chips on the order of the one percent of the total sample space can measure the pressure inside a DAC. The origin of the two ruby luminescence lines is illustrated in Fig. (2.5) where the 3d electronic levels of  $\text{Cr}^{3+}$  are plotted [152].

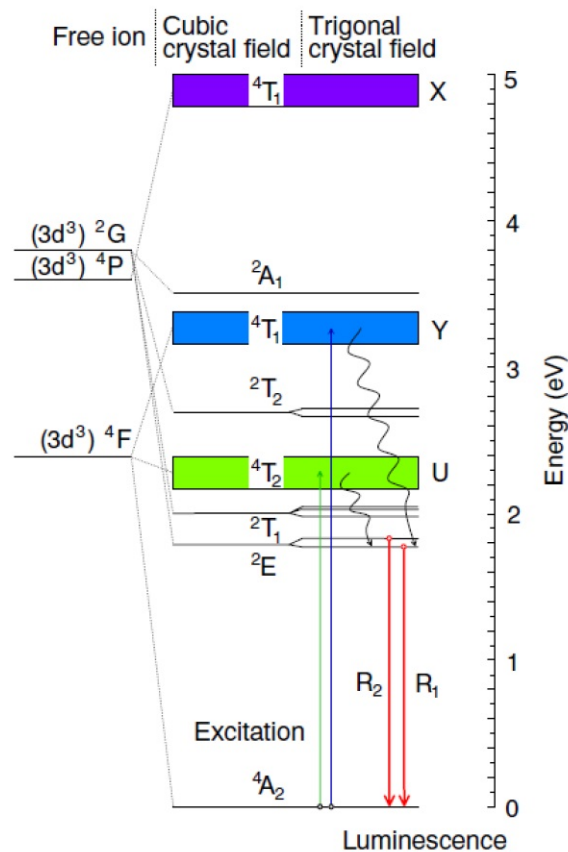


Figure 2.5: The 3d levels of  $\text{Cr}^{3+}$  in the free ion and in the cubic and trigonal crystal field of the ruby crystal  $\alpha\text{-Al}_2\text{O}_3$ . The 3d levels of the free  $\text{Cr}^{3+}$  ions are split under the cubic and trigonal crystal field. The absorption and emission processes related to the ruby photoluminescence are also indicated. Figure is taken from reference [152].

When, ruby crystal is excited with a laser (visible) it undergoes a transition to the Y and U band and then non-radiative de-excitation to the metastable states 2E ( $E_{1/2}$  and  $E_{3/2}$ ). Finally the de-excitation from the 2E states to the ground state (4A<sub>2</sub>) produce two strong luminescence lines R1 and R2. Under ambient conditions the R1 and R2 lines are observed at 6942.4 Å and 6929.2 Å respectively. Their splitting comes from spin-orbit interaction. Generally the shift in R1 line is used to determine the pressure. Both the pressure and the temperature affect the frequency of the R lines. Their effects are discussed separately.

### Temperature dependence of the R lines:

Figure 2.6 (a) illustrates the R-line spectra at various temperatures from 10 K to 300 K at ambient pressure [152]. When temperature is reduced, the R-lines shift to higher energy, their line widths decrease and the intensity ratio of R2/R1 also decreases. The main reason behind the change in the intensity ratio is that when the temperature is decreased the population of the R2 state (higher energy) becomes small compared to that of the R1 state (lower energy) and thus at low temperature, the R2 fluorescence line is suppressed and because of that reason R1-line is generally used to determine the pressure. Figure 2.6 (b) describes the temperature dependence of the R-lines frequencies from 4K to about 300K. Below ~100 K the frequencies of the R-lines become almost independent of the temperature.

At temperatures higher than room temperature the determination of pressure become difficult by this technique as at higher temperature the R-line emissions broaden further and their peak intensities decrease. For detail high temperature study of ruby luminescence spectra see the reference [153] and the citations therein. It is generally believed that the temperature and pressure dependences of these R-lines appear to be independent, easing the calculation of pressure for a given wavelength shift at a given temperature.

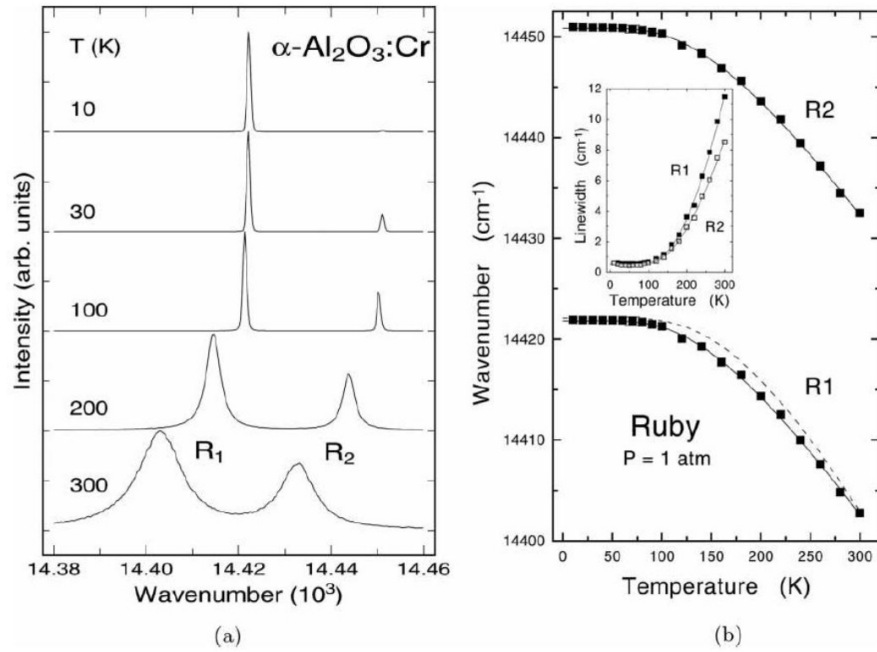


Figure 2.6: Temperature dependence of the luminescence spectra. (a) Spectra of a single crystal of sapphire (not intentionally doped with Cr) at different temperatures. Below  $T=50$  K, the line width is mainly limited by the spectrometer resolution and residual internal strain. (b) Energies of the R1 and R2 emission lines as a function of temperature. The inset shows the temperature dependence of the corresponding line widths. Figure is taken from [152].

### Pressure dependence of the R-lines:

Upon application of hydrostatic pressure, the ruby lattice is almost isotropically deformed [154], leading to the decrease of the distance between Cr and ions and therefore to the increase of the crystal field in the Cr ions. The increased crystal field changes the 3d level splitting of  $\text{Cr}^{3+}$  in such a way that the energy gap between the 2E state and the ground state becomes smaller. Therefore, the two ruby luminescence lines R1 and R2 are shifted towards lower energies and thus higher wavelengths. This is illustrated in figure (3.9) where the luminescence spectra of the R-lines are plotted at two different pressures at room temperature. The data was taken during one of the resistance measurement experiment mentioned in the current thesis. Since the development of the ruby luminescence manometer, a number of various calibrations of the fluorescence wavelength versus pressure have been used as

standards [153, 154]. These calibrations were done using different type of pressure mediums and the primary principle of these calibrations under different pressure conditions is to measure simultaneously the pressure-induced shift of the R1 line and the pressure induced change in the lattice parameters (using x-ray diffraction) of a reference sample with a known equation of state. Piermarini et al. [151] calibrated ruby versus the equation of state of NaCl up to 19.5 GPa in a 4:1 methanol: ethanol mixture and showed that the frequency shift of the R-lines is linear. This linearity is no longer valid for pressure above 30 GPa. Later Mao et al. [155] cali-

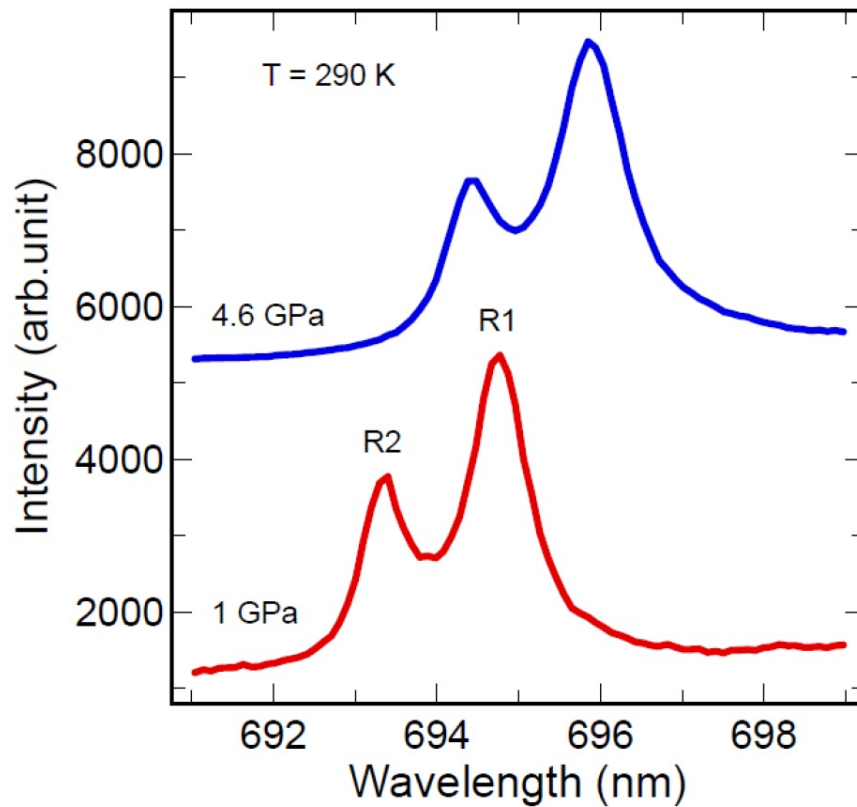


Figure 2.7: Normalized R-lines spectra taken at two different pressures (1 GPa and 4.6 GPa) at room temperature. Data is taken during one of the measurements in this thesis.

brated ruby up to 110 GPa using Cu as a pressure marker and the relation between pressure and the frequency shift of the ruby R1-line has been represented by the relation

$$P = \frac{A}{B} \left[ \left( 1 + \frac{\Delta\lambda}{\lambda_0} \right)^B - 1 \right] \quad (2.1)$$

where,  $A=1904$  GPa,  $B=7.665$ ,  $\lambda_0$  is the wavelength of the R1 line at ambient pressure and  $\Delta\lambda$  is the observed wavelength shift. In the current thesis A 532 nm diode laser (30 mW) was used for ruby fluorescence excitation. The spectrometer resolution was 0.05 nm FWHM, as calibrated by a mercury-argon source. Such system was actually used for the pressure calibration in experiments using optical cryostat.

**Effect of non-hydrostatic pressure on R-lines:**

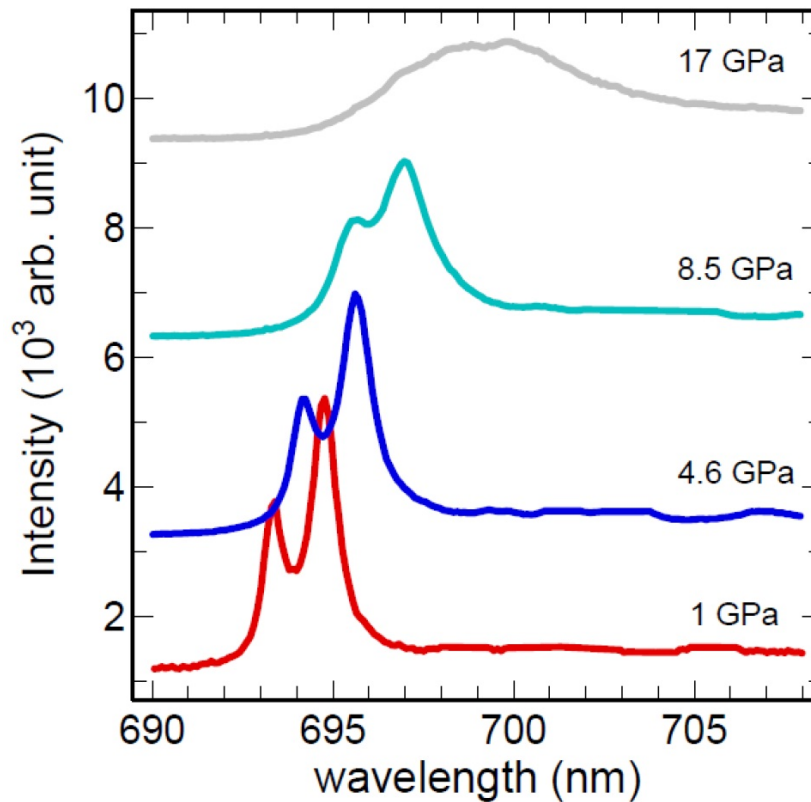


Figure 2.8: Ruby measurements taken at various pressures. Data is taken during one of the measurements in this thesis.

Application of non hydrostatic pressure broadens the R-lines and decreases the R1 to R2 separations. Figure 2.8 shows a typical plot of how the R-line become broadens during non-hydrostatic compression in one of the resistance measurement in the current thesis where solid NaCl was used as a pressure medium. This line broadening effect can be used to estimate the magnitude of non-hydrostatic pressure

components within the cell from the full width at half maximum (FWHM) of the R1 line [156].

## **2.3 Low temperature techniques at high pressure:**

### **2.3.1 Helium bath type cryostat:**

In the current thesis a helium bath cryostat (Cryovac) was employed for combined high pressure and low temperature resistance measurements. The basic layout of such a cryostat, with the high pressure DAC mounted in it, is shown in figure 2.9 [148]. The cryostat is described with four main chambers, one inside the other. The outer most chamber acts as a vacuum chamber which isolates the whole cryostat from the room temperature environment of the laboratory. The second chamber is the liquid nitrogen chamber which is filled with liquid nitrogen and it helps in pre-cooling the cryostat down to  $\sim 80$  K. The third chamber is the helium reservoir which contains liquid helium and is connected to the sample chamber, the fourth chamber, through a needle valve which allows and controls the helium flow through the sample chamber to control the temperature of the sample place. Two steel rods which are arranged to fit the threaded rods of the DAC inside the cryostat, allow the pressure tuning without removing the DAC from the cryostat. An electrical heater installed near the DAC, together with two silicon-diode thermometers and a temperature measurement and control unit (LakeShore, Cryogenic Temperature Controller) can stabilize the temperature within  $\sim 0.1$  K. The cryostat can be operated between room temperature and a temperature as low as 1.5 K which is reached by pumping the sample chamber by a high-vacuum pump. The quartz window at the bottom of the cryostat provides the optical access of the diamond anvil cell serving in-situ pressure measurement at room temperature as well as at low temperature.

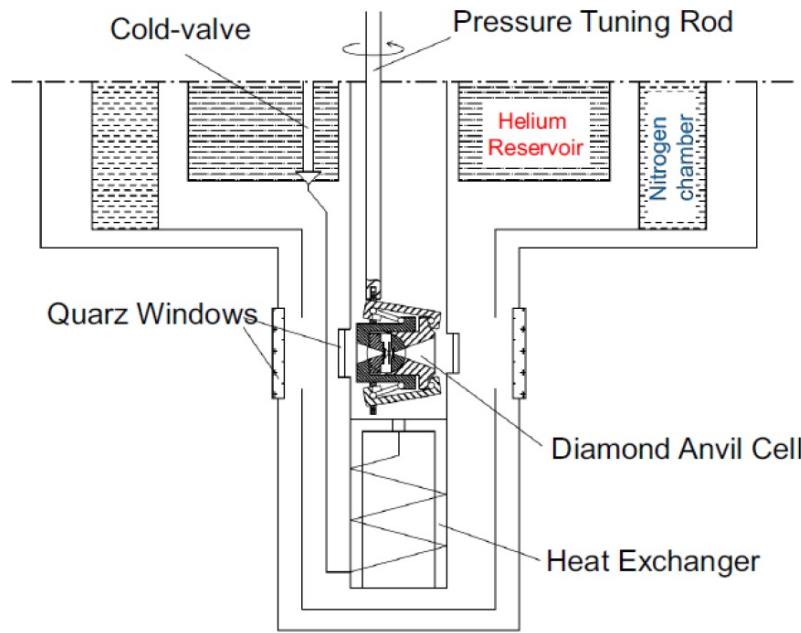


Figure 2.9: Layout of the DAC in the helium-bath cryostat. Pressure can be tuned by the pressure tuning rod without removing the DAC from the cryostat. Figure is taken from reference [148]

**Operation:** Figure 2.10 shows the schematic diagram of our cryogenic arrangement, using a liquid helium bath-type optical cryostat [157]. The cryostat design has been worked out in collaboration with MPI-Stuttgart to make it compatible for the DAC. After mounting the DAC inside the cryostat, the sample chamber is filled with helium gas which acts as the exchange gas. This is done by first evacuating the sample chamber and helium reservoir with a P1 pump (keeping H4, H5 and H8 valves open) and then filling with helium gas from the He recovery line back pressure (by putting off the P1 pump and keeping H4, H5 and H8 valves closed and opening H6 and H7 valves). The Cryostat Dewar is then evacuated by pump P3 and the outer jacket is pre-cooled with liquid nitrogen. After filling liquid helium in the reservoir, the K valve is opened to allow liquid helium to pass through the capillary. The DAC set temperature is then achieved by first manually controlling the helium evaporation rate through the membrane Pump P2 (keeping H6 closed) and finally by the heater-based temperature controller unit (Lakeshore 331).

DAC is optically accessible through the cryostat window (made of Suprasil). An optical setup helps measurement of ruby luminescence for in situ pressure measurement and to view the sample online during temperature sweeping. A low-power green laser (532 nm) is focused by a  $10\times$  objective onto the ruby sphere placed close to the sample inside the DAC and the luminescence light is collected by the same objective and focused onto the fiber head using an achromatic lens. To reject any stray light a low-pass edge filter (600 nm) is placed before the fiber head. The sample is viewed by a CCD camera and with a movable mirror M [157].

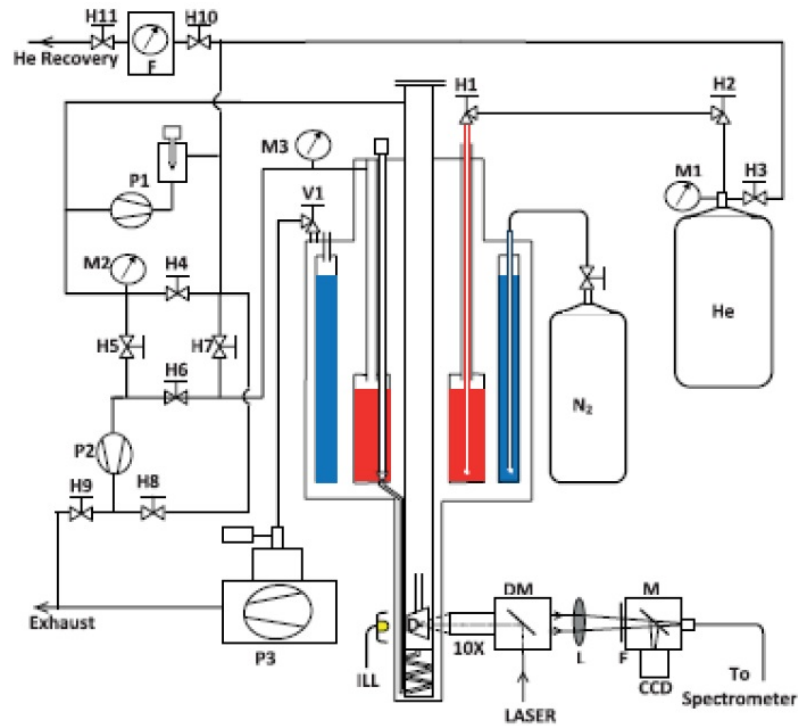


Figure 2.10: (Color online) Schematics of the cryogenic arrangement for DAC-based high pressure low temperature resistance measuring setup along with the in situ ruby pressure measurement facility and the sample viewing arrangement. Hs and V1 denote the valves, Ms, pressure gauge; P<sub>s</sub>, various types of vacuum pumps; F, helium gas flowmeter; DM, the dichroic mirror; M, silver-coated mirror,  $10\times$  objective; L, achromatic lens; F, edge filter; ILL, back illumination lamp and D, DAC. Figure is taken from reference [157]

### 2.3.2 Cryogenic S700X SQUID:

In this current thesis, a cryogenic S700X commercially available cryostat implementing DC SQUID (Fig. 2.11) is used for magnetic and magnetoresistance measurements at ambient pressure as well as at high pressure [137]. Various sample mounting procedure for ambient and high pressure measurements are discussed in their respective sections. Here I discuss the common temperature control procedure for all the measurements in SQUID. The inside of the variable temperature insert (VTI) is thermally isolated from the helium and nitrogen reservoirs by vacuum. Figure 2.11 (b) shows the schematic illustration of temperature control in the S700X. Liquid helium drawn from the helium reservoir passes through a needle valve. The impedance of the needle valve causes a sharp drop in pressure which vaporizes and cools the helium to around 1.5 K by the joule-Thomson effect. The low-pressure cold helium gas is then passed through a heat exchanger where it is warmed to the desired temperature by a heater, before being passed through the sample space. The sample space is then allowed to equilibrate with the temperature controlled gas at the desired temperature. Two thermometers A and B are used for temperature control. Thermometer A is located on the heat exchanger and effectively measures the temperature of the gas coming from the heat exchanger to the sample chamber. The actual temperature of the sample space is measured by B thermometer which is positioned in the sample space above the sample position. At least at low temperature where the heat capacity of the sample space (made from phosphor bronze) is small, highly-responsive temperature control is achieved. The temperature can be changed from 2 to 30 K in less than 30 seconds. The sample probe can also be inserted while the sample space is at low temperature; fully inserting an ambient pressure sample probe and allowing it to cool to 10 K takes only 20 to 30 minutes. The sample rod should be lowered smoothly in several steps because if it is inserted

all in one step the temperature of the sample space will increase rapidly and it will take more time to equilibrate at low temperature.

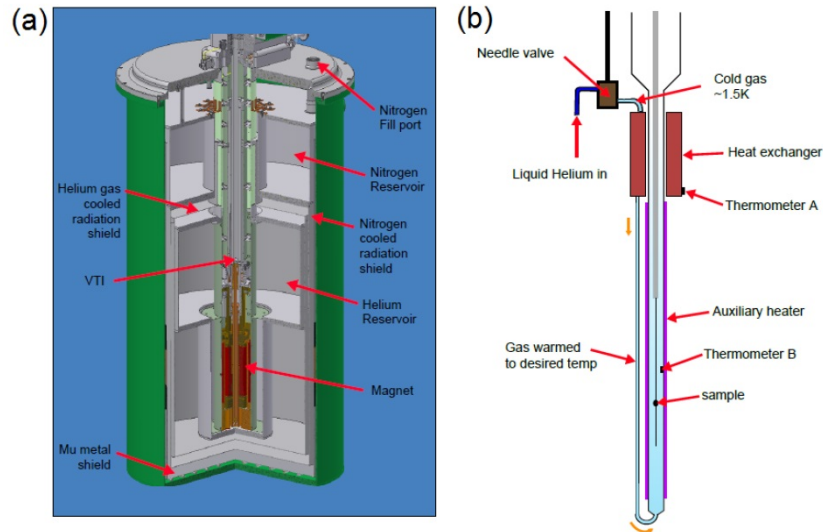


Figure 2.11: Diagram of the Cryogenic S700X SQUID magnetometer. (b) Schematic illustration of the temperature control in S700X SQUID. Figure is taken from reference [137].

### 2.3.3 Liquid Nitrogen based microscope cryostat:

For low temperature reflectance measurements at high pressures we use a liquid nitrogen based flow type microscope cryostat which is capable to cool the sample environment down to  $\sim 100$  K. Left panel of figure 2.12 shows the schematic of the cryostat and the top right figure shows the cryostat which was used for the low temperature measurements. The bottom right figure shows the DAC which was mounted in the cryostat for high pressure measurements. The cryostat has four accessible ports. First one is the nitrogen inlet. Second one is the nitrogen outlet. Third one goes to the vacuum pump to keep the whole cryostat isolated with the environment. And the fourth one is the electronic access to measure the temperature inside.

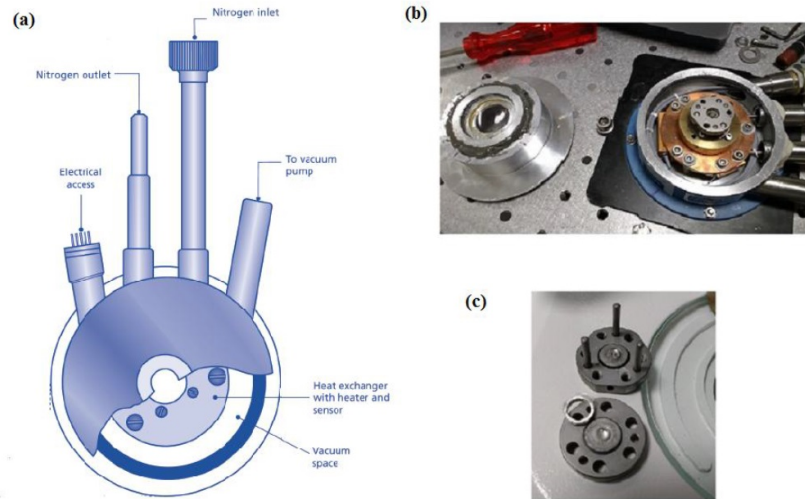


Figure 2.12: (a) Schematics of the cryostat and its components. (b) Figure of the cryostat used for high pressure low temperature IR reflectance measurements. (c) Picture of the DAC mounted inside the cryostat.

## 2.4 High pressure transport and magneto-transport techniques:

The association of the extreme conditions of high pressure, low temperature and magnetic field has led to diverse discoveries and considerably advanced our understanding of various systems where the coupling between the electronic, magnetic and lattice degrees of freedom gives rise to fascinating properties, both from a fundamental and applications oriented point of view [158]. Electrical transport experiments under high pressure and low temperature plays an important role to study the pressure induced superconductivity, metal insulator transition, quantum critical behaviour etc [159]. Recently some of the topological materials shows pressure induced superconductivity after complete suppression of the positive MR [31, 99]. Pressure dependent of Hall coefficient also gives very important information about the charge carrier density and the sign of the charge carriers in these materials [99]. So the high pressure transport measurements in combination with low temperature and magnetic field is very necessary to study the topological properties of the

materials used in the current thesis. The materials I investigate in the current thesis are non-magnetic materials. So details magnetic measurements under pressure are not necessary. But when pressure induced superconductivity is achieved in any materials we need to do the DC magnetic measurements in the vicinity of the superconducting transition temperature to know the bulk nature of the superconducting state. So here I discuss the detail techniques of high pressure and low temperature resistance measurements in a He<sup>4</sup> bath type cryostat, high pressure magnetotransport measurements and DC magnetic measurements.

### 2.4.1 Electrical resistance measurements under high-P and low-T:

DAC based low temperature resistance measurement techniques [160] have long been an important method in high pressure research. Although the recent development in the diamond anvil technique has enabled the high-pressure resistivity experiments to be done at Mbar pressures region [161], high-pressure resistivity experiments still contain large difficulties compared with other high pressure experiments such as x-ray diffraction and other optical measurements. The general problems are the large pressure gradients, the breaking of the leads, and their shorting to the metallic gasket [162]. Further there is frequent anvil failure when a metallic gasket is not used and hence the gasket is of importance in protecting the anvils. Therefore, the major challenge in making electrical resistance measurements at high pressures using a DAC lies in developing a gasket insulation method and reducing the pressure gradients in the sample. In the following section I explore a brief discussion of the van der Pauw methods [163] which we use to measure the resistance of arbitrarily shaped sample inside DAC followed by the measurement procedure.

**Van der Pauw methods:**

As in high pressure experiments, it is common that the sample does not have a well defined geometry and the sample volume is so restricted that it is very difficult to use the conventional four probe techniques in linear geometry to measure the resistance. In such a case, van der Pauw technique [163] is frequently used to determine the resistivity of the sample. The van der Pauw technique is applicable to accurately measure the resistivity of any arbitrary shaped sample (Fig. 2.13) provided the thickness of the sample is known and is uniform, the contact areas are small, and the contacts are all on the perimeter of the sample. Suppose small electrical contacts

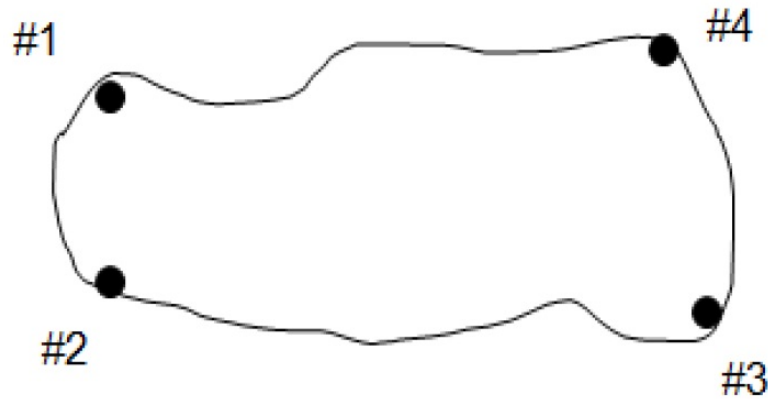


Figure 2.13: Schematic of van der Pauw configuration

are made at four points on the perimeter of an arbitrary shaped sample as shown in the figure (2.13). In this condition van der Pauw showed that the resistivity of the sample is given by the equation,

$$\exp\left(-\frac{\pi d}{\rho} R_{12,34}\right) + \exp\left(-\frac{\pi d}{\rho} R_{23,41}\right) = 1 \quad (2.2)$$

Where  $d$  and  $\rho$  is the thickness and the resistivity of the sample respectively,  $R_{12,34}$  is the resistance determined by dividing the voltage drop  $V_4 - V_3$  by the current going from 1 to 2 and  $R_{23,41}$  is defined similarly. If the points of electrical contact are positioned symmetrically around the perimeter of the sample of uniform resistivity

then  $R_{12,34} = R_{23,41}$  and the above equation reduces to

$$\rho = \frac{\pi d}{\ln(2)} R_{12,34} \quad (2.3)$$

After measurement of the thickness of the sample and the resistance values, the resistivity is determined simply by this equation. However, to apply the van der Pauw method, in DAC based high pressure resistivity measurements, there are various difficulties, such as, the contacts areas are often a significant fraction of the sample size, the sample are often completely irregular in shape and the in situ thickness of the pressurized sample is usually very difficult to determine. Instead of the above the above mentioned difficulties if one carefully arrange the four electrodes around the circumference of the sample inside a DAC, van der Pauw method is the best techniques to measure the resistivity in DAC based high pressure measurements [164].

#### **Measurements procedure:**

We perform high pressure resistance measurements under both quasi-hydrostatic pressure conditions with solid NaCl as a pressure medium and non-hydrostatic pressure condition without any pressure medium. First I will discuss the measurement procedure for quasi hydrostatic compression process thoroughly. Then I will discuss how we modify it for non-hydrostatic pressure measurements.

#### **Case I: Quasi-hydrostatic measurements:**

First a stainless steel gasket of initial thickness of 250  $\mu\text{m}$  is pre-indented to a thickness of  $\sim 80 \mu\text{m}$  by assembling the cell with the gasket between the anvils and slowly increasing the pressure to several GPa. After pre-indentation is done, I drill a hole at the centre of the pre-indented part of the gasket using tungsten drill bits of suitable diameters. The general rule is that the diameter of the drilled hole should be at most half of the diameter of the pre-indented area. As the culet size of the DAC used in our lab is  $\sim 450 \mu\text{m}$ , the hole diameter should be of the order

of  $\sim 200 \mu\text{m}$ . Nevertheless, the size of the hole diameter may vary depending upon the highest pressure we want to reach. Once the sample hole is drilled perfectly, the top side of the gasket is made electrically insulated to prevent shorts. This is done by applying a mixture of fine alumina powder ( $\text{Al}_2\text{O}_3$ : bulk modulus 240 GPa, 99.999 make: MV lab Inc, USA) and UHU hart transparent epoxy (UHU, GmbH) on the gasket and then the gasket with the insulated layers is indented to a thickness of  $\sim 100 \mu\text{m}$  by the same process of pre-indentation. Finally, I make a hole at the centre of the composite gasket such that the side wall of the sample chamber remains coated with the insulated paste to prevent the shorts between the sample and the gasket. Once the gasket is prepared the composite insulated gasket is kept at a safe place. Four insulated copper wires (diameter  $50 \mu\text{m}$ ) are placed on the diamond side surface from four sides and four platinum strips ( $4 \mu\text{m}$  thick) are then implemented symmetrically on the diamond culet (as shown in Fig. 2.14(b)) fixing one end of it with the respective copper wire end using silver paste. The drilled composite gasket is then placed, keeping the insulated side of it on the Pt implemented diamond culet. A tiny sample ( $\sim 50 \mu\text{m}$  to  $\sim 100 \mu\text{m}$ ) is then placed symmetrically connecting with the four Pt electrodes (Fig. 2.14(c)) and few ruby spheres are placed in the sample space to measure the pressure inside. Soft solid NaCl powder which remains insulating throughout the measured temperature and pressure range is used as the pressure transmitting medium. Above a pressure of  $\sim 3$  Kbar, the NaCl become transparent which also help to clearly observe the sample space. However, while loading the NaCl at the final stage, the sample, Pt strips and ruby positions are often found to be misplaced a little causing the sample or the Pt strips to come in contact with the metallic gasket, failing the experiment at much lower pressure than it is planned for. In an ideal condition, the sample should be connected symmetrically with the electrodes at the centre of the gasket hole and the insulated layer should be concentric within the metallic wall of the chamber up to a

very high pressure. In order to measure the sample pressure a laser spot of  $20\ \mu\text{m}$  is focused on one of the ruby sphere placed close to the sample. Our experimental set up allows to determine the pressure at any temperature. Sample resistance is measured by the four probe method using van der Pauw configuration as discussed above, with the help of 370 AC resistant bridge (Lakeshore). We can measure the resistance of any type of sample (single crystal, pressed powder, conducting or insulating) at low temperature down to 1.5 K and high pressure up to 45 GPa.

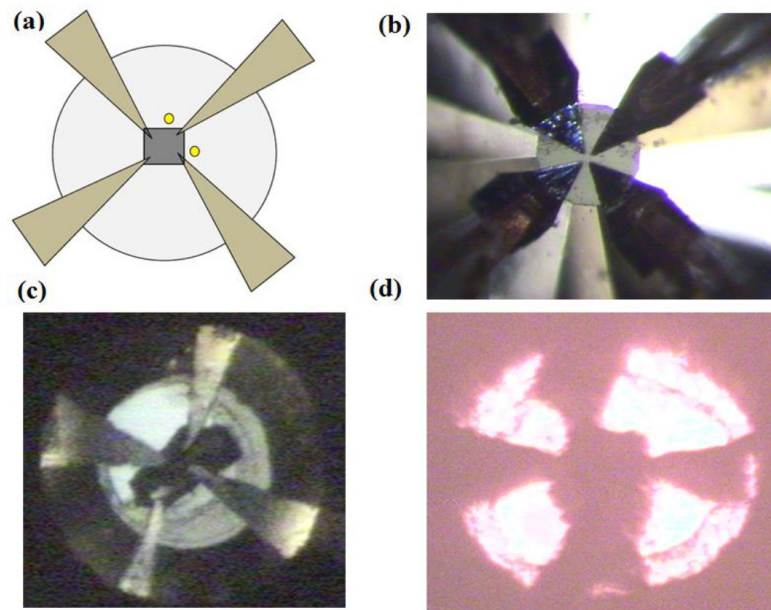


Figure 2.14: (a) Illustration of the typical van der Pauw configuration in a DAC. (b) Four platinum electrodes are arranged on top of one of the diamond culets. (c) Picture of the mounted sample attach with the electrodes. (d) Optical image of the sample space.

### Case II: Non-hydrostatic measurements:

For resistance measurements under non-hydrostatic condition a steel gasket is pre-incident ( $\sim 45\ \text{m}$  thick) and a hole of  $\sim 150\ \text{m}$  is drilled. The drilled gasket is then insulated by covering with a mixture of  $\text{Al}_2\text{O}_3$  and UHU epoxy and taking final indentation to  $\sim 80\ \mu\text{m}$  thick (composite gasket). This time we do not make any

hole at the centre portion of the gasket. So the central portion (of 150  $\mu\text{m}$  diameter) of the gasket is of only  $\text{Al}_2\text{O}_3$ + epoxy layer, whereas the outer portion is steel covered with the insulated layer. Four Pt stripes (4  $\mu\text{m}$  thick) which are used as electrodes are placed symmetrically on the insulated layers. A thin sample is then placed symmetrically on the electrodes to measure the resistance in van der Pauw configuration. No pressure medium is used which make the pressure condition very non-hydrostatic. This time also ruby fluorescence technique is used to determine the sample pressure and the same resistance meter is used to measure the resistance. Figure 2.15 illustrates the schematic of non-hydrostatic resistance measurements.

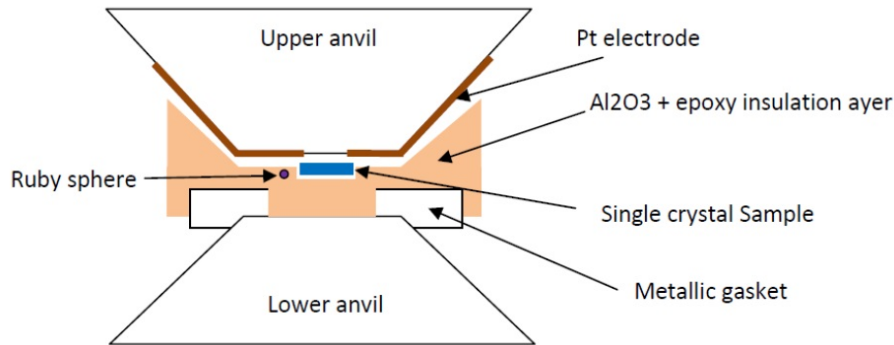


Figure 2.15: Schematics of the resistance measurements under non-hydrostatic condition.

### 2.4.2 Magnetoresistance and Hall Effect under pressure:

Magnetoresistance is a phenomenon in which the electrical resistance ( $R$ ) of a material changes by an applied magnetic field  $H$ . Usually the magnetoresistance (MR) is defined as the ratio

$$MR = \frac{R(H) - R(0)}{R(0)} \quad (2.4)$$

where,  $R(H)$  and  $R(0)$  are the resistance of the material with and without magnetic field respectively. For simple metals, the value of MR is usually very small, showing quadratic field dependence in low fields and saturating in high fields [113]. On the other hand Hall Effect measures the charge carrier density and also provides the

information on the sign of the charge carriers [164]. The Hall coefficient is generally defined as

$$R_H = \frac{E_y}{j_x B} = \frac{V_H}{IB/d} \quad (2.5)$$

where,  $R_H$  is the Hall coefficient,  $E_y$  is the transverse electric field,  $j_x$  is the longitudinal current density,  $B$  is the applied magnetic field perpendicular to both  $j_x$  and  $E_y$ ,  $V_H$  is the Hall voltage,  $I$  is the current and  $d$  is the sample thickness. If the electric current in a material is carried by a single band then the Hall coefficient is written as  $-(1/ne)$  or  $+(1/ne)$ , depending on whether the current is carried by electron and holes respectively and where  $n$  and  $e$  is the carrier density and electronic charge respectively [164]. Whereas, for semiconductors and semimetals in which both electron and holes are present the Hall coefficient is written as

$$R_H = \frac{-n\mu_e^2 + p\mu_h^2}{e(n\mu_e + p\mu_h)^2} \quad (2.6)$$

where  $n$  and  $p$  are the electron and hole densities and  $\mu_e$  and  $\mu_h$  are the electron and hole mobilities respectively. Recently extremely large and positive non-saturating magnetoresistance is observed in various topological materials including NbP [85], NbAs [86], WTe<sub>2</sub> [165], MOTE<sub>2</sub> [31] etc and Hall measurements reveals that among them some of the materials this effect is observed because of electron hole compensation effect [165]. Hence, it is interesting to investigate how the magnetoresistance and Hall coefficient changes with pressure in the topological materials. In the following section, detailed procedure of high pressure magnetoresistance and Hall Effect measurements are discussed.

In the Fig. (2.16) we represent the schematic illustration of high pressure magnetoresistance and Hall Effect measurements. Both the measurements are performed in van der Pauw configuration as shown in the figure. To measure the magnetoresistance and Hall coefficient, the earlier described non-magnetic Cu-Be DAC (easyLab) is prepared for quasi-hydrostatic measurements in a similar way as mentioned in the

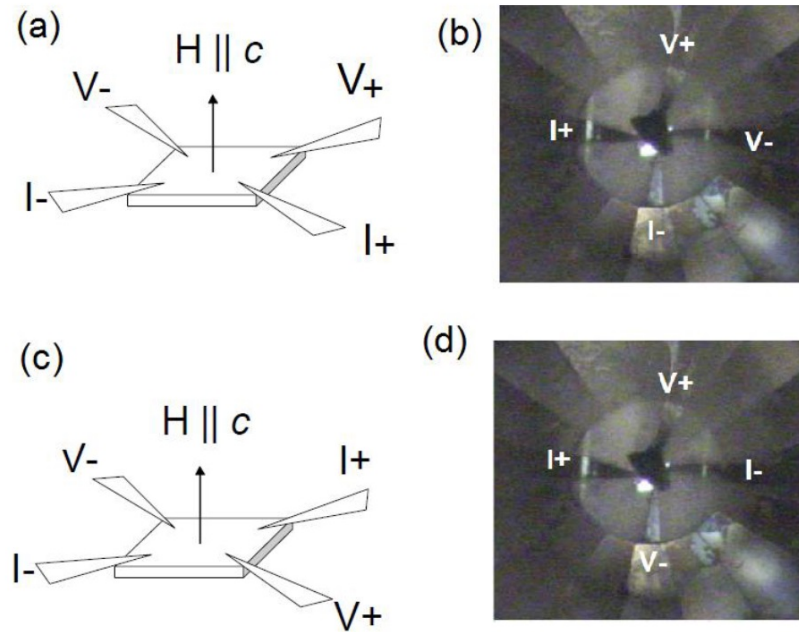


Figure 2.16: (a) Schematic for magnetoresistance measurements. (b) Picture of the sample attached with the electrodes. (c), (d) respective figures for Hall measurements.

case of DAC based cryostat measurements. Here we use Cu-Be gasket. Once the cell is prepared, it is inserted into the S700X SQUID magnetometer to measure the resistance under extreme condition of temperature down to 2 K, magnetic field up to 7 T and pressure up to  $\sim 12$  GPa. The magnetic field is applied along the  $c$ -axis direction as shown in the figure. Pressure inside the sample space is measured by ruby luminescence method.

### 2.4.3 High pressure magnetic measurements:

Among the other physical properties resistivity is one of the important property which can be measured as accurately under pressure as in ambient condition. However, particularly when applied to superconductivity, measurement of resistivity does not provide the full picture of the properties of the material. In the resistance measurements if we observe the resistance is vanishing below a certain temperature that does not mean that entirety of the sample is superconducting. If the current

can find a superconducting percolative path through the sample then the resistance will vanish even if the bulk of the sample is not superconducting: the superconductivity emerged from the impurities of surface effects will affect the measurements. Therefore resistive measurements are rarely sufficient to convince the scientific community of the intrinsic superconductivity of a new material or materials that become superconducting with the application of pressure.

Although, a jump in the specific heat capacity at the transition temperature provides a clear evidence for the bulk nature of the transition, such kind of measurements is exceptionally challenging under pressure. The details of bulk superconductivity of a superconducting sample can be alternatively probed by Meissner effect via the measurement of the sample's magnetization [166]. A significance of the infinite conductivity (zero resistivity) of a superconducting material is to screen the applied magnetic fields. Thus if one measures the temperature dependent magnetization ( $M$ ) or susceptibility ( $\chi$ ), a sharp drop will be observed at the transition temperature with  $\chi = -1$  (in CGS unit) corresponding to complete flux expulsion and therefore bulk superconductivity in the entirety of the sample [166, 167].

Same non-magnetic Cu-Be DAC used in magnetoresistance measurements has been used for high pressure magnetic measurements. The sample is placed in a hole drilled in non-magnetic Cu-Be gasket and is surrounded by the pressure transmitting medium (Daphne oil-7373 or solid NaCl). Pressure inside the sample chamber is measured by the same ruby luminescence method. Both zero field cooling (ZFC) and field cooling (FC) measurement is performed as a function of temperature in the vicinity of the transition temperature. For ZFC measurement, the temperature is cooled to 2K at zero field, then a magnetic field is applied and the measurement is done as the temperature increases. For FC measurements the temperature is cooled to 2K with a constant magnetic field and then the measurement is performed as the temperature increases. To extract the absolute value of the observed magnetic

susceptibility of the sample inside the pressure cell, we subtract the pressure cell contribution determined at different pressures and magnetic field. Figure shows the magnetic background of the cell at ambient pressure.

## 2.5 High pressure spectroscopic methods:

### 2.5.1 X-ray diffraction under pressure:

Powder x-ray diffraction is used as the primary technique for determining the structure of materials at high pressure [168]. Only angle-dispersive x-ray powder diffraction was performed at different pressures. All the XRD measurements were carried out using the previous mentioned MPI-Stuttgart version DAC. Stainless steel gaskets were used for all the measurements and had an initial thickness of  $\sim 250 \mu\text{m}$ . The gaskets were then pre-indented to a thickness of  $\sim 50\text{-}60 \mu\text{m}$  at the culet faces. A hole of the diameter of  $\sim 150 \mu\text{m}$  was then drilled in the centre of the each of the gaskets. The pre-indented and hole drilled gasket was then kept on the table part of the DAC. The sample and ruby ball were then placed into the hole and a pressure transmitting medium was put in as well. The DAC was immediately closed and slight pressure was given by tightening the screws to ensure the PTM, sample, and ruby sphere were trapped in the hole.

All X-Ray diffraction experiments included in the current thesis were performed at the XRD1 beamline of Elettra synchrotrone, Trieste, Italy. Fig. (2.17) shows a schematic of the XRD set up of a typical synchrotron beamline. A Si(111) double-crystal fixed-exit monochromator is used to select a typical working energy for high pressure experiments at 18 keV with a flux of  $10^{11}$  photons/s at 200 mA. The beam size on the sample is normally about  $70 \times 20 \mu\text{m}^2$ . Typical exposure times are 60 - 300s, depending on the scattering factor and the thickness of the sample.

The x-rays are directed into the DAC and diffracted due to the sample inside.

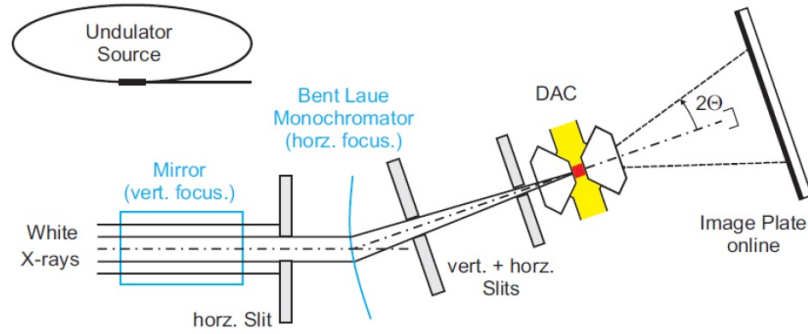


Figure 2.17: Schematic illustration of the x-ray powder diffraction setup at a typical synchrotron beamline. Figure is taken from reference [148].

The diffracted photons travel out the conical side of the DAC and are collected on an two-dimensional image plate detector. The detector position was initially calibrated using  $\text{CeO}_2$  powder, for which the lattice spacing is well known. The pressure inside the sample chamber was measured from the peak position of the pressure marker used. The raw data files obtained from the XRD measurements are then read into FIT2D software [169] which integrates the raw data files and produces intensity versus two-theta plot datasets. The integrated data is then analysed by GSAS software [170] which include two fitting methods. One is the Le-Bail method where one extracts only the lattice parameters and the other is Rietveld method where one can extract full structural details (the lattice parameters and the atomic coordinates) perfectly. If the crystal structure and the lattice parameters are known the unit cell volume of the material can be calculated. This method of analysis was applied for each pressure measurement, and with the unit cell volume at each pressure point known, a plot of the pressure and volume data with the fitted EOS can be obtained for the material.

### 2.5.2 IR reflectance measurements under pressure:

Infrared spectroscopy is one of the most popular spectroscopic techniques in solid-state physics. The simple reason for this is that nearly all materials exhibit a more or

less expressed structure of the absorption in the IR spectral range [49]. In infrared spectroscopy of solid the interaction of radiation with the system is studied over a wide range of temperatures and physical states. There are two different modes of IR spectroscopy: (i) Transmission mode (ii) Reflection mode. The reflection IR spectroscopy was developed using the combination of IR spectroscopy with reflection theories. The most important part of the IR spectroscopy was the development of the Fourier spectrometer. Fourier Transform Infrared (FTIR) spectroscopy is a very powerful technique to obtain the optical analysis from the far infrared ( $\sim 1$  meV) to ultraviolet ( $\sim 5$  eV) radiation. For the FTIR experiment we, generally, used a Michelson Interferometer as the spectrometer. The schematic of this interferometer is shown in the Fig. 2.18 [172]. Using a collimating mirror the IR radiation from a point source is sent to the beam splitter that separates it into two components. One of the components is sent to a steady mirror and the other is sent to a movable mirror. After reflection from both the mirrors, the signal is recombined in the beam splitter and focused on the detector. The detector detects the intensity of the radiation as a function of the optical path difference  $\delta$  generated by the scanning of the moving mirror of the interferometer. This is called the interferogram  $I_R(\delta)$  and it contains implicitly the whole frequency dependence of the light. The Fourier transform of  $I_R(\delta)$  permits to reconstruct the frequency spectrum of the light  $B(\omega)$  through the relation

$$B(\omega) \propto \int_a^b I_R(\delta) e^{-i\omega\delta} d\delta \quad (2.7)$$

where  $\omega$  is in  $\text{cm}^{-1}$  (wavenumbers). In the case of a monochromatic light source, the interferogram is a periodic sine function and the spectrum is a delta function centered at the frequency of the light.

In addition, the IR technique can be applied to a sample under high pressure using a diamond anvil cell (DAC), owing to the transparency of diamond over most of the IR region. This is also a great advantage of IR technique in comparison with

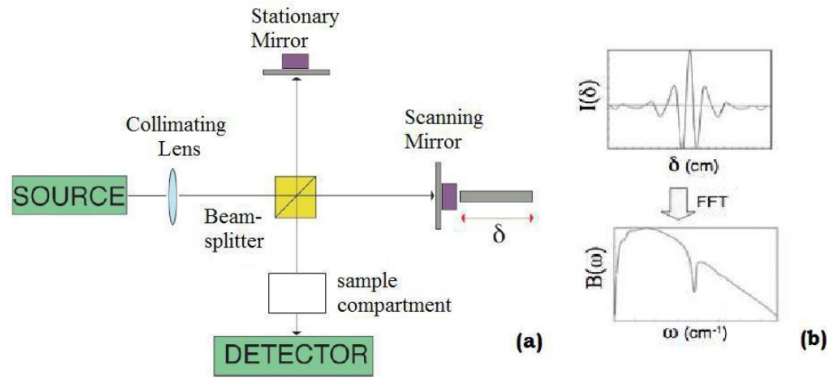


Figure 2.18: Schematic of a FTIR spectrometer. Figure is taken from reference [172].

other common spectroscopic techniques such as the photoemission and tunneling spectrosopes, since these latter techniques cannot be performed on a sample sealed in a pressure cell such as DAC. IR spectroscopy of solid under pressure is, however, technically challenging since the limited sample space available in a DAC allows only small sample sizes (50-200  $\mu\text{m}$ ) (strong diffraction occur because of higher wavelengths). Given a restricted sample space IR reflectivity study of a sample is very difficult to perform with a conventional (thermal) IR source (Glober) due to its low brightness. To overcome this difficulty it is very necessary to perform the measurements in Synchrotron. All the IR reflectance measurements were performed in FTIR mode at SISSI beamline of Elettra in Italy [173].

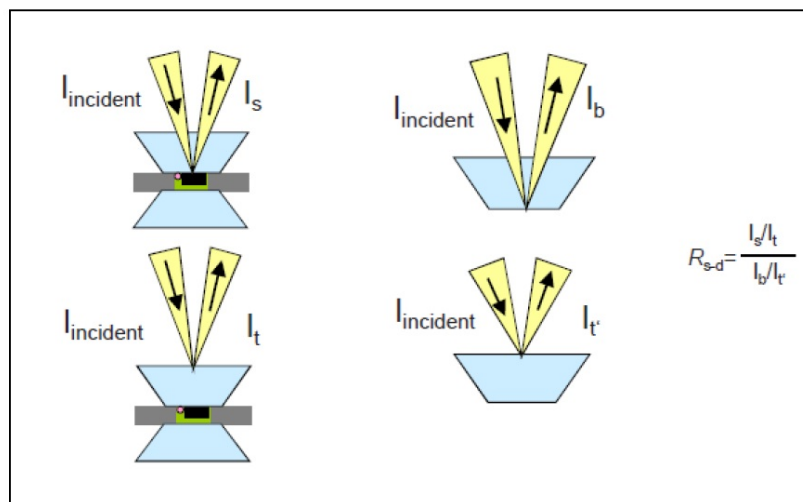


Figure 2.19: Experimental configuration of high pressure reflectivity measurements. Figure is taken from [149]

Fig. (2.19) shows the experimental configuration of high pressure reflectivity measurements. Here, also, we use the same DAC to perform the high pressure IR reflectance measurements. This DAC employs type II diamonds which are suitable for reflectance measurements as they do not contain nitrogen impurities. For high pressure reflectance measurements the most practical way to mount the sample is to mount it against the diamond surface of the DAC such that it remains in direct contact with the diamond window that faces the objective side. This method will ensure that we are measuring the intensity of the light reflected from the diamond-sample interface, rather than from the diamond-pressure medium surface. For this thin pallet of finely ground sample was placed in the gasket hole which was then filled with soft pressure medium such as alkali halides (e.g. KBr, KCl, CsBr, CsCl etc.) to ensure the hydrostatic conditions. The pressure inside the sample is measured by in-situ ruby luminescence techniques. At each pressure, the intensity,  $I_s(\omega)$ , of the radiation from the sample surface is measured and normalized with the intensity  $I_0(\omega)$  of the radiation reflected from the external face of the diamond window to get a quantity

$$r(\omega) = \frac{I_s(\omega)}{I_0(\omega)} \quad (2.8)$$

At the end of the pressure run another measurement is performed on the open diamond surface [ $I_d(\omega), I_0(\omega)$ ] by removing the sample from the DAC. The ratio

$$R(\omega) = \frac{I_d(\omega)}{I_0(\omega)} \quad (2.9)$$

is considered to be pressure independent. The reflectance  $R_{s-d}(\omega)$  at the sample diamond interfaces is thus obtained by the equation

$$R_{sd}(\omega) = \frac{r(\omega)}{R(\omega)} \times R_{dia} \quad (2.10)$$

Where,  $R_{dia} = [(n_{dia} - 1)/(n_{dia} + 1)]^2 = 0.1667$  and  $n_{dia}$  is the refractive index of diamond in air. Pressure was determined in situ by using the ruby-luminescence

technique. The real part of the optical conductivity was then derived from  $R_{s-d}(\omega)$  through Kramers-Kronig analysis. The low frequency data was extrapolated by Hagen Rubens formula ( $R = 1 - A\sqrt{\omega}$ ) and the high frequency reflectance data was extrapolated by  $R = c/\omega^4$  power law.

### Experimental set up:

In this section, I briefly discuss the experimental set up of the SISSI beamline of Elettra in Italy. Fig. 2.20 shows the schematic layout of the beamline. The radia-

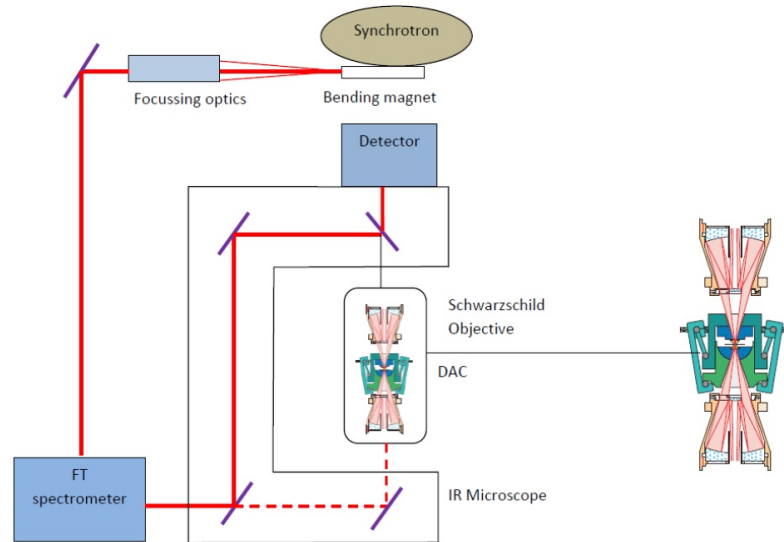


Figure 2.20: Schematic layout of the SISSI Beamline. Figure is taken from [149].

tion is extracted from a bending magnet and passes through diamond window and focusing optics. A slow vacuum valve isolates the vacuum system of the IR beamline from the ultrahigh vacuum of the storage ring. The IR beam enters the Bruker IFS-66v Michelson interferometer coupled to a Hyperion-2000 infrared microscope, which can work in the spectral region from far-IR to visible in both reflection and transmission modes. The infrared microscope has two identical Schwarzschild objectives; one of which is used to focus the light on the sample and the other serves as a condenser for transmission measurements.

For the high pressure measurements we mount the DAC in a home built holder

so that the DAC always remains in the same position. This holder is fixed to the microscope sample stage that allows to finely align the DAC. The adjustable field aperture (0.45 - 3.75 mm), which is mounted in the microscope is kept fixed in a way that it collects only the signal from the selected sample area in the DAC. Moreover, the mirrors that couple the microscope and the interferometer are aligned to match the focus of the IR radiation to the visible focus of the white light of the microscope, to be sure that alignment of the DAC is exactly the same for IR light. Furthermore, appropriate detectors (liquid helium-cooled bolometer for measurements in the FIR range, liquid nitrogen-cooled MCT for the MIR spectral range) and beamsplitters (Mylar lms for FIR, KBr for MIR) are employed, depending on the desired spectral range.

For low temperature measurements at high pressures, one piston cylinder type DAC was mounted inside the liquid nitrogen flow microscope cryostat (as described earlier) from Oxford, allowing cooling the DAC down to  $\sim 100\text{K}$ .

# Chapter 3

## Transport and spectroscopic investigations of $\text{TiTe}_2$ under pressure

### 3.1 Introduction

$\text{CdI}_2$ -structured transition metal dichalcogenide compounds (e.g.,  $1T$ - $\text{TiSe}_2$ ,  $1T$ - $\text{TiS}_2$ ) provide an important playground to reveal exotic ground-state electronic orders [188] by tuning the Fermi surface topology and many-body effects, either purely by lowering temperature [189–192] or by carrier doping [193–202] or applying external pressure [203–208]. The emergence of charge density wave (CDW) order at low temperature and its coexistence with superconductivity (SC) in some portion of the phase diagram have been of tremendous research interest in order to understand their origin and competitive nature [209]. The puzzling behavior of dichalcogenide SC is due to the presence of strong electron-phonon coupling and also the dome structure in the vicinity of the CDW-suppressed quantum critical point (QCP). In the BCS picture, the strong electron-phonon coupling is believed to be responsible for the emergence of both CDW and SC, where other effects such as local short-range interaction and structural disordering are able to explain the systematic suppression of CDW and SC, respectively, forming the dome structure [195, 210]. On the other hand, there is an unconventional SC scenario where CDW amplitude fluctuation is believed to be responsible for the Cooper pair formation [197, 205], where the relevant QCP might be near a hidden commensurate to incommensurate CDW transition [201, 207].

The recent discovery of nontrivial topological states in layered transition metal (TM) dichalcogenides has generated a tremendous impetus to study this family of compounds in the search for topological phases. A combination of enhanced

spin-orbit interaction and time-reversal symmetry makes TM ditellurides promising candidates for topological phases among other dichalcogenides. For example, besides having large nonsaturating magnetoresistance and pressure-driven superconductivity,  $\text{WTe}_2$  and  $\text{MoTe}_2$  are now canonical examples of type-II Weyl semimetals [104, 131]. Similarly,  $\text{PdTe}_2$  and  $\text{PtTe}_2$  are examples of Dirac semimetals [231, 232]. On the other hand, the type-II Weyl state has been realized in noncentrosymmetric layered  $\text{TaIrTe}_4$  [130, 233], and  $\text{ZrTe}_5$  is now an ideal Dirac semimetal exhibiting a novel chiral magnetic effect [234, 235]

$1T\text{-TiTe}_2$  is a conventional Fermi-liquid reference metal, often used to characterize the electronic structure of Cu-intercalated  $1T\text{-TiSe}_2$  [174, 194, 211]. In spite of that, only very few investigations have so far been reported on the pristine  $1T\text{-TiTe}_2$ , particularly due to the absence of CDW order at low temperature [125]. In comparison with its isomorphic  $1T\text{-TiSe}_2$ , the band structure of  $1T\text{-TiTe}_2$  shows enhanced indirect band overlap [having Te  $5p$  hole pockets at and Ti  $3d$  electron pockets at the L point of the Fermi surface (FS)], characterized by semimetallic resistivity at ambient condition [174, 175]. A larger Te spin-orbit interaction and enhanced p-d hybridization near Fermi level are expected to make the FS more susceptible to external parameters, such as intercalation [212], electrostatic field [213], or pressure. Indeed, recent theoretical studies have predicted that not only a suitable strain condition can induce phonon-mediated SC [126]; hydrostatic pressure and isovalent cation substitution may also lead to the emergence of nontrivial topological surface states in its bulk as well as monolayer form [72, 214]. The emergence of SC in the topological surface states is of fundamental interest from the point of view of the realization of topological superconductors, hosting massless Majorana fermions.

Although  $\text{TiTe}_2$  has been predicted to undergo a series of topological phase transitions under different strain conditions or isovalent cation substitution (within its structural stability range) [72, 214], the nature of the topological states has yet to

be investigated by surface-sensitive direct probes such as angle resolved photoelectron spectroscopy. While topologically distinct phases under hydrostatic pressures have been claimed for this compound by indirect methods (observing the phonon linewidth and resistivity anomaly at the transition) [187, 236], the predicted band topology from theoretical calculations is found to be inconclusive as the calculated band structure is found to be extremely sensitive to lattice parameters [72, 236]. Pressure-induced topological phases are alternatively probed by infrared reflectance measurements [65, 127]. 3D linear band crossing results in a characteristic linear frequency-dependent low-frequency optical conductivity in the case of 3D topological semimetals [80, 82, 237, 238]. 1T-structured  $\text{TiTe}_2$  is isostructural to  $1T\text{-TiSe}_2$ , the latter being a model system of layered dichalcogenides that illustrates competing electronic orders (charge density wave order and superconductivity) upon intercalation or by external pressure [193, 205].

Here, we have studied high pressure transport and spectroscopic investigations of both polycrystalline and single crystalline  $\text{TiTe}_2$  [187]. First, we have performed high pressure electrical measurements of polycrystalline  $\text{TiTe}_2$  at room temperature and confirmed the experimental verification of the topological phase transition. The results on polycrystalline sample reveal two isostructural electronic transitions and one structural transition at  $\sim 2$  GPa and  $\sim 4$  GPa and  $\sim 8$  GPa respectively.

Then, we report on the transport properties of pristine  $1T\text{-TiTe}_2$  single crystal under various quasihydrostatic and nonhydrostatic compressions [239]. In nearly hydrostatic condition, SC emerges at  $\sim 5$  GPa where the semimetallic positive magnetoresistance (MR) is found to decrease significantly, showing no apparent competing order in effect at FS. In contrast, application of nonhydrostatic pressure ( $\sim 1.8$  GPa) leads to dramatic changes in its resistance behavior to a characteristic of quasicommensurate CDW ordered state, as seen in isomorphic  $1T\text{-TaS}_2$  [182]. With increasing pressure, this resistance anomaly gets suppressed by a systematic decrease of overall

resistance and SC emerges at 6.2 GPa.  $T_c$  increases rapidly to 5.3 K up to 12 GPa, followed by a rather slow but monotonic increase up to 29 GPa, the highest pressure of this measurement. The SC state persists upon decompression at least down to 0.5 GPa, also coexisting with the re-entrant CDW-like phase (as verified from our electron diffraction measurement on the P-released sample). The persistent nature of SC at almost ambient pressure upon decompression is extremely rare, but highly desirable for practical applications. The pressure-quenchable SC state will also make the surface-sensitive measurements [angle resolved photoemission spectroscopy (ARPES)] accessible for further investigating their electronic origin and coexisting nature in this pristine compound and novel topological physics. The irreversible nature of structural evolution under nonhydrostatic compression further supports the resistance results and establishes the unique pressure-rescaled phase diagram.

Finally, we report high-pressure infrared spectroscopic study on pristine single crystal  $\text{TiTe}_2$  [240]. First, the emergence of new modes including Raman-active modes in the infrared phonon spectra indicates structural modification (with broken inversion symmetry) at a moderate pressure ( $\sim 2.5$  GPa). A structural transition to a noncentrosymmetric structure (with space group  $P3m1$ ) is estimated from this spectral analysis, in combination with high-pressure x-ray diffraction data. High pressure structural modification is believed to be responsible for the emergence of superconductivity with  $T_c \sim 6$  K under quasihydrostatic compression [239], contrasting an earlier theoretical prediction where  $\text{CdI}_2$ -type structure is assumed to be stable at high pressure [126]. An irreversible increase of low-energy optical conductivity spectral weight under quasihydrostatic pressures suggests irreversible modification of its electronic band structure, which is argued to be the reason for the pressure-quenched superconducting state. The structural transition at  $\sim 2.5$  GPa makes it necessary to revisit theoretically the high-pressure topological phases [72], keeping

in mind that the simple parity analysis may not be reliable for exploring possible band inversion in a noncentrosymmetric structure.

## 3.2 Experimental Details

### 3.2.1 Synthesis and characterization

#### *Synthesis*

TiTe<sub>2</sub> single crystals were grown using a chemical vapor transport technique, as described elsewhere [125]. Stoichiometric mixture of Ti (Alfa Aesar, purity 99.9%) and Te (Sigma Aldrich, purity 99.997%) powders were ground together, palletized and loaded into an evacuated quartz tube with sublimated iodine (with 5 mg/cc of quartz tube volume) as transport agent. All weighing and mixing was carried out in a glove box. The tube was sealed under vacuum and placed in a two-zone furnace. The hot zone was maintained at 800°C for 10 days and the cold zone was maintained at 700°C. Single crystalline flakes of thickness 0.01–0.05 mm and lateral dimension 1-2 mm are thus grown on the quartz tube inner surface (see right inset in Fig (3.1)), which has been used for our investigations after characterization.

#### *X-ray diffraction*

A few single crystals are then crushed into fine powder for investigating by powder x-ray diffraction measurement using lab x-ray source at room temperature (Cu-K $\alpha$  radiation). Figure 3.1 shows the recorded x-ray diffraction pattern which is found to fit very well with the known CdI<sub>2</sub>-type 1T-trigonal structure for this compound (S.G. P $\bar{3}$ m1) using Le-Bail profile fitting analysis (structure shown as inset,  $z_{\text{Te}}=0.255$  was used, as reported). Obtained lattice parameters are  $a=3.7677 \text{ \AA}$ ,  $c=6.4983 \text{ \AA}$ , in good agreement with reported results [125,175]. No trace of impurity was detected.

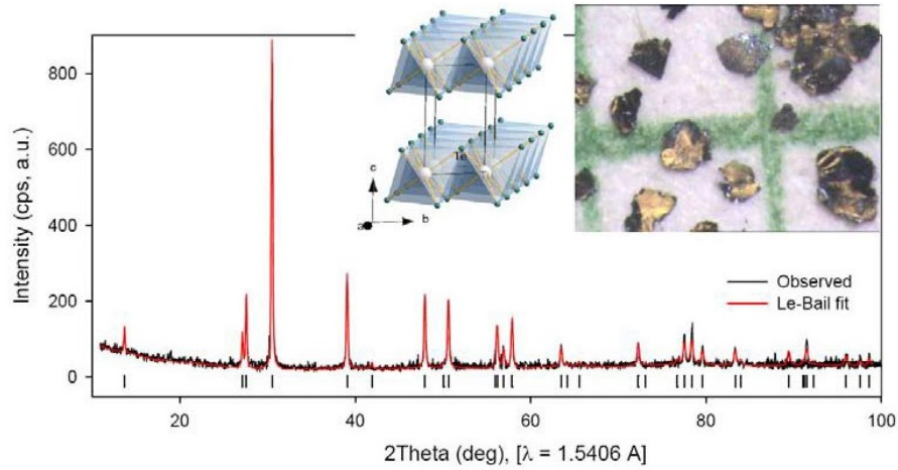


Figure 3.1: X-ray powder diffraction pattern of as grown  $1T$ - $\text{TiTe}_2$  at room temperature ( $\lambda=1.5406\text{\AA}$ ). Le-Bail fitted pattern using the known trigonal structure, as show in inset. Photograph of as grown single crystal flakes are also shown.

### *Low Energy Electron Diffraction:*

The atomic structures and orientation of the tiny single crystal flakes were directly measured by room temperature low energy electron diffraction (LEED) method. Analysis of the diffraction images (Fig.(3.2)), taken in both  $[001]$  and  $[100]$  zone-axis orientation, resulted in a similar centro-symmetric layered hexagonal  $\text{CdI}_2$  structure, as obtained from x-ray diffraction. No additional diffused scattering is observed indicating absence of any lattice superstructure at ambient pressure.

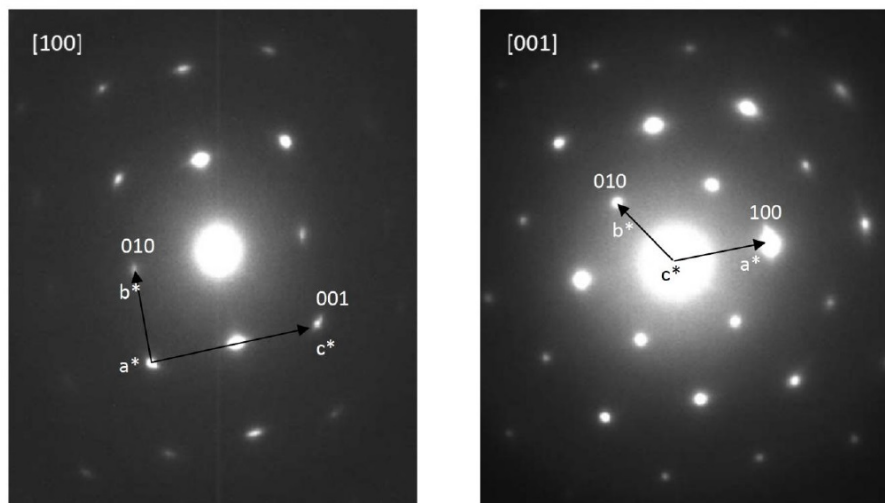


Figure 3.2: Reciprocal lattice patterns of  $1T$ - $\text{TiTe}_2$  single crystal from  $[100]$  and  $[001]$  axis directions obtained from Low Energy Electron Diffraction measurements at room temperature with the help of TEM JEOL 2000FX instrument.

***Resistivity at ambient pressure:***

Ambient pressure in-plane resistance has been measured in four-probe resistance measurements in the temperature range 1.4-300K with a big single crystal mounted on the Helium cryostat sample holder. Four electrodes, made of 10 micron diameter gold wires, were glued on the sample corners with the help of silver paste. Sample resistance decreases smoothly with decreasing temperature as shown in Fig.(3.3), matching well with the reported semi-metallic resistance behavior [125, 175]. The RRR ( $=R_{300K}/R_{10K}$ ) value was found  $\sim 4$ , agreeing well with the reported value on highly pure stoichiometric  $\text{TiTe}_2$  sample [125]. Moreover, no CDW transition like anomaly was detected in the whole temperature range.

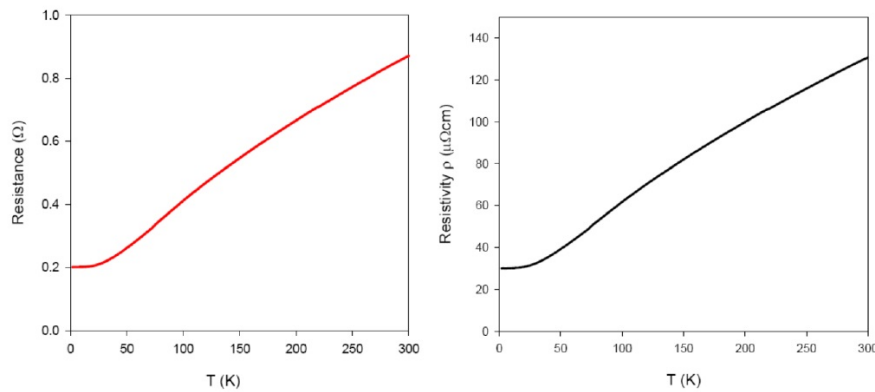


Figure 3.3: In-plane measured resistance data and obtained resistivity curves of  $\text{TiTe}_2$  single crystal in the temperature range 1.4 -300K.

***Magnetic measurement at ambient pressure:***

Magnetization measurements on the random oriented  $\text{TiTe}_2$  crystals have been performed in the zero field cooled (ZFC) warming cycle at applied magnetic field of 1 Tesla, using S700X SQUID magnetometer. Magnetization shows systematic paramagnetic upturn with lowering of temperature. The  $M$  - $T$  data can be well fitted with the Curie-Weiss behavior over the entire  $T$  range (see Fig.(3.4)), agreeing very well with recent report on stoichiometric sample [216]. This is however in contrast

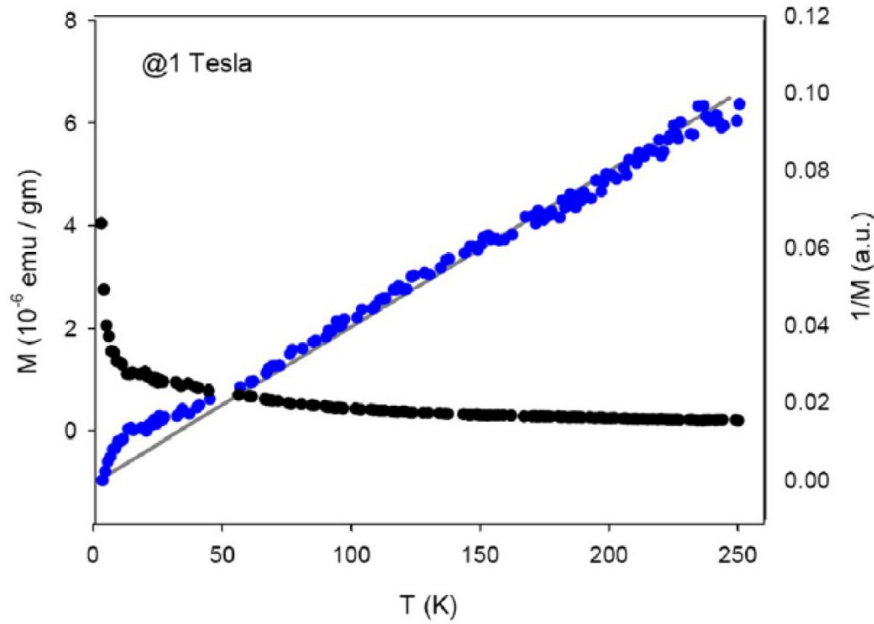


Figure 3.4: Zero field cooled (ZFC) magnetic susceptibility of as grown single crystals of  $\text{TiTe}_2$  over the temperature range 2-250K. Inverse susceptibility plot is also shown.

with an earlier report, where CDW like susceptibility anomaly was noticed at 150 K which was perhaps due to non-stoichiometric composition [175].

### 3.2.2 Resistance measurement techniques under pressure:

The resistance was measured using a standard four-probe technique (in van der Pauw configuration), with ac lock-in detection in two different high pressure arrangements; quasi-hydrostatic and non-hydrostatic.

#### *Quasi-hydrostatic compression:*

Temperature dependent electrical resistance was measured under quasi hydrostatic compression up to 13 GPa by standard four probe method using a miniature DAC, an optical cryostat and an ac-resistance bridge in combination with fine platinum electrodes fabricated on the diamond culet. The sample and electrodes were insulated from the metal gasket using an insulation layer of  $\text{Al}_2\text{O}_3$  and epoxy mixture.

The sample pressure was measured by in situ ruby luminescence method at any temperature. Powdered NaCl was used as the pressure transmitting medium (PTM) to maintain quasi hydrostatic pressure environments and to keep the electrodes in good contact with the sample. Detailed DAC preparation procedure is discussed in **chapter 2**.

***Non hydrostatic compression:***

High pressure resistance measurements under non hydrostatic condition was performed up to 29 GPa. Detailed description of the measurement procedure is given in **chapter 2**.

**Magnetoresistance and DC susceptibility measurements:**

For high-field measurements a nonmagnetic Cu-Be DAC (easyLab) was prepared for quasihydrostatic pressures (up to 9.5 GPa) and was inserted into a S700X SQUID magnetometer (Cryogenic) to study MR up to 7 T field and also dc susceptibility. Pressure was measured by ruby luminescence. Detailed procedure is given in **chapter 2**.

**3.2.3 Non hydrostatic XRD measurements:**

The high pressure powder XRD experiments were performed at the XRD1 beam line of the ELETTRA synchrotron facility, using the Stuttgart DAC with conical seats and diamond culet size of 450 $\mu\text{m}$ . A 150  $\mu\text{m}$  hole in a stainless steel gasket pre-indented to 70  $\mu\text{m}$  was completely filled with  $\text{TiTe}_2$  powders together with gold x-ray pressure marker [217]. No pressure transmitting medium was used to keep highly non-hydrostatic pressure condition. The measurements were carried out at  $T = 300$  K with the x-ray energy tuned to 17.712 keV ( $\lambda = 0.70001$  Å). The XRD patterns were collected on a Dectris Pilatus2M detector and these were converted

to  $I(2\theta)$  diffraction profiles using the FIT2D software [218]. The profiles were fitted using Le-Bail and Rietveld refinement procedures as implemented in the GSAS software [219]. Au diffraction peaks are found relatively sharp giving correct mean stress at the sample location.

### 3.2.4 IR reflectance measurements under pressure:

IR reflectance spectra under high pressures have been collected at the SISSI beamline of Elettra synchrotron facility, with the help of an IR microscope (Hyperion) equipped with a liquid-nitrogen-cooled HgCdTe (MCT) detector (for mid-IR measurements) and a liquid-helium-cooled Bolometer (for far-IR measurements) coupled to a Bruker Vertex 70v interferometer [242]. A thin single crystal with the flat surface (ab-plane) is placed against the diamond surface (of type II as diamond anvil) in the DAC gasket hole, which is then filled with a finely powdered CsI pressure medium to perform measurements under a quasihydrostatic pressure condition. Mid-IR reflectance at the sample-diamond interface are measured at room temperature in a wide frequency range ( $600\text{-}12\,000\text{ cm}^{-1}$ ) up to  $\sim 22$  GPa. For studying IR phonon spectra under high pressure (up to  $\sim 9$  GPa), far-IR reflectance measurements have been performed both at room temperature as well as at low temperature (down to 100 K) with the help of a  $\text{N}_2$ -flow microscope cryostat (Oxford Instruments).

At each pressure, the intensity of light  $I_s(\omega)$  reflected from the sample surface is measured and normalized with the light intensity  $I_0(\omega)$  reflected from the external face of a diamond window to obtain a quantity  $r(\omega) = I_s(\omega)/I_0(\omega)$ . At the end of the pressure run, another measurement is performed on the open diamond surfaces [ $I_d(\omega)$ ,  $I_0(\omega)$ ] by removing the sample. The diamond-air interface reflectivity in the measured frequency range  $R(\omega) = I_d(\omega)/I_0(\omega)$  is practically pressure-independent up to the highest pressure of this measurement [243]. The reflectance  $R_{s-d}(\omega)$  at

the sample-diamond interface is thus obtained from the equation  $R_{s-d}(\omega) = r(\omega)/R(\omega) \times R_{dia}$ , where  $R_{dia} = [n_d - 1/n_d + 1]^2$  ( $\approx 0.1667$ ) is the absolute reflectivity of the diamond-air interface,  $n_d$  being the real refractive index of diamond in air. For accuracy in the low-pressure measurements, sufficient initial pressure is applied to keep the sample in good contact with the diamond surface. Pressure inside the DAC was monitored by the in situ ruby luminescence method [244]. The data around  $2000 \text{ cm}^{-1}$  are affected by the multiphonon absorption in the diamond, therefore this energy range was cut out and interpolated using the Drude-Lorentz fitting of the reflectivity spectra for further analysis. The optical conductivity spectra  $\sigma_1(\omega)$  of  $\text{TiTe}_2$  are calculated from  $R_{s-d}(\omega)$  by using Kramers-Kronig (KK) analysis with appropriate phase factor correction, as described elsewhere [245].

### 3.3 Results and Discussions:

#### 3.3.1 Room temperature resistance measurements on polycrystalline $\text{TiTe}_2$ under pressure

$1T$ - $\text{TiTe}_2$  is expected to show metallic behavior due to the finite band overlap of the  $d$  orbitals of the Ti atom with the  $p$  orbitals of the Te atoms at ambient conditions [174]. The oxidation state of typical  $\text{CdI}_2$  structures such as  $\text{TiX}_2$  is given by  $\text{Ti}^{4+}(\text{X}^{2-})_2$  ( $\text{X} = \text{S}, \text{Se}, \text{and Te}$ ); here the amount of electron transfer from orbitals  $p$  to  $d$  is zero [181, 187]. However the overlap of the  $p$  orbitals with the  $d$  orbitals can lead to the transfer of  $n$  electrons per metal; then the oxidation formula can be changed into  $\text{Ti}^{(4-n)+}(\text{X}^{[2-(n/2)]-})_2$  [181, 187]. In the energy band diagram, the transition-metal Ti- $d$  orbitals are located just above the top of the  $p$  orbitals of Te chalcogen [181, 187]. These two orbitals can be overlapped either via the chemical or physical methods. Chemically, it can be achieved by decreasing the electronegativity of chalcogen X. As the electronegativity of Te is less than both Se and S, the top

portions of the  $p$  orbital bands are raised. Hence, the overlap of  $p$ - $d$  bands is more in Te than in Se and S atoms which leads to the behavior of  $\text{TiTe}_2$ ,  $\text{TiSe}_2$ , and  $\text{TiS}_2$  as metal, semimetal, and semiconductor, respectively. Physically, the overlap of the  $p$ - $d$  orbitals can be increased by reducing the Ti-X bond distance, which can be experimentally achieved using hydrostatic pressure [187].

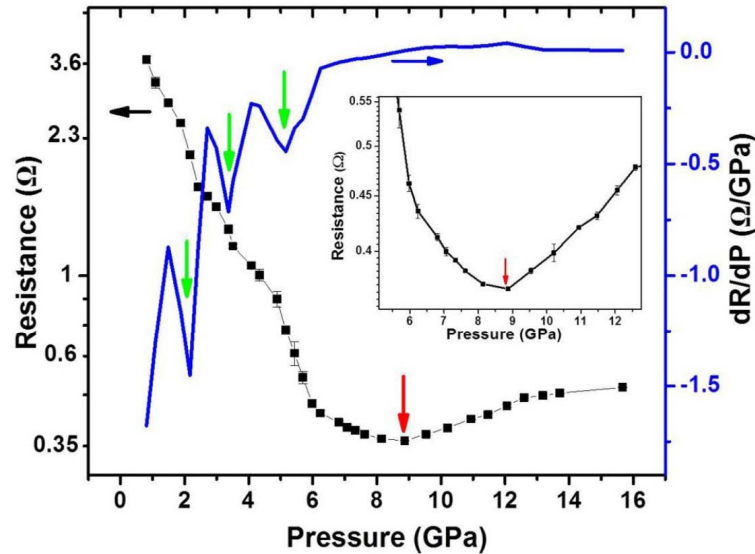


Figure 3.5: Pressure-dependent electrical resistance of  $\text{TiTe}_2$  (black square and a line corresponding to the left y axis) and its first derivative (blue line corresponding to the right y axis). The red arrow at  $\sim 8.8$  GPa indicates the structural transition. The solid green arrows at 2.1 GPa and 3.4 GPa indicate the isostructural electronic transitions in the trigonal ( $P\bar{3}m1$ ) phase. The inset highlights the resistance minimum in the vicinity of the structural transition [187].

Here, we have investigated the pressure-dependent resistance measurements of a polycrystalline  $1T$ - $\text{TiTe}_2$  sample at room temperature. The pressure dependence of the electrical resistance ( $R$ ) and its first derivative ( $dR/dP$ ) at room temperature for  $1T$ - $\text{TiTe}_2$  are illustrated in fig.(3.5) and reported in Ref. [187]. The resistance value is  $\sim 3.7 \Omega$  for the lowest measured pressure ( $\sim 0.8$  GPa). For the  $1T$ - $\text{TiTe}_2$  sample (single crystal), Koike et al. [125] and de Boer et al. [175] reported that the resistivity at room temperature is of the order of  $10^{-4} \Omega\text{cm}$  (at low temperature it is of the order of  $10^{-5} \Omega\text{cm}$ ). Then the resistance of a sample with a few microns thickness will be of the order of  $1 \Omega$ . In our measurements, it is  $3.7 \Omega$  at  $\sim 0.8$  GPa.

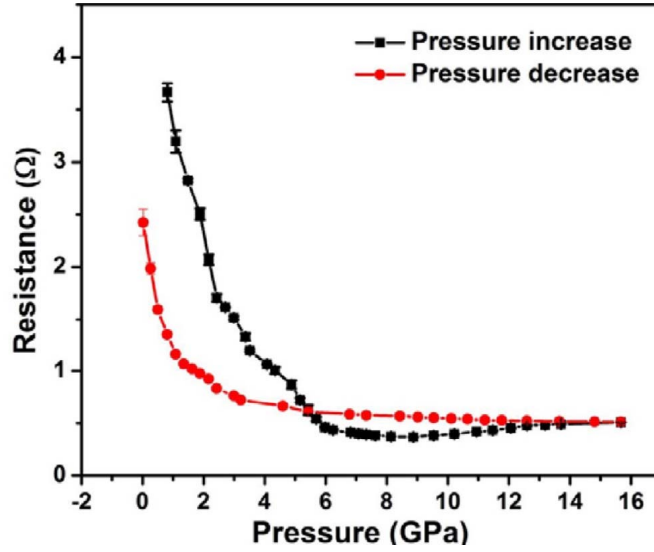


Figure 3.6: Pressure dependent electrical resistance plot for the  $\text{TiTe}_2$  compound up to  $\sim 16$  GPa. The significant hysteresis has been found between the pressure increasing and decreasing cycle [187].

So, its order of magnitude is more or less consistent with the literature [125, 175]. Because of the soft polycrystalline nature of the sample (small pressure can change the sample thickness by a huge amount), we have not measured the thickness of the sample at ambient pressure, and the low-pressure resistance measurements have no meaning (in the low-pressure region the intergrain contribution is large compared to the sample contribution) [187]. We have measured the resistance above a sufficient pressure ( $P > 0.8$  GPa) although at this pressure the intergrain contribution is there, but will definitely be small compared to the sample resistance. Therefore, we believe that the obtained resistance of the polycrystalline  $1T$ - $\text{TiTe}_2$  sample provides a real trend, without being affected by the wire-contact resistance or contribution of the intergrain barriers. As the pressure increases, the resistance of the  $\text{TiTe}_2$  sample quickly drops from  $\sim 3.7 \Omega$  at  $\sim 0.8$  GPa to  $\sim 0.37 \Omega$  at  $\sim 8.8$  GPa. As we further increase the pressure from  $\sim 8.8$  GPa the resistance starts to increase slowly with pressure (clearly seen in the inset of the fig.(3.5)) and at  $\sim 12.6$  GPa reaches a value of  $\sim 0.48 \Omega$  which is 30% more than that at  $\sim 8.8$  GPa. Above  $\sim 12.6$  GPa the resistance increases at a slower rate and the  $\sim 0.51 \Omega$  resistance at

$\sim 16$  GPa (the highest measured pressure of our experiment) is roughly 38% more than at  $\sim 8.8$  GPa [187]. The increase in resistance may be caused by sample size shrinkage. Fritsch et al. [182] suggested that the increase in resistance by the sample size shrinkage is about one third of the compressibility, which in the present case should be less than 10% below  $\sim 8.8$  GPa and 13% at 16 GPa based on the bulk modulus measurements of our XRD experiment. Thus, our result suggests that as the pressure increases,  $\text{TiTe}_2$  becomes more and more metallic only up to  $\sim 8.8$  GPa and the unusual increase of the resistance above  $\sim 8.8$  GPa should mainly result from the accompanying change in the crystal structure which is consistent with the structural transition from trigonal ( $P\bar{3}m1$ ) to monoclinic ( $C2/m$ ) as confirmed by XRD and Raman measurements at  $\sim 8$  GPa. This type of change in crystal symmetry along with abnormal resistance increase with pressure was also observed in  $\text{V}_2\text{O}_3$  [183]. It is also reported that the pressure-induced structural phase transitions of  $\text{Bi}_2\text{Te}_3$  and  $\text{As}_2\text{Te}_3$  induce a series of changes in the electrical resistivity [59,184]. In the low-pressure regime (below 8.8 GPa), the pressure dependent resistance curve shows three distinct slope changes at  $\sim 2.1$  GPa,  $\sim 3.4$  GPa, and  $\sim 5.1$  GPa which are identified by the minima of the  $P$  vs  $dR/dP$  curve. These inflection points cannot be associated with structural phase transitions since high-pressure XRD and Raman measurements reveal the structural stability of the ambient-pressure  $P\bar{3}m1$  structure up to  $\sim 8$  GPa and are associated with isostructural electronic transitions. The first two points ( $\sim 2.1$  GPa and  $\sim 3.4$  GPa) are consistent with our XRD and Raman measurements ( $\sim 2$  GPa and  $\sim 4$  GPa). Here, we would like to mention that anomalies in pressure-dependent transport (resistivity) measurements at room temperature were observed in  $\text{BiTeBr}$  during the TQPT at 2.1 GPa [185]. The third transition point at  $\sim 5.1$  GPa is not seen in XRD and Raman measurement. We have seen from XRD that the strains build up in the pressure range of 4-8 GPa followed by a structural phase transition at  $\sim 8.8$  GPa. In addition, we observe the

broad nature of the minimum at  $\sim 5.1$  GPa of the  $dR/dP$  curve. Hence, the anomaly at  $\sim 5.1$  GPa may be the signature of the precursor effect for the structural transition. We observe a considerable hysteresis between the pressure-increasing and pressure-decreasing cycle, which confirms the first-order nature of the transition at  $\sim 8.8$  GPa (see Fig.(3.6) [187]). The irreversibility of the resistance upon decompression is noted, and which may happen for various reasons. (i) One of the most important reason is that we might not have given sufficient time for releasing (for example, see supplementary of Ref. [186,187]). The other reasons are (ii) irreversible changes in the shape and size of the materials upon decompression, and that (iii) the high-pressure structural transition may not be completely reversible. Here the structure is entirely reversible, inferred from the high-pressure XRD and Raman data, and hence this possible reason is ruled out. But, the first two possibilities are not entirely ruled out and could play an important role in the observed irreversibility of the resistance. More importantly, the isostructural and structural transition observed in resistance studies is consistent with multiple techniques such as XRD and Raman measurements over similar pressure regions (Figure 3.7) , which further ascertain that the transitions are intrinsic [187]. The small difference in transition pressure observed with respect to XRD and Raman could be mainly due to the sensitiveness of these techniques, error in pressure measurement, and the degree of hydrostatic conditions produced by PTM used in these experiments [187].

### 3.3.2 Low temperature resistance measurements on single crystalline $\text{TiTe}_2$ under pressure

In Fig. 3.8, semimetallic  $R(T)$  curves at all pressures under quasihydrostatic conditions closely resemble the one at ambient pressure. With an increase in pressure, the overall resistance decreases systematically, indicating an enhanced metallic character. At 5 GPa, a significant resistance drop below 2.5 K indicates the onset of

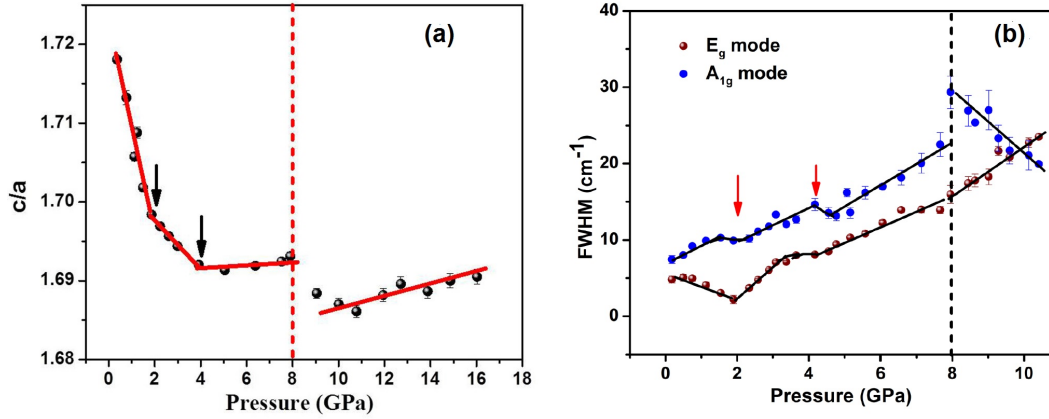


Figure 3.7: (a)  $c/a$  ratio as a function of pressure for polycrystalline  $1T$ -TiTe<sub>2</sub>. (b) FWHM of  $A_{1g}$  and  $E_g$  mode as a function of pressure. The solid and vertical dotted lines signify a guide to the eye and structural phase transition, respectively.

SC transition (inset of Fig.3.8(a)).  $T_c$  increases monotonically (Fig.3.8(b)), with  $dT_c/dP = 0.35$  K/GPa. Below 7.5 GPa, SC transition is not complete at the lowest  $T$  (1.4 K) of our setup and so zero resistance is not achieved. To demonstrate that the zero resistance at higher pressures represented the SC state, we measured resistance drop at 8.9 GPa under magnetic field and found a significant decrease in  $T_c$  (Fig.3.8(c)).

To understand the evolution of electronic structure exhibiting SC, we carried out magnetoresistance (MR) and Hall measurements at high  $P$  (with  $H = 7$  T along the  $c$  axis). Fig.3.9(a) displays the effect of high field on the low- $T$  longitudinal resistance ( $R_{xx}$ ) at various hydrostatic pressures. The measured MR at 10 K is plotted as a function of pressure in Fig.3.9(c). The paramagnetic semimetallic positive MR at 0.5 GPa agrees well with the reported result of stoichiometric  $1T$ -TiTe<sub>2</sub> at ambient pressure [216]. With increasing pressure, MR decreases by a factor of 3 at 5 GPa, where SC emerges. As  $T_c$  increases with pressure, MR gets further suppressed, but remains positive. The hole-dominated positive Hall coefficient  $R_H$ , as obtained from the measured transverse resistance ( $R_{xy}$ ), also agrees well with an earlier report [125].  $R_H$  remains almost pressure independent up to 5 GPa, above which it starts decreasing rapidly (see Fig.3.9(d)) showing increased effective carrier concentration,

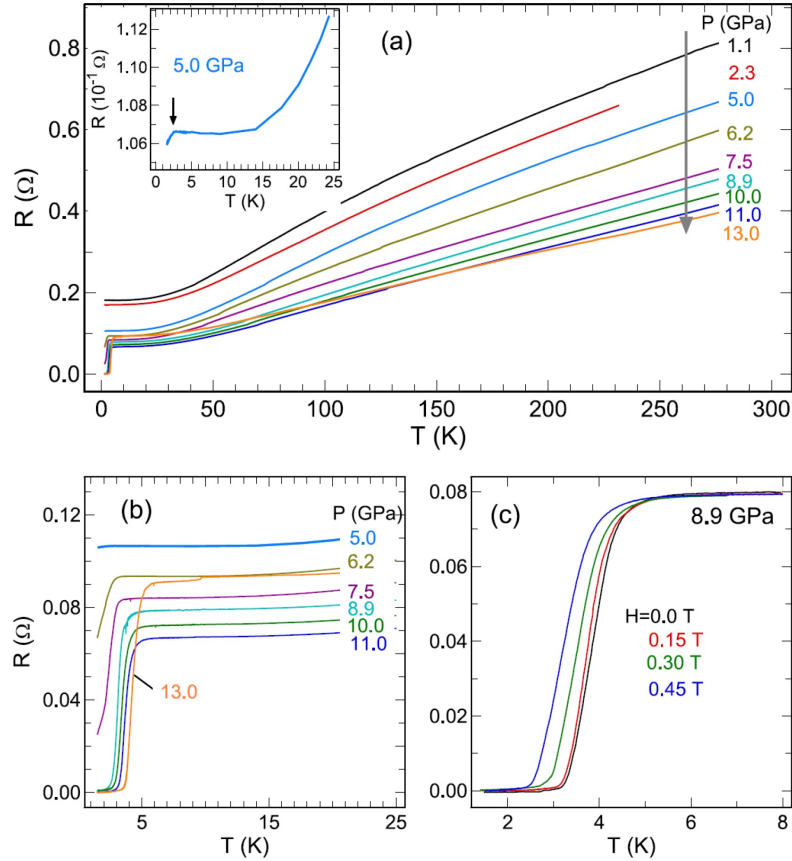


Figure 3.8: (a) In-plane resistance of 1T-TiTe<sub>2</sub> as a function of temperature at various quasi-hydrostatic pressures. Inset shows a significant resistance drop below SC onset  $T_c$  2.5 K at 5 GPa. (b) The magnified R-T data near SC transition at various pressures. (c) Variation of the R-T curve near  $T_c$  under magnetic fields at 8.9 GPa.

which is also supported by the observed enhanced RRR value above this pressure.

In addition to these, the magnetic field dependence of the semi-metallic positive magneto-resistance (MR) of TiTe<sub>2</sub> single crystal (with  $H \parallel c$  configuration) has been investigated under quasi-hydrostatic pressures up to 9.5 GPa. Fig.(3.10) shows the  $H^2$  dependence of the isothermal ( $T = 10$  K) MR at different pressures. The linear behavior at high field up to 3 GPa indicates that isothermal MR comes from the contribution of the Lorentz force to the carriers under magnetic field. Although the MR remains positive at all pressures over the entire field range (up to 7 T), a nonlinear behavior appears at 5 GPa and it becomes significantly complex at 7.5 GPa, with a almost saturation in MR near  $\sim 3.5$  T field, followed by a rapid increase

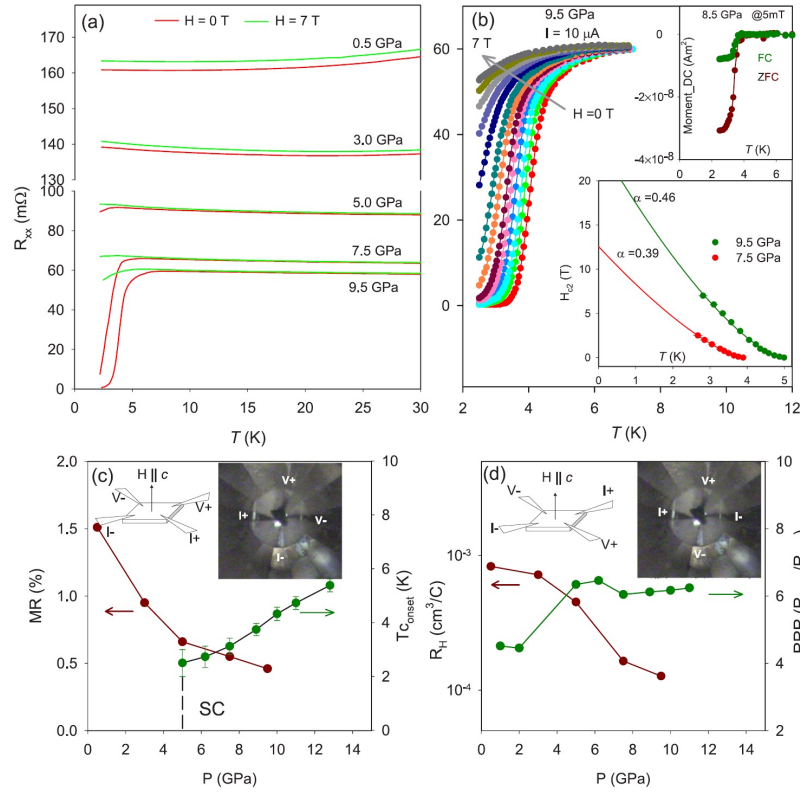


Figure 3.9: (a) Low-T longitudinal resistance, measured at zero field and at 7 T, at various quasi-hydrostatic pressure. (b)  $R(T)$  plots across  $T_c$  at 9.5 GPa under different fields up to 7 T. Lower inset: plots of  $T_c$  vs  $H$  at 7.5 and 9.5 GPa; solid lines are best fits using the empirical formula  $H_{c2}(T) = H_{c2}(1 - T/T_c)^{1+\alpha}$ . Upper inset: dc susceptibility of the SC state at 8.5 GPa. Plots of (c) magnetoresistance  $MR$  (%) =  $[(R_{7T} - R_{0T}) \times 100 / R_{0T}]$  at 10 K and onset  $T_c$  and (d) Hall coefficient  $R_H$  at 10 K and RRR ( $=R_{280K}/R_{10K}$ ) as a function of pressure. Insets are schematic illustrations.

and finally linear  $H^2$  dependence at further high field. To understand this feature we can think of two component contributions, possibly of two band origin. However, at  $P=9.5$  GPa, this anomaly reduces further and almost linear behavior is established. In the two band model (appropriate for  $\text{TiTe}_2$  having Te  $5p$  hole pocket and Ti  $3d$  electron pocket at the Fermi Surface), the magnetoresistance  $MR$  can be expressed as,

$$MR = \frac{n_e \mu_e n_h \mu_h (\mu_e + \mu_h)^2 (\mu_0 H)^2}{(\mu_e n_h + \mu_h n_e)^2 (\mu_e \mu_h)^2 (\mu_0 H)^2 (n_h - n_e)^2} \quad (3.1)$$

where  $\mu$ ,  $n$  are the mobility and carrier concentrations in the above electron and hole bands. In an almost compensated semimetallic state,  $n_h \cong n_e$  and so  $MR \propto H^2$ . The

anomalous non linear behavior between 5 and 7.5 GPa clearly indicates the changes in charge carriers in these two bands, which eventually favors the superconductivity to emerge.

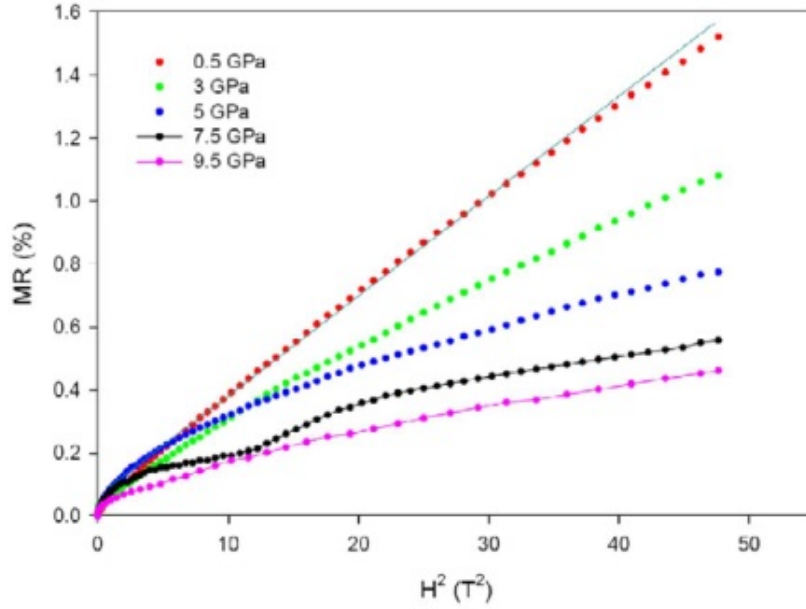


Figure 3.10: Plots of magneto-resistance (MR %) data at 10 K as a function of squared magnetic field at various quasi-hydrostatic pressures

In Fig.3.9(b), we plot the field variation of  $R$  (T) at 9.5 GPa around  $T_c$ . The zero resistance state (with  $T_c \sim 5$ K at  $H = 0$ T) is gradually lifted with increasing magnetic field, resulting in a systematic decrease in  $T_c$ . At a magnetic field of 7 T the superconducting transition almost smears out. In the  $T_c - H$  plot [as shown in the inset of Fig.3.9(b)], a positive curvature close to  $T_c$  ( $H = 0$ ) clearly indicates the deviation of a single-band model of the Werthamer-Helfand-Hohenberg theory for the upper critical field  $H_{c2}(T)$  [220] and suggests a need for two-band analysis, as in the case of  $\text{NbS}_2$  and  $\text{NbSe}_2$  [221, 222]. The experimental data  $H_{c2}(T)$ , when fitted with the empirical formula [223],  $H_{c2}(T) = H_{c2}(1 - T/T_c)^{1+\alpha}$ , estimates  $H_{c2} > 10$  T, which is larger than  $2H\text{-NbSe}_2$  [221] and  $1T\text{-TiSe}_2$  [205] and also higher than the BCS weak-coupling Pauli limit  $H_p = 1.86 \times T_c(0) \sim 9.3$  T. This is in stark contrast with other layered chalcogenides, where Pauli-limited behavior of the upper

critical field has been observed [205,221,222]. However, strong spin-orbit coupling in reduced dimension or local disorder can suppress paramagnetic pair breaking effect and violate the Pauli limit by a factor of 3-6 in the case of the dirty limit of BCS Superconductors [224, 225]. Higher field measurements at further low temperature are needed for better insight in this regard. Low-T resistivity data of 1T-TiTe<sub>2</sub> gives mean free path  $\lambda = 7$  nm [226], which is of the same order of the estimated coherence length  $\xi_{GL} = \sqrt{\phi_0/2\pi H_{c2}(0)} = 3.6$  nm and so the observed superconductivity is of multiband BCS type, but not in the clean limit regime. With the coherence length being greater than the interplane separation, the superconductivity is of three dimensional (3D) nature. Moreover,  $H_{c2}$  vs  $T_c$  plots at 7.5 and 9.5 GPa are in good agreement as per BCS estimation  $H_{c2}(0) \propto T_c^2$ .

To understand the bulk nature of the observed superconductivity at high pressures we have performed dc susceptibility measurements of the pressurized sample at 8.5 GPa ((with H || c configuration, in the MCell Ultra DAC of easyLab) using the SQUID magnetometer using 5 mT excitation field (in ZFC and FC schemes, see figure 3.11 (a)). In order to get rid of any spurious magnetic impurity, all electrode lead connections were removed and the outer part of the cell was cleaned thoroughly before this measurement. The (background) magnetic moment of the DAC at the same pressure was measured after removing the sample and was subtracted from the previous data, to get the tiny sample magnetic moment. We have not attempted to measure the weight of this sample to get the absolute diamagnetic susceptibility; however, a rough estimate shows the SC shielding fraction to be  $\sim 60-80\%$ , clearly indicating bulk nature of the SC of this pressurized sample.

The four-probe resistance measurement was performed at the same pressure (8.5 GPa) at two different current excitations (10 mA and 1 mA) 3.11 (b). The lower excitation current shows higher zero resistance SC transition ( $T_{c0}$ ), agreeing very well with the onset of perfect diamagnetic behavior. Inset of 3.11 (b) shows the first

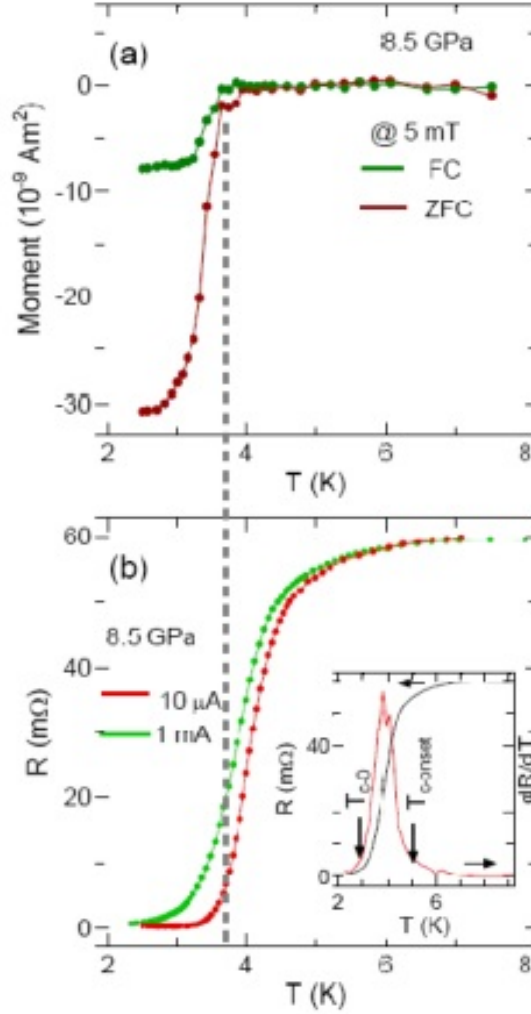


Figure 3.11: (a) DC magnetic susceptibility measured near superconducting  $T_c$  at 8.5 GPa under ZFC and FC scheme. (b) Resistance measurements across the SC  $T_c$  at 8.5 GPa at two different excitation currents (10 mA and 1 mA). Inset shows the first derivative of resistance data of 1 mA current excitation, to determine the onset and zero resistance SC  $T_c$ .

derivative of resistance data of 1 mA current excitation, to determine the onset and zero resistance SC  $T_c$ .

Bulk Superconductivity in a sample is also lifted as the current excitation is increased. As the in-plane current density increases and approaches the critical current density, superconducting  $T_c$  systematically decreases and vanishes completely above that. In Fig.(3.12), we plot the change in SC resistance drop near  $T_c$  of the pressurized sample at 7.8 GPa by varying the excitation currents. At 31.6 mA current, SC completely disappears, we can estimate in-plane critical current density  $J_c$

$= I_c/A$ ,  $A$  being the sample area of cross-section ( $\sim 10 \mu\text{m} \times 30 \mu\text{m}$ ). Therefore,  $J_c \cong 10^4 \text{A/cm}^2$ , of the same order of magnitude to that of  $\text{NbSe}_2$  single crystal [228].

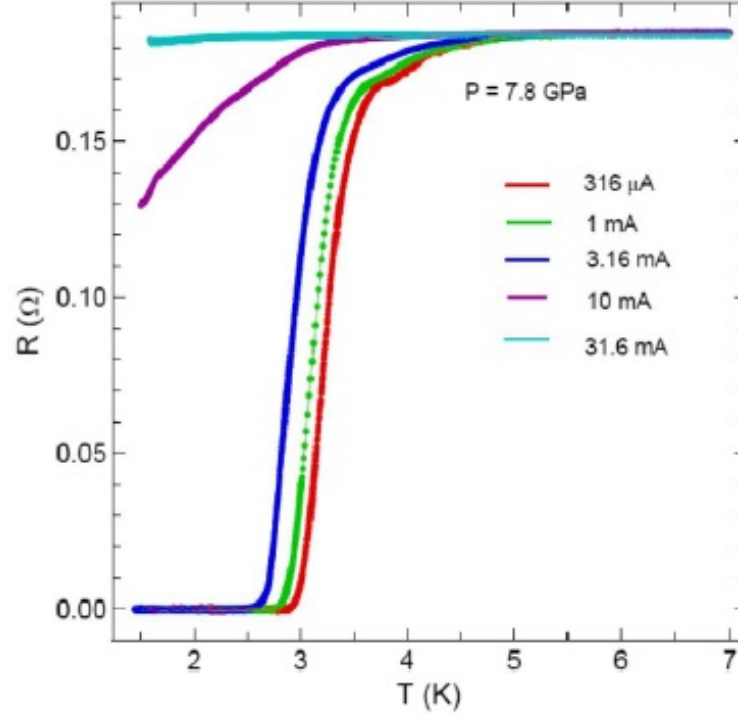


Figure 3.12: Excitation (current) dependence of SC  $T_c$  of the pressurized sample (7.8 GPa).

Now we present  $R(T)$  under nonhydrostatic compression. Here a thin single crystal  $\text{TiTe}_2$  is placed onto the insulated gasket (without drilling a hole), without a pressure medium. Figure 3.13 shows in-plane  $R(T)$  under various compressive pressures and upon decompression. At a small nonhydrostatic  $P$  ( $\sim 1.8$  GPa), the ambient semimetallic  $R$  changes abruptly into a broad humplike  $R$ - $T$  curve with overall  $R$  increased by two orders of magnitude [Fig.3.13(a)]. With increasing  $P$ , the overall  $R$  systematically decreases, but retains the hump feature up to 6.2 GPa. The hysteresis in the cooling and heating cycle of the  $R$ - $T$  curve (shown for 6.2 GPa data) evidences the first-order transition, as observed in the  $1T$ - $\text{TaS}_2$  quasicommensurate charge density wave ordered state having phase-separated domain structures [204]. We believe the CDW like ordering temperature is above room temperature. The

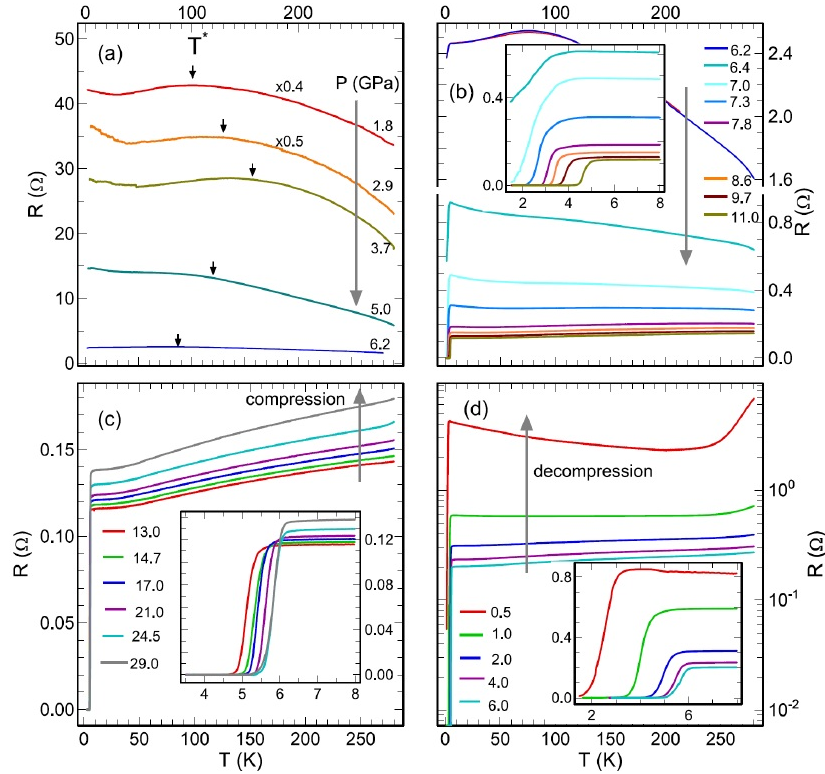


Figure 3.13: Temperature-dependent in-plane resistance of  $1T$ - $\text{TiTe}_2$  single crystal under (a)-(c) various nonhydrostatic compression up to 29 GPa and (d) decompression pressures. Insets in respective panels show magnified R-T data near superconducting transitions at various pressures.

observed low-T resistance upturn below 40 K also gets suppressed along with the hump, indicating superstructure-related localization being its origin. The broad R hump moves to higher T (as shown by its characteristic temperature  $T^*$ ) as P increases to 3.7 GPa. Above this pressure,  $T^*$  decreases before the feature gets unresolved above 6.4 GPa, while the unconventional metallic behavior ( $dR/dT < 0$ ) persists up to  $\sim 8.6$  GPa [Fig.3.13(b)]. A sharp resistance drop indicating SC onset is observed at 6.2 GPa, although a complete zero resistance is seen only above 7 GPa.  $T_c$  increases with increasing pressure at the same rate of hydrostatic compression. At higher P the system enters into conventional metallic regime (with  $dR/dT > 0$ ), also exhibiting SC up to the highest P (29 GPa) of this measurement. Above 12 GPa,  $T_c$  continues to increase only with marginal positive slope  $dT_c/dP \sim 0.06$  K/GPa [Fig.3.13(c)].

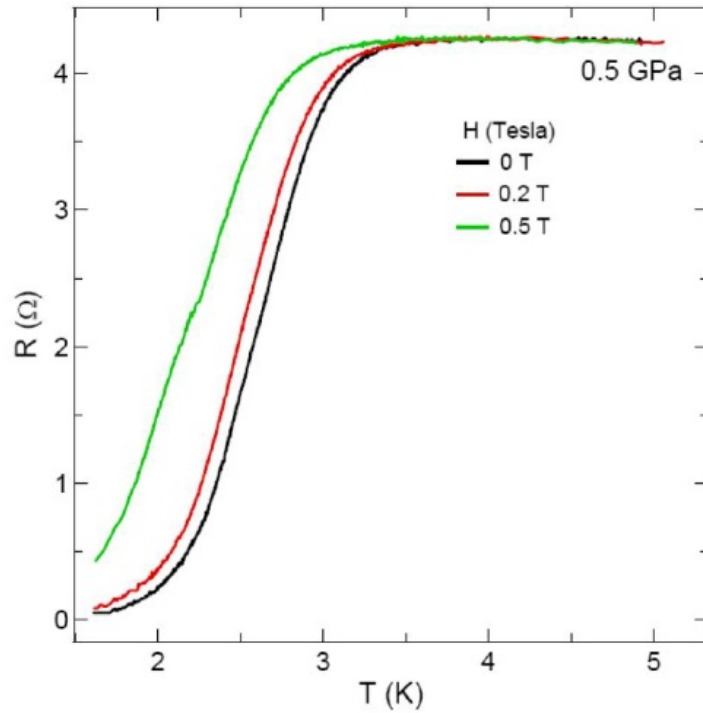


Figure 3.14: Field dependence of the resistance drop near SC transition of the pressure released sample (0.5 GPa) from uniaxially compressed to 29 GPa.

While releasing nonhydrostatic pressure, the normal metallic  $R(T)$  is maintained down to 2 GPa and much to our surprise, the sharp SC transition is found to persist down to the lowest pressure (0.5 GPa), till the Pt lead remains in good pressure contacts with the sample [Fig. 3.13(d)]. Below 2 GPa, the normal state resistance above  $T_c$  displays unconventional metallic behavior, as was observed at 7 GPa during compression. At 0.5 GPa, SC onset  $T_c \sim 3.2$  K and zero resistance is achieved at 1.6 K. Systematic lifting of this resistance drop under applied magnetic field further confirms the SC transition [Fig.(3.14)]. The irreversible nature and enhancement of  $T_c$  under decompression have recently been reported on layered chalcogenide compound  $\text{In}_2\text{Se}_3$  [227]. This was attributed to the quenchable high-P phase (that hosts SC) as a result of 2D to 3D structural crossover, but eventually SC vanishes below 10 GPa as the system returns to the low-P phase. We report here that  $1T\text{-TiTe}_2$  is the first compound to show the persistence nature of SC even after almost complete release of pressure. In quasihydrostatic decompression, SC vanishes below

5 GPa. Therefore the persistence nature of SC in  $1T$ - $\text{TiTe}_2$  can be attributed to structural irreversibility resulting from the nonhydrostatic compression.

### 3.3.3 High Pressure X-ray Diffraction under non-hydrostatic compression:

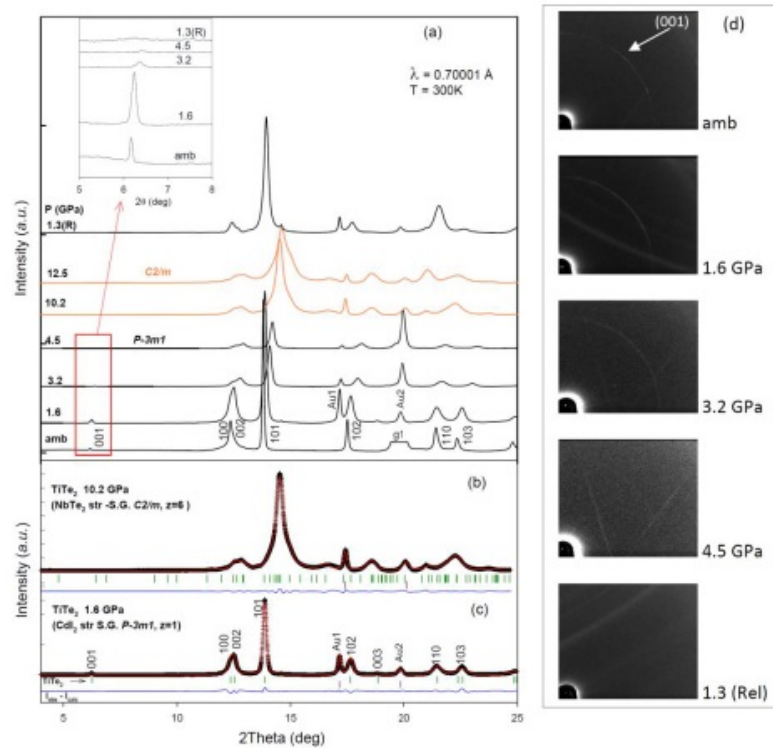


Figure 3.15: (a) Angle dispersive x-ray powder diffraction of  $1T$ - $\text{TiTe}_2$  at some selected pressures at  $T = 300$  K. A clear structural phase transition takes place above 10.2 GPa where additional peaks appear in the diffraction data. (c) Rietveld profile fitted XRD pattern of  $\text{TiTe}_2$  in its trigonal phase (space group  $P\bar{3}m1$ ) at 1.6 GPa and (b) Le-Bail profile fitted pattern in the  $\text{NbTe}_2$  structured monoclinic phase (space group  $C2/m$ ,  $z=6$ ) at 10.2 GPa. The black crosses are background subtracted data points, the red line represents the fitted pattern, green tick marks are the calculated Bragg reflections and the residuals are shown by the blue line. Inset, the (001) peak intensity of the trigonal phase gets suppressed irreversibly above 4.5 GPa, which can be visibly observable in image pattern too, shown in (d)

Powder diffraction patterns at various non-hydrostatic pressure conditions are shown in Fig. 3.15. The room temperature trigonal  $\text{CdI}_2$ -type phase, which is identified by the single sharp Bragg peak at  $13.7^\circ$ , is found to be stable up to  $\sim 10$  GPa, above which this peak starts broadening with emergence of shoulder peaks on

both sides. This indicates a structural transition into a low symmetry phase. From the group-subgroup analysis, the new phase can be indexed as of NbTe<sub>2</sub> structured monoclinic phase (space group C2/m, z=6), due to distortion in the Te-Ti-Te layer, making it of zigzag pattern (see Fig.3.16(a), (b)). In this structure, consecutive Ti1 sites octahedra are compressed in the direction perpendicular to layer plane while Ti2 sites have regular octahedra. A significant volume drop indicates first order nature of this structural transition. The structural parameters of both the phases are given in Table 3.1.

Pressure	Space Group	Lattice parameters (Å)	Atomic coordinates	Ti-Te	Ti-Te-Ti Angle (°)	Ti-Te-Ti Layer thickness (2zc) Å
1 bar	P $\bar{3}$ m1 (Z = 1)	a=b=3.7677(4) c = 6.4983 (9)	Ti: 1a(0,0,0) Te: 2d1/3,2/3,z z = 0.255(1) Rietveld fit merit $\chi^2 = 0.161$ $R_p = 0.046$ $^wR_p = 0.067$	2.735(4)	87.087(15)	3.314(5)
10.2 GPa	C2/m z = 6	a = 12.965(15) b = 3.7017(6) c = 8.7135 (5) $\gamma = 105.75 (5)^\circ$	Ti1:2a(0,0,0) Ti2:4i(0.36,0,0.709) Te1:4i(0.969,0,0.69) Te2:4i(0.703,0,0.621) Te3:4i(0.35,0,0.99) Le-Bail fit merit $\chi^2 = 0.21$ $R_p = 0.19$ $^wR_p = 0.287$			zig-zag layer 3.153-3.262(12)

Table 3.1: Lattice parameters and internal coordinates of TiTe<sub>2</sub> phases obtained from non-hydrostatic pressure studies

Now, in the stability range of the trigonal phase, we see systematic change of the (001) Bragg peak intensity. Up to  $\sim 2$  GPa, this peak intensity increases and then it decreases monotonically before it vanishes irreversibly above 5 GPa. As the trigonal structure has one free coordinate (zTe) and we have phase pure diffraction patterns, this motivated us to perform Rietveld refinement analysis for detailed structural evolution. Fig.3.16 (c) shows the variation of volume per formula unit

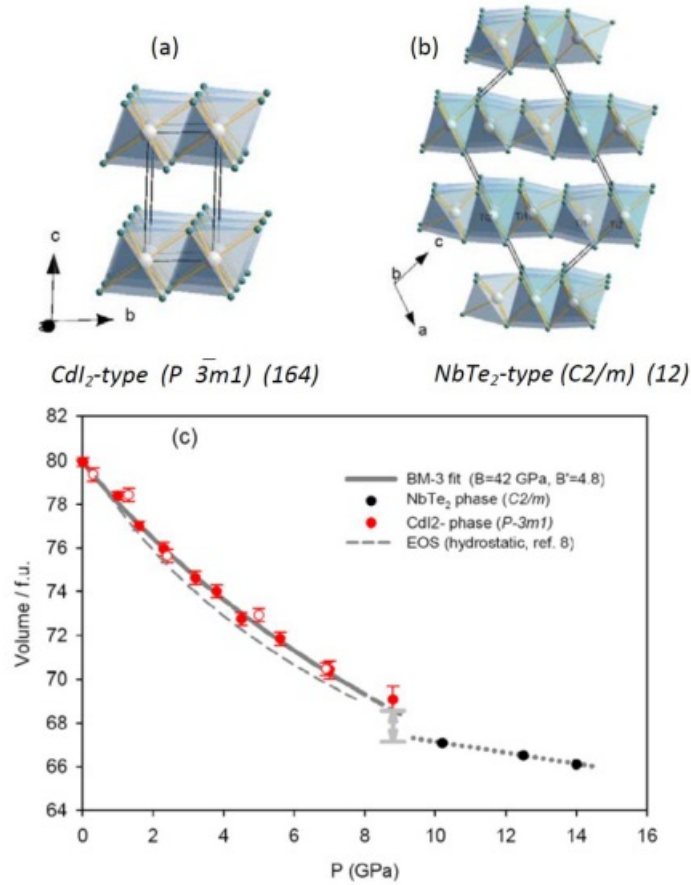


Figure 3.16: TiTe<sub>2</sub> in its (a) trigonal (CdI<sub>2</sub>-type)  $P\bar{3}m1$  space group at 1 bar and (b) monoclinic (NbTe<sub>2</sub>-type)  $C2/m$  space group at 10.2 GPa. The Ti atoms are represented by silver spheres, Te atoms are represented by green spheres. (c) Volume per formula unit as plotted as a function of pressure, open circles are during decompression; dashed line is the EOS found in hydrostatic case (obtained from ref. [187]).

as a function of pressure. The data up to 8 GPa when fitted with 3rd order Birch-Murnaghan EOS, gives  $B = 420.8$  GPa, with  $B' = 4.8 \pm 0.5$ . For comparison, we have plotted the EOS found in case of hydrostatic compression ( $B = 28.60$  GPa and  $B' = 7.19$ , ref. [187]), where  $B'$  indicates soft nature of the solid. In non-hydrostatic case,  $B'$  is like that of a relatively hard solid (sample becomes rather stiff) agreeing with the observed rather high  $B$  value. However, the bulk compressibility at higher  $P$  (depend on both  $B$  and  $B'$ ) is only "slightly" less in non-hydrostatic case. This becomes apparent when non-hydrostatic  $V(P)$  are fitted with  $B' = 7.19$  (fixed as in hydrostatic), we get  $B = 30.21.8$  GPa (slightly less compressible than hydrostatic),

but the fitting is worse as seen in large fitting error. This further confirms that the microscopic compression mechanism is different in two cases, as apparent from irreversible Van-der Waal spacing change above 4 GPa.

More interestingly, the  $c/a$  ratio is found to deviate strongly above 5 GPa in non-hydrostatic compression (Fig.3.17(a)). Under hydrostatic compression [187], above this  $P$  the compression becomes almost isotropic ( $c/a$  ratio  $P$ -independent) whereas, in non-hydrostatic compression  $c/a$  ratio continues to decrease till the structural transition. However, in both cases the structural transition occurs at nearly same pressure ( $\sim 10$  GPa).

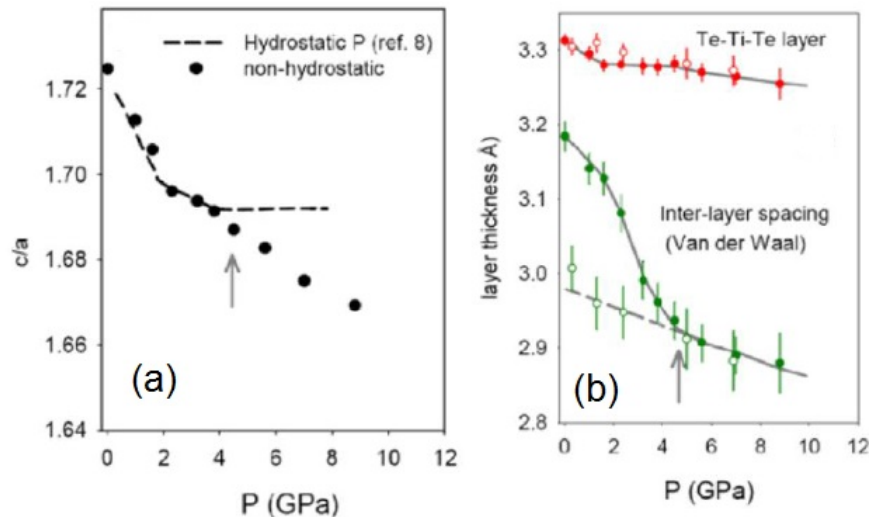


Figure 3.17: (a)  $c/a$  ratio as a function of pressure; dashed line is from hydrostatic pressure study (ref. [187]) (b) Te-Ti-Te layer and interlayer thickness variation as a function of pressure.

Hydrostatic data being not from single phase [187], demands further work to find the high pressure structure. From the refined positional coordinates of Te, we have tried to look the structural parameters that can correlate our resistance data. We have looked at the pressure dependence of the Te-Ti-Te covalent layer and the interlayer Van der Waal gap (Fig.3.17(b)). We find that the covalent layer thickness systematically decreases with small signatures of anomaly at 2 GPa and 5 GPa. But, the interlayer Van der Waal spacing shows prominent change in compression

behavior at these pressures and also the irreversible behavior (open circles), clearly indicates change in bond characteristics, might be a change from quasi-2D to 3D networking (as indicated in ref. [187]).

The results are summarized in the novel phase diagram of  $1T$ -TiTe<sub>2</sub> under non-hydrostatic compressions (Fig.(3.18)). Although apparently the semimetallic state disappears above 1.8 GPa, a similar  $P$  variation of  $T_c$  as in the hydrostatic case suggests SC originating from the same semimetallic microstructure. Due to highly anisotropic axial compressibility, a drastic reduction in van der Waal interlayer spacing is observed, which probably helps CDW-like superstructures formation (having interdomain semimetallic undeformed regions) [197]. However, at elevated pressure the system becomes more isotropic, resulting in reduced deviatoric stress and so the CDW-like domains (or its coherence length) shrink in size and the semimetallic regions grow, responsible for the emergence of SC. A slightly higher critical pressure (6.2 GPa), compared to hydrostatic compression (where bulk semimetallic regions are present completely) further supports this explanation. This result is in disagreement with the real-space coexistence of CDW and SC as reported in  $1T$ -TaS<sub>2</sub> [202, 206]. However, we cannot rule out the possibility of SC emerging from any hidden incommensurate CDW instability [201, 207] that may be present in semimetallic state, which demands high-resolution structural investigation on the single crystal. The observed BCS nature of SC also hints at an enhanced electron-phonon coupling being the dominant mechanism for the formation of the CDW-like state. The slope change in SC  $T_c$  near 12 GPa can be associated with the structural transition to the NbTe<sub>2</sub>-structured high-pressure phase [197], but demands a structural study below  $T_c$  for better understanding.

At much higher compression (for  $P > 12$  GPa), the layered structure evolves into a 3D network (making Te-Te bonding between Te-Ti-Te layers) in an irreversible manner (as evidenced from reduced vdW gap at pressure release below 5 GPa), and

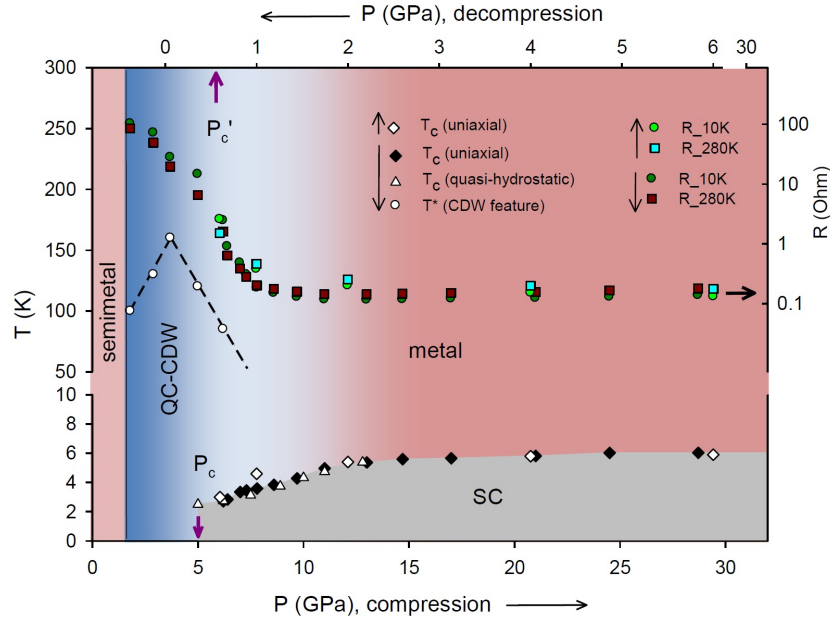


Figure 3.18: The phase diagram for 1T-TiTe<sub>2</sub> under nonhydrostatic compression (bottom pressures) and decompression (top pressures). Resistances at 10 and 280 K have been plotted on logarithmic scale (labels on the right axis, arrows in legends indicate corresponding scale). Top decompression pressure scale has been adjusted in order to match the T<sub>c</sub>'s and resistance values roughly with that of compression. P<sub>c</sub> denotes onset pressure and zero resistance SC has been observed at P/c upon decompression.

so modifies the density of states at Fermi energy and phonon dispersion. The enhanced metallic character of the 3D network is maintained down to 2 GPa, where the T<sub>c</sub> and resistance values are as per the extrapolated values from that above 12 GPa. Below 2 GPa, enhanced resistance in unconventional metallic regime and decrease of T<sub>c</sub> indicate the existence of SC with re-emergence of weak CDW-like order. Our electron diffraction study on this retrieved sample shows additional superstructure spots [Fig.(3.19)], evidencing possible CDW ordered phase at room temperature. As the SC volume fraction could not be measured on the retrieved sample, the filamentary nature of the recovered superconductivity cannot be ruled out. Further experiments on the pressure-released sample and theoretical calculations are required to fully understand the persistence nature of the superconductivity and reemergent CDW-like resistance anomaly Fig.(3.19).

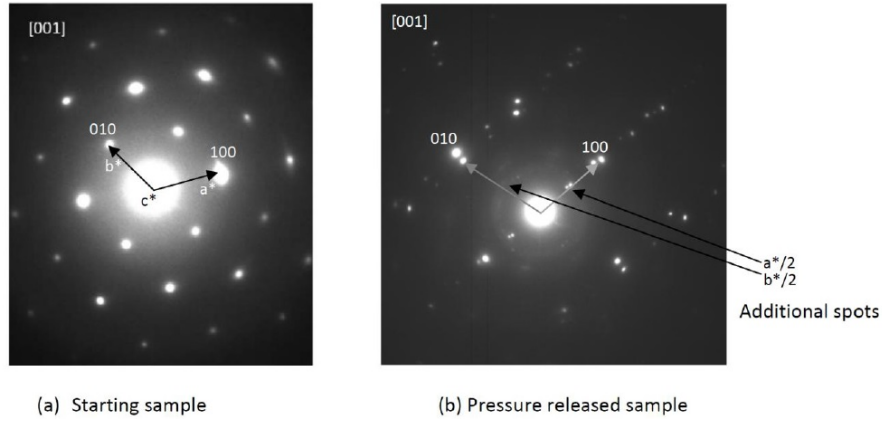


Figure 3.19: [001] zone axis LEED pattern of (a) the starting sample and (b) pressure released sample

### 3.3.4 Infrared spectroscopic measurements in single crystalline $1T$ - $\text{TiTe}_2$ under pressure

Pristine  $1T$ - $\text{TiTe}_2$  single crystals in this study are from the same batch of our transport measurements and were grown by a conventional vapor transport method (with iodine as the transport agent) [239]. Fig.3.20(a) shows the variation of superconducting  $T_c$  as a function of pressure where the persistence of superconductivity (with enhanced  $T_c$ ) is observed upon decompression. To understand this exotic pressure dependence, we have performed detailed high-pressure x-ray diffraction measurements (see the supplementary material of Ref. [239]). High-quality x-ray diffraction patterns are obtained up to a pressure of  $\sim 9$  GPa (beyond which Bragg peaks get significantly broadened due to structural disorder), and structural evolution was analyzed by Rietveld refinement using GSAS software [241]. Although the trigonal structure was found to be stable up to  $\sim 10$  GPa, the interlayer (van der Waal) spacing is found to decrease rapidly above  $\sim 2.5$  GPa in an irreversible manner [Fig.3.20(b)]. For a better understanding of the low-pressure structural modification, we have now performed detailed infrared spectroscopic measurements in both far-IR and mid-IR ranges.

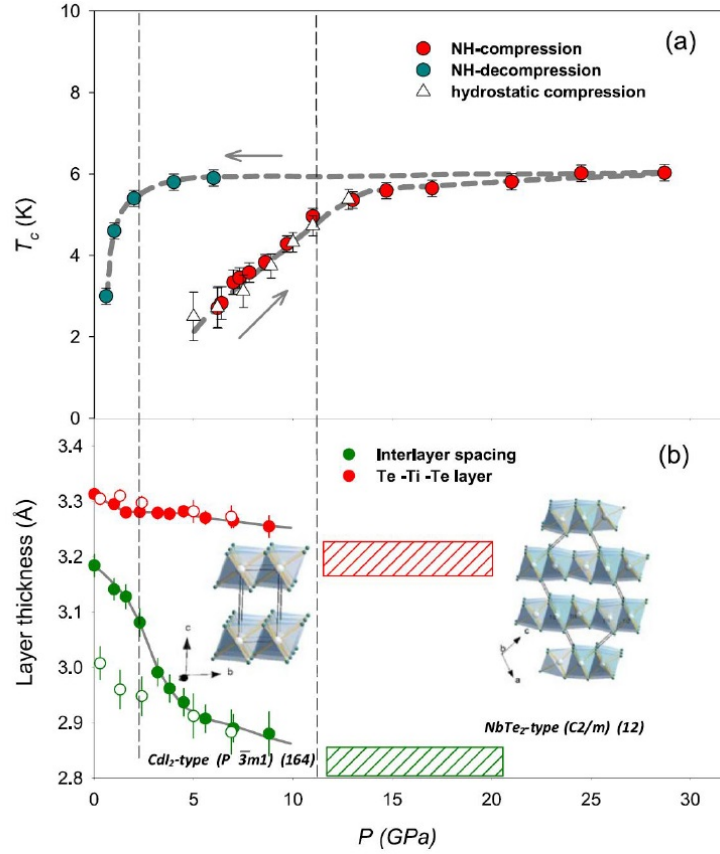


Figure 3.20: (a) Superconducting transition temperature ( $T_c$ ) variation of  $TiTe_2$  under various compression and decompression pressures. (b) Te-Ti-Te layer and interlayer thickness variation as a function of pressure, as determined from Rietveld refinement of x-ray diffraction patterns. Hatched regions denote the respective average layer thickness in the high-pressure monoclinic structure. The anomalous change in interlayer spacing at  $\sim 2.5$  GPa and the structural transition at 11 GPa are marked by vertical dashed lines.

### Far-IR studies under high pressure

Group-theoretical analysis of  $1T'$ - $TiTe_2$  predicts nine vibrational modes at the point of the Brillouin zone, represented by  $\Gamma = A_{1g} + E_g(2) + 2A_{2u} + 2E_u(2)$ . The  $A_{1g}$  and  $E_g$  modes are Raman-active with corresponding frequencies  $\sim 141$  and  $\sim 105/120$   $cm^{-1}$ , respectively. Contradictory frequency assignments of the  $E_g$  modes have been reported primarily due to the presence of a disorder-induced mode [187,213,236,246]. High-pressure Raman measurements show phase stability up to 8 GPa. However, the emergence of a tiny peak in Raman spectra has been ascribed as an IR mode due to inversion symmetry breaking as the system enters the topologically nontrivial

phase [236], which makes it necessary to study further the IR-active phonon modes under pressure. Although no IR phonon spectra of  $1T$ -TiTe<sub>2</sub> have been reported so far, several other isostructural layered dichalcogenides have been studied by IR spectroscopic measurements in connection with charge density wave transitions [195, 247–249].

In Fig.3.21(a) we show the IR reflectance at the diamond-sample interface at 1 GPa in the frequency range 120-10,000 cm<sup>-1</sup>. Also shown in this figure are the fitted reflectance spectra using the Drude-Lorentz oscillator model (shown in orange). The calculated reflectance is given by  $R_{s-d} = |(\sqrt{\epsilon} - n_d)/(\sqrt{\epsilon} + n_d)|^2$ , where the complex dielectric constant of the sample  $\epsilon = \epsilon_1 + i\epsilon_2$  can be expressed as a sum of Drude and Lorentz oscillators:

$$\epsilon(\omega) = \epsilon_\infty - \frac{\omega_p^2}{\omega^2 + i\omega/\tau} + \sum \frac{S_i^2}{\omega_i^2 - \omega^2 + i\omega/\tau} \quad (3.2)$$

The reflectance spectra at 1 GPa are fitted well with two zero-frequency oscillators (Drude feature), and several high energy broad Lorentz oscillators. A better fit of the reflectance spectra with double Drude peaks (with different broadening) is achieved due to dramatically different scattering rates of two types of carriers in semimetallic TiTe<sub>2</sub> [249, 250]. Comparing the band masses of Te  $5p$  holes (light) and Ti  $3d$  electrons (heavy), the broad Drude peak (width  $\sim 1200$  cm<sup>-1</sup>) is assigned to holes, and the narrow Drude peak (width  $\sim 180$  cm<sup>-1</sup>) to electrons [174].

In Fig.3.21(b) are shown the far-IR reflectance spectra at several increased pressures at room temperature. The oscillatory feature at 220 cm<sup>-1</sup> (as shown by the red vertical line) matches very well with the calculated frequency of the Eu phonon mode of  $1T$ -TiTe<sub>2</sub> [126]. The A<sub>2u</sub> mode that is expected at higher frequency has not been detected in this unpolarized measurement possibly because of its weak intensity and increased noise in this frequency range. At 2.3 GPa, a new mode starts appearing at  $\sim 250$  cm<sup>-1</sup>. As this mode appears only at higher pressure, the

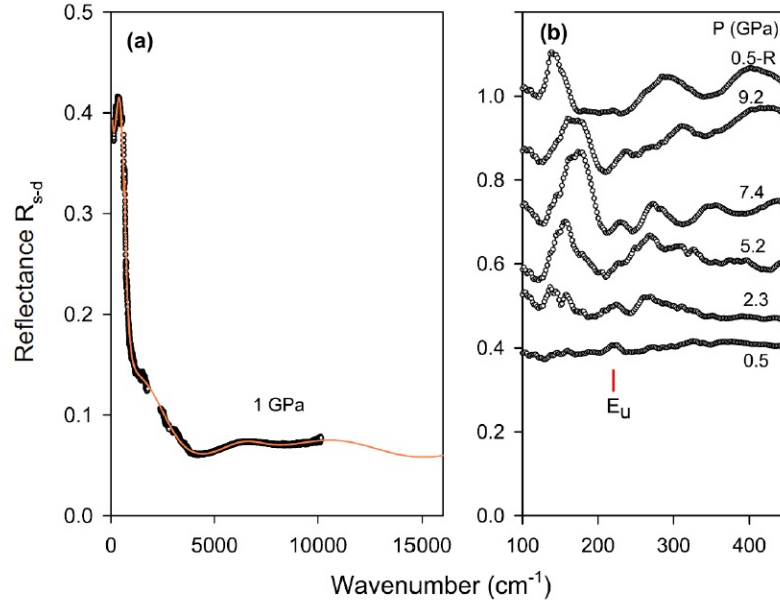


Figure 3.21: (a) Room-temperature IR reflectance spectra at the diamond-sample interface  $R_{s-d}(\omega)$  for  $1T$ - $\text{TiTe}_2$  at 1 GPa. Open circles are the experimental data, and the orange solid line is the calculated reflectance spectra using Drude-Lorentz oscillators (shown up to  $16\,000\text{ cm}^{-1}$ ). (b) Room-temperature far-IR  $R_{s-d}(\omega)$  spectra at various high pressures. Spectra at higher pressures are arbitrarily shifted. R represents the released pressure.

possibility of this mode being an  $A_{2u}$  mode may be ruled out. Also, the emergence of a single peak at this frequency further rules out the possibility of superlattice formation due to CDW-like transition. This can thus be associated with the structural modification, as supported by the rapid decrease of interlayer spacing at this pressure. At 2.3 GPa, additional sharp phononic reflectance features start appearing below  $200\text{ cm}^{-1}$ , suggesting the appearance of additional IR phonon modes. These modes gain intensity at higher pressures. Above 7.4 GPa, a broad spectral modulation emerges as a result of enhanced transmission through the sample, indicating a possible pressure-driven change in low energy charge dynamics [65], as discussed in the next section.

Fig.3.22 shows the KK transformed frequency dependence of the imaginary part of the dielectric response from the measured far-IR reflectance spectra at various high pressures and also at low temperatures (100, 150, 200, and 300 K). At the

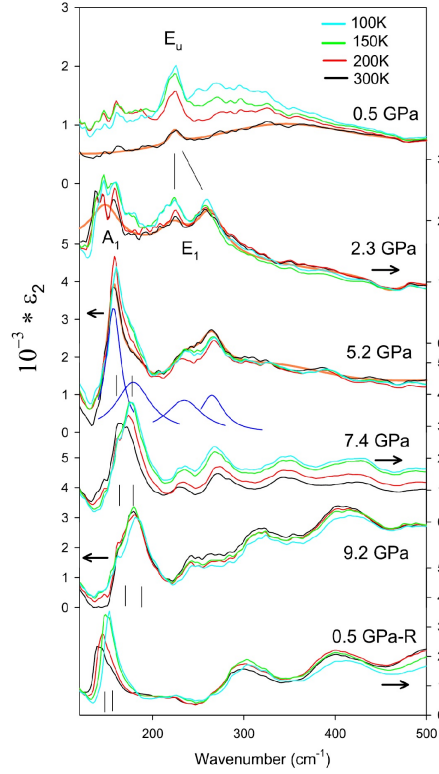


Figure 3.22: Imaginary part of dielectric response (as derived from reflectance spectra using KK transformation; see the text) for  $1T$ - $\text{TiTe}_2$ , at various high pressures and at low temperatures. Room-temperature spectra at 0.5, 2.3, and 5.2 GPa have been fitted with Lorentzian peaks. The decomposed phonon peaks are shown in blue for spectra at 5.2 GPa (fit shown in orange).  $E_u$  corresponds to the IR phonon mode from centrosymmetric ambient structure ( $P\bar{3}m1$ ), whereas  $E_1$  and  $A_1$  modes represent phonon modes of the high-pressure noncentrosymmetric structure ( $P3m1$ ). Doublets represent two inequivalent Te sites of the high-pressure phase. R represents the released pressure.

lowest pressure (0.5 GPa), the  $E_u$  IR-active phonon mode is clearly seen at  $\sim 220$   $\text{cm}^{-1}$ . Upon lowering the temperature to 100 K, this mode becomes sharper and its intensity increases. At a pressure of 2.3 GPa, we observe the clear emergence of new modes. The mode at  $250$   $\text{cm}^{-1}$  can be assigned as the splitting of the  $E_u$  mode, indicating two distinct Ti-Te bond lengths in the unit cell. This can be attributed to a subtle structural transition, which has not been detected by our x-ray power diffraction measurement [239]. The newly emerged low-frequency mode near  $140$   $\text{cm}^{-1}$  matches very well with the strong  $A_{1g}$  Raman mode [187, 246]. The appearance of sharp Raman modes in IR spectra is a clear signature of the loss of

inversion symmetry in its crystal structure. As no additional Bragg peak is seen in our high-resolution x-ray powder diffraction pattern, we can only assign this subtle structural modification as the inversion symmetry breaking type of structural transition ( $P\bar{3}m1$ - $P3m1$ ) that maintains the lattice structure, but breaks the trigonal symmetry of the Te position. A small change in Bragg peak intensity associated with the Te site change is beyond the detection limit in our XRD analysis [239], and therefore an accurate determination of two Te coordinates (1b and 1c Wyckoff positions) has not been attempted. For that, a more rigorous high-pressure mode at  $250\text{ cm}^{-1}$  can be assigned as the splitting of the Eu mode, indicating two distinct Ti-Te bond-length in the unit cell. This can be attributed to a subtle structural transition, that has not been detected by our x-ray powder diffraction measurement.<sup>25</sup> The newly emerged low frequency mode near  $140\text{ cm}^{-1}$  matches very well with the strong  $A_{1g}$  Raman mode [187, 246]. The appearance of sharp Raman modes in IR spectra is the clear signature of loss of inversion symmetry in its crystal structure. As no additional Bragg peak is seen in our high resolution x-ray powder diffraction pattern, we can only assign this subtle structural modification as the inversion symmetry breaking type of structural transition ( $P\bar{3}m1$ - $P3m1$ ) that maintains the lattice structure, but breaks the trigonal symmetry of the Te position. Small change in Bragg peak intensity associated with the Te site change is beyond the detection limit in our XRD analysis <sup>25</sup> and therefore accurate determination of two Te coordinates (1b and 1c Wyckoff positions) has not been attempted. For that, a more rigorous high pressure single crystal XRD measurement is thus recommended. According to the new space group, all nine zone-center modes ( $\Gamma = 3A_1 + 3E_1(2)$ ) are both Raman and IR active. The two  $E_1$  modes count for four modes and the doublet structure near  $140\text{ cm}^{-1}$  represents  $A_1$  modes corresponding to two Te sites. While the  $A_{2u}$  mode being very weak in the low P structure, remains undetected also at higher pressures, the Ti  $E_1$  mode (a reminiscent of Raman  $E_g$  mode) is expected at

further lower frequency than our present measurement range. With further increasing pressure, the frequency of the new modes increases agreeing with the reported pressure dependence of Raman modes. These modes gather intensity at higher pressures with systematic peak broadening. No further phonon spectral change is noticed up to 9.2 GPa. In the reported high pressure Raman measurement [187] the doublet feature due to this subtle structural transition is obscured possibly because of peak broadening (also note that defect induced Raman band must be absent in this IR spectra). The spectra remain almost unchanged with lowering temperature, indicating no clear signature of any superlattice formation due to anticipated long range CDW order under non-hydrostatic compression [239]. The reason may be the quasi-hydrostatic condition in the present study due to use of CsI as pressure medium. Upon release of pressure the new modes of the structural modification are retained down to 0.5 GPa, indicating irreversible nature of the inversion symmetry breaking structural transition at 2.3 GPa.

### Mid-IR studies under high pressure

To understand the associated change in electronic band structure and low energy charge dynamics, we have investigated mid-IR reflectance of  $\text{TiTe}_2$  under various quasi-hydrostatic pressures. Fig. 3.23(a) shows the mid-IR reflectance at the sample-diamond interface at room temperature up to 22 GPa. The local minima at  $1000 \text{ cm}^{-1}$  is identified as the screened plasma frequency ( $\omega_{sp}$ ) which remains mostly unchanged up to the highest pressure of this measurement. However, the overall reflectance increases systematically upon increasing pressure, indicating increased metallic character at high pressure agreeing with our reported transport measurements [187, 239]. Sharp two-phonon diamond absorption in the spectral range  $1800\text{-}2300 \text{ cm}^{-1}$  has been cut out and replaced by linear interpolation. Fig. 3.23(b) shows the real part of the optical conductivity (OC) in the spectral range

600-10000  $\text{cm}^{-1}$ , as obtained by the KK transformation of the reflectance spectra. For this purpose, the measured reflectance is fitted by Drude-Lorentz model (as shown in Fig 3.21a) and the reflectance is extrapolated beyond the measured range (covering the spectral range 10-50000  $\text{cm}^{-1}$ ). For the high frequency region, a broad high energy Lorentz oscillator has been used with peak position at 24000  $\text{cm}^{-1}$  (3 eV). In absence of the measured reflectance in the high frequency range under pressure, we get reliable KK transformed optical conductivity spectra as this high energy interband transition comes from higher lying Ti eg bands having a negligible pressure dependence (discussed later). Thus obtained OC is further analyzed by independent DL fit, and the obtained oscillators are found to agree well with those from reflectance fit, which further confirms the reliability of our KK analysis. The low-frequency OC spectra change rapidly by gaining spectral weight with increasing pressure. Across the pressure range 2.1-3.8 GPa, a significant transfer of spectral weight from the high-frequency to the low-frequency region across 7500  $\text{cm}^{-1}$  is noticed, which can be associated with the structural transition at this pressure, as discussed above.

By first inspecting the spectra at various low pressures [Fig. 3.24(a)], we observe three broad peaks at  $\sim 2000$ , 5500, and 9000  $\text{cm}^{-1}$ , marked as  $\alpha$ ,  $\beta$ , and  $\gamma$ , respectively, above the Drude contribution. At the lowest pressure (1 GPa), the spectral weight of the  $\alpha$  peak is rather weak. This peak can be identified as the pseudogap feature observed in many 2D correlated metals [244, 251–253], whose origin has been argued in terms of the emergence of short-range charge density wave (CDW) fluctuation, a precursor of CDW transition. However, such low-energy bands in WTe<sub>2</sub> and NbP have alternatively been explained in terms of interband transitions between spin-orbit-split parallel bands near the Fermi level [83, 250]. At higher pressure (1.5 GPa), the plasma frequency is redshifted with the narrowing of the Drude part with simultaneous enhancement of this peak intensity, indicating spectral weight transfer

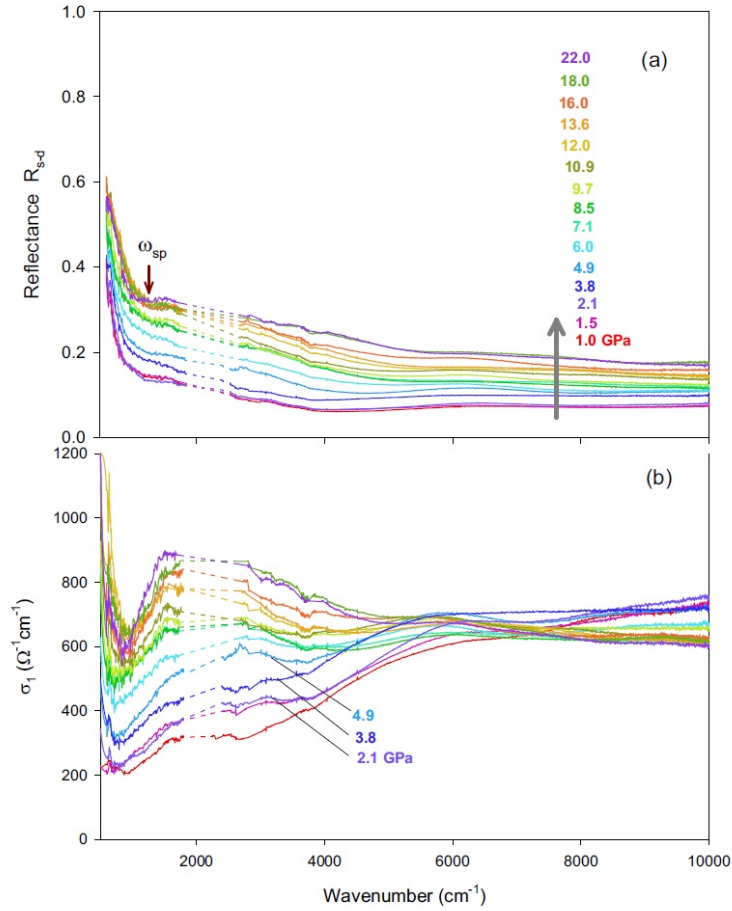


Figure 3.23: Reflectance  $R_{s-d}$  at the sample-diamond interface at various increasing pressures up to 22 GPa.  $\omega_{sp}$  indicates the screen plasma frequency. (b) Calculated real part of optical conductivity  $\sigma_1(\omega)$  at various pressures. The same color code has been used in both panels for each pressure.

from the Drude region to this peak. A sudden loss of free carrier in gaining this peak thus supports the former explanation of the excitonic correlation origin of this peak. Also, the presence of this peak at all pressures, and its pressure-independent peak energy, rule out its origin from interband transition in Weyl-type electronic structure [237,238].

The high-frequency bands ( $\beta$  and  $\gamma$ ) can be understood as the electronic interband transitions as depicted in Fig. 3.24(b). Band-structure calculations show that Te  $5p$  valence bands cross the Fermi level at  $\Gamma$  and A points forming cylindrical hole pockets, and the Ti  $3d(d_z^2)$  conduction band crosses at L and M points

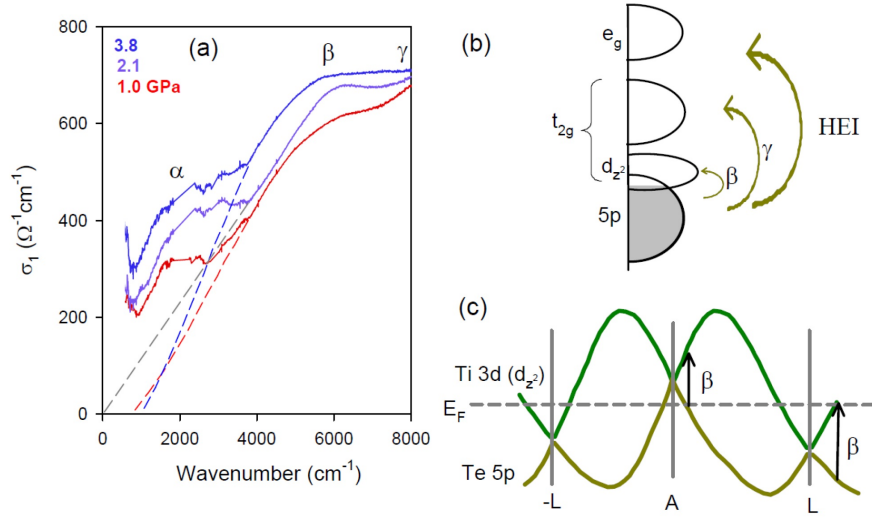


Figure 3.24: (Color online) (a) Re Optical conductivity  $\sigma_1(\omega)$  at various low pressures up to 3.8 GPa. (b) A schematic illustration of the electronic states near Fermi level in  $1T$ - $\text{TiTe}_2$  structure. The Drude part as well as the band originate from the intraband transition and correlation effects, whereas the MIR bands ( $\alpha$  and  $\beta$ ) and an high energy band HEI arise due to various interband transitions. (c) Sketch of band structure along L-A-L symmetry line of the Brillouin zone with the Fermi level in dashed line

forming electron pockets [174]. The mid-IR  $\beta$  band arises from the interband transitions between these bands, whereas the  $\gamma$  band can be thought of as an interband transition between 5p valence bands and other 3d  $t_{2g}$  bands, split off from  $d_z^2$  by trigonal distortion. The higher-lying 3d  $e_g$  bands (centered at  $\sim 3$  eV) give rise to an additional highenergy interband transition. A schematic band dispersion close to the Fermi level along the L-A-L symmetry line of the BZ is shown in Fig. 3.24 (c). As pressure-induced band inversion at A and/or L point has been theoretically predicted in the trigonal phase [72, 236], possibilities of linear band crossing near these points have been illustrated at moderate high pressures. The broken inversion symmetry above 2 GPa (as already discussed) in the presence of strong spin-orbit interaction thus may turn this compound as Weyl semimetal, with Weyl nodes being above Fermi level near A point and/or below Fermi level near L point. As the optical signature of the Weyl semimetal is the linear frequency dependence of optical conductivity spectra, we can expect such ( $\sigma(\omega) \propto \omega$ ) dependence for the band.

A clear transition from sublinear to linear ( $\sigma(\omega)$ ) in the frequency range 3600-5700  $\text{cm}^{-1}$  of the band has indeed been noticed at 2.1 GPa (see Fig. 3.24 (a)), speculating a possible transition from a gapped semimetal to Weyl semimetal at this pressure. The low frequency region is however obscured by the intraband transition ( $\alpha$  band). This linear ( $\sigma(\omega)$ ) dependence is observed only within a small pressure range. At 3.8 GPa linear ( $\sigma(\omega)$ ) disappears and the system enters into a gapped semimetallic state. The gap value has been estimated 120 meV by extrapolating the steeply increasing part of  $\beta$ -band ( $\sigma(\omega)$ ) to zero (shown by dashed lines in Fig 3.24 (a)). Pressure-induced band gap closing-opening in BiTeI has recently been proposed as the signature of topological quantum phase transition. The subtle structural modification at 2.1 GPa thus tunes the band structure of  $\text{TiTe}_2$  (also band inversion due to topological phase transition), resulting in linear band crossing and formation of Weyl nodes.

Above 3.8 GPa, a conspicuous change of the OC spectra is noticed [Fig. 3.23(b)]. The Drude part and the  $\alpha$  band gain spectral weight systematically with increasing pressure, whereas the high-frequency spectral weight above 7500  $\text{cm}^{-1}$  (comprised of  $\gamma$  and HEI bands) decreases. In Fig.3.25(a), the KK-transformed real part of the optical conductivity at 6 GPa and its spectral analysis by Drude-Lorentz oscillator fitting are shown. For better fitting, two Drude peaks have been used (as discussed in the far-IR section). The dc conductivity at this pressure is also plotted in this figure (the error in determining resistivity from measured resistance at this pressure is also shown). In Fig. 3.25(b) we plot the spectral weight of both Drude components ( $D_1$  and  $D_2$ ) as a function of pressure. The uncertainty in  $D_2$  SW is found to be higher, possibly due to a lack of measured data in the low-frequency region.  $D_2$  spectral weight remains almost unchanged with a marginal increase at high pressure.  $D_1$  spectral weight marginally decreases up to 2.1 GPa [see Fig.3.25(b)], but at 3.8 GPa this increases drastically and then increases

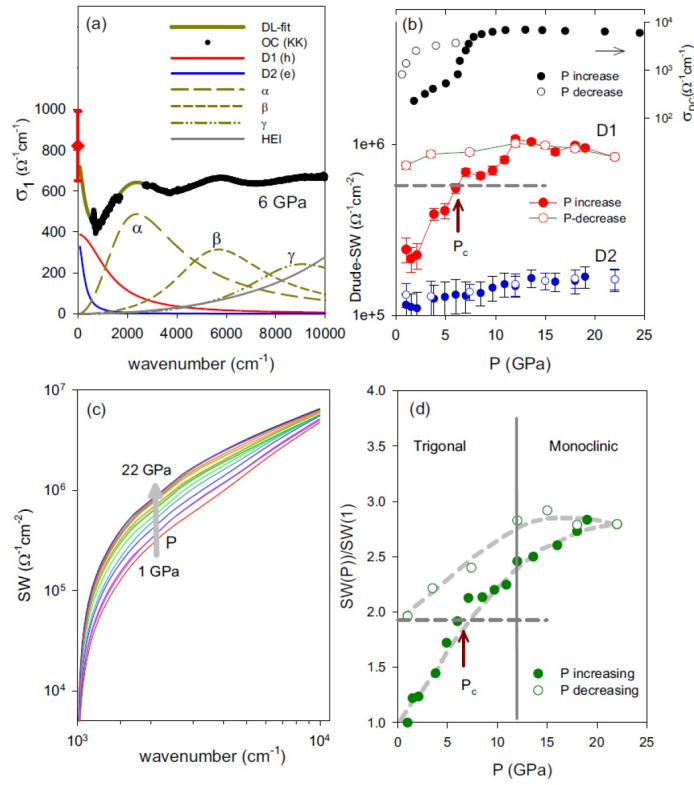


Figure 3.25: (a) Drude-Lorentz fit (thick dark yellow) of the optical conductivity (solid circle) at 6 GPa. The fit is composed of two Drude responses and several Lorentzian features. dc conductivity ( $\sigma_{dc} = 1/\rho_{dc}$ ) is also shown at  $\omega = 0$  at this pressure (red diamond). (b) Drude spectral weight of the D1 peak (hole) and the D2 peak (electron) as a function of pressure (increasing and decreasing). Room-temperature dc conductivity  $\sigma_{dc}$  has been plotted from high-pressure resistance measurement. (c) Integrated spectral weight  $\text{SW} = \int_{\Omega_0}^{\Omega} \sigma(\omega) d(\omega)$  for increasing pressures with  $\Omega_0 = 1000 \text{ cm}^{-1}$ . (d) Pressure-dependent spectral weight variation, normalized to the lowest pressure value at  $3000 \text{ cm}^{-1}$  upon compression and decompression pressures.

monotonically at even higher pressures. The rapid increase in the number of Drude carriers ( $N_{eff} \propto \text{SW}$ ) at this pressure agrees very well with our high-pressure Hall measurements [239]. The integrated spectral weight (SW) increases with pressure, but it appears to converge above  $10\,000 \text{ cm}^{-1}$  as a result of large spectral transfer from the high-energy region to the Drude response and the correlation dominated  $\alpha$  band [see Fig.3.25(c)], featuring the involvement of strong electronic correlation. The high-pressure enhanced metallic character is in good agreement with increased dc conductivity [shown in the upper panel of Fig.3.25(b)]. As superconductivity emerges at  $\sim 6 \text{ GPa}$  ( $P_c$ ) [?], the corresponding Drude SW (and thus the resulting

carrier concentration or the density of states near the Fermi level) may be considered as the threshold value (shown by the horizontal dashed line). The pressure dependence of the integrated spectral weight up to  $3000 \text{ cm}^{-1}$ , normalized with respect to the initial pressure value  $[\text{SW}(P)/\text{SW}(1)]$  [Fig. 3.25(d)], shows a systematic enhancement in the low-frequency region, with a subtle anomalous change in its pressure slope near the critical pressure  $P_c$ .

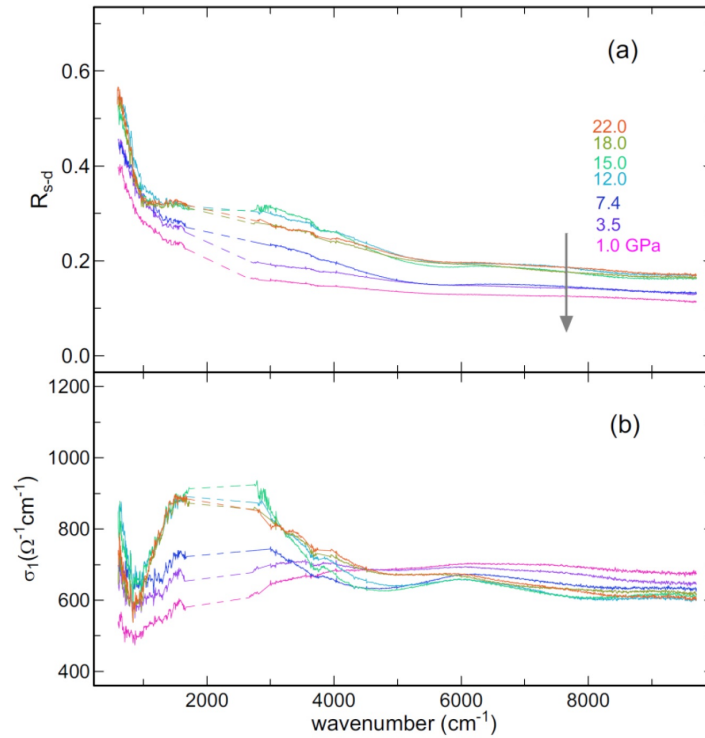


Figure 3.26: (a) Reflectance  $R_{s-d}$  at the sample-diamond interface at various decreasing pressures from 22 GPa. (b) Calculated optical conductivity  $\sigma_1(\omega)$  at various pressures.

Now we look at the spectra upon decompression from 22 GPa (Fig. 3.26). Both reflectance as well as the optical conductivity remain almost unchanged down to 12 GPa (in the high-pressure monoclinic phase). The relatively sharp feature (local minima) at screened plasma frequency in the reflectance spectra and also the narrow Drude response are apparent in this pressure range. Below this pressure, the overall reflectance starts decreasing with a featureless Drude upturn, indicating reduced metallic character. The intensity of the characteristic peak of correlated

metal at  $2000\text{ cm}^{-1}$  also reduces. However, both spectra when compared with increasing pressure cycle clearly indicate an irreversible nature upon the lowering of pressure. In Fig. 3.25(b) we have plotted the Drude SW at these released pressures (open circles). Although the D2 SW starts decreasing below 12 GPa, it remains significantly high (above the threshold value of this SW, marked by a dashed line for superconductivity to emerge) even at the lowest released pressure (1 GPa). This is consistent with the observed phonon modes upon pressure release, and thus the irreversible nature of the structural transition at 2.5 GPa. It is thus concluded that the noncentrosymmetric structure (SG: P3m1) of  $\text{TiTe}_2$  is responsible for the emergence of superconductivity with enhanced  $T_c$ , and the irreversibility of this structural transition effectively helps superconductivity to persist at the lowest released pressure [239]. The relative integrated SWs up to  $3000\text{ cm}^{-1}$  at these released pressures have also been plotted in Fig. 3.25(d). This also shows a clear irreversible pressure dependence; the SW remains mostly unchanged in the high-pressure monoclinic phase and starts decreasing below 12 GPa. The SW value at the lowest released pressure remains twice as high as its initial value. Thus enhanced electronic correlation in the system also seems pressure-quenched.

### 3.4 Conclusions:

In conclusion, pressure dependent electrical resistance measurement is carried out on polycrystalline  $\text{TiTe}_2$  up to  $\sim 16$  GPa. This results is accompanied by high pressure Raman, XRD and theoretical band structure calculations. The detailed results and discussions is reported in reference [187]. The anomalous increase in resistance near  $\sim 8.8$  GPa is associated with structural phase transition from trigonal to monoclinic structure confirmed by XRD and Raman measurements. The anomalies at  $\sim 2$  GPa and  $\sim 4$  GPa are indicated as isostructural electronic transitions which are closely

related to the theoretical predictions and hence may be due to nontrivial TQPT and trivial metallic transition, respectively [187].

In addition to that, pristine  $1T$ - $\text{TiTe}_2$  single crystals show pressure-induced SC transition above 5 GPa. Small nonhydrostatic  $P$  changes the  $T$ -dependence resistance drastically without affecting SC state, suggesting the emergence of phase separated CDW-like domains within semimetallic regions.  $T_c$  continues to increase with  $P$  with a slope change at  $\sim 12$  GPa, where the structural property is believed to change from 2D to 3D character. Upon decompression from 29 GPa, the SC state persists down to 0.5 GPa where weak CDW order reappears, establishing a novel electronic phase diagram. Pressure-quenchable SC and its large upper critical field make  $1T$ - $\text{TiTe}_2$  a promising candidate for practical application. The decompression-driven observed pressure rescaling is of fundamental importance in layered SC, demanding further experimental and theoretical investigations. The present study also provides a unique opportunity to investigate a  $P$ -quenched SC sample for electronic structure by surface-sensitive techniques such as ARPES, ellipsometry, etc.

Furthermore, IR reflectance measurements have been performed on single-crystal  $1T$ - $\text{TiTe}_2$  under high pressure. Our far-IR measurements help to identify a subtle and irreversible structural transition at 2.3 GPa into a noncentrosymmetric structure (space group  $P3m1$ ). High-pressure measurements in the mid-IR spectral range help us to understand the pressure evolution of the charge dynamics (Drude part and intraband transition) and several interband transitions. At a low pressure (2 GPa),  $\sigma(\omega)$  linearity of the low frequency optical conductivity indicates possible topological phase transition from a gapped semimetal into a Weyl semimetallic state. A detailed theoretical investigation is thus warranted incorporating the above results in order to characterize the novel topological state at this pressure. Across the structural transition, a rapid spectral weight transfer from a high energy to a low-energy range across  $7500 \text{ cm}^{-1}$  is observed. The irreversible structural modification

at this pressure (with a rapid decrease of interlayer spacing, as determined from our previous XRD measurements) results in a dramatic change in low-energy electronic structure with enhanced Drude spectral weight (increased free carrier/metallicity), favoring superconductivity to emerge with a high transition temperature. This spectral weight transfer is found to be irreversible, as supported from irreversible structural modification [as shown in Fig.3.20(b)] under nonhydrostatic compression. This result also helps us understand the persistence of a superconducting state upon decompression. The low-energy characteristic band (near  $2000\text{ cm}^{-1}$ ) of 2D correlated metal also gains in intensity irreversibly, indicating increased electronic correlation at higher pressure and its persistence nature. The broken inversion symmetry in the high-pressure structure in the presence of strong spin-orbit interaction may turn this gapped semimetallic compound into a possible topological semimetal, warranting more detailed high-pressure optical measurements and also further theoretical investigations incorporating the above results in order to characterize possible topological phases.

# Chapter 4

## High pressure structural and electrical investigations of $\text{Sb}_2\text{S}_3$

### 4.1 Introduction

The  $\text{Sb}_2\text{S}_3$  (stibnite) material is a wide bandgap semiconductor with a bandgap  $E_g \sim 1.7$  eV [116]. This material belongs to  $\text{A}_2\text{B}_3$  (A=Bi, Sb, As; B = S, Se, Te) series and constitute a promising candidate for solar energy conversion and optoelectric application [117, 118]. Among these, at ambient conditions, the heavier  $\text{Bi}_2\text{Se}_3$ ,  $\text{Bi}_2\text{Te}_3$  and  $\text{Sb}_2\text{Te}_3$  crystallize in a rhombohedral structure (SG R-3m,  $Z = 3$ ), which is composed of layers of  $\text{AB}_6$  octahedra stacked perpendicular to the long  $c$ -axis [254] and the lighter  $\text{Bi}_2\text{S}_3$ ,  $\text{Sb}_2\text{S}_3$ , and  $\text{Sb}_2\text{Se}_3$  materials on the other hand, crystallize in an orthorhombic phase (SG Pnma,  $Z = 4$ ,  $\text{U}_2\text{S}_3$ -type), made up of  $\text{AB}_7$  and  $\text{AB}_{7+1}$  polyhedra [255]. The heavier three compounds, at ambient pressure, are found to be 3D topological insulator with a single Dirac cone on the surface [45, 46] and the application of high pressure can induce various novel phenomena such as structural phase transitions [27, 28], electronic topological transitions (ETT) or the Lifshitz transition [61], insulator to metal transitions [59] and superconductivity [57, 60]. Although the structure of the lighter three compounds falls into a completely different class, they also exhibit similar phenomena under pressure and a very common feature of all these  $\text{A}_2\text{B}_3$  compounds is the existence of ETT below  $\sim 6$  GPa [74, 119, 257].

Previously, Y. A. Sorb et al. [119] and Ilias et al. [120] observed that  $\text{Sb}_2\text{S}_3$  shows a clear evidence of isostructural electronic topological transition (ETT) near  $\sim 5$  GPa. Another structural phase transition was also observed near  $\sim 15$  GPa by Ilias et al. but the new structure was not identified [120]. Whereas J.Ibanez et al.

shows that there is neither a pressure induced second order phase transition nor an electronic topological transition in  $\text{Sb}_2\text{S}_3$  and the ambient Pnma structure is stable up to  $\sim 25$  GPa [121]. To reach a clear conclusion about the structural modifications a detailed high pressure structural investigation is needed. In addition to that the isostructural  $\text{Sb}_2\text{Se}_3$  shows insulator to metal transition at 3 GPa and pressure induced superconductivity above 10 GPa [74]. So the pressure induced metallization and superconductivity study of  $\text{Sb}_2\text{S}_3$  will be helpful to understand the electrical characteristics of the  $\text{A}_2\text{B}_3$ -type compounds. Recently Lidong Dai et al. discovered pressure induced irreversible metallization in  $\text{Sb}_2\text{S}_3$  at  $\sim 34$  GPa on the basis of temperature dependent (80-240 K) electrical conductivity measurement [122]. The detailed study of the pressure dependent activation gap in the insulating region was not investigated and no low temperature investigation below 80 K was reported to observe pressure induced superconductivity. Beside this their temperature dependant conductivity data was reported in a gap of  $\sim 20$  K. So to verify the claim of their pressure induced irreversible metallization and to observe any pressure induced superconductivity detailed high pressure investigations of temperature dependent resistance measurements are needed.

Here we present high pressure XRD measurements up to  $\sim 25$  GPa and electrical resistivity measurement up to  $\sim 45$  GPa. Two structural anomalies are observed from our XRD measurements. First anomaly near  $\sim 6$  GPa is identified as pressure induced electronic topological transition and the second anomaly near  $\sim 10$  GPa is identified as the structural transition to a monoclinic structure. High pressure resistance measurements reveal persistence insulating behaviour up to the highest pressure ( $\sim 45$  GPa) of the measurements.

## 4.2 Experimental details:

The pure phase polycrystalline  $\text{Sb}_2\text{S}_3$  compound was synthesized by solid state reaction method which is described elsewhere [119].

The sample was then used for high pressure X-ray powder diffraction. High pressure X-ray powder diffraction experiment was performed at the XRD1 beamline of Elettra Synchrotron, Italy in two different pressure environments. A diamond anvil cell (DAC) was used for pressure generation. In one case a monochromatic X-ray with a wavelength of  $0.7 \text{ \AA}$  was used for the diffraction experiment up to  $\sim 12 \text{ GPa}$  and a methanol-ethanol-water (MEW 16:3:1) mixture was used as the pressure transmitting medium (PTM) for getting nearly hydrostatic conditions. In the other case the wavelength was  $0.5007 \text{ \AA}$  for the diffraction experiment up to  $\sim 24 \text{ GPa}$  and silicone oil was used as the PTM which does not mention the hydrostatic environments well. In both cases gold was used as the X-ray pressure marker and the two dimensional diffraction patterns were recorded using Dectris Pilatus 2M imaging plate detector and then integrated to 1D diffraction profile (Intensity Vs.  $2\theta$ ) with the help of FIT2D software. The detailed structural analysis was then performed with GSAS Le-Bail refinement analysis program as discussed in **chapter 2**.

Temperature dependent electrical resistance was measured under high pressure up to  $\sim 45 \text{ GPa}$  by standard quasi-four probe method using an optical cryostat as discussed in **chapter 2**.

## 4.3 Results and Discussions:

### 4.3.1 High pressure XRD measurements:

Our first measurement is limited up to 12 GPa. Corresponding selected diffraction patterns at various pressures are shown in figure 4.1 (a). A new bragg peak is detected at near  $\sim 8$  GPa. This is a clear indication of a structural phase transition and from group-subgroup analysis, the new phase is identified as monoclinic phase with space group of  $P2_1/m$ .

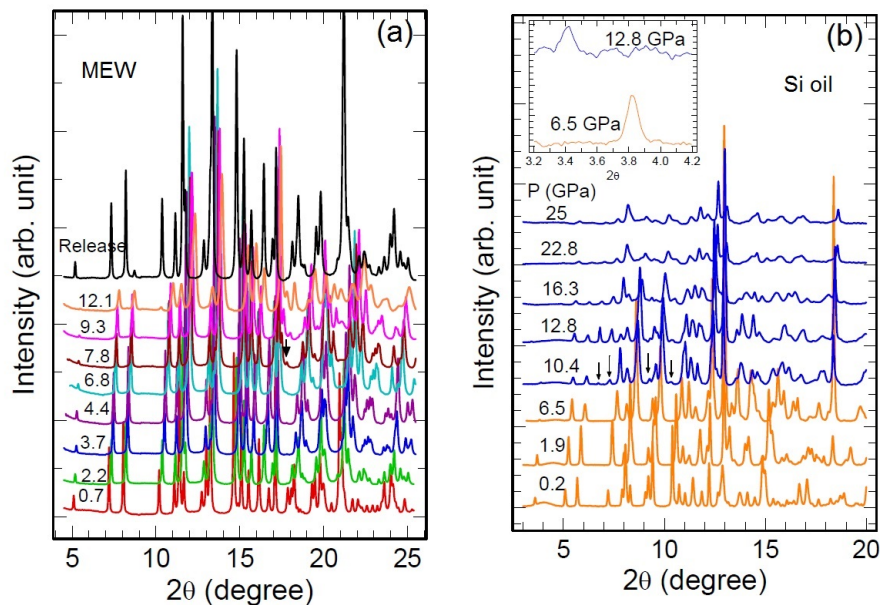


Figure 4.1: (a),(b) Selected X-ray diffraction patterns at various pressures at two different measurements. The new peaks are indicated by black arrows. The inset of (b) shows the low angle new peak which is not clearly seen in the main figure

Fig. 4.1 (b) shows the selected diffraction patterns at various pressures in our second measurements. We see that as the pressure increases all the diffraction peaks shift to the higher angle and become broad systematically. In the diffraction pattern at 10.4 GPa we observe five new Bragg peaks which are indicated by black arrows. In the inset we can clearly see the low angle new peak which was not clearly seen in the main figure. The appearances of the new Bragg peaks in this measurement also suggest a clear structural transition of  $Sb_2S_3$  near  $\sim 10$  GPa. The

small difference in transition pressure may arise from the different pressure condition of the measurements. Examples of refined XRD spectra before and after structural transition are displayed in figure 4.2 along with the corresponding crystal structure.

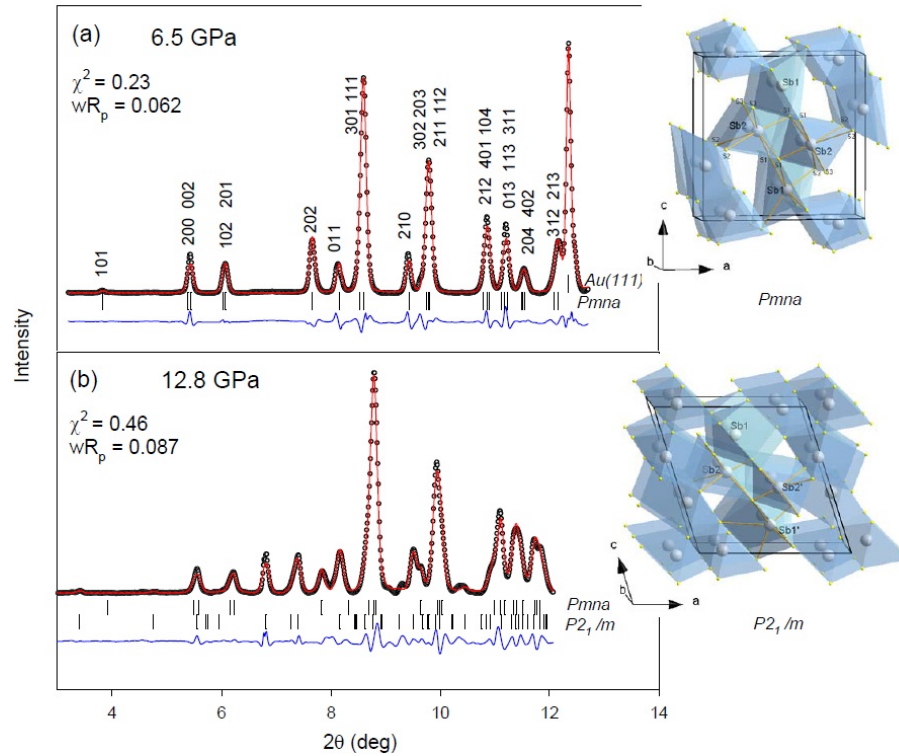


Figure 4.2: (a),(b) Refined XRD patterns of  $\text{Sb}_2\text{S}_3$  at 6.5 GPa ( $Pnma$ ) and at 12.8 GPa ( $Pnma+P2_1/m$ ). Dots indicate the measured spectra and the red solid red lines represent the best refinements. Blue lines represent the difference spectra between the measured and the refined patterns. Bragg peak positions are marked by vertical lines. Insets show the corresponding crystal structures.

We have calculated the lattice parameters and the unit cell volume for both the phases. Figure 4.3(a) shows the reduced lattice parameters as a function of pressure. Clear slope change is observed near 6 GPa.  $a/c$  ratio also shows a minimum around this pressure as shown in figure 4.3 (c). Both these observations indicate presence of pressure induced Lifshitz transition at this critical pressure,  $P_c$  (6 GPa). Figure 4.3 (d) shows anomalous change in compressibility near  $P_c$  which further supports this isostructural transition. A significant volume drop is observed at this pressure where the structural transition is observed. This indicates the first order nature of

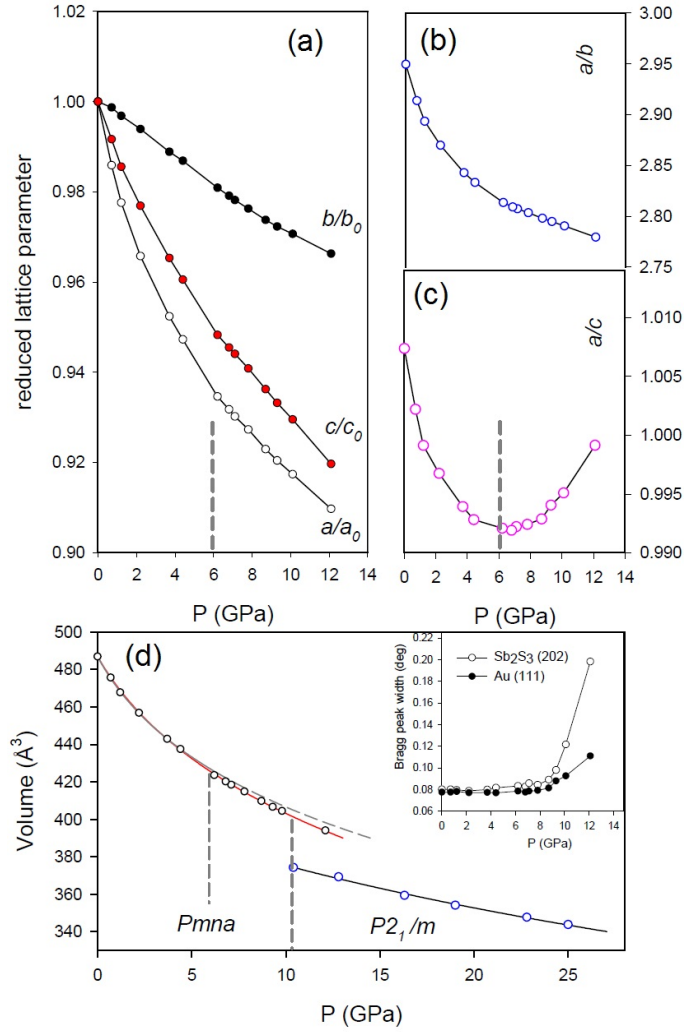


Figure 4.3: (a) Reduced lattice parameters as a function of pressure. (b)  $a/b$  ratio as a function of pressure (c)  $a/c$  ratio as a function of pressure (d) Plot of the unit cell volume as a function of pressure. The inset shows the pressure dependence of the Bragg peak width of  $\text{Sb}_2\text{S}_3$  (202) peak and Au (111) peak.

the transition. Inset of figure 4.3(d) shows pressure dependence of the Bragg peak width of sample (202) peak and Au (111) peak which supports the hydrostaticity of our measurements at least up to 9 GPa, well above the critical pressure ( $P_c$ ) for Lifshitz transition.

### 4.3.2 High pressure transport measurements:

To determine whether or not  $\text{Sb}_2\text{S}_3$  undergoes insulator to metal transformation under pressure, temperature-dependence resistance measurement was carried at several

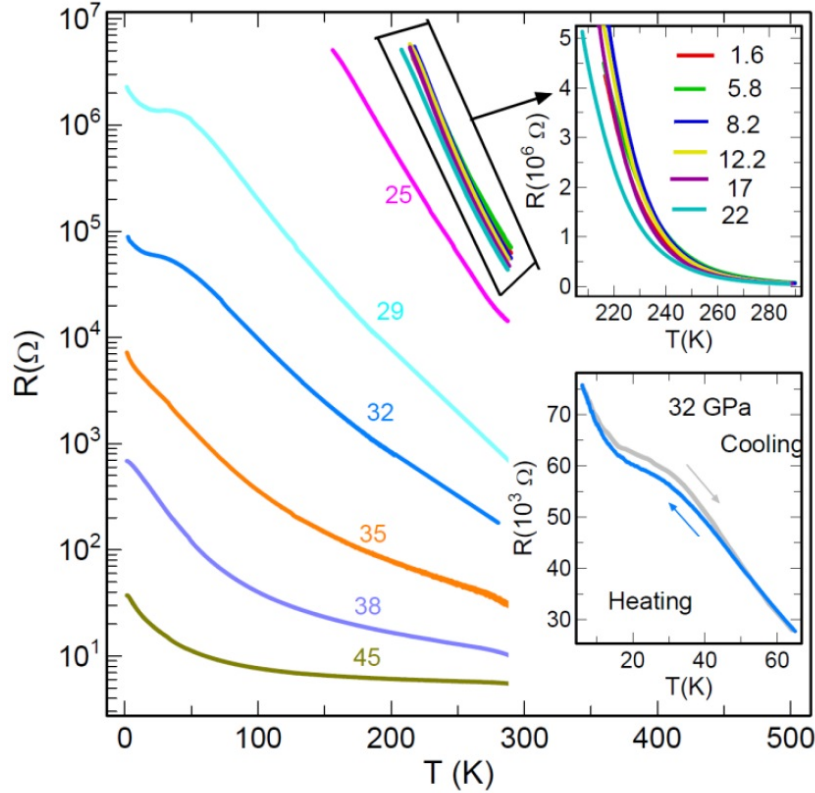


Figure 4.4: Temperature dependence electrical resistance of  $\text{Sb}_2\text{S}_3$  under various pressures up to 45 GPa. The upper inset shows the enlarged  $R(T)$  plot at lower pressure up to 22 GPa and the lower inset shows the hysteresis in  $R(T)$  curve during cooling and heating at 32 GPa.

pressures up to  $\sim 45$  GPa as shown in Fig.4.4. The resistances are plotted on a logarithmic scale in order to facilitate comparison between the various curves. At 1.6 GPa, the first pressure of our measurement, the resistance shows an exponential increase upon decreasing the temperature. From the exponential fitting of resistance ( $R(T) = R(0) \times \exp(E_g/2K_B T)$ ), the estimated band-gap is  $\sim 635$  meV at this pressure. This value of the bandgap is much less than the reported optical bandgap which may be because of the polycrystalline nature of our sample. As we increase the pressure the low temperature resistance increases (shown in the upper inset of Figure 3) up to 8.2 GPa and then started to decrease above this pressure. From the figure it is clearly observed that up to  $\sim 22$  GPa the pressure has very little effect on the system. Although, above  $\sim 22$  GPa the insulating behavior becomes suppressed

the system remains insulating up to the highest pressure of our measurement unlike the results by Lidong Dai et. al., where they have shown that  $\text{Sb}_2\text{S}_3$  becomes metallic above 32 GPa [122]. In the intermediate pressure range, from 29 GPa to 32 GPa, a low temperature resistance kink is observed which is first order in nature as we see a hysteresis in the  $R(T)$  curve during cooling and heating at 32 GPa (lower inset of the Fig. 4.4). This can possibly be due presence of structural transition at low temperature. Low temperature structural investigations under pressure are needed to confirm this transition. With increasing pressure the transition temperature decreases and eventually vanishes above  $\sim 35$  GPa.

As a structural or isostructural phase transition is often accompanied by an electronic changes, we plot the ratio of the resistances at  $T = 280$  K and  $T=220$  K as a function of pressure in Fig. 4.5(a). We could not measure the resistance of the sample below 220 K in the low pressure region as the used resistance bridge is limited to measure a resistance below  $5 \times 10^6 \Omega$ . For that we choose the ratio  $R(280 \text{ K})/R(220 \text{ K})$  so that we can get all the data points to explain the results. We observe an anomalous minimum in the pressure dependence resistance ratio near  $\sim 5.8$  GPa which support the earlier observed second order isostructural phase transition near this pressure. Above  $\sim 5.8$  GPa the resistance ratio increases with pressure up to 12.2 GPa and above this pressure the resistance started to decrease which is related to the structural transition near  $\sim 10$  GPa observed from our high pressure XRD measurements. Above 22 GPa this resistance ratio started to decrease rapidly which is more clear from the logarithmic plot of the room temperature resistance (inset of the Fig. 4.5a). The possible reason of the rapid decrease in room temperature ratio is due to the structural disorder above 20 GPa as suggested by Ilias et al. [120]. Upon complete decompression the resistance returns to its original value. Hence we infer that the structural phase transition occurred at  $\sim 10$  GPa has a great possibility to be reversible. In Fig. 4.5(b) we have plotted  $\log(R)$  as a function of  $1000/T$  at

several pressures. From the linear fitting of this plot (lower inset of the Fig. 4.5(b)) we have calculated the activation energy gap at each pressure. Initially band gap increases with pressure up to 12 GPa with an inflection point near  $\sim 5.8$  GPa and above  $\sim 22$  GPa it decreases drastically. The starting point of the decrease in band gap is related to the structural transition observed from our XRD measurements. In the whole pressure range the changes of the activation energy with pressure are well consisted with the change of the resistance with pressure.

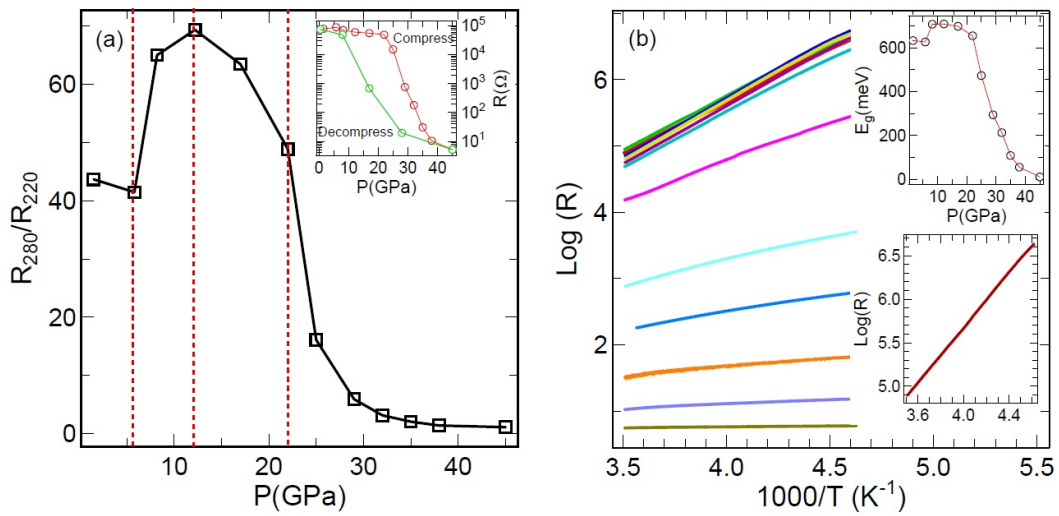


Figure 4.5: (a) Resistance ratio ( $R(T=280\text{ K})/R(T=220\text{ K})$ ) as a function of pressure. The inset shows the pressure dependences of the resistance at 280 K upon both compression and decompression. (b)  $\text{Log}(R)$  as a function of  $1000./T$  at several pressures. The upper inset shows the variation of the band gap with pressure and the lower inset shows the linear fitting of the above mentioned plot at 1.5 GPa in the temperature range 215K to 290K.

In Fig 4.6 we plot the temperature dependence of the resistance at several pressures upon decompression down to 0.5 GPa. We observed that the lowest pressure resistance is completely reversible upon decompression unlike the Ref. [122] where the author show an irreversibility of the structure and the metalicity upon pressure decompression. Although the pressure dependent band gap varies differently, the lower pressure values are very close which again supports the observed reversibility.

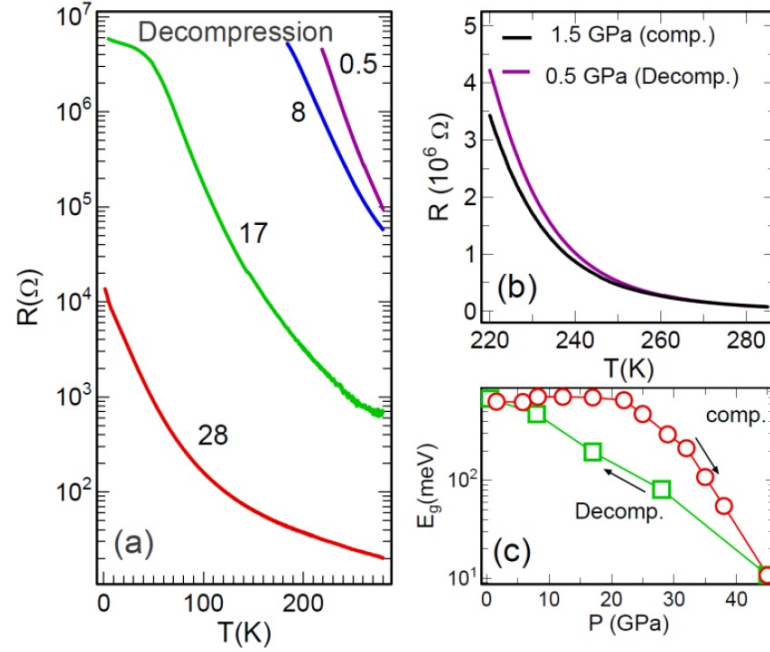


Figure 4.6: (a) Temperature dependence of resistance at various pressures upon decompression. (b) Comparison of the  $R(T)$  behavior between 1.5 GPa during compression and 0.5 GPa during decompression. (c) Variation of the band gap during compression and decompression.

### 4.3.3 Discussions:

The first high pressure structural investigation on  $\text{Sb}_2\text{S}_3$  up to  $\sim 10$  GPa reveals that upon increasing pressure the lone electron pair activity decreases which may result in a structural phase transition and a change in the electronic properties [256]. Then in 2015, using high pressure Raman spectroscopy, resistance and XRD measurements, Y.A Sorb et al. reported that  $\text{Sb}_2\text{S}_3$  showed a pressure induced isostructural ETT near  $\sim 5$  GPa. They have also observed a plausible structural phase transition above  $\sim 20$  GPa [119]. In 2016, Ilias et al., by their XRD and Raman measurements, revealed two phase transitions at  $\sim 5$  GPa and  $\sim 15$  GPa. The anomaly at  $\sim 5$  GPa was identified as a second order isostructural ETT similar to the earlier measurements and the second transition was identified as a structural transition but they have not identified the new phase due to the onset of structural disorder above 20 GPa. Upon decompression from 53 GPa they have recovered an amorphous state [120]. Later,

in the same year, J.Ibanez et al. reported that there was no clear evidence either for a pressure-induced second-order IPT or for an ETT in  $\text{Sb}_2\text{S}_3$  near 5 GPa [121]. Furthermore, they did not find any evidence for a first order structural phase transition up to  $\sim 25$  GPa. Their theoretical calculation predicted insulator to metal transition in  $\text{Sb}_2\text{S}_3$  above  $\sim 15$  GPa [121]. Recently, using Raman spectroscopy measurements, Lidong Dai et al. reported a clear evidence for an IPT near  $\sim 5$  GPa. Additionally, they have reported pressure induced semiconductor to metal transition near  $\sim 34$  GPa which showed persistence upon decompression [122]. We have tabulated a comparison between the different results on  $\text{Sb}_2\text{S}_3$  to date in table 4.1 which also includes a comparison with the isostructural  $\text{Sb}_2\text{Se}_3$  and  $\text{Bi}_2\text{S}_3$ . Our XRD results up to 25 GPa clearly indicate two structural anomaly at  $\sim 6$  GPa and  $\sim 10$  GPa which are indicated as second order isostructural and first order structural transitions respectively. From our systematic temperature dependent resistance measurements at different pressures we clearly observe that the system remain insulating up to the highest pressure ( $\sim 45$  GPa) of our measurements which is much higher than the critical pressure ( $\sim 34$  GPa) where Lidong Dai et al. reported the pressure induced metallization. Additionally we report reversibility of the electrical resistance which is contradictory to the results of the irreversible metallization upon decompression. So from our result we may infer that although, the isostructural  $\text{Bi}_2\text{S}_3$  and  $\text{Sb}_2\text{Se}_3$  show pressure induced metallization at  $\sim 20$  GPa and  $\sim 3$  GPa respectively,  $\text{Sb}_2\text{S}_3$  remains insulating up to  $\text{Sb}_2\text{S}_3 45$  GPa. Structural transition near  $\sim 10$  GPa in  $\text{Sb}_2\text{S}_3$  may be the possible reason of the stable electronic structure in the higher pressure phase whereas in  $\text{Sb}_2\text{Se}_3$  and  $\text{Bi}_2\text{S}_3$  the ambient pressure phases were stable up to 40 and 55 GPa respectively. As we are limited with the highest pressure in our DAC, it will be interesting to study higher pressure investigations.

Compounds	ST (GPa)	ETT (GPa)	IMT (GPa)	SC (GPa)
Sb <sub>2</sub> Se <sub>3</sub>	-	~2.5 [74]	~3 [74]	~10 [74]
Bi <sub>2</sub> S <sub>3</sub>	-	~5 [257]	~20 [257]	-
Sb <sub>2</sub> S <sub>3</sub>	~20 [119]	~4 [119]	-	-
Sb <sub>2</sub> S <sub>3</sub>	~15 [120]	~5 [120]	-	-
Sb <sub>2</sub> S <sub>3</sub>	No ST [121]	No ETT	-	-
Sb <sub>2</sub> S <sub>3</sub>	~15 [122]	~5 [122]	~34 [122]	-
Sb <sub>2</sub> S <sub>3</sub>	~10 [This work]	~6	No IMT up to ~45 GPa	-

Table 4.1: Comparison of the different transition reported to date in Sb<sub>2</sub>S<sub>3</sub> and the isostructural Sb<sub>2</sub>Se<sub>3</sub> and Bi<sub>2</sub>S<sub>3</sub>. ST, ETT, IMT and SC represent the structural transition, electronic topological transition, insulator to metal transition and superconductivity respectively.

## 4.4 Conclusions:

High pressure structural investigation of Sb<sub>2</sub>S<sub>3</sub> is carried out by synchrotron based XRD measurements up to ~25 GPa and electrical transport measurements is also performed under pressure up to 45 GPa. Some earlier high pressure investigations of Sb<sub>2</sub>S<sub>3</sub> have already been reported such as electronic topological transition (ETT), structural transition and insulator to metal transition. All the high pressure results on pressure induced ETT and structural transition remain controversial. Recently pressure induced metallization was discovered using temperature dependent (80 - 240K) electrical conductivity measurement under pressure (24 - 34 GPa) [122]. In addition to that the persistence of the pressure induced metallization was also claimed under decompression. In our investigations we have carefully studied the structural properties to resolve the controversy about both isostructural and the structural transitions. Our XRD measurements reveal a clear structural transition near ~10 GPa and ETT near ~6 GPa. From our systematic investigations of temperature dependence resistance measurement under several pressures we confirm

that no pressure induced metallization is there up to  $\sim 45$  GPa and the electrical resistance are completely reversible under decompression. Thus we may conclude that the system shows persistence insulating behaviour up to 45 GPa with an isostructural transition near  $\sim 6$  GPa and a structural transition near  $\sim 10$  GPa. No signature of pressure induced topological quantum phase transition (TQPT) was observed in this compound.

# Chapter 5

## High pressure electrical transport and optical reflection study of $\text{AgBiSe}_2$

### 5.1 Introduction

Topological Insulators (TIs) are characterized by insulating bulk states but conducting surface states which are protected by time reversal symmetry (TRS) [2, 34]. Among the diverse families of three-dimensional (3D) TIs, the  $\text{A}_2\text{B}_3$  series of compounds such as  $\text{Bi}_2\text{Se}_3$ ,  $\text{Bi}_2\text{Te}_3$  and  $\text{Sb}_2\text{Te}_3$  are the most familiar topological insulators at ambient conditions [44, 46, 176]. Recent high pressure studies in these compounds have shown that all the  $\text{A}_2\text{B}_3$  series of TI compounds show pressure-induced electronic topological transition (ETT) below 6 GPa [59, 62]. Application of pressure also induced semiconductor to metal transition and superconductivity on these compounds [27, 57, 62, 110]. It is also verified that the application of pressure improve the thermoelectric properties of the semiconductor chalcogenides and that the high pressure investigations of these materials could help in the design of better thermoelectric materials by substituting external pressure by chemical pressure [259, 260].

Dimetal Chalcogenide,  $\text{AgBiSe}_2$ , is a well-known narrow bandgap ( $\sim 0.6$  eV) semiconductor with a tremendous impact for thermoelectric applications due to its low intrinsic thermal conductivity [123, 258]. At ambient conditions it crystallizes in ordered hexagonal structure (S.G : P-3m, Z=3) [Fig.5.1]. Its narrow optical bandgap of  $\sim 0.6$  eV implies that  $\text{AgBiSe}_2$  is on the border of pressure induced insulator to metal transition which is an important subject of condensed matter physics. Presence of bond anharmonicity in  $\text{AgBiSe}_2$  causes intrinsic low lattice thermal conductivity which originates high thermoelectric figure-of-merit (ZT) of  $\sim 1$ .  $\text{AgBiSe}_2$  also

exhibits strong spin orbit coupling (SOC) and it has a symmetrical equivalence with  $\text{Bi}_2\text{Se}_3$ . High pressure investigations will thus help to understand whether  $\text{AgBiSe}_2$  exhibits similar pressure response to that of  $\text{Bi}_2\text{Se}_3$  and it will also be useful for the fabrications of semiconductor device operating in the mechanically strained environment. No low temperature measurements was also reported to search pressure induced superconductivity similar to the topological insulators.

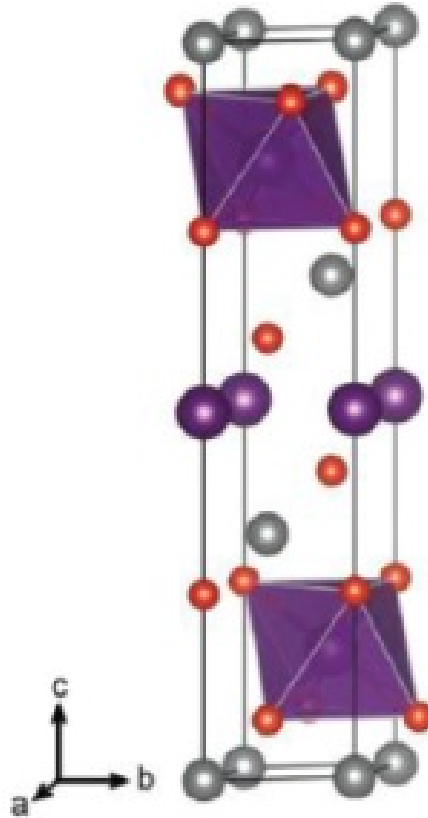


Figure 5.1: Crystal Structure of  $\text{AgBiSe}_2$

Here, we report the signature of the pressure induced electronic topological transition (ETT) and semiconductor-to-metal transition in  $\text{AgBiSe}_2$  using synchrotron based mid-IR reflectivity and electrical transport measurements. IR-reflectivity data reveals an abrupt change in the interband transition above  $\sim 2$  GPa. Optical conductivity spectral weight in the low energy region also shows anomalous change above 2 GPa. Pressure dependent room temperature resistance measurement was performed

in two independent experiments. Both the measurements show an anomalous behaviour of pressure dependent resistance above 2 GPa which is similar to that of the 3D topological insulators  $\text{Bi}_2\text{Se}_3$  and  $\text{Bi}_2\text{Te}_3$ . Low temperature resistance measurements also show a change in behavior of the temperature dependence resistances above 2 GPa. All the observations confirm the pressure induced ETT in  $\text{AgBiSe}_2$  above  $\sim 2$  GPa. Higher pressure IR-reflectivity measurements also reveal overall increase in optical conductivity in the whole energy range above  $\sim 8$  GPa and over the same pressure range the high pressure resistance measurements show a sign change in the temperature dependence of the  $dR/dT$  which confirm the pressure induced semiconductor to metal transition in  $\text{AgBiSe}_2$  near  $\sim 8$  GPa. We have not observed any evidence of pressure induced superconductivity in our transport measurements up to 11.5 GPa.

## 5.2 Experimental Details:

Temperature dependent electrical resistance was measured under high pressure up to 11.5 GPa by standard quasi-four probe method as discussed in **chapter 2**.

Pressure dependent MIR reflectance measurements were carried out on polycrystalline  $\text{AgBiSe}_2$  in the frequency range 700 to 10000  $\text{cm}^{-1}$  at SISSI beamline of the Elettra Synchrotron Facility. The reflectance spectra were collected with the help of an IR microscope (Hyperion) equipped with a liquid nitrogen cooled HgCdTe (MCT) detector, coupled to a Bruker IFS66v interferometer. The DAC was mounted with type IIa synthetic diamond anvils for this measurement. A thin pellet of finely ground sample was placed in the gasket hole, which was then filled with KCl as the pressure medium. detailed measurement procedure is discussed in **chapter 2**.

## 5.3 Results:

### 5.3.1 Mid-IR reflectance measurements:

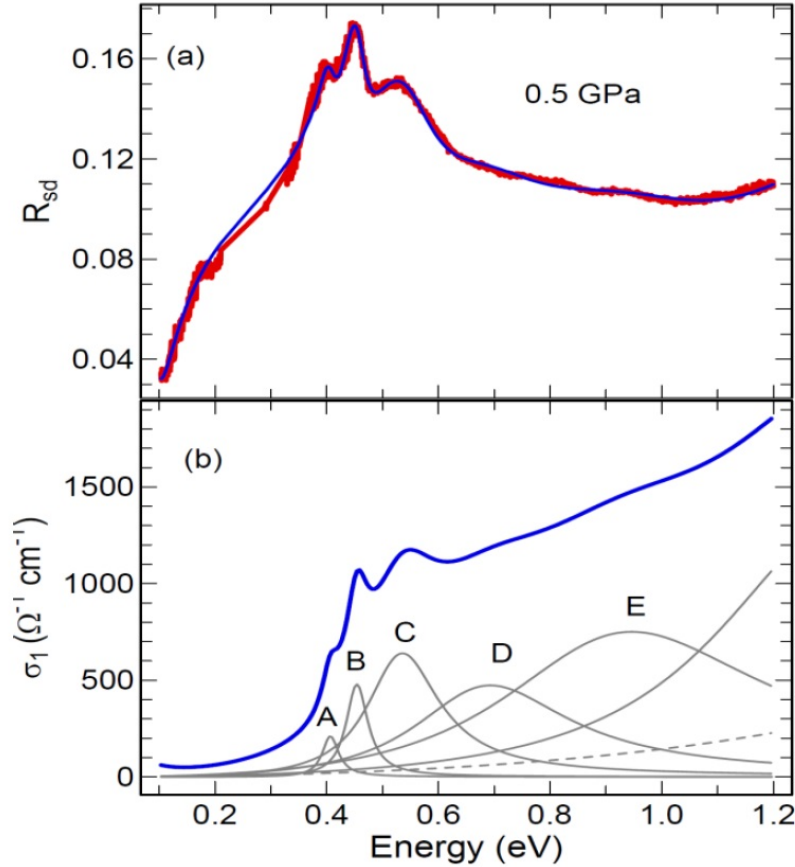


Figure 5.2: (a) Reflectance Spectra of  $\text{AgBiSe}_2$  at 0.5 GPa. The Blue line is the fit of the reflectance spectrum with Lorentz oscillators. (b) Optical Conductivity obtained from the fitted reflectance data with Lorentz oscillators. The Five main interband transition in the experimental range are labelled as A, B, C, D and E.

Fig. 5.2 (a) shows the Drude-Lorentz fitting of the reflectance data at 0.5 GPa. The optical conductivity spectrum was then obtained from the same oscillators used to fit the reflectance data. In the reflectance data several interband transition are clearly observed. Within our experimental range there are five main contributions which are labelled as A, B, C, D and E in Fig. 5.2 (b). The reflectance and the conductivity spectrum reveal that  $\text{AgBiSe}_2$  are strongly insulating with effectively no signature of free carriers in the experimental spectral range. A, B and C interband

transitions are very close in energy and one possible origin of the three distinct transitions is that they originate from slightly different regions of the band structure. At higher pressures the band structure may be slightly smeared out making the C transition indistinguishable.

Fig. 5.3 shows the real part of the converted optical conductivity at various pressures. There is a huge change in the conductivity spectra between 0.5 GPa and 1.3 GPa which may be due to the structural phase transition from hexagonal [P-3m1, space group (S.G) 164, Z=3] to rhombohedral [R-3m, space group (S.G) 164, Z=1] near 0.7 GPa [124]. At 0.5 GPa the lowest interband transitions A, B and C are distinguishable but as we increase the pressure these three peak merge into two peaks above 1.3 GPa. At 1.3 GPa  $\sigma_1$  shows identical behaviour to that of the isostructural Bi<sub>2</sub>Se<sub>2</sub>Te [49]. As we increase the pressure the spectral weight of the A, B and C interband transitions gradually decreases as shown in 5.3 (c) and above 7.8 GPa it becomes completely zero. So A, B, and C interband transition is due to the transitions between valence band and conduction bands and the bandgap is closed above 7.8 GPa.

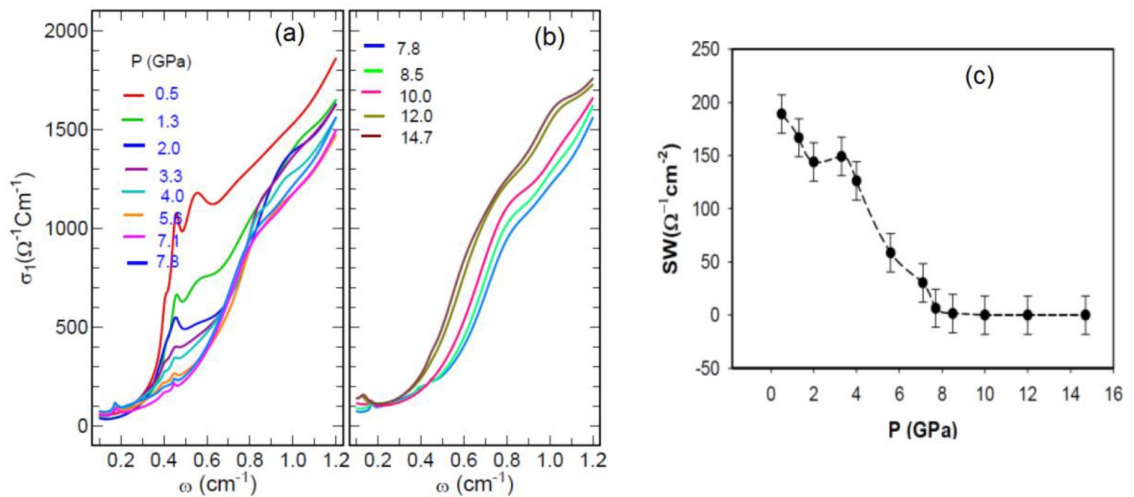


Figure 5.3: (a), (b) Real part of the optical conductivity ( $\sigma_1(\omega)$ ) spectra at various pressures. (c) Pressure dependence of the spectral weight for the A, B and C interband transitions.

Fig. 5.4 (a) shows the reflectance spectra at two different pressures of 5.6 GPa

and 10 GPa. At 5.6 GPa the reflectance spectrum shows typical semiconducting behaviour but at  $\sim 10$  GPa a clear change in the reflectance occurs with a huge increase of reflectance by  $\sim 100\%$  at low energy. The reflectance spectrum shows metallic behaviour with low energy Drude behaviour with a reflectance minimum near 0.2 eV. Fig. 5.4 (b) shows the pressure dependence of optical conductivity ( $\sigma_1(\omega)$ ) at two different energy. Two inflection points are observed near 2 GPa and 7.1 GPa which are indicated as pressure induced ETT and semiconductor-to-metal transition respectively [124]. Fig. 5.4 (c) and (d) shows the spectral weight variation as a function of pressure at two different energy regions. Two kinks observed near the same pressures further confirm the ETT and semiconductor-to-metal transition respectively [124].

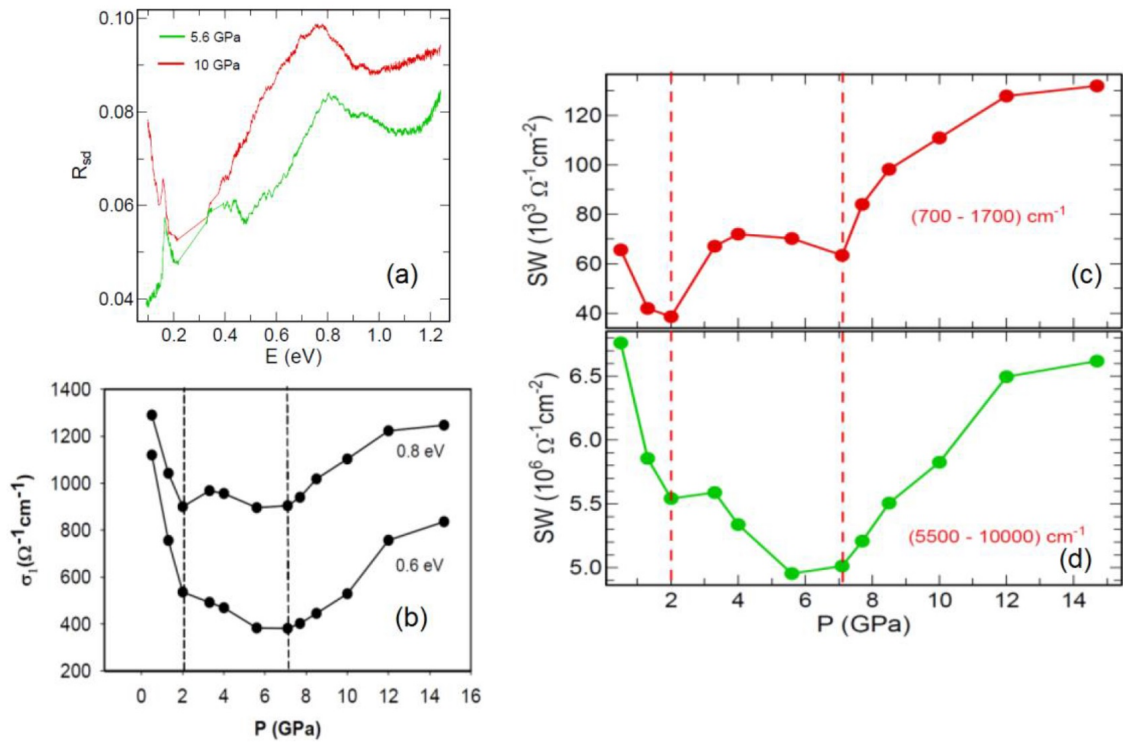


Figure 5.4: (a) Real part of the measured reflectance at 5.6 GPa and 10.0 GPa. (b) Pressure dependences of  $\sigma_1(\omega)$  at two different energies. (c) (d) Variation of the spectral weight as a function of pressure at two different energy regions.

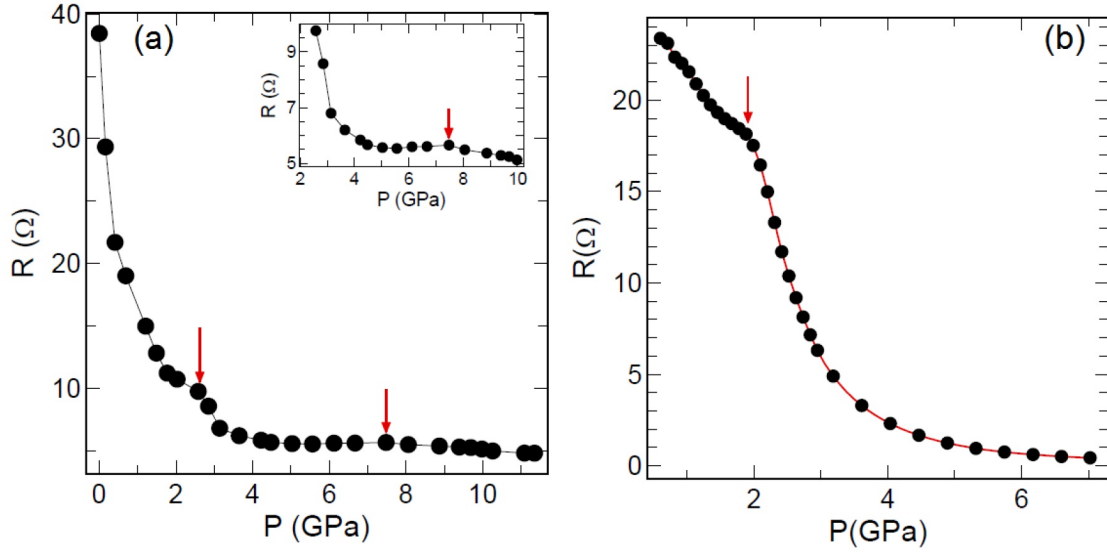


Figure 5.5: (a) and (b) Room temperature resistance as a function of pressure in two independent measurements. Inset of figure (a) shows the enlarge view in the vicinity of insulator to metal transition [3].

### 5.3.2 Resistance measurements:

Two independent room temperature resistance measurements were performed under pressure (Fig 5.5). In our first experiment the resistance of polycrystalline  $\text{AgBiSe}_2$  was measured in quasi four probe configuration up to 11.5 GPa. The second experiment was carried out in standard four probe configuration up to 7 GPa. Both the measurement show a sudden drop in resistance above 2 GPa confirming the ETT near this pressure [124]. Another kink in pressure dependence resistance is observed below  $\sim 8$  GPa indicating the semiconductor to metal transition near this pressure [124].

To clearly observe the resistance behaviour around the ETT, we have plotted the temperature dependent resistances in the low pressure region in Fig. 5.6. At 0.6 GPa the resistance first increases with decreasing temperature with a resistance plateau developed at low temperature. This is the common transport signature of a typical topological insulator [56]. Such topological insulator kind resistance behaviour is observed up to 2 GPa in  $\text{AgBiSe}_2$  and above this pressure resistance shows

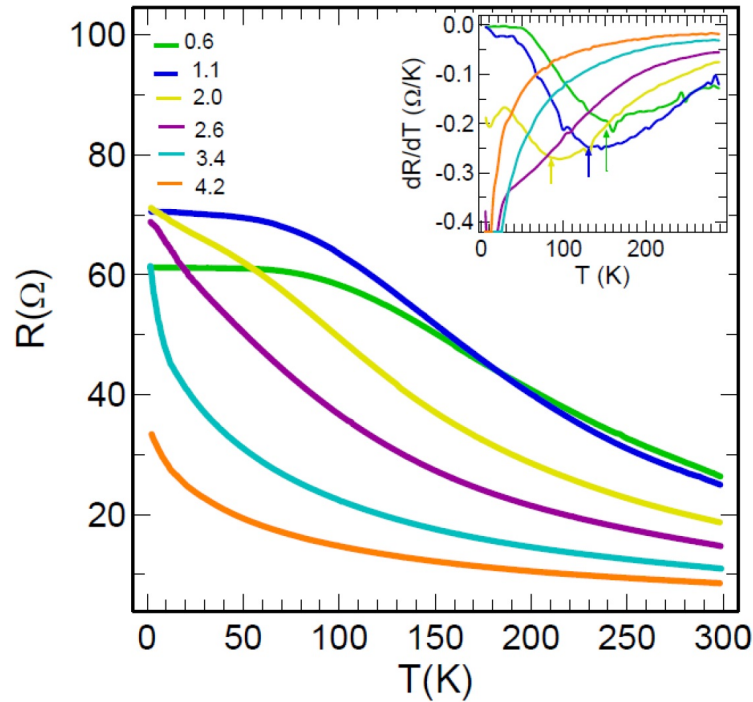


Figure 5.6: Temperature dependence resistance in the vicinity of the transition pressure. The inset shows the  $dR/dT$  as a function of temperature at the respective pressures.

activation kind semiconducting behaviour. Temperature dependence  $dR/dT$  curves (inset) show more prominent changes where, the  $dR/dT$  minimum (corresponding to the plateau temperature) shifts lower as we increase the pressure and vanishes above 2 GPa. Thus our temperature dependent resistance measurements give a clear evidence of the electronic transition above 2 GPa which may be concluded as a possible topological insulator to activation kind of semiconductor transition. Further theoretical investigations of band inversion are needed to confirm this electronic transition as topological quantum phase transition (topological insulator to conventional insulator transition). The topological character after the structural transition near 0.7 [124] should also be reinvestigated.

Fig. 5.7 shows the temperature (300 K-20 K) dependent resistances of  $\text{AgBiSe}_2$  in a logarithmic scale at all pressures up to 11.5 GPa. The system remains semiconducting up to 7.6 GPa but further increase of the pressure above 7.6 GPa turns the

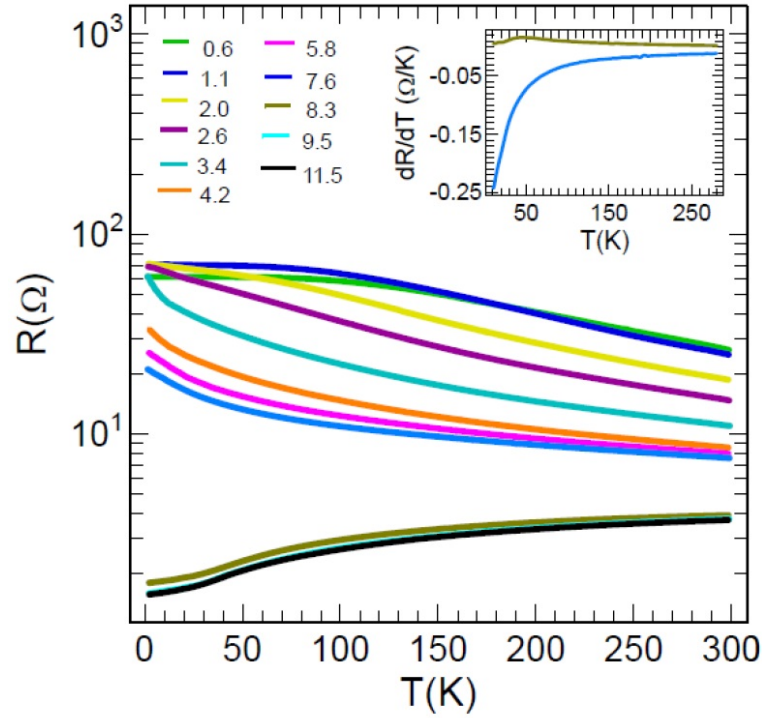


Figure 5.7: Electrical resistances of AgBiSe<sub>2</sub> as a function of temperature at different pressures up to 11.5 GPa. The inset shows the  $dR/dT$  as a function of temperature at 7.6 GPa and 8.3 GPa.

system into metallic. From the behaviour of the  $dR/dT$  the inset clearly demonstrates the semiconductor to metal transition above 7.6 GPa ( $dR/dT > 0$ ).

## 5.4 Discussions:

Here we discuss how the pressure changes the optical gap in AgBiSe<sub>2</sub> compared to the other related compounds such as Bi<sub>2</sub>Te<sub>3</sub>, Bi<sub>2</sub>Se<sub>3</sub> and Bi<sub>2</sub>Te<sub>2</sub>Se. In Bi<sub>2</sub>Te<sub>3</sub> Vilaplana et. al. reported that the application of pressure reduced the gap from  $\sim 170$  meV to  $\sim 120$  meV by applying 6 GPa [28]. In Bi<sub>2</sub>Se<sub>3</sub> it is observed that the optical gap is increased from  $\sim 170$  meV at ambient pressure to  $\sim 450$  meV at 8 GPa [261]. Whereas in Bi<sub>2</sub>Te<sub>2</sub>Se the gap edge is fairly modest up to 4 GPa and a steep decrease in the gap value begins above 4 GPa and by 8 GPa the gap has moved from  $\sim 340$  meV to  $\sim 250$  meV [49]. In our case the determination of the optical band gap is very difficult due to the presence of the strong two phonon

absorption of diamond in the gap edge region. From the electrical measurements we have calculated the bandgap in the temperature range of 200 K-300 K and plotted in Fig. 5.8 (a). The fittings of the  $\log(R)$  Vs.  $1/T$  in the insulating region is shown in Fig. 5.8 (b). The bandgap is reduced from  $\sim 50$  meV at ambient pressure to  $\sim 14$  meV at 7.6 GPa and closes above this pressure.

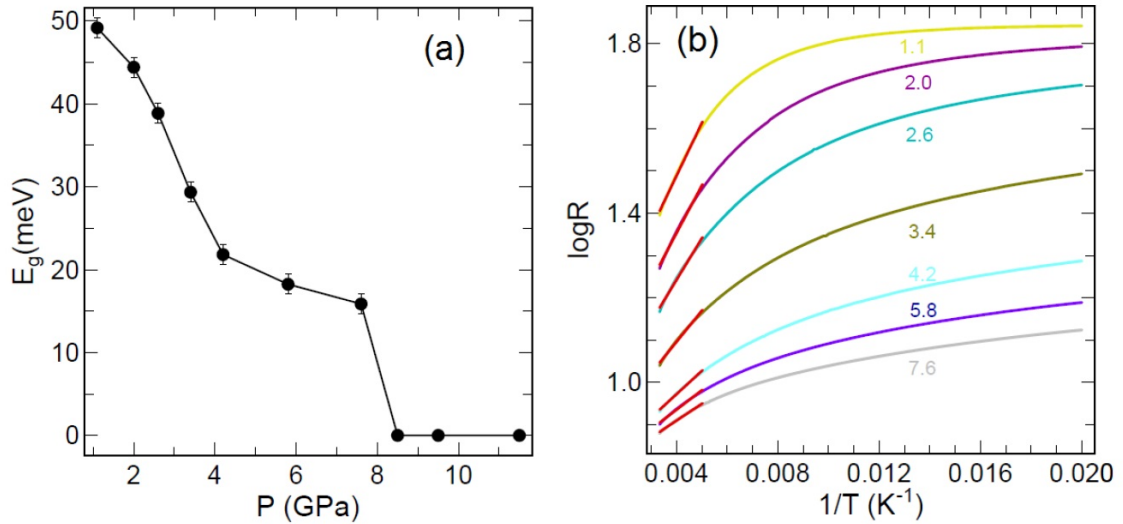


Figure 5.8: (a) Pressure dependent of the band-gap measured from the resistance measurement. (b)  $\log(R)$  Vs.  $1/T$  plot at the insulating region.

A comparison (table 5.1) of the pressure induced ETT, insulator to metal transition and superconductivity with the related compounds is also very important. From table 5.1, we can observe that the pressure induced ETT and the insulator to metal transition occur at comparable pressures in all compounds. There is a change in the critical pressure where the superconductivity occurs. In  $\text{Bi}_2\text{Se}_3$ , the superconductivity occurs at 12 GPa followed by a structural transition but in  $\text{Bi}_2\text{Te}_3$  and in  $\text{Sb}_2\text{Te}_3$  the superconductivity occurs before structural transition which is very important to realize the topological superconductivity in these materials. Similar to  $\text{Bi}_2\text{Te}_2\text{Se}$ , no pressure induced superconductivity was observed in  $\text{AgBiSe}_2$  up to 11.5 GPa from the high pressure transport measurements.

Compounds	ETT (GPa)	MIT(GPa)	SC (GPa)
Bi <sub>2</sub> Se <sub>3</sub>	~5 [61]	~10 [62]	~12 [27]
Bi <sub>2</sub> Te <sub>3</sub>	~4 [61]	~9 [263]	~4 [57]
Sb <sub>2</sub> Se <sub>3</sub>	~3 [61]	~	~4 [60]
Bi <sub>2</sub> Te <sub>2</sub> Se	~4 [262]	~8 [49]	~
AgBiSe <sub>2</sub>	~3 [ [124], This work ]	~8 [ [124], This work ]	~

Table 5.1: Comparison of the different transition reported to date in AgBiSe<sub>2</sub> and other isostructural compounds. ST, ETT, IMT and SC represent the structural transition, electronic topological transition, insulator to metal transition and superconductivity respectively.

## 5.5 Conclusions:

In summary we have obtained the independent and consistent experimental evidence of the pressure induced electronic topological transition and semiconductor-to-metal transition in polycrystalline AgBiSe<sub>2</sub> using infrared spectroscopy and electrical transport measurements. Signatures of both the transitions are clear in both the spectroscopic and transport data. The observations of the clear change in the interband transitions above 2 GPa from the IR spectroscopic measurements and a clear change in the resistance behaviour above 2 GPa in the transport measurements confirm the ETT near this pressure. The sign change of the temperature dependent  $dR/dT$  near 8 GPa and the closing of the band gap above 8.5 GPa further confirm the semiconductor to metal transition. No pressure induced superconductivity was observed up to the highest pressure (11.5 GPa) of our transport measurements.

# Chapter 6

## High pressure magneto-resistance measurements on Weyl semimetals NbP and NbAs

### 6.1 Introduction

Recent discovery of Weyl semimetals (WSMs) have attracted increasing research interest as a new family of topological materials. In the band structure, they show linearly dispersed band crossing in three dimensional (3D)  $k$ -spaces near Fermi level and can be considered as a 3D analog of graphene [77, 78, 109, 112]. Both, NbP and NbAs are recently discovered type- I Weyl semimetals which crystallize in a noncentrosymmetric tetragonal lattice structure but preserve the time reversal symmetry [25]. There are other WSMs as type-II weyl semimetals like  $\text{WTe}_2$ ,  $\text{MoTe}_2$  and  $\text{TaIrTe}_4$  [30, 31, 104, 130]. Transport signatures of such topological semimetals are that they exhibit Chiral anomaly induced negative magnetoresistance, extreme magnetoresistance (XMR) and ultrahigh mobility [89, 264, 265].

Nevertheless, the topology of Fermi surface of such materials can be modified by small changes of the Fermi energy [109, 112]. And high pressure has always been considered a powerful tool to tune the electronic structure of a material, which promises a possible route to shift the energies of the Weyl points of a Weyl semimetal [109]. Thus, it would be very interesting to study the pressure effects on Weyl semimetals and whether pressure can induce other novel phenomena in these topological WSMs [109]. Topological superconductors (TSCs) may also be obtained by applying pressure on topological semimetals. For instance pressure induced superconductivity is observed in  $\text{WTe}_2$  [30],  $\text{MoTe}_2$  [31] and TaP [29] after simultaneous suppression of extreme MR. The high-pressure phase of TaAs is recognized as a new type of topological WSM [112]. High pressure studies on NbAs

suggest that no structural changes or superconductivity was observed in NbAs up to  $\sim 20$  GPa [86, 105]. Whereas a dramatic change of temperature dependence of resistivity of NbP and TaP is explained in terms of the pressure dependence shifts of the Weyl points [110]. ETT is also observed in both NbP and NbAs [111, 266]. But high pressure magnetoresistance and Hall measurements are still missing in these compounds.

Here we have studied high pressure magnetoresistance and Hall measurements of NbP and NbAs and compared with the ambient pressure results. High pressure Structural investigations have also been carried out in these compounds.

## 6.2 Experimental techniques:

Single crystals of NbP and NbAs were grown by chemical vapor transport techniques as discussed elsewhere [85].

High pressure X-ray powder diffraction experiments of NbP and NbAs were performed at the XRD1 beamline of Elettra Synchrotron, Italy up to  $\sim 5$  GPa and 13 GPa respectively. A diamond anvil cell (DAC) was used for pressure generation and a monochromatic X-ray with a wavelength of 0.70001  $\text{\AA}$  was used for both the diffraction experiments. More details on XRD techniques can be found in **chapter 2**.

High pressure magneto-transport measurements on NbP and NbAs were performed using a non magnetic Cu-Be DAC suitable for SQUID magnetometer. Resistance was measured under extreme conditions of high pressure up to  $\sim 6$  GPa, low temperature down to 2 K and high magnetic field up to 7 T as discussed in **chapter 2**.

## 6.3 Results on NbP:

### 6.3.1 XRD measurements:

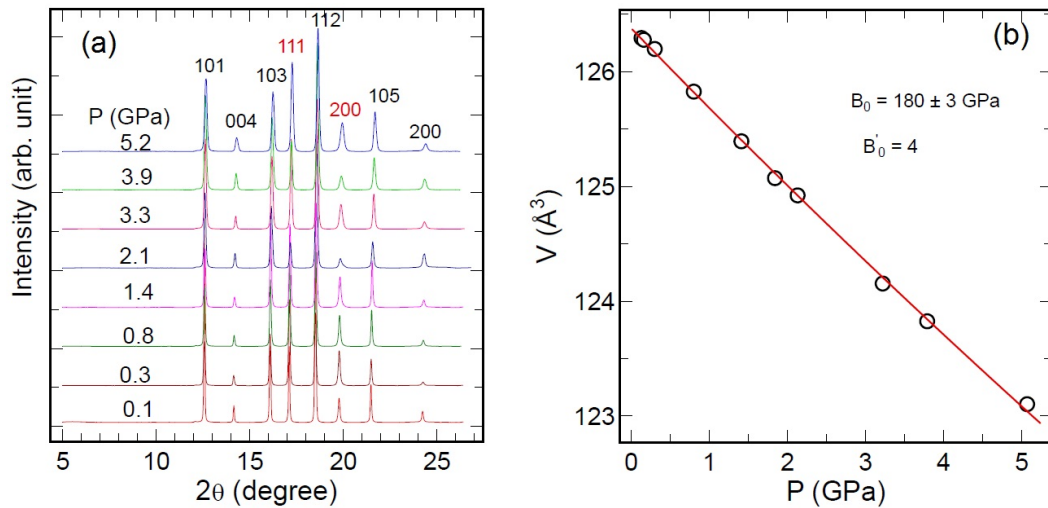


Figure 6.1: (a) Selected XRD patterns of NbP under various pressures up to 5.2 GPa at room temperature with  $\lambda = 0.7001 \text{ \AA}$ . (b) Unit cell volume as a function of pressure for NbP. The solid line represents the fitted results using the third order Birch-Murnaghan equation of state.

High pressure X-ray powder diffraction was performed up to  $\sim 5.2$  GPa and Fig 6.1 (a) shows the selected XRD patterns at various pressures. The ambient pressure phase is stable up to the highest pressure of the measurement. Fig. 6.1 (b) shows pressure dependence of unit cell volume. Bulk modulus is estimated to be  $\sim 180$  GPa as calculated from the third order Birch murnaghan EOS. Its bulk modulus is similar to NbAs but it is more stable compared to TaAs.

### 6.3.2 Resistance measurements:

Fig. 6.2 (a) shows the temperature dependence normalized resistance of single crystal NbP under several pressures up to 6.1 GPa at zero field as well as at 7 T. Earlier metallic behavior was reported at ambient pressure and zero field [85]. At a small pressure of 0.7 GPa, the room temperature resistance decreases upon cooling down to  $\sim 55$  K and for lower temperature it increases i.e. resistance data shows a

minimum  $T_m$  around  $\sim 55$  K at 0.7 GPa. When a magnetic field of 7 T is applied at this pressure the resistance curve shows complete semiconducting behavior as shown in the same graph with identical colour at respective pressures and such magnetic field induced semiconducting behavior at 0.7 GPa is similar to that of the ambient pressure field dependence [85]. At the highest pressure of 6.1 GPa, the resistance also shows complete semiconducting behaviour.

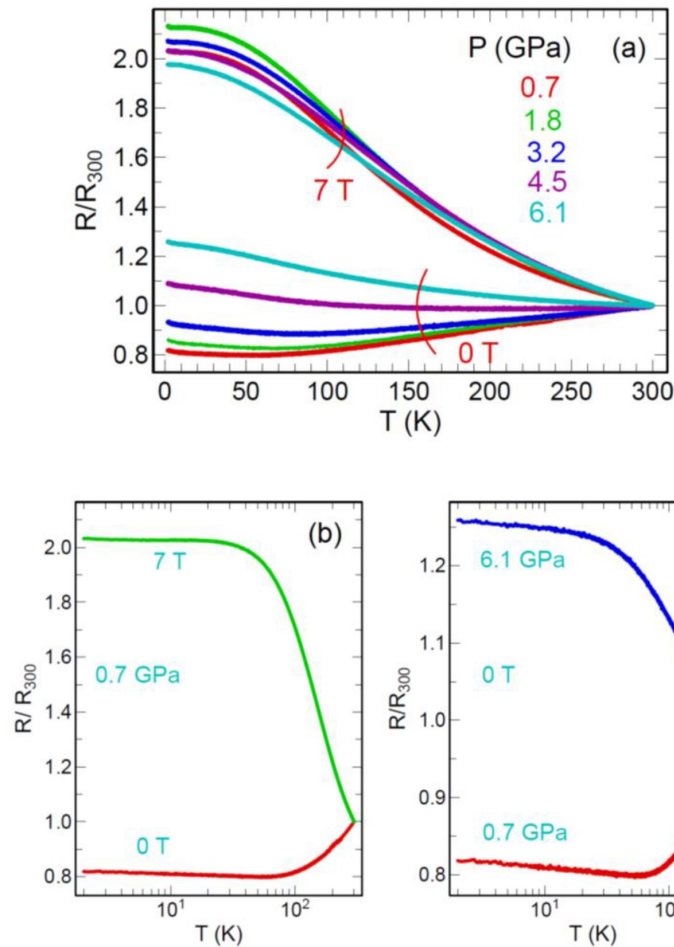


Figure 6.2: (a) Normalized Electrical resistance plotted as a function of temperature at various pressures up to 6.1 GPa at zero field as well as at 7 T. (b), (c) Comparison of the effect of magnetic field and pressure on NbP. (b) At 0.7 GPa, the normalized resistance of NbP is plotted as a function of temperature at zero field (red line) and at a field of 7 T (Green). (c) Temperature dependence normalized resistance at 0.7 (Red) GPa and at 6.1 (Blue) GPa with no applied magnetic field

Fig. 6.2 (b), (c) compare the effect of magnetic field with the effect of applied pressure on the temperature dependence normalized resistance of single crystal NbP.

A complete semiconducting like increase in resistance is observed with decreasing the temperature when a magnetic field of 7 T is applied at 0.7 GPa as shown in Fig. 6.2 (b). Fig. 6.2 (c) illustrates that the resistance shows analogous behavior under application of pressure of 6.1 GPa. Therefore if we compare the effect of pressure and magnetic field and it may be concluded that, the increase of magnetic field is equivalent to increase in pressure as both the external parameters induce same phenomenological changes in the normalized resistance of NbP.

Fig. 6.3 (a) shows the temperature dependence resistance under several pressures at zero field in a semi log scale. In this plot the resistance minimum behavior is clearly observed and most importantly, a resistance plateau is developed at low temperature. As the pressure is increased, resistance minimum shifts to higher temperature and the system become completely semiconducting at the highest pressure of the measurement.

Such kind of temperature behavior is called turn-on temperature behavior. Similar turn-on and plateau behavior at low temperature was reported in wide range of topological semimetals under applied magnetic field [55]. NbP is the only compound which shows such behavior under applied magnetic field as well as under applied pressure. To obtain the pressure dependence of the turn-on temperature  $T_m$  and plateau temperature  $T_i$ ,  $dR/dT$  is plotted as a function of temperature and  $T_m$  and  $T_i$  are defined as shown in the Fig. 6.3 (b).  $T_i$  remains almost independent of pressure but  $T_m$  increases significantly with pressure as shown in Fig. 6.3 (c).

### 6.3.3 Hall Measurements:

Hall Effect measurement was performed to determine the nature of the charge carriers. Fig. 6.4 shows the field dependence of Hall resistance ( $R_{xy}$ ) at two different pressures at 2 K with the applied magnetic field perpendicular to the current. At 0.7 GPa, the Hall resistance shows nonlinear behavior and it is initially positive

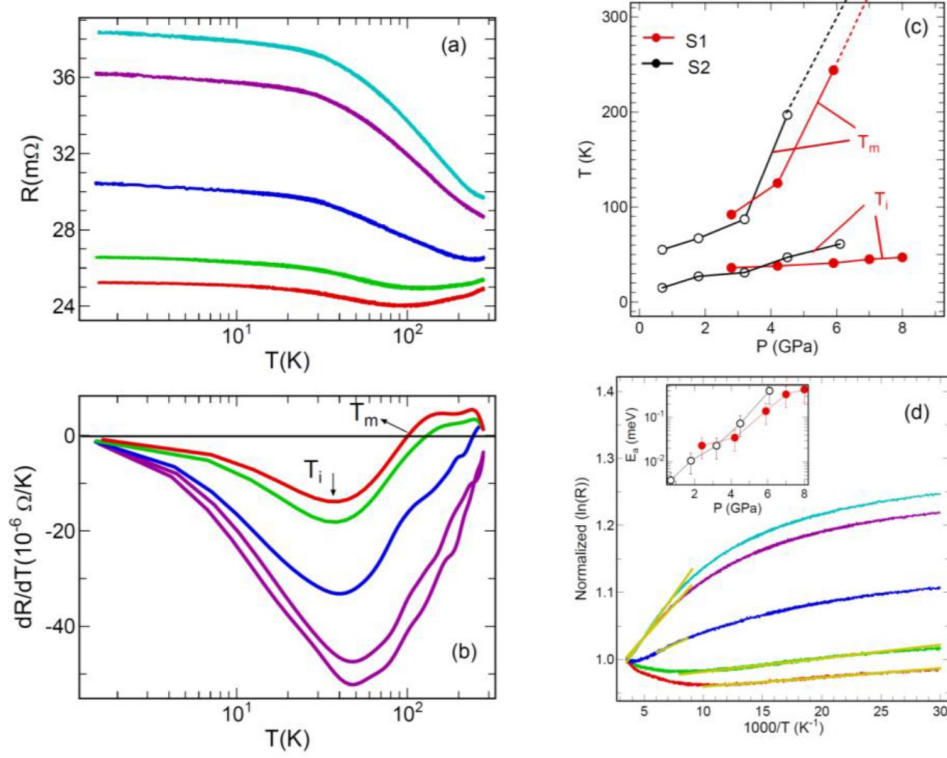


Figure 6.3: (a) Temperature dependence resistance under various pressures in a semi log scale (b)  $dR/dT$  as function of temperature defining the transition temperatures  $T_m$  and  $T_i$  (c) Pressure dependence of  $T_m$  and  $T_i$  (d) Normalized  $\ln(R)$  as a function of  $1000/T$ . The yellow lines represent the fitting results  $R(T) = R(0) + e^{E_a/2KT}$ . Inset shows the pressure dependence of the activation gap.

below  $\sim 4$  T but changes sign from positive to negative at higher magnetic field. As we increase the pressure, the sign reversal field decreases. Now, in conventional two band model the Hall coefficient can be written as,

$$R_H(B) = \frac{(n_h \mu_h^2 - n_e \mu_e^2)^2 + (n_h - n_e) (\mu_h \mu_e B)^2}{e (n_h \mu_h + n_e \mu_e)^2 + (n_h - n_e)^2 (\mu_h \mu_e B)^2}, \quad (6.1)$$

where,  $e$  represents the electronic charge,  $n_{e(h)}$  and  $\mu_{e(h)}$  represent the carrier concentrations and mobilities of the electrons (holes). At low field limit this expression reduces to,

$$R_H(B) \sim \frac{1 (n_h \mu_h^2 - n_e \mu_e^2)^2}{e (n_h \mu_h + n_e \mu_e)^2} \quad (6.2)$$

And at high field limit it is written as,

$$R_H(B) \sim \frac{1}{e (n_h - n_e)} \quad (6.3)$$

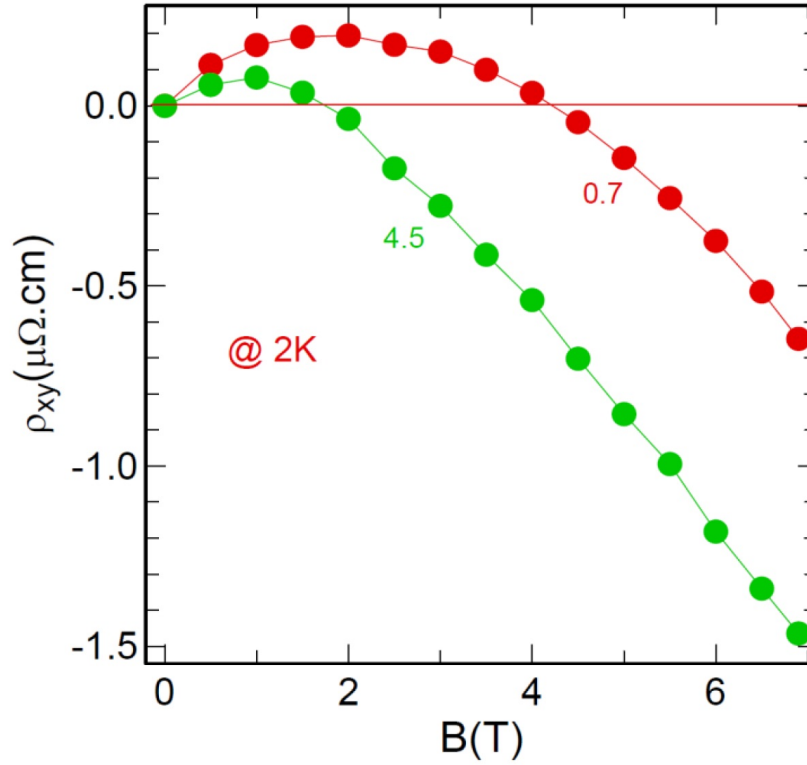


Figure 6.4: Magnetic field dependence of the Hall resistance at two different pressures up to 7 T.

The nonlinearity in field dependence Hall resistance always comes from the presence of two kinds of carriers. The positive Hall resistance at low field suggests that holes with high mobility and higher carrier concentration dominate over the low mobility electrons. High field sign reversal is observed when the hole concentration become much smaller than the electron concentrations as suggested by equation 6.3. Decrease in sign reversal field with pressure indicates the decrease in hole mobility with pressure. Similar nonlinearity and sign reversal in hall resistivity was observed in NbSb<sub>2</sub> [95], NbAs<sub>2</sub> [269], ZrSiS [270] and WTe<sub>2</sub> [271] at ambient pressure which confirmed the multi band effects in these compounds.

#### 6.3.4 MR measurements:

At the lowest pressure (0.7 GPa) of our measurements the MR is about  $\sim 254\%$  at 7 T. This value is much smaller than the ambient pressure value (of the order of  $10^5\%$ ) as measured by Shekhar et al. [85]. There are two possible main reasons behind

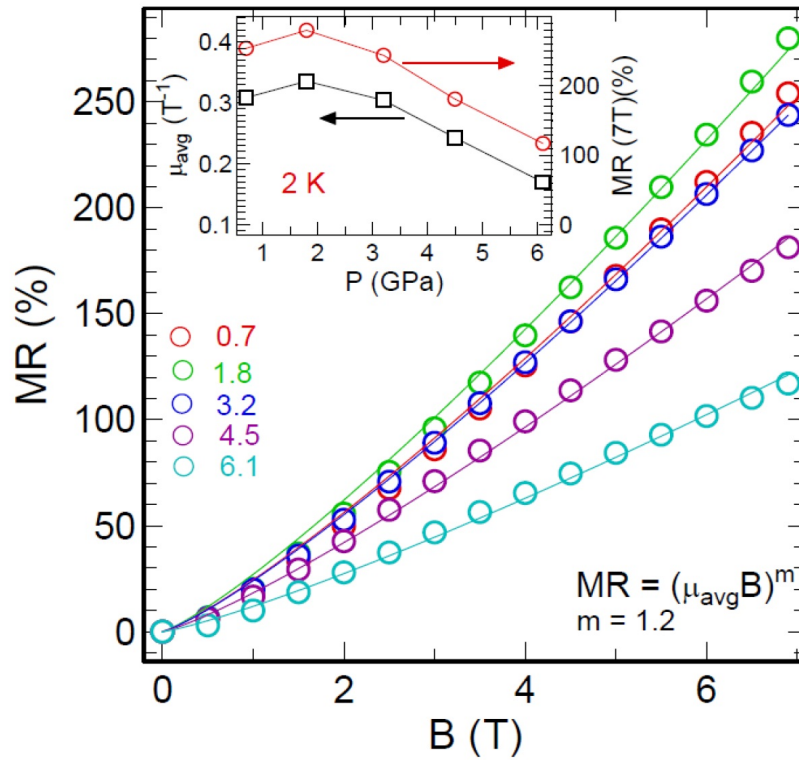


Figure 6.5: Field dependence magnetoresistance of NbP single measured at 2 K under several pressures up to 6.1 GPa. The inset shows the pressure dependent average mobility and MR ( at 7 T). Average mobility  $\mu_a$  at each pressure is obtained by fitting the field dependence MR to the formula  $MR = (\mu_a B)^m$  with  $m=1.2$ . Both  $\mu_{avg}$  and MR show similar pressure dependence.

this: (i) In high pressure measurements the direction of the magnetic field with respect to the current direction is not well defined; (ii) Use of solid pressure medium creates non-uniform stress under pressure which may decrease the mobility of the carriers as well as the MR. Similar reduction in MR under pressure was observed in TaP [29] and NbAs<sub>2</sub> [269].

The average mobility of the charge carriers can be obtained by using the power-law  $MR = (\mu_a B)^m$ , where  $m$  measures the accuracy of the electron hole compensation. For perfect electron hole compensation  $m = 2$ . At ambient pressure  $\mu_a = 220 T^{-1}$  with  $m = 1.2$  which implies that the electron hole compensation is not so perfect in NbP as suggested by the earlier works. In this work, field dependence MR data at all pressures are fitted with the aforementioned equation keeping  $m = 1.2$  fixed. The solid lines with respective colors represent the fittings of the MR data

of respective pressures (Fig 6.5). At 0.7 GPa,  $\mu_a \sim 0.3$  which is much smaller than the ambient pressure value. This clearly indicates that the huge reduction of the mobility under non-uniform pressure of 0.7 GPa from ambient pressure causes the huge reduction of MR as mentioned earlier. Upon increasing pressure, both  $\mu_a$  and MR show similar pressure dependence which further suggests that the suppression of MR is closely related to the reduction of the average mobility under pressure.

## 6.4 Results on NbAs

### 6.4.1 XRD under pressure:

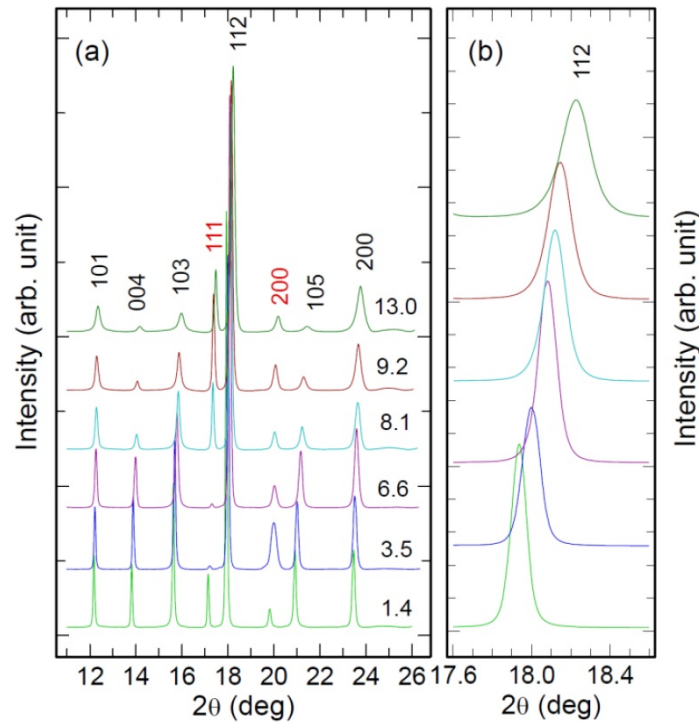


Figure 6.6: (a) Powder XRD patterns of NbAs at selected pressures. The wavelength of the used monochromatic X-ray was  $0.70001 \text{ \AA}$ . (b) Evolution of the (112) peak as a function of pressure.

High pressure XRD measurements were performed to verify the structural stability of NbAs up to  $\sim 13$  GPa. Figure 6.6(a) displays the selected XRD patterns at various pressures at room temperature. At 1.4 GPa, the lowest pressure of our measurements all the peaks can be fitted with the ambient  $I4_1md$  structure. Apart

from the slight right shifts of all the peaks, as shown for the major 112 peak in Fig 6.6(b), application of pressure does not significantly change the diffraction profiles throughout the applied pressure range. So the ambient structure is stable up to the highest pressure of our measurements. This result is similar to both the earlier measurements where the authors have reported that the ambient NbAs structure is stable up to 26 GPa [105,266]. To determine the bulk modulus ( $B_0$ ) of the ambient structure of NbAs we fitted the  $V$  vs  $P$  data by 3rd order Birch-Murnaghan equation of state (Fig. 6.7). The obtained fitting parameters are; Bulk modulus ( $B_0$ ) =  $174 \pm 3.8$  GPa,  $B_0' = 3.5$  and  $V_0 = 139.0 \text{ \AA}^3$ . The obtained bulk modulus is consistent with the earlier measurements ( $B_0 = 180$  GPa) and comparable with the other compounds in TaAs family.

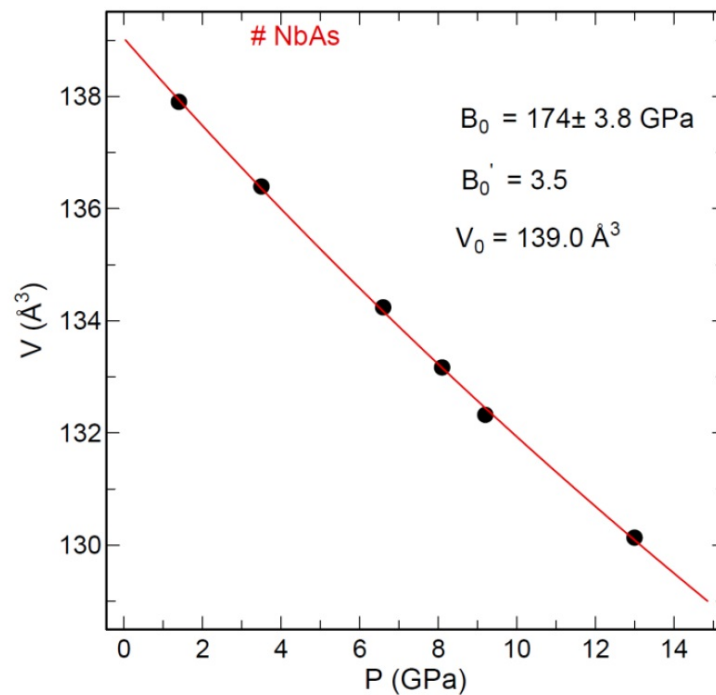


Figure 6.7: Pressure dependence of the unit cell volume of NbAs. Solid line represents the fitted  $3_{rd}$  order Birch-Murnaghan equation of state.

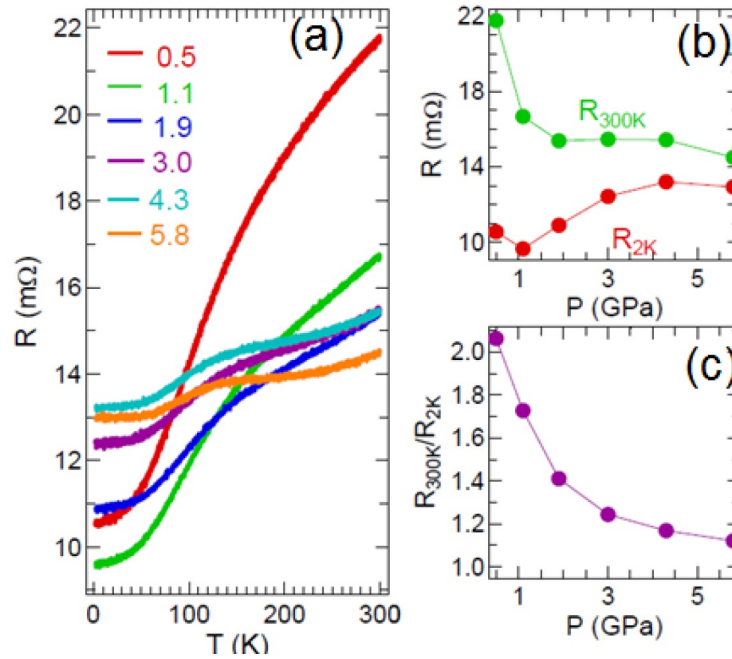


Figure 6.8: (a) Electrical resistance ( $R(T)$ ) as a function of temperature under various pressures up to 5.8 GPa. (b) Pressure dependent resistance at two different temperatures of 300 K and 2K. (c) Resistance ration ( $R_{300}/R_{2K}$ ) as a function of pressure.

### 6.4.2 High Pressure Magnetotransport measurements on NbAs:

Fig. 6.8 (a) shows the temperature dependence resistance under various pressures up to 5.8 GPa. At a initial pressure of 0.5 GPa the resistance shows semimetallic behavior similar to ambient pressure behavior [105]. As we increase the pressure room temperature resistance decreases with pressure whereas the low temperature resistance first decreases up to  $\sim 1.1$  GPa and then increases above this pressure as shown in Fig. 6.8 (b).

Fig. 6.8 (c) shows the resistance ratio ( $R_{300K}/R_{2K}$ ) as a function of pressure. Resistance ratio systematically decreases with pressure which indicates that the metallicity is decreasing in NbAs with increasing pressure. But up to the maximum pressure of our measurement the system remains metallic unlike the pressure induced non-metallic transition in NbP.

Fig. 6.9 shows the temperature dependence normalized resistance at various

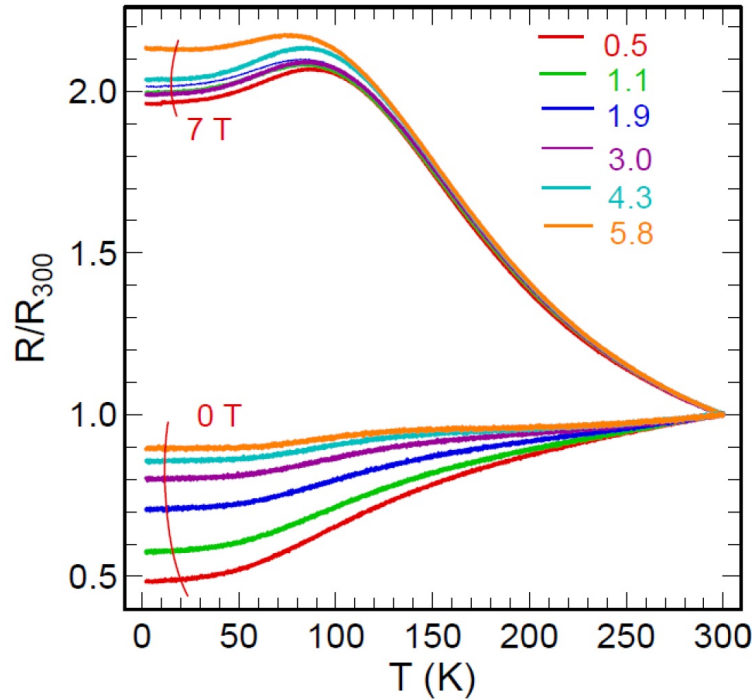


Figure 6.9: Temperature dependence normalized electrical resistance at various pressures and magnetic fields.

pressures and magnetic fields. Pressure induced suppression of metallicity is more clear from the ambient field curves and we may conclude that higher pressure may transform this system into non metallic system similar to the case of NbP. Magnetic field induced metallic to non metallic transition is observed in all pressure similar to ambient pressure [88,105]. Apart from that a peak like behaviour is observed in the temperature dependence resistance under magnetic field, with negligible pressure dependence of its peak position. Similar peak like resistance behaviour was also observed in NbAs [267], TaAs [112], ZrTe<sub>5</sub> and HfTe<sub>5</sub> [268] at ambient pressure but the origin of this is not well established.

Fig. 6.10 (a) shows field dependence magnetoresistance (MR) at 2K under various pressures. Asymmetric field dependence originates from the Hall contributions. At initial pressure of 0.5 GPa MR is about 600 % at 7 T and 2 K. The possible reasons of smaller value of this MR than the ambient pressure value have been discussed earlier. As we increase the pressure MR value systematically decreases with

pressure. Fig. 6.10 (b) shows the field dependence of Hall resistivity and the inset shows the enlarge view at low field. Hall resistivity changes systematically with pressure within our experimental pressure range. As the pressure is increased hall resistivity changes from nonlinear field dependence to almost linear field dependence behaviours which indicate the system changes from a two carrier to a single carrier system under pressure.

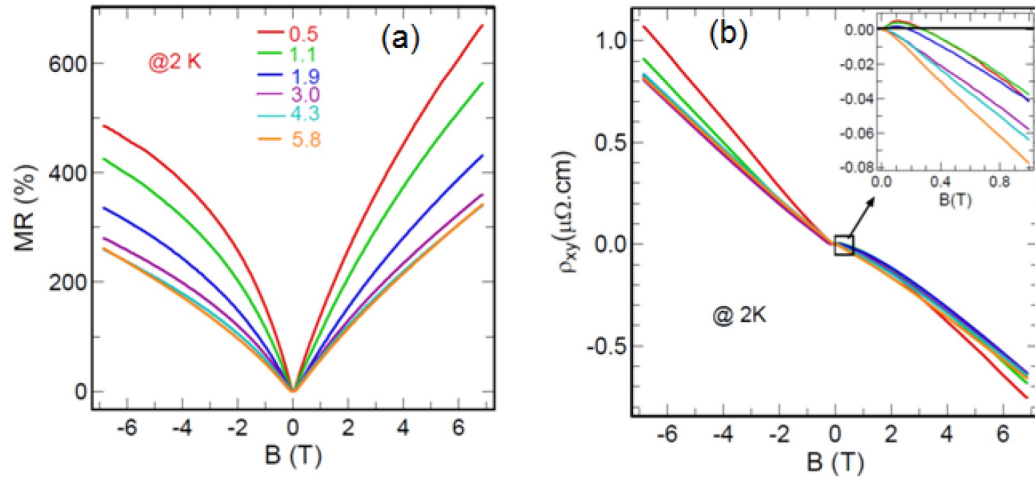


Figure 6.10: (a) Field dependence magnetoresistance (MR) at 2K under various pressures up to 5.8 GPa. (b) Field dependence Hall resistivity under similar environments. The inset shows the enlarge view of the Hall resistivity at low field.

Fig. 6.11 (a) and (b), respectively, illustrate the temperature dependence MR and Hall resistivity at 7 T under various pressures. Both MR and Hall resistivity at 0.5 GPa show similar temperature dependence to that of the ambient pressure behaviour [88,105] and pressure systematically suppress both MR and absolute value of the Hall resistivity which is more clear in the inset of Fig. 6.11 (b).

## 6.5 Discussions:

The transport signature of topological insulator is an initial increase in resistance followed by a resistance plateau.  $\text{SmB}_6$  is an ideal example of topological insulator at ambient pressure [54,56]. Magnetic field induced topological insulator like transport behaviour has been observed in various kind of topological semimetals including

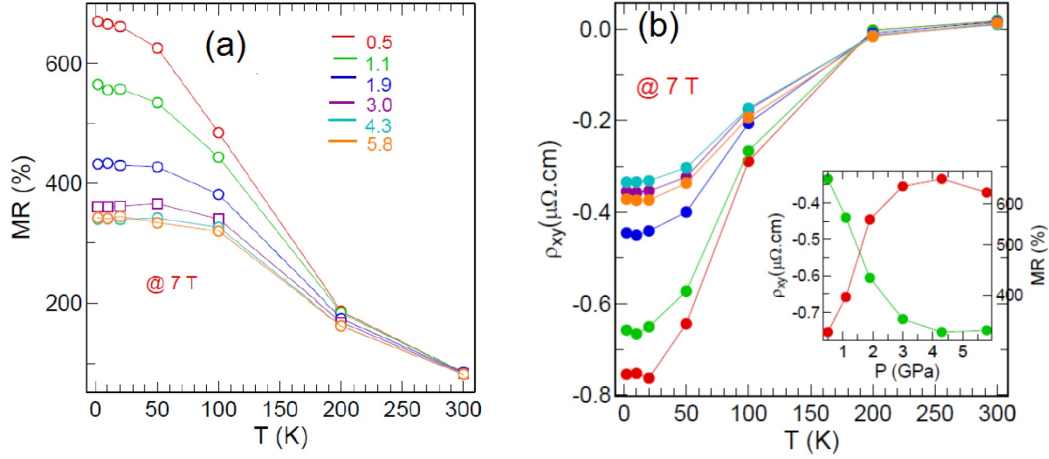


Figure 6.11: (a) Temperature dependence of MR at 7 T under various pressures. (b) Temperature dependence of hall resistivity at 7 T under various pressures. The inset shows pressure dependence of MR and Hall resistivity at 2K and 7 T.

LaSb and NbP [54, 85]. But the main problem is that, whenever the magnetic field is applied the time reversal symmetry (TRS) is no more preserved in the system. Thus the magnetic field induced non-metallic behaviour cannot be concluded as topological insulating behaviour. But similar transport behaviour is observed in NbP under applied pressure. As pressure does not change the time reversal symmetry of a system, we can conclude this transition as possible Weyl semimetal to topological insulator transition under pressure. One point is to remember that in case of topological insulator system like  $\text{SmB}_6$  [56], the bulk resistance is very large and in comparison of that the non metallic resistance in NbP under pressure is very small. Thus to confirm this transition as pressure induced Weyl semimetal to topological insulator transition, further verification is needed.

## 6.6 Conclusions:

Here we present our detailed high pressure-low temperature resistivity and magneto-resistance results on single crystal NbP and NbAs up to  $\sim 7$  GPa. Pressure induced metallic to non-metallic transition is observed in NbP. The insulating like resistivity followed by plateau reveals the possible Weyl semimetal to topological insulator

transition under pressure. NbP is the only compound which shows such behavior under applied magnetic field as well as under applied pressure. NbAs also shows field induced nonmetallic behavior at high pressure similar to the ambient pressure. Pressure reduced the metallicity and higher pressure may transform this system into a non-metallic system Similar to NbP. Pressure also suppresses both MR and the magnitude of Hall resistivity. No structural transition up to  $\sim 13$  GPa.

# Chapter 7

## High pressure transport and magneto-transport measurements in the type-II Weyl semimetal TaIrTe<sub>4</sub>

### 7.1 Introduction

In WSMs a linear crossing of two Weyl bands occurs at the Fermi level giving rise to a gapless bulk state and they are realised in the materials where either time-reversal or inversion symmetry is broken [77, 78]. Depending on the tilting of the Weyl cones and whether the Lorentz symmetry is respected, these Weyl semimetals (WSMs) can be divided into two topologically distinct types: type-I WSMs and type-II WSMs [77, 78]. Recently, orthorhombic binary compounds MTe<sub>2</sub> (M = W, Mo) and ternary compound TaIrTe<sub>4</sub> has been predicted and experimentally identified as type II WSMs [114, 115, 130, 233, 274]. TaIrTe<sub>4</sub> crystallizes in the same noncentrosymmetric orthorhombic structure as WTe<sub>2</sub> and MoTe<sub>2</sub> but in contrast to those the size of the unit cell is doubled in the b-direction (figure 7.1).

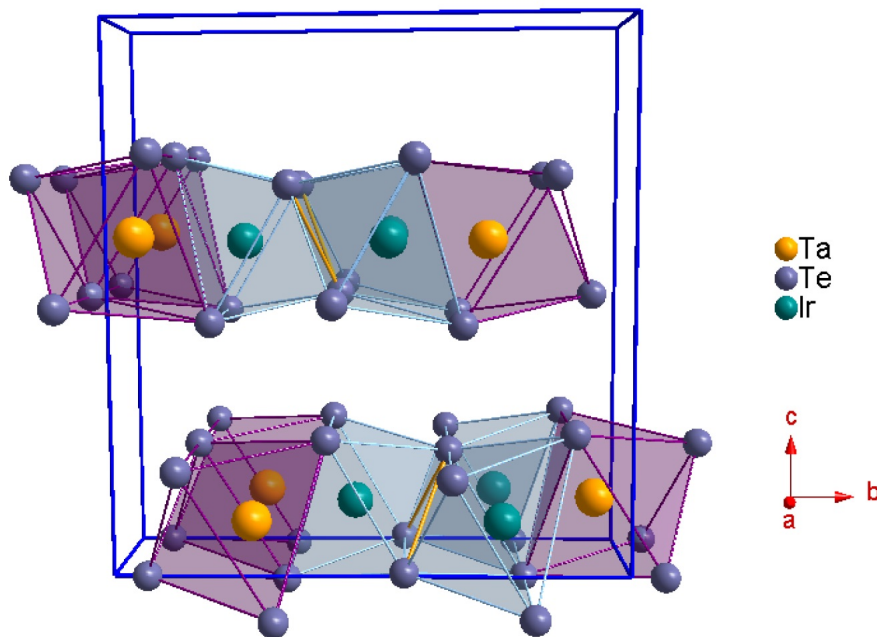


Figure 7.1: Crystal structure of TaIrTe<sub>4</sub>; space group 31 (Pmn2<sub>1</sub>).

Two recent high pressure investigations on  $\text{WTe}_2$  reveal that application of pressure successfully induce superconductivity in this compound [30,99]. Both the results suggest that the superconducting transition temperature ( $T_c$ ) shows dome-shaped pressure dependence and the emergence of superconductivity occurs after significant suppression of magnetoresistance. The sister compound,  $\text{MoTe}_2$  also exhibits superconductivity ( $T_c = 0.1$  K) at ambient pressure [31]. Application of pressure establishes the similar dome-shaped superconducting phase diagram [31]. So the similar high pressure investigations on the iso-structural  $\text{TaIrTe}_4$  will help to understand the general dome shaped superconducting phase diagram which may provides insights into the interplay between superconductivity, topological physics and extreme magnetoresistance (XMR).

Earlier theoretical calculations demonstrated that  $\text{TaIrTe}_4$  is a type-II Weyl semimetal with the simplest possible arrangement of four Weyl points occurring at very similar points in k-space [130]. This is, further, realized experimentally by direct observation of the topological surface states and Fermi arcs with a unique spin texture [233]. Unconventional surface superconductivity with quasi-1D characteristics coexisting with strong Shubnikov de Haas (SdH) oscillations is also discovered in  $\text{TaIrTe}_4$  single crystals with an onset transition temperature ( $T_c$ ) up to 1.54 K [115]. The observed unconventional superconductivity with the p-wave pairing and the nontrivial topological properties revealed by quantum oscillations demonstrate that  $\text{TaIrTe}_4$  might be a candidate for topological superconductors [115]. But another recent report observed that no superconductivity was observed below  $\sim 23.8$  GPa and pressure induced superconductivity was observed at this pressure with a transition temperature of  $\sim 2.1$  K [114]. Their structural investigations revealed pressure induced structural distortion near the critical pressure which changed the topology of the Fermi surface which concluded that the pressure induced superconductivity was no longer topological in nature. Therefore the nature of the superconductivity

in TaIrTe<sub>4</sub> remained controversial [114, 115].

Thus, high pressure reinvestigation is needed to verify the general dome shaped superconducting phase diagrams observed in the iso-structural WTe<sub>2</sub> and MoTe<sub>2</sub> and to conclude about the robustness of the unconventional nature of the superconductivity observed at the ambient pressure. This will help to comment about the topological features of TaIrTe<sub>4</sub>.

Here we investigate high pressure transport and magnetotransport measurements on polycrystalline TaIrTe<sub>4</sub> along with high pressure XRD measurements. Pressure induced superconductivity is observed at the initial pressure of the measurements. Superconducting transition temperature shows dome shaped pressure dependence similar to the other type-II WSMs like WTe<sub>2</sub> and MoTe<sub>2</sub>. High pressure structural investigations reveal phase stability of the ambient pressure structure up to the highest pressure of the measurements ( $\sim 11$  GPa).

## 7.2 Experimental Details:

Polycrystalline TaIrTe<sub>4</sub> compounds were synthesized from a reaction of the powder of the elementary materials in an atomic ratio of Ta:Ir:Te = 1:1:20. Elementary materials were ground, palletized and placed inside a quartz tube under vacuum. The tube was then placed in a furnace, heated up to 1000 °C and slowly cooled down (2 °C/h) to 700 °C. Black polycrystalline sample was identified and characterized by XRD measurement.

Temperature dependent electrical resistance and magnetoresistance were measured under high pressure up to  $\sim 13$  GPa by using a non magnetic Cu-Be diamond anvil cell compatible for a SQUID magnetometer as discussed in **chapter 2**. High pressure structural investigation has also been carried out in this compound up 11

GPa using Synchrotron based X-ray diffraction studies under non-hydrostatic pressure condition in order to correlate structural and electronic evolution with identical pressure environment. Detailed measurement procedure can be found in **chapter 2**.

## 7.3 Results:

### 7.3.1 Resistance and magnetoresistance measurements under pressure

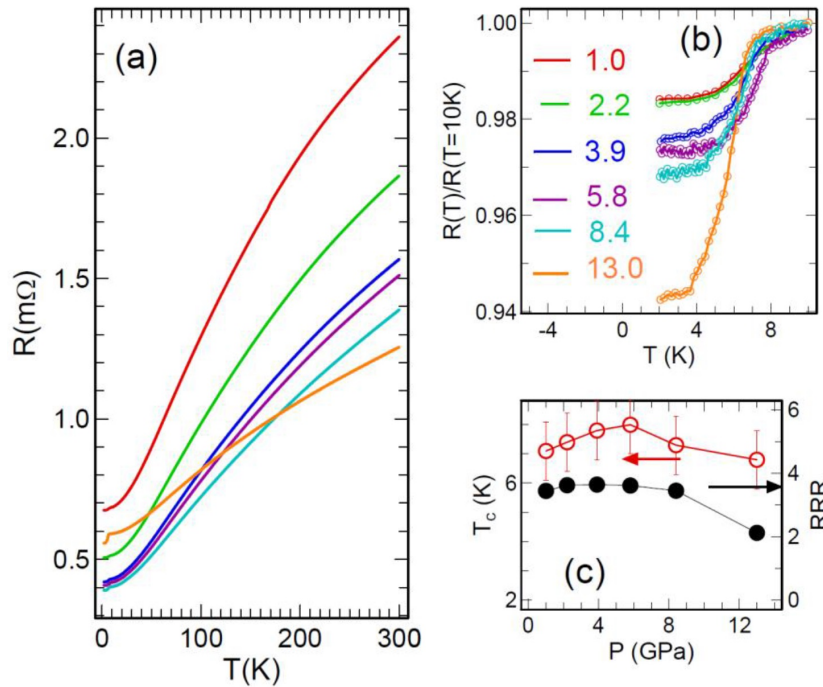


Figure 7.2: (a) Temperature dependence of electrical resistance of polycrystalline TaIrTe<sub>4</sub> sample under various pressures up to 13 GPa. (b) Temperature dependence of normalized resistance displaying the superconducting transition temperature. (c) Pressure dependence of  $T_c$  and RRR.

Figure 7.2 (a) shows the temperature dependence electrical resistance of polycrystalline TaIrTe<sub>4</sub> at various pressures up to 13 GPa. At the initial pressure (1.0 GPa) of the measurements the resistance shows metallic behaviour similar to the ambient pressure behaviour. In addition to that a low temperature resistance drop

around  $\sim 7$  K is observed at this pressure which is suggested as the pressure induced superconductivity in the powdered  $\text{TaIrTe}_4$  compound and as the pressure is increased further the drop become more pronounced as shown in figure 7.2 (b). Figure 7.2 (c) shows pressure dependence of superconducting transition temperature ( $T_c$ ) and residual resistance ration, RRR ( $\text{RRR} = R(300\text{K}) / R(10\text{K})$ ).  $T_c$  shows dome shaped superconducting phase diagram similar to  $\text{WTe}_2$  and  $\text{MoTe}_2$ . Although RRR remains almost unchanged at lower pressure range, it starts decreasing above  $\sim 5$  GPa, indicating poor metallic character at high pressure which resulted in reduced  $T_c$  at high pressure. Superconducting zero resistance is not observed in our measurements which might be due to surface or filamentary nature of the superconductivity that needs further investigations.

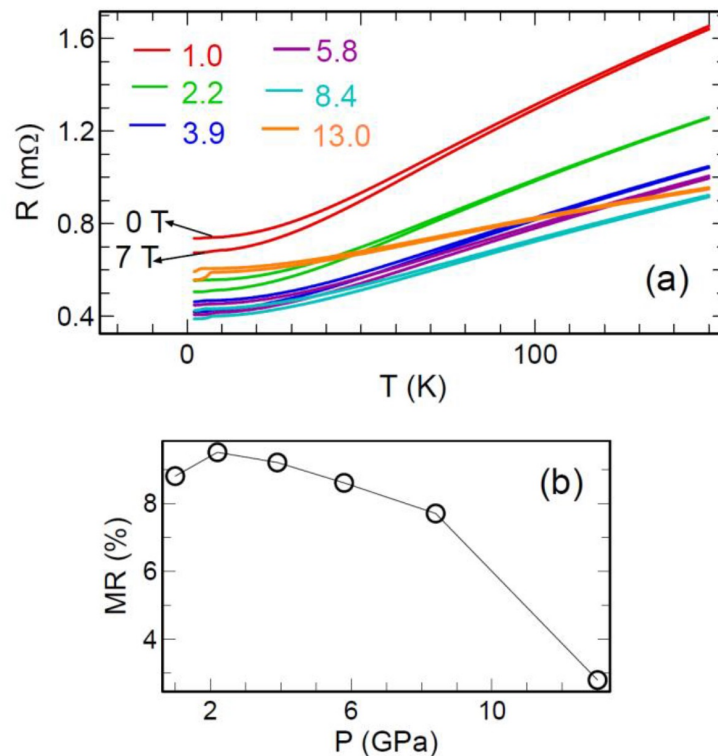


Figure 7.3: (a) Temperature dependence of resistance at various pressures and magnetic fields. (b) MR as a function of pressure

Figure 7.3 (a) shows the resistance of polycrystalline  $\text{TaIrTe}_4$  as a function of temperature at various pressures and magnetic fields. As the pressure is increased

the magneto-resistance decreases which is more clearly observed in figure 7.3 (b). MR marginally increases up to  $\sim 2$  GPa and then starts decreasing.

Figure 7.4 (a) and 4 (b) show the temperature dependence resistance in the vicinity of  $T_c$  under various magnetic fields at 8.4 and 13.0 GPa respectively. At both the pressures,  $T_c$  shifts to lower temperature as the field is increased. These measurements support the resistance drop as superconducting transition for this powdered TaIrTe<sub>4</sub> sample.

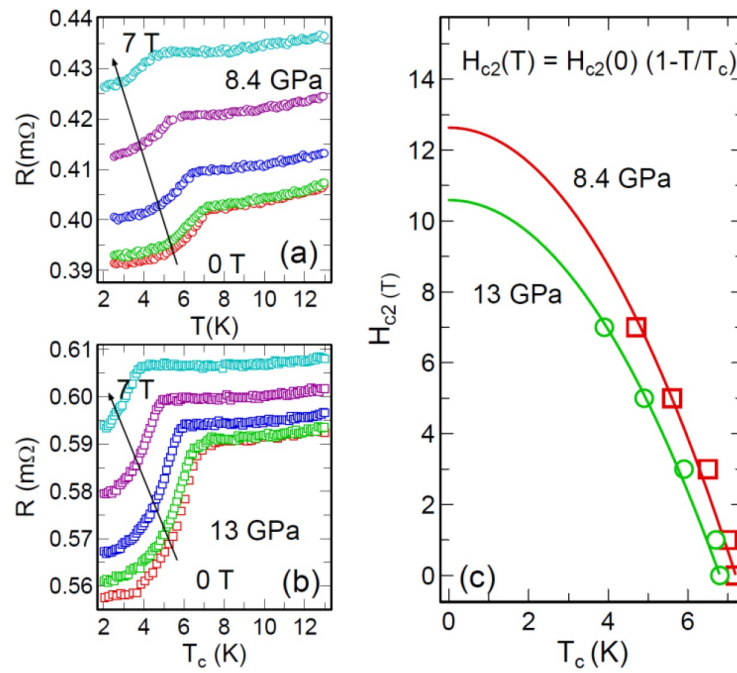


Figure 7.4: (a), (b) Temperature dependence of resistance at various magnetic fields measured as 8.4 GPa and 13 GPa respectively. (c) Corresponding  $H_{c2}$  Vs.  $T_c$  plots

In figure 7.4(c)  $H_{c2}$  is plotted as a function of  $T_c$  at two different pressures. These data are well fitted with the Ginzburg -Landau equation  $H_{c2}(T) = H_{c2}(0) \times (1 - T/T_c)^2$ , where  $H_{c2}(0)$  is the zero temperature upper critical field. From the fitting we can estimate the  $H_{c2}(0)$  as  $\sim 13$  T and  $\sim 11$  T at 8.4 GPa and 13 GPa respectively. In case of WTe<sub>2</sub> [30] and MoTe<sub>2</sub> [31] temperature dependent positive curvature in  $H_{c2}$  was observed which is absent in case of TaIrTe<sub>4</sub> and the value of  $H_{c2}(0)$  is much very compared to these compounds. From the estimated upper critical field we can calculate the Ginzburg-Landau coherence length  $\xi_{GL} = \sqrt{\Phi_0/2\pi H_{c2}(0)} = \sim 5$  nm is

much less compared to  $\text{WTe}_2$  and  $\text{MoTe}_2$  [30,31]. It can also be noticed that the estimated value of  $H_{c2}(0)$  is comparable to Bardeen, Cooper and Schrieffer (BCS) weak-coupling Pauli limit,  $H_p = 1.86 \times T_c$ .

### 7.3.2 XRD measurements under pressure:

High pressure synchrotron based XRD measurements were carried out to identify any structural transition in our experimental pressure range. Figure 7.5 shows the XRD patterns at various pressures up to 13 GPa. The result indicates no structural transition up to 13 GPa i.e the ambient structure is stable in our experimental pressure range.

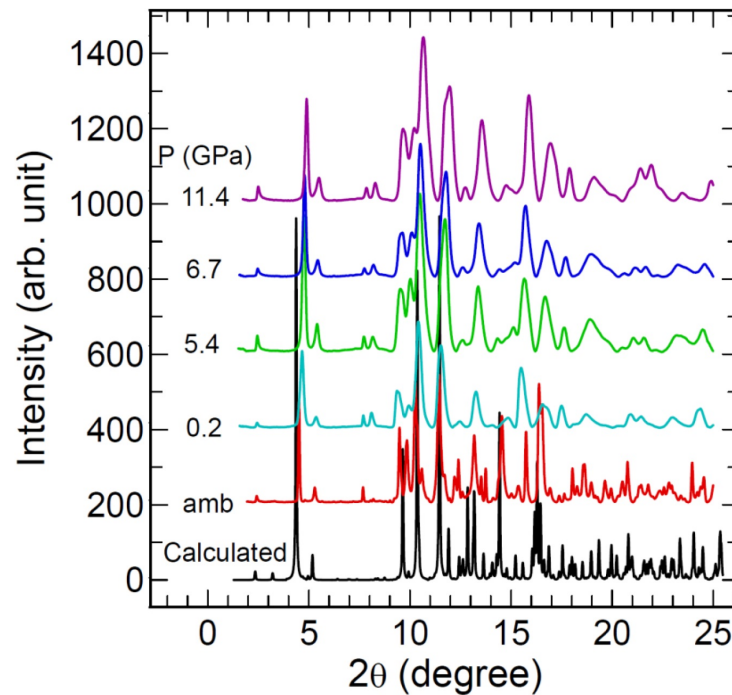


Figure 7.5: Synchrotron based XRD patterns of  $\text{TaIrTe}_4$  at various pressures up to 11.4 GPa ( $\lambda = 0.4957 \text{ \AA}$ ).

In figure 7.6, we have plotted the unit cell volume of  $\text{TaIrTe}_4$  as a function of pressure. This data is fitted with third order Birch-Murnaghan equation of state. Bulk modulus is estimated as 126.8 GPa which is very large compared to  $\text{WTe}_2$  i.e  $\text{TaIrTe}_4$  is less compressible compared to iso-structural  $\text{WTe}_2$  [275].

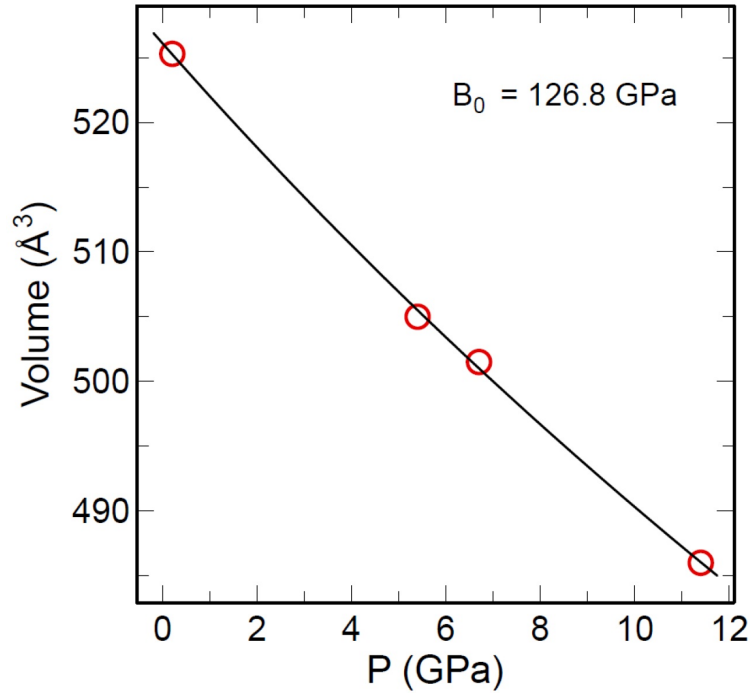


Figure 7.6: Unit cell volume as a function of pressure in polycrystalline TaIrTe<sub>4</sub>. Black solid line represents the fitting line based on third order Birch-Murnaghan equation of state.

## 7.4 Discussions:

Observed superconducting properties of TaIrTe<sub>4</sub> remain controversial. In one study, unconventional surface conductivity with p-wave pairing is reported at ambient pressure with superconducting transition temperature ( $T_c$ ) ranging from  $\sim 1.19$  K to  $\sim 1.54$  K depending upon the RRR ratio of various TaIrTe<sub>4</sub> which indicates that the  $T_c$  strongly depends on the metallicity of the sample [115]. Appearance of superconductivity in ambient pressure Weyl semimetallic phase concluded that TaIrTe<sub>4</sub> might be a possible candidate for topological superconductors [115]. In another study, no superconductivity was observed at ambient pressure down to 0.5 K. Even, no pressure induced superconductivity was observed up to 23.8 GPa. Superconductivity emerged at this pressure by simultaneous structural distortion leading to change in the topology of the band structure [114]. Our result shows superconductivity at the ambient pressure Weyl semimetallic phase with much enhanced  $T_c$

compare to ref. [115] and  $T_c$  shows dome shaped pressure dependence similar to the other type-II Weyl semimetal,  $WTe_2$  and  $MoTe_2$ . Thus our results support that  $TaIrTe_4$  might be a possible topological superconductor similar to the report by Y Xing et al. [115] but further verifications are needed to confirm this.

## 7.5 Conclusions:

Temperature dependence of electrical resistance and room temperature XRD measurement has been performed on polycrystalline  $TaIrTe_4$  under various pressures. Low temperature resistance drop is observed at 1.0 GPa and becomes more and more pronounced as we increase the pressure. This low temperature drop below 7 K is recognized as superconductivity as confirmed by the field dependent measurements. Transition temperature ( $T_c$ ) shows dome shaped pressure dependence similar to  $WTe_2$  and  $MoTe_2$ . Our XRD measurement reveals no structural transition up to 11.4 GPa which indicates that the superconductivity appears in the ambient pressure Weyl semimetallic phases. Thus our result of pressure induced superconductivity might be concluded as topological superconductivity in  $TaIrTe_4$ .

# Chapter 8

## Conclusions and Outlook

The current thesis experimentally investigates the effect of high pressure on some selected topological compounds. Electrical and structural evolutions of some topological compounds have been studied by means of various transport and spectroscopic techniques under extreme conditions of high pressure, low temperature and high magnetic fields. Both, experimental and theoretical research in topological materials ranging from insulators to metals has attracted much attention in condensed matter physics because of their variety of the electronic band structure. Pressure is always an ideal tuning parameter which can induces various interesting phenomena in these compounds without introducing chemical disorder. In this chapter I will summarize the main experimental results in this thesis and explain what future high pressure experiments can be performed on each of the compounds separately.

### **TiTe<sub>2</sub>**

High pressure transport and spectroscopic studies have been performed on both single crystalline and polycrystalline  $1T$ -TiTe<sub>2</sub>. Theoretical prediction of pressure induced series of topological transitions is confirmed with a structural transition from trigonal to monoclinic structure at  $\sim 8.8$  GPa.

Pressure induced superconductivity is observed above 5 GPa during both hydrostatic and non-hydrostatic compression. Application of non-hydrostatic pressure induces quasicommensurate CDW transition near 1.8 GPa and most surprisingly persistent nature of superconductivity is observed upon decompression at least down to 0.5 GPa with the coexistence of re-entrant CDW state. Upon increasing pressure transition temperature increases with increasing of pressure irrespective of the

compression conditions. The pressure quenchable superconductivity and relatively high upper critical field, makes  $1T$ -TiTe<sub>2</sub> unique among the other layered dichalcogenides and similar non-hydrostatic compression and decompression study are very important for the other layered compounds in this series. The decompression driven observed pressure induced superconductivity also provides a unique opportunity to investigate a pressure quenched superconducting sample for electronic structure by surface-sensitive techniques such as ARPES, ellipsometry, etc.

Infrared reflectance measurement has also been performed on single crystalline  $1T$ -TiTe<sub>2</sub> under pressure up to 22 GPa. The observed conspicuous changes of infrared phonon spectra, in combination with x-ray diffraction data, provide clear evidence of an irreversible structural transition into a noncentrosymmetric space group ( $P\bar{3}m1$  -  $P3m1$ ) at a low pressure ( $\sim 2.3$  GPa), before undergoing a subsequent transition to a monoclinic phase ( $C2/m$ ) above 12 GPa. The pressure-induced irreversible gain of the low-frequency spectral weight of optical conductivity further supports the above crystal structure modification. The irreversible structural modification and associated change in electronic structure have been argued to be responsible for the emergence of superconductivity with enhanced  $T_c$  and its persistence upon decompression. The low-pressure structural instability in  $1T$ -TiTe<sub>2</sub> makes it necessary to revisit the theoretical investigation of its topological nature.

### **Sb<sub>2</sub>S<sub>3</sub>**

Pressure induced structural and electronic investigations have been performed on Sb<sub>2</sub>S<sub>3</sub> by synchrotron based XRD and temperature dependent resistance measurements. Our XRD measurements up to 25 GPa reveal a clear structural phase transition near  $\sim 10$  GPa and ETT near 6 GPa. Temperature dependent (290 K - 1.6 K) resistance measurements were performed under several pressures up to 45 GPa. The activation energy decreases with applied pressure but the gap does not close

up to the highest pressure of our measurement i.e. the system remains insulating up to 45 GPa and the experimental band gap is reversible under decompression which contradicts with the recent results where the authors show pressure induced irreversible metallization at  $\sim 32$  GPa. So our results solve the controversy about the high pressure structural transition and conclude that  $\text{Sb}_2\text{S}_3$  shows persistence metallic character up to  $\sim 45$  GPa with an iso-structural transition near  $\sim 6$  GPa and a structural transition near  $\sim 10$  GPa. Higher pressure measurements beyond 45 GPa will be very important to observe possible pressure induced metallization and superconductivity in superconductivity in  $\text{Sb}_2\text{S}_3$ .

### **AgBiSe<sub>2</sub>**

The signature of the pressure induced electronic topological transition (ETT) and semiconductor-to-metal transition is reported in  $\text{AgBiSe}_2$  using synchrotron based mid-IR reflectivity and electrical resistance measurements. Pressure induced ETT is confirmed above 2 GPa and semiconductor to metal transition is observed near 8.5 GPa. No pressure induced superconductivity was observed up to 11.5 GPa. Higher pressure measurements are desirable to search for pressure induced superconductivity similar to the iso-structural  $\text{Bi}_2\text{Se}_3$  and  $\text{Bi}_2\text{Te}_3$ .

### **NbP and NbAs**

High pressure magnetoresistance and Hall measurement has been studied on two type-I Weyl semimetals NbP and NbAs and the results are compared with LaSb and  $\text{SmB}_6$ . Application of pressure transform NbP into a non-metallic system with low temperature resistance plateau which is indicated as a possible Weyl Semimetal to topological insulator transition. NbP becomes the first compound which shows such behaviour under pressure as well as under magnetic field. Pressure induced superconductivity may be expected at higher pressure similar to TaP. Field induced non-metallic behaviour is also observed in NbAs. Pressure reduces the metallicity

and similar pressure induced metal to non-metal transition may be observed at higher pressure. Theoretical prediction shows that when NbAs crystal is compressed it shows a structural phase transition at 31 GPa similar to TaAs where this transition is observed at 14 GPa. As the transport measurements in TaAs show that the structural transition affects its transport properties, it is also important to observe the effect of the structural transition at 31 GPa in NbAs to its transport properties.

### **TaIrTe<sub>4</sub>**

High pressure structural and transport investigation has been studied on polycrystalline TaIrTe<sub>4</sub>. Pressure induced superconductivity is observed with a superconducting transition temperature  $T_c$  of 7 K.  $T_c$  shows domed shaper pressure dependence similar to the other type-II Weyl semimetals like WTe<sub>2</sub> and MoTe<sub>2</sub>. XRD measurement reveals no structural transition up to 11.5 GPa which indicates that the superconductivity appears in the ambient pressure Weyl semimetallic phase. Thus the observed superconductivity may be concluded as possible topological superconductivity but further verifications are needed to confirm this.

Finally, I would like to include hear a more general remark regarding the purpose and importance of this thesis. This work is fully experimental and we have obtained various meaningful results on the behaviour of selected topological compounds using different sophisticated equipments suitable under extreme conditions. We have explained our experimental findings on the basis of empirical and phenomenological concepts. Pressure induced metallization, superconductivity and ETT has been studied in various compounds and corresponding structural stability has also been discussed. Our findings can provide the basic information needed for testing and validating the existing theoretical models on topological materials, as well as for the development of new approaches. Similar investigations on other topological compounds will be very exciting to understand the interplay between XMR, topological

states and Superconductivity in these compounds under pressure.

## Bibliography

- [1] Anderson, P.W., Basic Notions of Condensed Matter Physics (Westview Press, Boulder, CO) (1997).
- [2] X. L. Qi, S. C. Zhang, Topological insulators and superconductors, Rev. Mod. Phys. 83, 1057-1110 (2011).
- [3] K. v. Klitzing, G. Dorda, and M. Pepper, New Method for High-Accuracy Determination of the Fine-Structure Constant Based on Quantized Hall Resistance, Phys. Rev. Lett. 45, 494(1980).
- [4] R. B. Laughlin, Quantized Hall conductivity in two dimensions, Phys. Rev. B 23, 5632 (1981).
- [5] F. D. M. Haldane, Model for a Quantum Hall Effect without Landau Levels: Condensed-Matter Realization of the "Parity Anomaly", Phys. Rev. Lett. 61, 2015 (1988).
- [6] R. Yu, W. Zhang, H. J. Zhang, S. C. Zhang, X. Dai, and Z. Fang, Quantized anomalous Hall effect in magnetic topological insulators, Science 329, 61 (2010).
- [7] S. S. Zhang, H. Fan, and W. M. Liu, Interaction- and filling induced quantum anomalous Hall effect in ultracold neutral Bose-Fermi mixtures on a hexagonal lattice, Phys.Rev.A.87.023622 (2013).
- [8] Su-Yang Xu, Discoveries of New Topological States of Matter Beyond Topological Insulators, Princeton University (2014)
- [9] S. Murakami, N. Nagaosa, and S. C. Zhang, Spin-Hall Insulator, Phys. Rev. Lett. 93, 156804 (2004).
- [10] C. L. Kane and E. J. Mele, Quantum Spin Hall Effect in Graphene, Phys. Rev. Lett. 95, 226801(2005)
- [11] Kane, C. L., and E. J. Mele,  $\mathbb{Z}_2$  Topological Order and the Quantum Spin Hall Effect Phys. Rev. Lett. 95, 146802(2005).

## References

---

- [12] L. Fu, C. L. Kane, and E. J. Mele, Topological Insulators in Three Dimensions, *Phys. Rev. Lett.* 98, 106803 (2007).
- [13] J. E. Moore, and L. Balents, Topological invariants of time-reversal-invariant band structures, *Phys. Rev. B* 75, 121306(2007)
- [14] R. Roy, Topological phases and the quantum spin Hall effect in three dimensions, *Phys. Rev. B* 79, 195322 (2009).
- [15] A. P. Schnyder, S. Ryu, A. Furusaki, and A.W.W. Ludwig, Classification of topological insulators and superconductors in three spatial dimensions, *Phys. Rev. B* 78, 195125 (2008).
- [16] A. Kitaev, Periodic table for topological insulators and superconductors, *AIP Conf. Proc.* 1134, 22 (2009).
- [17] X. L. Qi, T. L. Hughes, S. Raghu, and S. C. Zhang, Time-Reversal-Invariant Topological Superconductors and Superfluids in Two and Three Dimensions, *Phys. Rev. Lett.* 102, 187001 (2009).
- [18] T.V. Bay, T. Naka, Y. K. Huang, H. Luigjes, M. S. Golden, and A. de Visser, Superconductivity in the Doped Topological Insulator  $\text{Cu}_x\text{Bi}_2\text{Se}_3$  under High Pressure, *Phys. Rev. Lett.* 108, 057001 (2012).
- [19] K. Manikandan, Shruti, P. Neha, G. Kalai Selvan, B. Wang, Y. Uwatoko, K. Ishigaki, R. Jha, V. P. S. Awana, S. Arumugam and S. Patnaik, Possibility for conventional superconductivity in  $\text{Sr}_{0.1}\text{Bi}_2\text{Se}_3$  from high-pressure transport studies, *EPL* 118, 47008 (2017).
- [20] A.M. Nikitin, Y. Pan, Y.K. Huang, T. Naka, A. de Visser, High-pressure study of the basal-plane anisotropy of the upper critical field of the topological superconductor  $\text{Sr}_x\text{Bi}_2\text{Se}_3$  , *Phys. Rev. B* 94 144516 (2016).
- [21] S. M. Young, S. Zaheer, J. C. Y. Teo, C. L. Kane, E. J. Mele, and A. M. Rappe, Dirac semimetal in three dimensions, *Phys. Rev. Lett.* 108, 140405 (2012).

## References

---

- [22] Z. Wang,, Y. Sun, X. Q. Chen, C. Franchini, G. Xu, H. Weng, X. Dai, and Z. Fang, Dirac semimetal and topological phase transitions in  $A_3Bi$  ( $A= Na, K, Rb$ ), Phys. Rev. B 85, 195320 (2012).
- [23] Z. Wang, H.Weng, Q. Wu, X. Dai, Z. Fang, Three-dimensional Dirac semimetal and quantum transport in  $Cd_3As_2$ , Phys. Rev. B 88, 125427 (2013).
- [24] S. M. Huang, S. Y. Xu, I. Belopolski, C. C. Lee, G. Chang, B. Wang, N. Alidoust, G. Bian, M. Neupane, C. Zhang, S. Jia, A. Bansil, H. Lin and M. Z. Hasan, A Weyl fermion semimetal with surface Fermi arcs in the transition metal monophnictide TaAs class, Nature Communications 6, 7373 (2015).
- [25] H. Weng, C. Fang, Z. Fang, B. A. Bernevig, X. Dai, Weyl semimetal phase in noncentrosymmetric transition-metal monophosphides, Phys. Rev. X 5, 011029 (2015).
- [26] K. Kirshenbaum, P. S. Syers, A. P. Hope, N. P. Butch, J. R. Jeffries, S. T. Weir, J. J. Hamlin, M. B. Maple, Y. K. Vohra, and J. Paglione, Pressure-Induced Unconventional Superconducting Phase in the Topological Insulator  $Bi_2Se_3$ , Phys. Rev. Lett. 111, 087001 (2013).
- [27] P. P. Kong, J. L. Zhang, S. J. Zhang, J. Zhu, Q. Q. Liu, R. C. Yu, Z. Fang, C. Q. Jin, W. G. Yang, X. H. Yu, J. L. Zhu and Y. S. Zhao. Superconductivity of the topological insulator  $Bi_2Se_3$  at high pressure. J Phys-Condensed Matter, 25, 362204 (2013).
- [28] R. Vilaplana, D. Santamaria-Perez, O. Gomis, F. J. Manjon, J. Gonzalez, A. Segura, A. Munoz, P. Rodriguez-Hernandez, E. Perez-Gonzalez, V. Marn-Borras, V. Munoz-Sanjose, C. Drasar, and V. Kucek, Structural and vibrational study of  $Bi_2Se_3$  under high pressure, Phys. Rev. B 84, 184110 (2011).
- [29] Y. Li, Y. Zhou, Z. Guo, F. Han, X. Chen, P. Lu, X. Wang, C. An, Y. Zhou, J. Xing, G. Du, X. Zhu, H. Yang, J. Sun, Z. Yang, W. Yang, H. K. Mao, Y. Zhang and H. H. Wen, Concurrence of superconductivity and structure transition in Weyl semimetal TaP under pressure. NPJ Quantum Materials 2, 66 (2017).

## References

---

- [30] X. C. Pan, X. Chen, H. Liu, Y. Feng, Z. Wei, Y. Zhou, Z. Chi, L. Pi, F. Yen, F. Song, X. Wan, Z. Yang, B. Wang, G. Wang, and Y. Zhang, Pressure-driven dome-shaped superconductivity and electronic structural evolution in tungsten ditelluride, *Nature Communication* 6, 7805 (2015).
- [31] Y. Qi, P. G. Naumov, M. N. Ali, C. R. Rajamathi, W. Schnelle, O. Barkalov, M. Hanfland, S.-C. Wu, C. Shekhar, Y. Sun, V. Su, M. Schmidt, U. Schwarz, E. Pippel, P. Werner, R. Hillebrand, T. Forster, E. Kampert, S. Parkin, R. J. Cava, C. Felser, B. Yan, and S. A. Medvedev, Superconductivity in Weyl semimetal candidate  $\text{MoTe}_2$ , *Nature Communication* 7, 11038 (2016).
- [32] Y. Zhou, X. Chen, R. Zhang, J. Shao, X. Wang, C. An, Y. Zhou, C. Park, W. Tong, L. Pi, Z. Yang, C. Zhang and Y. Zhang, Pressure-induced reemergence of superconductivity in topological insulator  $\text{Sr}_{0.065}\text{Bi}_2\text{Se}_3$ , *Phys. Rev. B*, 93 144514 (2016).
- [33] M.P. Smylie, K. Willa, K. Ryan, H. Claus, W. K. Kwok, Y. Qiu, Y.S. Hor, U. Welp, An increase in  $T_c$  under hydrostatic pressure in the superconducting doped topological insulator  $\text{Nb}_{0.25}\text{Bi}_2\text{Se}_3$ , *Physica C: Superconductivity and its applications*, 543, 58-61 (2017).
- [34] M. Z. Hasan and C. L. Kane, Colloquium: Topological insulators, *Rev. Mod. Phys.* 82, 3045-67 (2010).
- [35] E. burstein, A. H. Macdonald and P. J. Stiles, Contemporary concepts of condensed matter science, *Topological Insulators, Volume 6*, (2013).
- [36] B. A. Bernevig, T. L. Hughes, and S. C. Zhang, Quantum spin Hall effect and topological phase transition in  $\text{HgTe}$  quantum wells, *Science*, 314, 1757 (2006).
- [37] M. Konig, S. Wiedmann, C. Brune, A. Roth, H. Buhmann, L. W. Molenkamp, X. L. Qi, and S. C. Zhang, Quantum spin Hall insulator state in  $\text{HgTe}$  quantum wells", *Science* 318, 766 (2007).
- [38] A. Roth, C. Brne, H. Buhmann, L. W. Molenkamp, J. Maciejko, X. L. Qi, and S. C. Zhang, Nonlocal transport in the quantum spin Hall state, *Science*, 325, 294 (2009).

## References

---

- [39] C. Brune, A. Roth, H. Buhmann, E. M. Hankiewicz, L. W. Molenkamp, J. Maciejko, X. L. Qi, and S. C. Zhang, Spin polarization of the quantum spin Hall edge states, *Nat. Phys.*, 8, 485-490 (2013).
- [40] S. Murakami, Quantum Spin Hall Effect and Enhanced Magnetic Response by Spin-Orbit Coupling, *Phys. Rev. Lett.* 97, 236805 (2006).
- [41] C. X. Liu, T. L. Hughes, X.L. Qi, K. Wang, and S. C. Zhang, Quantum Spin Hall Effect in Inverted Type-II Semiconductors, *Phys. Rev. Lett.* 100, 236601(2008).
- [42] A. Shitade, H. Katsura, J. Kunes, X. L. Qi, S.C. Zhang, and N. Nagaosa, 2009, Quantum Spin Hall Effect in a Transition Metal Oxide  $\text{Na}_2\text{IrO}_3$ , *Phys. Rev. Lett.* 102, 256403 (2009).
- [43] D. Hsieh, D. Qian, L. Wray, Y. Xia, Y. S. Hor, R. J. Cava and M. Z. Hasan, A topological Dirac insulator in a quantum spin Hall phase. *Nature* 452, 970 (2008).
- [44] Y. Xia, D. Qian, D. Hsieh, L. Wray, A. Pal, H. Lin, A. Bansil, D. Grauer, Y. S. Hor, R. J. Cava, and M. Z. Hasan, "Observation of a large-gap topological-insulator class with a single Dirac cone on the surface", *Nature Physics* 5, 398 (2009).
- [45] H. Zhang, C. X. Liu, X. L. Qi, X. Dai, Z. Fang, S. C. Zhang, Topological insulators in  $\text{Bi}_2\text{Se}_3$ ,  $\text{Bi}_2\text{Te}_3$  and  $\text{Sb}_2\text{Te}_3$  with a single Dirac cone on the surface *Nature Physics* 5, 438 (2009).
- [46] Y. L. Chen, J. G. Analytis, J. H. Chu, Z. K. Liu, S. K. Mo, X. L. Qi, H. J. Zhang, D. H. Lu, X. Dai, Z. Fang, S. C. Zhang, I. R. Fisher, Z. Hussain, Z. X. Shen, Experimental Realization of a Three-Dimensional Topological Insulator,  $\text{Bi}_2\text{Te}_3$ , *Science* 325, 178 (2009).
- [47] S. Q. Shen, *Topological Insulators; Dirac equation in condensed matters*, Springer, (2013).

## References

---

- [48] Z. Ren, A. A. Taskin, S. Sasaki, K. Segawa, and Y. Ando, Large bulk resistivity and surface quantum oscillations in the topological insulator  $\text{Bi}_2\text{Te}_2\text{Se}$ , *Phys. Rev. B* 82, 241306(R) (2010).
- [49] A. Akrap, M. Tran, A. Ubaldini, J. Teyssier, E. Giannini, and D. v. d. Marel, P. Lerch and C. C. Homes, Optical properties of  $\text{Bi}_2\text{Te}_2\text{Se}$  at ambient and high pressures, *Phys.Rev.B* 86, 235207 (2012).
- [50] A. Sklenar, C. Drasar A. Krejcova, P. Lostak, Optical Properties of  $\text{Bi}_2\text{Se}_{3-x}\text{As}_x$  Single Crystals, *Cryst. Res.Technol.* 35, 1069 (2000).
- [51] T. Plechacek, J. Navratil, and J. Horak, Free Current Carrier Concentration and Point Defects in  $\text{Bi}_{2-x}\text{Sb}_x\text{Se}_3$  Crystals, *J. Solid State Chem.* 165, 35 (2002).
- [52] D. X. Qu, Y. S. Hor, J. Xiong, R. J. Cava, N. P. Ong, Quantum Oscillations and Hall Anomaly of Surface States in the Topological Insulator  $\text{Bi}_2\text{Te}_3$ , *Science* 329, 821 (2010).
- [53] S. Xu, L. Wray, Y. Xia, R. Shankar, A. Petersen, A. Fedorov, H. Lin, A. Bansil, Y. Hor, D. Grauer, R. Cava, and M. Hasan, Discovery of several large families of Topological Insulator classes with backscattering-suppressed spin-polarized single-Dirac-cone on the surface, arXiv:1007.5111 (2010) (unpublished)
- [54] F. F. Tafti, Q. D. Gibson, S. K. Kushwaha, N. Haldolaarachchige and R. J. Cava, Resistivity plateau and extreme magnetoresistance in  $\text{LaSb}$ , *Nature Physics* 12(3), 272-277 (2016).
- [55] F. F. Tafti, Q. Gibson, S. Kushwaha, J. W. Krizan, N. Haldolaarachchige, and R. J. Cava, Temperature-field phase diagram of extreme magnetoresistance, *PNAS*, 113 (25), E3475 (2016).
- [56] D. J. Kim, J. Xia and Z. Fisk, Topological surface state in the Kondo insulator samarium hexaboride, *Nature Mater.* 13, 466-470 (2014).
- [57] J. L. Zhang, S. J. Zhang, H. M. Weng, W. Zhang, L. X. Yang, Q. Q. Liu, S. M. Feng, X. C. Wang, R. C. Yu, L. Z. Cao, L. Wang, W. G. Yang, H.

## References

---

- Z. Liu, W. Y. Zhao, S. C. Zhang, X. Dai, Z. Fang, and C. Q. Jin, Pressure-induced superconductivity in topological parent compound  $\text{Bi}_2\text{Te}_3$ , PNAS, 108, 24 (2011).
- [58] K. Matsubayashi, T. Terai, J. S. Zhou, and Y. Uwatoko, 2014, Superconductivity in the topological insulator  $\text{Bi}_2\text{Te}_3$  under hydrostatic pressure, Phys. Rev. B 90, 125126 (2014).
- [59] J. Zhang, C. Liu, X. Zhang, F. Ke, Y. Han, G. Peng, Y. Ma, and C. Gao, Electronic topological transition and semiconductor-to-metal conversion of  $\text{Bi}_2\text{Te}_3$  under high pressure, Appl. Phys. Lett. 103, 052102 (2013).
- [60] J. Zhu, J. L. Zhang, P. P. Kong, S. J. Zhang, X. H. Yu, J. L. Zhu, Q. Q. Liu, X. Li, R. C. Yu, R. Ahuja, W. G. Yang, G. Y. Shen, H. K. Mao, H. M. Weng, X. Dai, Z. Fang, Y. S. Zhao and C. Q. Jin, Superconductivity in topological insulator  $\text{Sb}_2\text{Te}_3$  induced by pressure, Scientific Reports, 3, 2016 (2013).
- [61] F. J. Manjon, R. Vilaplana, O. Gomis, E. Perez-Gonzalez D. Santamaria-Perez, V. Marin-Borras A. Segura J. Gonzalez, P. Rodriguez-Hernandez, A. Munoz, C. Drasar, V. Kucek, V. Munoz-Sanjose, High-pressure studies of topological insulators  $\text{Bi}_2\text{Se}_3$ ,  $\text{Bi}_2\text{Te}_3$ , and  $\text{Sb}_2\text{Te}_3$ , Phys. Status Solidi B 250, No. 4, 669-676 (2013).
- [62] J. Zhang, Y. Han, C. Liu, X. Zhang, F. Ke, G. Peng, Y. Ma, Y. Ma, and C. Gao, Semiconductor-to-metal transition of  $\text{Bi}_2\text{Se}_3$  under high pressure, Appl. Phys. Lett. 105, 062102 (2014).
- [63] M. S. Bahramy, B. J. Yang, R. Arita, and N. Nagaosa, Emergence of non-centrosymmetric topological insulating phase in  $\text{BiTeI}$  under pressure, Nature Communications 3, 679 (2012).
- [64] J. Park, K. H. Jin, Y. J. Jo, E. S. Choi, W. Kang, E. Kampert, J. S. Rhyee, S. H. Jhi and J. S. Kim, Quantum Oscillation Signatures of Pressure-induced Topological Phase Transition in  $\text{BiTeI}$ , Scientific Reports, 5, 15973, (2015).

## References

---

- [65] X. Xi, C. Ma, Z. Liu, Z. Chen, W. Ku, H. Berger, C. Martin, D. B. Tanner, and G. L. Carr, Signatures of a pressure-induced topological quantum phase transition in BiTeI. *Phys. Rev. Lett.* 111, 155701 (2013).
- [66] M. K. Tran, J. Levallois, P. Lerch, J. Teyssier, A. B. Kuzmenko, G. Auts, O. V. Yazyev, A. Ubaldini, E. Giannini, D. van der Marel, A. Akrap, Infrared- and Raman-Spectroscopy Measurements of a Transition in the Crystal Structure and a Closing of the Energy Gap of BiTeI under Pressure, *Phys. Rev. Lett.* 112, 047402 (2014).
- [67] Y. Qi, W. Shi, P. G. Naumov, N. Kumar, R. Sankar, W. Schnelle, C. Shekhar, F. C. Chou, C. Felser, B. Yan and S. A. Medvedev, Topological Quantum Phase Transition and Superconductivity Induced by Pressure in the Bismuth Tellurohalide BiTeI, *Adv. Mater.* 29, 1605965 (2017).
- [68] J. J. Ying, V. V. Struzhkin, Z. Y. Cao, A. F. Goncharov, H. K. Mao, F. Chen, X. H. Chen, A. G. Gavriliuk, and X. J. Chen, Realization of insulating state and superconductivity in the Rashba semiconductor BiTeCl, *Phys. Rev. B* 93, 100504(R) (2016).
- [69] Y. Qi, W. Shi, P. Werner, P. G. Naumov, W. Schnelle, L. W. Kumari G. Rana, S. Parkin, S. A. Medvedev, B. Yan, C. Felser, Pressure-induced superconductivity and topological quantum phase transitions in a quasi-one-dimensional topological insulator: Bi<sub>4</sub>I<sub>4</sub>, *npj, Quantum materials* 3, 4 (2018)
- [70] A. Pisoni, R. Gal, A. Zeugner, V. Falkowski, A. Isaeva, H. Huppertz, G. Auts, O. V. Yazyev, and L. Forr, Pressure effect and superconductivity in the  $\beta$ -Bi<sub>4</sub>I<sub>4</sub> topological insulator, *Phys. Rev. B* 95, 235149 (2017).
- [71] I. Crassee, F. Borondics, M. K. Tran, G. Auts, A. Magrez, P. Bugnon, H. Berger, J. Teyssier, O. V. Yazyev, M. Orlita, and A. Akrap, BiTeCl and BiTeBr: A comparative high-pressure optical study, *Phys. Rev. B* 95, 045201 (2017).
- [72] Q. Zhang, Y. Cheng, and U. Schwingenschlogl, Series of topological phase transitions in TiTe<sub>2</sub> under strain, *Phys. Rev. B* 88, 155317 (2013).

## References

---

- [73] V. P. Cuenca-Gotor, J. A. Sans, J. Ibez, C. Popescu. O. Gomis, R. Vilaplana, F. J. Manjn, A. Leonardo, E. Sagasta, A. Surez-Alcubilla, G. Gurtubay, M. Mollar, and A. Bergara, Structural, Vibrational, and Electronic Study of  $\alpha$ -As<sub>2</sub>Te<sub>3</sub> under Compression, *J. Phys. Chem. C* 2016, 120, 19340?19352 (2016).
- [74] P. P. Kong, F. Sun, L. Y. Xing, J. Zhu, S. J. Zhang, W. M. Li, Q. Q. Liu, X. C. Wang, S. M. Feng, X. H. Yu, J. L. Zhu, R. C. Yu, W. G. Yang, G. Y. Shen, Y. S. Zhao, R. Ahuja, H. K. Mao, and C. Q. Jin, Superconductivity in strong spin orbital coupling compound Sb<sub>2</sub>Se<sub>3</sub>, *Scientific Reports* 4, 6679 (2014).
- [75] M. Yang, Y. Z. Luo, M. G. Zeng, L. Shen, Y. H. Lu, J. Zhou, S. J. Wang, I. K. Sou, and Y. P. Feng, Pressure induced topological phase transition in layered Bi<sub>2</sub>S<sub>3</sub>, *Phys.Chem.Chem.Phys.*, 19, 29372 (2017).
- [76] Q. Zhang, Y. Cheng and U. Schwingenschlogl, Emergence of topological and topological crystalline phases in TlBiS<sub>2</sub> and TlSbS<sub>2</sub>, *Scientific Reports* 5, 8379(2015).
- [77] L. M. Schoop, F. Pielhofer, and B. V. Lotsch, Chemical Principles of Topological Semimetals, *Chem. Mater.*, 30, 3155-3176 (2018).
- [78] N.P. Armitage, E.J. Mele, and Ashvin Vishwanath, Weyl and Dirac semimetals in three-dimensional solids, *Rev. Mod. Phys.* 90, 015001 (2018).
- [79] A. Bacsı and A. Virosztek, Low-frequency optical conductivity in graphene and in other scale-invariant two-band systems, *Phys. Rev. B* 87, 125425 (2013).
- [80] B. Xu, Y. M. Dai, L. X. Zhao, K.Wang, R. Yang,W. Zhang, J. Y. Liu, H. Xiao, G. F. Chen, A. J. Taylor, D. A. Yarotski, R. P. Prasankumar, and X. G. Qiu, Optical spectroscopy of the Weyl semimetal TaAs, *Phys. Rev. B* 93, 121110 (2016).
- [81] K. F. Mak, M. Y. Sfeir, Y. Wu, C. H. Lui, J. A. Misewich, and T. F. Heinz, Measurement of the Optical Conductivity of Graphene, *Phys. Rev. Lett.* 101, 196405 (2008).

## References

---

- [82] R. Y. Chen, S. J. Zhang, J. A. Schneeloch, C. Zhang, Q. Li, G. D. Gu, and N. L. Wang, Optical spectroscopy study of the three-dimensional Dirac semimetal  $\text{ZrTe}_5$ , *Phys. Rev. B* 92, 075107 (2015).
- [83] D. Neubauer, A. Yaresko, W. Li, A. Lhle, R. Hbner, M. B. Schilling, C. Shekhar, C. Felser, M. Dressel, and A. V. Pronin, Optical conductivity of the Weyl semimetal NbP, *Phys. Rev. B* 98, 195203 (2018).
- [84] S. Wang, B. C. Lin, A. Q. Wang, D. P. Yu and Z. M. Liao, Quantum transport in Dirac and Weyl semimetals: a review, *Advances in Physics: X*, 2:3, 518-544 (2017).
- [85] C. Shekhar, A. K. Nayak, Y. Sun, M. Schmidt, M. Nicklas, I. Leermakers, U. Zeitler, Y. Skourski, J. Wosnitza, Z. Liu, Y. Chen, W. Schnelle, H. Borrmann, Y. Grin, C. Felser and B. Yan, Extremely large magnetoresistance and ultrahigh mobility in the topological Weyl semimetal candidate NbP, *Nature Physics* 11(8):645-649 (2015).
- [86] Y. Luo, N. J. Ghimire, E. D. Bauer, J. D. Thompson and F. Ronning, 'Hard' crystalline lattice in the Weyl semimetal NbAs, *J. Phys.: Condens. Matter* 28 055502 (2016).
- [87] C. Zhang, J. Sun, F. Liu, A. Narayan, N. Li, X. Yuan, Y. Liu, J. Dai, Y. Long, Y. Uwatoko, J. Shen, S. Sanvito, W. Yang, J. Cheng, and F. Xiu, Evidence for pressure-induced node-pair annihilation in  $\text{Cd}_3\text{As}_2$ , *Phys. Rev. B* 96, 155205 (2017).
- [88] N. J. Ghimire, Y. Luo, M. Neupane, D. J. Williams, E. D. Bauer and F. Ronning, Magnetotransport of single crystalline NbAs, *J Phys Condens Matter* 27(15), 152201 (2015).
- [89] X. Huang, L. Zhao, Y. Long, P. Wang, D. Chen, Z. Yang, H. Liang, M. Xue, H. Weng, Z. Fang, X. Dai, and G. Chen, Observation of the chiral-anomaly-induced negative magnetoresistance in 3d Weyl semimetal TaAs, *Phys Rev X* 5(3), 031023 (2015).

## References

---

- [90] M. N. Ali, J. Xiong, S. Flynn, J. Tao, Q. D. Gibson, L. M. Schoop, T. Liang, N. Haldolaarachchige, M. Hirschberger, N. P. Ong and R. J. Cava, Large, non-saturating magnetoresistance in  $\text{WTe}_2$ , *Nature* 514(7521), 205-208 (2014).
- [91] S. Khim, K. Koepernik, D.V. Efremov, J. Klotz, T. Frster, J. Wosnitza, M.I. Sturza, S. Wurmehl, C. Hess, J. van den Brink, and B. Behner, Magnetotransport and de Haas-van Alphen measurements in the type-II Weyl semimetal  $\text{TaIrTe}_4$ , *Phys. Rev. B* 94, 165145 (2016).
- [92] J. Xiong, S. K. Kushwaha, T. Liang, J. W. Krizan, M. Hirschberger, W. Wang, R. J. Cava, N. P. Ong, Evidence for the chiral anomaly in the Dirac semimetal  $\text{Na}_3\text{Bi}$ , *Science* 350(6259), 413-416 (2015).
- [93] T. Liang, Q. Gibson, M. N. Ali, M. Liu, R. J. Cava, N. P. Ong, Ultrahigh mobility and giant magnetoresistance in the Dirac semimetal  $\text{Cd}_3\text{As}_2$ , *Nature Mater* 14(3) 280-284 (2015).
- [94] E. Mun, H. Ko, G. J. Miller, G. D. Samolyuk, S. L. Budko, and P. C. Canfield, Magnetic field effects on transport properties of  $\text{PtSn}_4$ , *Phys Rev B* 85(3), 035135 (2012).
- [95] K. Wang, D. Graf, L. Li, L. Wang, C. Petrovic, Anisotropic giant magnetoresistance in  $\text{NbSb}_2$ , *Scientific Reports* 4, 7328 (2014).
- [96] Y. Li, L. Li, J. Wang, T. Wang, X. Xu, C. Xi, C. Cao, and J. Dai, Resistivity plateau and negative magnetoresistance in the topological semimetal  $\text{TaSb}_2$ , *Phys. Rev. B* 94, 121115 (2016).
- [97] Q. Li, D. E. Kharzeev, C. Zhang, Y. Huang, I. Pletikosi, A. V. Fedorov, R. D. Zhong, J. A. Schneeloch, G. D. Gu, and T. Valla, Chiral magnetic effect in  $\text{ZrTe}_5$ , *Nature Physics*, 12, 550-554 (2016).
- [98] Y. Qi, W. J. Shi, P. G. Naumov, N. Kumar, W. Schnelle, O. Barkalov, C. Shekhar, H. Borrmann, C. Felser, B. H. Yan, and S. A. Medvedev, Pressure-driven superconductivity in the transition-metal pentatelluride  $\text{HfTe}_5$ , *Phys.Rev.B* 94, 054517 (2016).

## References

---

- [99] D. Kang, Y. Zhou, W. Yi, C. Yang, J. Guo, Y. Shi, S. Zhang, Z. Wang, C. Zhang, S. Jiang, A. Li, K. Yang, Q. Wu, G. Zhang, L. Sun, and Z. Zhao, Superconductivity emerging from a suppressed large magnetoresistant state in tungsten ditelluride, *Nature Communication* 6, 7804 (2015).
- [100] Y. Li, C. An, C. Hua, X. Chen, Y. Zhou, Y. Zhou, R. Zhang, C. Park, Z. Wang, Y. Lu, Y. Zheng, Z. Yang and Z. A. Xu, Pressure-induced superconductivity in topological semimetal NbAs<sub>2</sub>, *npj Quantum Materials*, 3:58 (2018).
- [101] Y. Zhou, J. Wu, W. Ning, N. Li, Y. Du, X. Chen, R. Zhang, Z. Chi, X. Wang, X. Zhu, P. Lu, C. Ji, X. Wan, Z. Yang, J. Sun, W. Yang, M. Tian, Y. Zhang, and H.-k. Mao, Pressure-induced superconductivity in a three-dimensional topological material ZrTe<sub>5</sub>, *PNAS* 113, 2904 (2016).
- [102] Y. Qi, W. Shi, P. G. Naumov, N. Kumar, W. Schnelle, O. Barkalov, C. Shekhar, H. Borrmann, C. Felser, B. Yan, and S. A. Medvedev, Pressure-driven superconductivity in the transition-metal pentatelluride HfTe<sub>5</sub>, *Phys. Rev. B* 94, 054517 (2016).
- [103] F. F. Tafti, M. S. Torikachvili, R. L. Stillwell, B. Baer, E. Stavrou, S. T. Weir, Y. K. Vohra, H.-Y. Yang, E. F. McDonnell, S. K. Kushwaha, Q. D. Gibson, R. J. Cava, and J. R. Jeffries, Tuning the electronic and the crystalline structure of LaBi by pressure: From extreme magnetoresistance to superconductivity, *Phys.Rev.B* 95 014507 (2017).
- [104] A. A. Soluyanov, D. Gresch, Z. Wang, Q. Wu, M. Troyer, X. Dai, and B. A. Bernevig, Type-II Weyl semimetals, *Nature (London)* 527, 495 (2015).
- [105] J. Zhang , F. L. Liu, J. K. Dong, Y. Xu, N. N. Li, W. G. Yang and S. Y. Li, Structural and Transport Properties of the Weyl Semimetal NbAs at High Pressure, *Chin. Phys. Lett.* 32 097102 (2015).
- [106] L. X. Yang, Z. K. Liu, Y. Sun, H. Peng, H. F. Yang, T. Zhang, B. Zhou, Y. Zhang, Y. F. Guo, M. Rahn, D. Prabhakaran, Z. Hussain, S. K. Mo, C. Felser, B. Yan, and Y. L. Chen, Weyl semimetal phase in the non-centrosymmetric compound TaAs, *Nature Physics* 11, 728 (2015).

## References

---

- [107] S.Y. Xu, I. Belopolski<sup>1</sup>, N. Alidoust, M. Neupane, G. Bian, C. Zhang, R. Sankar, G. Chang, Z. Yuan, C. C. Lee, S. M. Huang, H. Zheng, J. Ma, D. S. Sanchez, B. Wang, A. Bansil, F. Chou, P. P. Shibayev, H. Lin, S. Jia, M. Z. Hasan, Discovery of a Weyl fermion semimetal and topological Fermi arcs, *Science* 349, 613 (2015).
- [108] B.Q. Lv, H.M. Weng, B.B. Fu, X.P. Wang, H. Miao, J. Ma, P. Richard, X.C. Huang, L.X. Zhao, G.F. Chen, Z. Fang, X. Dai, T. Qian, and H. Ding, Experimental Discovery of Weyl Semimetal TaAs, *Phys. Rev. X* 5, 031013 (2015).
- [109] R. D. dos Reis, S. C. Wu, Y. Sun, M. O. Ajeesh, C. Shekhar, M. Schmidt, C. Felser, B. Yan, and M. Nicklas, Pressure tuning the Fermi surface topology of the Weyl semimetal NbP, *Phys.Rev.B*.93.205102 (2016).
- [110] M. Einaga, K. Shimizu, J. Hu, Z. Q. Mao, and A. Politano, Resistivity of Weyl semimetals NbP and TaP under pressure, *Phys. Status Solidi RRL*, 1700182 (2017).
- [111] S. N. Gupta, A. Singh, K. Pal, D. V. S. Muthu, C. Shekhar, Yanpeng Qi, Pavel G. Naumov, Sergey A. Medvedev, C. Felser, U. V. Waghmare, and A. K. Sood, Pressure-induced Lifshitz transition in NbP: Raman, x-ray diffraction, electrical transport, and density functional theory, *PhysRevB*.97.064102 (2018)
- [112] Y. Zhou, P. Lu, Y. Du, X. Zhu, G. Zhang, R. Zhang, D. Shao, X. Chen, X. Wang, M. Tian, J. Sun, X. Wan, Z. Yang, W. Yang, Y. Zhang, and D. Xing, Pressure-Induced New Topological Weyl Semimetal Phase in TaAs, *Phys. Rev. Lett.* 117.146402 (2016).
- [113] P.L. Cai, J. Hu, L.P. He, J. Pan, X.C. Hong, Z. Zhang, J. Zhang, J. Wei, Z.Q. Mao, and S.Y. Li, Drastic pressure effect on the extremely large magnetoresistance in WTe<sub>2</sub>, *Phys. Rev. Lett.* 115, 057202 (2015).
- [114] S. Cai, E. Emmanouilidou, J. Guo, X. Li, Y. Li, K. Yang, A. Li, Q. Wu, N. Ni, and L. Sun, Observation of superconductivity in the pressurized Weyl-semimetal candidate TaIrTe<sub>4</sub>, *Phys.Rev.B* 99 020503 (2019).

## References

---

- [115] Y. Xing, Z. Shao, J. Ge, J. Wang, Z. Zhu, J. Liu, Y. Wang, Z. Zhao, J. Yan, D. Mandrus, B. Yan, X. J. Liu, M. Pan, and J. Wang, Surface Superconductivity in the type II Weyl Semimetal TaIrTe<sub>4</sub>, arxiv:1805.10883 (2018).
- [116] A. Efstathiou and E. R. Levin, Optical Properties of As<sub>2</sub>Se<sub>3</sub>, (As<sub>x</sub>Sb<sub>1-x</sub>)<sub>2</sub>Se<sub>3</sub>, and Sb<sub>x</sub>S<sub>3</sub>, J. Opt. Soc. Am. 58, 373 (1968).
- [117] O. Savadogo, and K. C. Mandal, Studies on new chemically deposited photoconducting antimony trisulphide thin films Sol. Energy Mater. Sol. Cells 26, 117 (1992).
- [118] K. Y. Rajpure, and C. H. Bhosale, Preparation and characterization of spray deposited photoactive Sb<sub>2</sub>S<sub>3</sub> and Sb<sub>2</sub>Se<sub>3</sub> thin films using aqueous and non-aqueous media, Mater. Chem. Phys. 73, 6 (2002).
- [119] Y A Sorb, V Rajaji1, P S Malavi, U Subbarao, P Halappa, S C Peter, S Karmakar and C Narayana, Pressure-induced electronic topological transition in Sb<sub>2</sub>S<sub>3</sub>, J. Phys.: Condens.Matter 28, 015602, (2016).
- [120] I. Efthimiopoulos, C. Buchan and Y. Wang, Structural properties of Sb<sub>2</sub>S<sub>3</sub> under pressure: evidence of an electronic topological transition, Scientific Reports 6, 24246 (2016).
- [121] J. Ibanez, J. A. Sans, C. Popescu, J. Lopez-Vidrier, J. J. Elvira-Betanzos, V. P. Cuenca-Gotor, O. Gomis, F. J. Manjon, P. Rodriguez-Hernandez, and A. Munoz, Structural, Vibrational, and Electronic Study of Sb<sub>2</sub>S<sub>3</sub> at High Pressure, J. Phys. Chem. C , 120, 10547-10558 (2016).
- [122] L. Dai, K. Liu, H. Li, L.Wu, H. Hu, Y. Zhuang, L. Yang, C. Pu, and P. Liu, Pressure-induced irreversible metallization accompanying the phase transitions in Sb<sub>2</sub>S<sub>3</sub>, Phys. Rev. B., 97.024103 (2018).
- [123] S. N. Guin, V. Srihari and K. Biswas, Promising thermoelectric performance in n-type AgBiSe<sub>2</sub>: effect of aliovalent anion doping, J. Mater. Chem. A, 3, 648-655 (2015).
- [124] V. Rajaji, P. S. Malavi, S. S. R. K. C. Yamijala, Y. A. Sorb, U. Dutta, S. N. Guin, B. Joseph, S. K. Pati, S. Karmakar, K. Biswas, and C. Narayana,

## References

---

- Pressure induced structural, electronic topological, and semiconductor to metal transition in AgBiSe<sub>2</sub>, *Appl. Phys. Lett.* 108, 213902 (2016).
- [125] Y. Koike, M. Okamura, T. Nakanomyo, and T. Fukase, Log T Dependence of Resistivity and Negative Magnetoresistance in the Layered Compound TiTe<sub>2</sub>, *J. Phys. Soc. Jpn.* 52, 597 (1983).
- [126] R. C. Xiao, W. J. Lu, D. F. Shao, J. Y. Li, M. J. Wei, H. Y. Lv, P. Tong, X. B. Zhua, and Y. P. Sun, Manipulating superconductivity of 1T-TiTe<sub>2</sub> by high pressure, *J. Mater. Chem. C* 5, 4167 (2017).
- [127] E. Uykur, R. Sankar, D. Schmitz, and C. A. Kuntscher, Optical spectroscopy study on pressure-induced phase transitions in the three-dimensional Dirac semimetal Cd<sub>3</sub>As<sub>2</sub>, *Phys. Rev. B* 97, 195134 (2018).
- [128] G. Chang, S.-Y. Xu, H. Zheng, C.-C. Lee, S.-M. Huang, I. Belopolski, D. S. Sanchez, G. Bian, N. Alidoust, T.-R. Chang, C.-H. Hsu, H.-T. Jeng, A. Bansil, H. Lin, and M. Z. Hasan, Signatures of Fermi Arcs in the Quasiparticle Interferences of the Weyl Semimetals TaAs and NbP, *Phys. Rev. Lett.* 116, 066601 (2016).
- [129] Z. P. Guo, P. C. Lu, T. Chen, J. F. Wu, J. Sun, and D. Y. Xing, High-pressure phases of Weyl semimetals NbP, NbAs, TaP, and TaAs, *Sci. China-Phys. Mech. Astron.* 61, 038211 (2018).
- [130] K. Koepernik, D. Kasinathan, D. V. Efremov, S. Khim, S. Borisenko, B. Buchner, and J. vandenBrink, TaIrTe<sub>4</sub>: A ternary type-II Weyl semimetal, *Phys. Rev. B* 93, 201101 (2016).
- [131] K. Deng, G. Wan, P. Deng, K. Zhang, S. Ding, E. Wang, M. Yan, H. Huang, H. Zhang, Z. Xu, J. Denlinger, A. Fedorov, H. Yang, W. Duan, H. Yao, Y. Wu, S. Fan, H. Zhang, X. Chen and S. Zhou, Experimental observation of topological Fermi arcs in type-II Weyl semimetal MoTe<sub>2</sub>, *Nature Physics* 12, 1105 (2016).
- [132] S. J. Zhang, J. L. Zhang, X. H. Yu, J. Zhu, P. P. Kong, S. M. Feng, Q. Q. Liu, L. X. Yang, X. C. Wang, L. Z. Cao, W. G. Yang, L. Wang, H. K. Mao,

## References

---

- Y. S. Zhao, H. Z. Liu, X. Dai, Z. Fang, S. C. Zhang, and C. Q. Jin, The comprehensive phase evolution for  $\text{Bi}_2\text{Te}_3$  topological compound as function of pressure, *Journal of Applied Physics* 111, 112630 (2012)
- [133] A.R. West, "Solid State Chemistry and its Applications", John Wiley and Sons (1984).
- [134] H. Schafer, *Chemische Transportreaktionen*. Weinheim: Verlag Chemie; (1962).
- [135] M. Binnewies, R. Glaum, M. Schmidt, P. Schmidt, *Chemical Vapor Transport Reactions-Methods, Materials, Modeling, Advanced Topics on Crystal Growth*, Sukarno Olavo Ferreira, IntechOpen, (2012).
- [136] W. C. Michels "Electrical Measurement in their Applications", Van Nostrand, N. York, (1957).
- [137] S700X SQUID Magnetometer UserManual v0.99. Cryogenic Ltd.
- [138] M.A. Van Hove; W.H. Weinberg; C. M. Chan, *Low-Energy Electron Diffraction*. Springer-Verlag, Berlin Heidelberg New York (1986).
- [139] K. Oura, V. G. Lifshits, A. A. Saranin, A. V. Zotov; M. Katayama, *Surface Science*. Springer-Verlag, Berlin Heidelberg New York, pp. 1-45 (2003).
- [140] P. W. Bridgman, *The Physics of High Pressure*, G. Bell and Sons, LTD, London, 2 edition, (1949).
- [141] D. J. Dunstan, I. L. Spain, *Technology of diamond anvil high-pressure cells: I. Principles, design and construction*, *J. Phys. E: Sci. Instrum.* 22, 913 (1989).
- [142] I. L. Spain, D. J. Dunstan, *The technology of diamond anvil high-pressure cells: II. Operation and use*, *J. Phys. E: Sci. Instrum.* 22 923-33 (1989).
- [143] A. Jayaraman, *Diamond anvil cell and high-pressure physical investigations*, *Rev. Mod. Phys.* 55, 65, (1983).
- [144] A. Jayaraman, *Ultrahigh pressures*, *Rev. Sci. Instrum.* 57, 1013, (1986).

## References

---

- [145] M. Eremets, *High Pressure Experimental Methods*, Oxford University Press, Oxford, (1996).
- [146] L. Dubrovinsky, N. Dubrovinskaia, V. B. Prakapenka, A. M. Abakumov, Implementation of micro-ball nanodiamond anvils for high-pressure studies above 6 Mbar, *Nature Communication* 3:7, 1163 (2012).
- [147] L. Dubrovinsky, N. Dubrovinskaia, E. Bykova, M. Bykov, V. Prakapenka, C. Prescher, K. Glazyrin, H. P. Liermann, M. Hanfland, M. Ekholm, Q. Feng, L. V. Pourovskii, M. I. Katsnelson, J. M. Wills and I. A. Abrikosov, The most incompressible metal osmium at static pressures above 750 gigapascals, *Nature*, 525:226-22 (2015).
- [148] Ilias Efthimiopoulos, *High-pressure structural and spectroscopic studies on transition metal compounds*, Ph.D thesis, Department of Physics, Aristotle University of Thessaloniki (2010).
- [149] Pallavi Malavi, *Investigation of pressure-induced structural and electronic properties of some novel transition metal compounds at low temperatures*, Ph.D thesis, University of Mumbai (2016).
- [150] J. D. Barnett, S. Block, and G. J. Piermarini, An Optical Fluorescence System for Quantitative Pressure Measurement in the Diamond-Anvil Cell, *Rev. Sci. Instrum.* 44, 1 (1973).
- [151] G. J. Piermarini, S. Block, J. D. Barnett, and R. A. Forman, Calibration of the pressure dependence of the R1 ruby fluorescence line to 195 kbar, *J. Appl. Phys.* 46, 2774 (1975).
- [152] K. Syassen, Ruby under pressure, *High Pres. Res.* 28, 75 (2008).
- [153] D.D. Ragan, R. Gustavsen, and D. Schiferl, Calibration of the ruby R1 and R2 fluorescence shifts as a function of temperature from 0 to 600 K, *J. Appl. Phys.* 72, p. 5539 (1992).
- [154] O. L. Anderson, The use of ultrasonic measurements under modest pressure to estimate compression at high pressure, *J. Phys. Chem. Sol.* 27, 547 (1966).

## References

---

- [155] H. K. Mao J. Xu P. M. Bell, Calibration of the ruby pressure gauge to 800 kbar under quasi-hydrostatic conditions, *J. Geo. Res.* 91, 4673, (1986).
- [156] K. Asaumi and A. L. Ruoff, Nature of the state of stress produced by xenon and some alkali iodides when used as pressure media. *Phys. Rev. B*, 33(8):5633-5636, (1986).
- [157] S. Karmakar, Measurement of improved pressure dependence of superconducting transition temperature, *High Pressure Research: An International Journal*, 33:2, 381-391 (2013).
- [158] T. Nakanishi, N. Takeshita, and N. Mri, A newly developed high-pressure cell by using modified Bridgman anvils for precise measurements in magnetic fields at low temperatures, *Review of Scientific Instruments* 73, 1828 (2002).
- [159] Y. Zhou, B. Zhang, X. Chen, C. Gu, C. An, Y. Zhou, K. Cai, Y. Yuan, C. Chen, H. Wu, R. Zhang, C. Park, Y. Xiong, X. Zhang, K. Wang, Z. Yang, Pressure-Induced Metallization and Robust Superconductivity in Pristine 1T-SnSe<sub>2</sub>, *Adv. Electron. Mater*, 1800155, (2018).
- [160] R. L. Reichlin , Measuring the electrical resistance of metals to 40 GPa in the diamond?anvil cell, *Review of Scientific Instruments* 54, 1674 (1983).
- [161] Maddury Somayazulu, Muhtar Ahart, Ajay K. Mishra, Zachary M. Geballe, Maria Baldini, Yue Meng, Viktor V. Struzhkin, and Russell J. Hemley, Evidence for superconductivity above 260 K in lanthanum superhydride at megabar pressures, *Phys. Rev. Lett.* 122, 027001(2019).
- [162] R. Vaidya, N. Vhatt, S. G. Patel, A. R. Jani, A. Garg, V. Vijayakumar, and B. K. Godwal, Electrical resistance measurements under pressure on NbTe<sub>2</sub> single crystal, *High Press. Res.* 23, 379 (2003).
- [163] L.J. Philips, van der Pauw, A method of measuring specific resistivity and hall effect of disks of arbitrary shape, *Res.Rep.*, 13, 1, 1958.
- [164] S. Weir, Electrical Transport Experiments at High Pressure, SUSSP, High Pressure Physics Skye, United Kingdom (2008).

## References

---

- [165] Y. Luo, H. Li, Y. M. Dai, H. Miao, Y. G. Shi, H. Ding, A. J. Taylor, D. A. Yarotski, R. P. Prasankumar, and J. D. Thompson, Hall effect in the extremely large magnetoresistance semimetal WTe<sub>2</sub>, *Appl. Phys. Lett.* 107, 182411 (2015).
- [166] N.W. Ashcroft and N.D. Mermin. *Solid State Physics*. (1976).
- [167] P. Brown, High-pressure states of bismuth, Ph.D thesis, Department of Physics University of Cambridge (2017).
- [168] G. J. Piermarini, and C. E. Weir, A diamond Cell for X-ray Diffraction Studies at High Pressures, *J. Res. Natl. Bur. Stand. (US)*, 66A, 325(1962).
- [169] A. P. Hammersley, S. O. Svensson, M. Hanfland, A. N. Fitch, and D. Hausermann, Twodimensional detector software: From real detector to idealised image or two-theta scan, *High Pres. Res.* 14, 235 (1996).
- [170] R. B. von Dreele and A. C. Larson, General Structure Analysis System (GSAS), Los Alamos National Laboratory Report LAUR 86-748 (2004).
- [171] Hans Kuzmany, *Solid-State Spectroscopy: An introduction*, second Edition (2009).
- [172] Paola Di Pietro, Optical Properties of Bismuth-based Topological Insulators, Ph.D thesis, Sapienza-University of Rome (2012).
- [173] Alessandro Nucara, Stefano Lupi, and Paolo Calvani, The infrared synchrotron radiation beamline at the third generation light source ELETTRA, *Review of Scientific Instruments* 74, 3934 (2003).
- [174] R. Claessen, R. O. Anderson, G.-H. Gweon, J. W. Allen, W. P. Ellis, C. Janowitz, C. G. Olson, Z. X. Shen, V. Eyert, M. Skibowski, K. Friemelt, E. Bucher, and S. Hfner, Complete band-structure determination of the quasi-two-dimensional Fermi-liquid reference compound TiTe<sub>2</sub>, *Phys. Rev. B* 54(4), 2453 (1996).
- [175] D. K. G. de Boer, C. F. van Bruggen, G. W. Bus, R. Coehoorn, C. Haas, G. A. Sawatzky, H. W. Myron, D. Norman, and H. Padmore, Titanium ditelluride:

## References

---

- Band structure, photoemission, and electrical and magnetic properties, *Phys. Rev. B* 29, 6797 (1984).
- [176] H. Zhang, C. X. Liu, X. L. Qi, Xi Dai, Z. Fang and S.C. Zhang, Topological insulators in  $\text{Bi}_2\text{Se}_3$ ,  $\text{Bi}_2\text{Te}_3$  and  $\text{Sb}_2\text{Te}_3$  with a single Dirac cone on the surface, *Nature Physics* volume 5, pages 438-442 (2009).
- [177] W. Liu, X. Peng, C. Tang, L. Sun, K. Zhang, and J. Zhong, Anisotropic interactions and strain-induced topological phase transition in  $\text{Sb}_2\text{Se}_3$  and  $\text{Bi}_2\text{Se}_3$ , *Phys. Rev. B* 84, 245105 (2011).
- [178] W. Li, X. Y. Wei, J. X. Zhu, C. S. Ting, and Y. Chen, Pressure-induced topological quantum phase transition in  $\text{Sb}_2\text{Se}_3$ , *Phys. Rev. B* 89, 035101 (2014).
- [179] A. Bera, K. Pal, D. V. S. Muthu, S. Sen, P. Guptasarma, U. V. Waghmare, and A. K. Sood, Sharp Raman Anomalies and Broken Adiabaticity at a Pressure Induced Transition from Band to Topological Insulator in  $\text{Sb}_2\text{Se}_3$ , *Phys. Rev. Lett.* 110, 107401 (2013).
- [180] J. C. Chervin, B. Canny, and M. Mancinelli, Ruby-spheres as pressure gauge for optically transparent high pressure cells, *High Pressure Res.* 21, 305 (2002).
- [181] E. Canadell, S. Jobic, R. Brec, J. Rouxel, and M. H. Whangbo, Importance of short interlayer Te-Te contacts for the structural distortions and physical properties of  $\text{CdI}_2$ -type layered transition-metal ditellurides, *J. Solid State Chem.* 99, 189 (1992).
- [182] G. Fritsch, W. Dyckhoff, W. Pollich, and E. Liischer, Dependence on pressure and temperature of the electrical resistivity of the amorphous alloys:  $\text{Co}_{80}\text{P}_{20}$  and  $\text{Pd}_{80}\text{Si}_{20}$  *J. Phys. F: Met. Phys.* 15, 1537 (1985).
- [183] Y. Ding, C. C. Chen, Q. Zeng, H. S. Kim, M. J. Han, M. Balasubramanian, R. Gordon, F. Li, L. Bai, D. Popov, S. M. Heald, T. Gog, H. K. Mao, and M. van Veenendaal, Novel High-Pressure Monoclinic Metallic Phase of  $\text{V}_2\text{O}_3$ , *Phys. Rev. Lett.* 112, 056401 (2014).

## References

---

- [184] J. Zhao, L. Yang, Z. Yu, Y. Wang, C. Li, K. Yang, Z. Liu, and Y. Wang, Structural Phase Transitions and Metallized Phenomena in Arsenic Telluride under High Pressure, *Inorg. Chem.* 55, 3907 (2016).
- [185] A. Ohmura, Y. Higuchi, T. Ochiai, M. Kanou, F. Ishikawa, S. Nakano, A. Nakayama, Y. Yamada, and T. Sasagawa, Pressure-induced topological phase transition in the polar semiconductor BiTeBr, *Phys. Rev. B* 95, 125203 (2017).
- [186] E. Greenberg, B. Hen, S. Layek, I. Pozin, R. Friedman, V. Shelukhin, Y. Rosenberg, M. Karpovski, M. P. Pasternak, E. Sterer, Y. Dagan, G. Kh. Rozenberg, and A. Palevski, Superconductivity in multiple phases of compressed GeSb<sub>2</sub>Te<sub>4</sub>, *Phys. Rev. B* 95, 064514 (2017).
- [187] V. Rajaji, U. Dutta, P. C. Sreeparvathy, S. C. Sarma, Y. A. Sorb, B. Joseph, S. Sahoo, S. C. Peter, V. Kanchana, and C. Narayana, Structural, vibrational, and electrical properties of 1T-TiTe<sub>2</sub> under hydrostatic pressure: Experiments and theory, *Phys. Rev. B* 97, 085107 (2018).
- [188] R. Klemm, *Layered Superconductors* (Oxford University Press, Oxford, UK, 2012), Vol. 1.
- [189] F. Clerc, C. Battaglia, M. Bovet, L. Despont, C. Monney, H. Cercellier, M. G. Garnier, P. Aebi, H. Berger, and L. Forro, Lattice-distortion-enhanced electron-phonon coupling and Fermi surface nesting in 1T-TaS<sub>2</sub>, *Phys. Rev. B* 74, 155114 (2006).
- [190] K. Rossnagel, L. Kipp, and M. Skibowski, Charge-density-wave phase transition in 1T-TiSe<sub>2</sub>: Excitonic insulator versus band-type Jahn-Teller mechanism, *Phys. Rev. B* 65, 235101 (2002).
- [191] T. E. Kidd, T. Miller, M. Y. Chou, and T. C. Chiang, Electron-Hole Coupling and the Charge Density Wave Transition in TiSe<sub>2</sub>, *Phys. Rev. Lett.* 88, 226402 (2002).
- [192] J. P. Castellan, S. Rosenkranz, R. Osborn, Q. Li, K. E. Gray, X. Luo, U. Welp, G. Karapetrov, J. P. C. Ruff, and J. van Wezel, Chiral Phase Transition in Charge Ordered 1T-TiSe<sub>2</sub>, *Phys. Rev. Lett.* 110, 196404 (2013).

## References

---

- [193] E. Morosan, H. W. Zandbergen, B. S. Dennis, J. W. G. Bos, Y. Onose, A. P. R. T. Klimczuk, N. P. Ong, and R. J. Cava, Superconductivity in  $\text{Cu}_x\text{TiSe}_2$ , *Nature Physics* 2, 544 (2006).
- [194] J. F. Zhao, H. W. Ou, G. Wu, B. P. Xie, Y. Zhang, D. W. Shen, J. Wei, L. X. Yang, J. K. Dong, M. Arita, H. Namatame, M. Taniguchi, X. H. Chen, and D. L. Feng, Evolution of the Electronic Structure of  $1T\text{-Cu}_x\text{TiSe}_2$ , *Phys. Rev. Lett.* 99, 146401 (2007).
- [195] S. Y. Li, G. Wu, X. H. Chen, and L. Taillefer, Single-Gap s-Wave Superconductivity near the Charge-Density-Wave Quantum Critical Point in  $\text{Cu}_x\text{TiSe}_2$ , *Phys. Rev. Lett.* 99, 107001 (2007).
- [196] G. Wu, H.X. Yang, L. Zhao, X. G. Luo, T. Wu, G. Y. Wang, and X. H. Chen, Transport properties of single-crystalline  $\text{Cu}_x\text{TiSe}_2$ , *Phys. Rev. B* 76, 024513 (2007).
- [197] H. Barath, M. Kim, J. F. Karpus, S. L. Cooper, P. Abbamonte, E. Fradkin, E. Morosan, and R. J. Cava, Quantum and Classical Mode Softening Near the Charge-Density-Wave-Superconductor Transition of  $\text{Cu}_x\text{TiSe}_2$ , *Phys. Rev. Lett.* 100, 106402 (2008).
- [198] R. Ang, Y. Tanaka, E. Ieki, K. Nakayama, T. Sato, L. J. Li, W. J. Lu, Y. P. Sun, and T. Takahashi, Real-Space Coexistence of the Melted Mott State and Superconductivity in Fe-Substituted  $1T\text{TaS}_2$ , *Phys. Rev. Lett.* 109, 176403 (2012).
- [199] R. Ang, Y. Miyata, E. Ieki, K. Nakayama, T. Sato, Y. Liu, W. J. Lu, Y. P. Sun, and T. Takahashi, Superconductivity and bandwidth-controlled Mott metal-insulator transition in  $1T\text{-TaS}_{2-x}\text{Se}_2$ , *Phys. Rev. B* 88, 115145 (2013).
- [200] Y. Liu, D. F. Shao, L. J. Li, W. J. Lu, X. D. Zhu, P. Tong, R. C. Xiao, L. S. Ling, C. Y. Xi, L. Pi, H. F. Tian, H. X. Yang, J. Q. Li, W. H. Song, X. B. Zhu, and Y. P. Sun, Nature of charge density waves and superconductivity in  $1T\text{-TaSe}_{2-x}\text{Te}_x$ , *Phys. Rev. B* 94, 045131 (2016).

## References

---

- [201] A. Kogar, G. A. de la Pena, S. Lee, Y. Fang, S. X. L. Sun, D. B. Lioi, G. Karapetrov, K. D. Finkelstein, J. P. C. Ruff, P. Abbamonte, and S. Rosenkranz, Observation of a Charge Density Wave Incommensuration Near the Superconducting Dome in  $\text{Cu}_x\text{TiSe}_2$ , *Phys. Rev. Lett.* 118, 027002 (2017).
- [202] S. Yan, D. Iaiia, E. Morosan, E. Fradkin, P. Abbamonte, and V. Madhavan, Influence of Domain Walls in the Incommensurate Charge Density Wave State of Cu Intercalated  $1T\text{-TiSe}_2$ , *Phys. Rev. Lett.* 118, 106405 (2017).
- [203] C. S. Snow, J. F. Karpus, S. L. Cooper, T. E. Kidd, and T. C. Chiang, Quantum Melting of the Charge-Density-Wave State in  $1T\text{-TiSe}_2$ , *Phys. Rev. Lett.* 91, 136402 (2003).
- [204] B. Sipos, A. F. Kusmartseva, A. Akrap, H. Berger, L. Forr, and E. Tutis, From Mott state to superconductivity in  $1T\text{-TaSe}_2$ , *Nature Materials* 7, 960 (2008).
- [205] A. F. Kusmartseva, B. Sipos, H. Berger, L. Forr, and E. Tuti, Pressure Induced Superconductivity in Pristine  $1T\text{-TiSe}_2$ , *Phys. Rev. Lett.* 103, 236401 (2009).
- [206] T. Ritschel, J. Trinckauf, G. Garbarino, M. Hanfland, M. v. Zimmermann, H. Berger, B. Bchner, and J. Geck, Pressure dependence of the charge density wave in  $1T\text{-TaSe}_2$  and its relation to superconductivity, *Phys. Rev. B* 87, 125135 (2013).
- [207] Y. I. Joe, X. M. Chen, P. Ghaemi, K. D. Finkelstein, G. A. de la Pea, Y. Gan, J. C. T. Lee, S. Yuan, J. Geck, G. J. MacDougall, T. C. Chiang S. L. Cooper, E. Fradkin and P. Abbamonte, Emergence of charge density wave domain walls above the superconducting dome in  $1T\text{-TiSe}_2$ , *Nature Physics* 10, 421 (2014).
- [208] B.Wang, Y. Liu, K. Ishigaki, K.Matsubayashi, J. Cheng,W. Lu, Y. Sun, and Y. Uwatoko, Pressure-induced bulk superconductivity in a layered transition-metal dichalcogenide  $1T\text{-tantalum selenium}$ , *Phys. Rev. B* 95, 220501 (2017).
- [209] S. Kawasaki, Y. Tani, T. Mabuchi, K. Kudo, Y. Nishikubo, D. Mit-suoka,M.Nohara, and G.-Q.Zheng, Coexistence of multiple charge-density

## References

---

- waves and superconductivity in SrPt<sub>2</sub>As<sub>2</sub> revealed by As75-NMR/NQR and Pt195-NMR, Phys.Rev.B 91, 060510 (2015).
- [210] M. Calandra and F. Mauri, Charge-Density Wave and Superconducting Dome in TiSe<sub>2</sub> from Electron-Phonon Interaction, Phys. Rev. Lett. 106, 196406 (2011).
- [211] R. Claessen, R. O. Anderson, J. W. Allen, C. G. Olson, C. Janowitz, W. P. Ellis, S. Harm, M. Kalning, R. Manzke, and M. Skibowski, Fermi-liquid line shapes measured by angle-resolved photoemission spectroscopy on 1T-TiTe<sub>2</sub>, Phys. Rev. Lett. 69, 808 (1992).
- [212] N. V. Baranov, V. G. Pleshchev, N. V. Selezneva, E. M. Sherokalova, A.V.Korolev, V.A. Kazantsev, and A.V. Proshkin, Ferromagnetism and structural transformations caused by Cr intercalation into TiTe<sub>2</sub>, J. Phys.: Condens. Matter 21, 506002 (2009).
- [213] J. Khan, C. M. Nolen, D. Teweldebrhan, D. Wickramaratne, R. K. Lake, and A. A. Balandin, Anomalous electron transport in back-gated field-effect transistors with TiTe<sub>2</sub> semimetal thin-film channels, Appl. Phys. Lett. 100, 043109 (2012).
- [214] Z. Zhu, Y. Cheng, and U. Schwingenschlgl, Topological Phase Diagrams of Bulk and Monolayer TiS<sub>2-x</sub>Te<sub>x</sub>, Phys. Rev. Lett. 110, 077202 (2013).
- [215] J. Zabaleta, S. C. Parks, B. Baum, A. Teker, K. Syassen, and J. Mannhart, Electrical transport measurements of thin film samples under high hydrostatic pressure, Rev. Sci. Instrum. 88, 033901 (2017).
- [216] Y. Guo, J. Dai, J. Zhao, C.Wu, D. Li, L. Zhang, W. Ning, M. Tian, X. C. Zeng, and Y. Xie, Large Negative Magnetoresistance Induced by Anionic Solid Solutions in Two-Dimensional Spin-Frustrated Transition Metal Chalcogenides, Phys. Rev. Lett. 113, 157202 (2014).
- [217] A. Dewaele, P. Loubeyre, and M. Mezouar, Equations of state of six metals above 94 GPa, Phys. Rev. B 70, 094112 (2004).

## References

---

- [218] Hammersley A, Computer Program FIT2D (Grenoble: ESRF) (1998)
- [219] Larson A C and von Dreele R B, Report LAUR 86748 Los Alamos National Lab, NM (1998)
- [220] N. R. Werthamer, E. Helfand, and P. C. Hohenberg, Temperature and Purity Dependence of the Superconducting Critical Field,  $H_{c2}$ . III. Electron Spin and Spin-Orbit Effects, *Phys. Rev.* 147, 295 (1966).
- [221] H. Suderow, V. G. Tissen, J. P. Brison, J. L. Martinez, and S. Vieira, Pressure Induced Effects on the Fermi Surface of Superconducting  $2H\text{-NbSe}_2$ , *Phys. Rev. Lett.* 95, 117006 (2005).
- [222] V. G. Tissen, M. R. Osorio, J. P. Brison, N. M. Nemes, M. Garcia-Hernandez, L. Cario, P. Rodire, S. Vieira, and H. Suderow, Pressure dependence of superconducting critical temperature and upper critical field of  $2H\text{-NbS}_2$ , *Phys. Rev. B* 87, 134502 (2013).
- [223] K. H. Müller, G. Fuchs, A. Handstein, K. Nenkov, V. N. Narozhnyi, and D. Eckert, The upper critical field in superconducting  $\text{MgB}_2$ , *J. Alloys Compd.* 322, L10 (2001).
- [224] X. Xi, Z. Wang, W. Zhao, J.-H. Park, K. T. Law, H. Berger, L. Forr, J. Shan, and K. F. Mak, Ising pairing in superconducting  $\text{NbSe}_2$  atomic layers, *Nature Physics* 12, 139 (2016).
- [225] Y. Lu, T. Takayama, A. F. Bangura, Y. Katsura, D. Hashizume, and H. Takagi, Superconductivity at 6 K and the Violation of Pauli Limit in  $\text{Ta}_2\text{Pd}_x\text{S}_5$ , *J. Phys. Soc. Jpn.* 83, 023702 (2014).
- [226] P. B. Allen and N. Chetty,  $\text{TiTe}_2$ : Inconsistency between transport properties and photoemission results, *Phys. Rev. B* 50, 14855 (1994).
- [227] F. Ke, H. Dong, Y. Chen, J. Zhang, C. Liu, J. Zhang, Y. Gan, Y. Han, Z. Chen, C. Gao, J. Wen, W. Yang, X. J. Chen, V. V. Struzhkin, H.K.Mao, B. Chen, Decompression-Driven Superconductivity Enhancement in  $\text{In}_2\text{Se}_3$ , *Adv. Mater.* 29, 1701983 (2017).

## References

---

- [228] R. Pervin, M. Krishnan, A. K. Rana, M. Kannan, S. Arumugam, and P. M. Shirage, Enhancement of superconducting critical current density by Fe impurity substitution in NbSe<sub>2</sub> single crystals and the vortex pinning mechanism, *Phys. Chem. Chem. Phys.* 19, 11230 (2017).
- [229] K. v. Klitzing, G. Dorda, and M. Pepper, New Method for High-Accuracy Determination of the Fine-Structure Constant Based on Quantized Hall Resistance, *Phys. Rev. Lett.* 45, 494 (1980).
- [230] D. B. Tanner and T. Timusk, *Physical Properties of High Temperature Superconductors III* (World Scientific, Singapore, 1992).
- [231] L. Yan, Z. J. Zhou, Y. Li, L. C. Tian, L. A.-Ji, H. Cheng, D. Ying, X. Yu, H. S. Long, Z. Lin, Liu Guo-Dong, Dong Xiao-Li, Zhang Jun, Chen Chuang-Tian, Xu Zu-Yan, Weng Hong-Ming, Dai Xi, Fang Zhong and Zhou Xing-Jiang, Identification of Topological Surface State in PdTe<sub>2</sub> Superconductor by Angle-Resolved Photoemission Spectroscopy, *Chin. Phys. Lett.* 32, 067303 (2015).
- [232] M. Yan, H. Huang, K. Zhang, E. Wang, W. Yao, K. Deng, G. Wan, H. Zhang, M. Arita, H. Yang, Zhe Sun, Hong Yao, Yang Wu, Shoushan Fan, Wenhui Duan and Shuyun Zhou, Lorentz-violating type-II Dirac fermions in transition metal dichalcogenide PtTe<sub>2</sub>, *Nat. Commun.* 8, 257 (2017).
- [233] E. Haubold, K. Koepernik, D. Efremov, S. Khim, A. Fedorov, Y. Kushnirenko, J. van den Brink, S. Wurmehl, B. Behner, T. K. Kim, M. Hoesch, K. Sumida, K. Taguchi, T. Yoshikawa, A. Kimura, T. Okuda, and S. V. Borisenko, Experimental realization of type-II Weyl state in noncentrosymmetric TaIrTe<sub>4</sub>, *Phys. Rev. B* 95, 241108 (2017).
- [234] R. Y. Chen, Z. G. Chen, X.-Y. Song, J. A. Schneeloch, G. D. Gu, F. Wang, and N. L. Wang, Magnetoinfrared Spectroscopy of Landau Levels and Zeeman Splitting of Three-Dimensional Massless Dirac Fermions in ZrTe<sub>5</sub>, *Phys. Rev. Lett.* 115, 176404 (2015).
- [235] Q. Li, D. E. Kharzeev, C. Zhang, Y. Huang, I. Pletikosic, A. V. Fedorov, R. D. Zhong, J. A. Schneeloch, G. D. Gu, and T. Valla, Chiral magnetic effect in ZrTe<sub>5</sub>, *Nat. Phys.* 12, 550 (2016).

## References

---

- [236] M. Zhang, X. Wang, A. Rahman, Q. Zeng, D. Huang, R. Dai, Z. Wang, and Z. Zhang, Pressure-induced topological phase transitions and structural transition in  $1T$ -TiTe<sub>2</sub> single crystal, *Appl. Phys. Lett.* 112, 041907 (2018).
- [237] M. Chinotti, A. Pal, W. J. Ren, C. Petrovic, and L. Degiorgi, Electrodynamic response of the type-II Weyl semimetal YbMnBi<sub>2</sub>, *Phys. Rev. B* 94, 245101 (2016).
- [238] S. I. Kimura, H. Yokoyama, H. Watanabe, J. Sichelschmidt, V. Suss, M. Schmidt, and C. Felser, Optical signature of Weyl electronic structures in tantalum pnictides TaPn (Pn= P, As), *Phys. Rev. B* 96, 075119 (2017).
- [239] U. Dutta, P. S. Malavi, S. Sahoo, B. Joseph, and S. Karmakar, Pressure-induced superconductivity in semimetallic  $1T$ -TiTe<sub>2</sub> and its persistence upon decompression, *Phys. Rev. B* 97, 060503(R) (2018).
- [240] U. Dutta, S. Sahoo, P. S. Malavi, F. Piccirilli, P. Di Pietro, A. Perucchi, S. Lupi, and S. Karmakar, Infrared spectroscopic measurements of structural transition and charge dynamics  $1T$ -TiTe<sub>2</sub> under pressure, *Phys. Rev. B* 99, 125105 (2019).
- [241] A. C. Larson and R. B. von Dreele, Report No. LAUR 86-748 (Los Alamos National Lab, Los Alamos, NM, 1986).
- [242] S. Lupi, A. Nucara, A. Perucchi, P. Calvani, M. Ortolani, L. Quaroni, and M. Kiskinova, Performance of SISSI, the infrared beamline of the ELETTRA storage ring, *J. Opt. Soc. A* B 24, 959 (2007).
- [243] M. I. Eremets and Y. A. Timofeev, Miniature diamond anvil cell: Incorporating a new design for anvil alignment, *Rev. Sci. Instrum.* 62, 3123 (1992).
- [244] H. Mao, J. Xu, and P. Bell, Calibration of the ruby pressure gauge to 800 kbar under quasi-hydrostatic conditions, *J. Geophys. Res.* 91, 4673 (1986).
- [245] A. Pashkin, M. Dressel, and C. A. Kuntscher, Pressure-induced deconfinement of the charge transport in the quasi-one-dimensional Mott insulator (TMTTF)<sub>2</sub>AsF<sub>6</sub>, *Phys. Rev. B* 74, 165118 (2006).

## References

---

- [246] M. Hangyo, S.-I. Nakashima, and A. Mitsuishi, Raman spectroscopic studies of  $\text{MX}_2$ -type layered compounds, *Ferroelectrics* 52, 151 (1983).
- [247] G. Lucovsky, R. M. White, J. A. Benda, and J. F. Revelli, Infrared-Reflectance Spectra of Layered Group-IV and Group-VI Transition-Metal Dichalcogenides, *Phys. Rev. B* 7, 3859 (1973).
- [248] G. Lucovsky, W. Y. Liang, R. M. White, and K. R. Pisharody, Reflectivity studies of Ti- and Ta-dichalcogenides: Phonons, *Solid State Commun.* 19, 303 (1976).
- [249] K. Velebit, P. Pop?cevic, I. Batistic, M. Eichler, H. Berger, L. Forr, M. Dressel, N. Bariic, and E. Tuti, Scattering-dominated high-temperature phase of  $1T\text{-TiSe}_2$ : An optical conductivity study, *Phys. Rev. B* 94, 075105 (2016).
- [250] C. C. Homes, M. N. Ali, and R. J. Cava, Optical properties of the perfectly compensated semimetal  $\text{WTe}_2$ , *Phys. Rev. B* 92, 161109 (2015).
- [251] V. Vescoli, L. Degiorgi, H. Berger, and L. Forro, Dynamics of Correlated Two-Dimensional Materials: The  $2\text{H-TaSe}_2$  Case, *Phys. Rev. Lett.* 81, 453 (1998).
- [252] B. Ruzicka, L. Degiorgi, H. Berger, R. Gaal, and L. Forro, Charge Dynamics of  $2\text{H-TaSe}_2$  along the Less-Conducting  $c$ -Axis, *Phys. Rev. Lett.* 86, 4136 (2001).
- [253] S. V. Dordevic, D. N. Basov, R. C. Dynes, and E. Bucher, Anisotropic electrodynamics of layered metal  $2\text{H-NbSe}_2$ , *Phys. Rev. B* 64, 161103 (2001).
- [254] Y. Feutelais, B. Legendre, N. Rodier, and V. Agafonov, A study of the phases in the bismuth-tellurium system, *Mater. Res. Bull.* 28, 591 (1993).
- [255] P. Bayliss, and W. Nowacki, Refinement of the crystal structure of stibnite,  $\text{Sb}_2\text{S}_3$ , *Z. Krist.* 135, 308 (1972).
- [256] L. F. Lundegaard, R. Miletich, T. Balic-Zunic, E. Makovicky, Equation of state and crystal structure of  $\text{Sb}_2\text{S}_3$  between 0 and 10 GPa, *Phys Chem Minerals* 30: 463-468 (2003).

## References

---

- [257] C. Li , J. Zhao, Q. Hu, Z. Liu , Z. Yu, H. Yan, Crystal structure and transporting properties of  $\text{Bi}_2\text{S}_3$  under high pressure: Experimental and theoretical studies, *Journal of Alloys and Compounds*, 688, 32 (2016).
- [258] D. T. Morelli, V. Jovovic and J. P. Heremans, Intrinsically Minimal Thermal Conductivity in Cubic I-V-VI<sub>2</sub> Semiconductors, *Phys. Rev. Lett.* 101, 035901 (2008).
- [259] D. A. Polvani, J. F. Meng, N. V. Chandra Shekar, J. Sharp, and J. V. Badding, Large Improvement in Thermoelectric Properties in Pressure-Tuned p-Type  $\text{Sb}_{1.5}\text{Bi}_{0.5}\text{Te}_3$ , *Chem. Mater.* 13, 2068 (2001).
- [260] N. V. Chandra Shekar, D. A. Polvani, J. F. Meng, and J. V. Badding, Improved thermoelectric properties due to electronic topological transition under high pressure, *Physica B* 358, 14 (2005).
- [261] A. Segura, V. Panchal, J. F. Sanchez-Royo, V. Marn-Borrs, V. Muoz-Sanjos, P. Rodriguez-Hernandez, A. Muoz, E. Prez-Gonzalez, F. J. Manjn, and J. Gonzalez, Trapping of three-dimensional electrons and transition to two-dimensional transport in the three-dimensional topological insulator  $\text{Bi}_2\text{Se}_3$  under high pressure, *Phys. Rev. B* 85, 195139 (2012).
- [262] M. B. Nielsen, P. Parisiades, S. R. Madsen and M. Bremholm, High-pressure phase transitions in ordered and disordered  $\text{Bi}_2\text{Te}_2\text{Se}$ , *Dalton Trans.* 21;44(31) (2015).
- [263] A. Gaul, Q. Peng, D. J. Singh, G. Ramanath, T. Borca-Tasciuc, Pressure-induced insulator-to-metal transitions for enhancing thermoelectric power factor in bismuth telluride-based alloys, *Phys.Chem.Chem.Phys.* 24;19(20) (2017).
- [264] C. Zhang, C. Guo, H. Lu, X. Zhang, Z. Yuan, Z. Lin, J. Wang, and S. Jia, Large magnetoresistance over an extended temperature regime in monophosphides of tantalum and niobium, *Phys. Rev. B* 92, 041203 (2015).
- [265] Z. Wang, Y. Zheng, Z. Shen, Y. Lu, H. Fang, F. Sheng, Y. Zhou, X. Yang, Y. Li, C. Feng, and Z. A. Xu, Helicity-protected ultrahigh mobility Weyl fermions in NbP, *Phys. Rev. B* 93, 121112 (R) (2016).

## References

---

- [266] S. N. Gupta, A. Singh, K. Pal, D V S Muthu, C. Shekhar, Moaz A Elghazali, Pavel G Naumov, Sergey A Medvedev, C Felser, U V Waghmare and A K Sood, Pressure-induced Lifshitz and structural transitions in NbAs and TaAs: experiments and theory, *J. Phys.: Condens. Matter* 30 185401 (2018).
- [267] X. Yang, Y. Li, Z. Wang, Y. Zheng, and Z. A. Xu, Chiral anomaly induced negative magnetoresistance in topological Weyl semimetal NbAs, arXiv:1506.03190 (2015).
- [268] T. M. Tritt, N. D. Lowhorn, R. T. Littleton, IV, A. Pope, C. R. Feger, and J. W. Kolis, Large enhancement of the resistive anomaly in the pentatelluride materials  $\text{HfTe}_5$  and  $\text{ZrTe}_5$  with applied magnetic field, *Phys. Rev. B* 60, 7816-7819 (1999).
- [269] Y. Y. Wang, Q. H. Yu, P. J. Guo, K. Liu, and T. L. Xia, Resistivity plateau and extremely large magnetoresistance in  $\text{NbAs}_2$  and  $\text{TaAs}_2$ , *Phys. Rev. B* 94.041103 (2016).
- [270] R. Singha, A. K. Pariari, B. Satpati, P. Mandal, Transport properties of Dirac semimetal  $\text{ZrSiS}$ , *Proceedings of the National Academy of Sciences*, 114 (10) 2468-2473 (2017).
- [271] R. Jha, R. Higashinaka, T. D. Matsuda, R. A. Ribeiro, Y. Aoki, Anomalous magnetotransport properties of high-quality single crystals of Weyl semimetal  $\text{WTe}_2$ : Sign change of Hall resistivity, *Physica B* 536 68-71 (2018).
- [272] C. L. Zhang, S. Y. Xu, I. Belopolski, Z. Yuan, Z. Lin, B. Tong, G. Bian, N. Alidoust, C. C. Lee, S. M. Huang, T. R. Chang, G. Chang, C. H. Hsu, H. T. Jeng, M. Neupane, D. S. Sanchez, H. Zheng, J. Wang, H. Lin, C. Zhang, H. Z. Lu, S. Q. Shen, T. Neupert, M. Z. Hasan and S. Jia, Signature of Adler-Bell-Jackiw chiral anomaly in a Weyl fermion semimetal, *Nature Communications* 7, 10735 (2016).
- [273] H. Nielsen and M. Ninomiya, The Adler-Bell-Jackiw anomaly and Weyl fermions in a crystal, *Physics Letters B* 130, 389-396 (1983).

## References

---

- [274] I. Belopolski, P. Yu, D. S. Sanchez, Y. Ishida, T. R. Chang, S. S. Zhang, S. Y. Xu, H. Zheng, G. Chang, G. Bian, H. T. Jeng, T. Kondo, H. Lin, Z. Liu, S. Shin and M. Z. Hasan, Signatures of a time-reversal symmetric Weyl semimetal with only four Weyl points, *Nature Communications*, 8, 942 (2017).
- [275] Y. Zhou, X. Chen, N. Li, R. Zhang, X. Wang, C. An, Y. Zhou, X. Pan, F. Song, B. Wang, W. Yang, Z. Yang, and Y. Zhang, Pressure-induced Td to 1T' structural phase transition in  $WTe_2$ , *AIP Advances* 6, 075008 (2016).